# Airborne Aerosol Particle Measurements With a Focus On Conditions of High Humidity and Charged Mineral Dust

**Dissertation**

der Mathematisch-Naturwissenschaftlichen Fakultät
der Eberhard Karls Universität Tübingen
zur Erlangung des Grades eines
Doktors der Naturwissenschaften
(Dr. rer. nat.)

vorgelegt von
VASILEIOS SAVVAKIS
aus Chania, Griechenland

Tübingen
2024

Gedruckt mit Genehmigung der Mathematisch-Naturwissenschaftlichen Fakultät der Eberhard Karls Universität Tübingen.

Tag der mündlichen Qualifikation: 04.12.2024

| | |
|---|---|
| Dekan: | Prof. Dr. Thilo Stehle |
| 1. Berichterstatter: | Prof. Dr. Jens Bange |
| 2. Berichterstatter: | Prof. Dr. Jean Sciare |

*If you wish to make an apple pie from scratch, you must first invent the universe.*

---

Carl Sagan

# Abstract

Air pollution pervades every aspect of the modern world. Since the last century, the ongoing necessity for deeper comprehension of aerosol particle mechanics and behavior within the atmosphere, has become as crucial as ever. The aim of this work was to develop small-sized sensor systems for short-term aerosol measurements with a small uncrewed aircraft system (UAS), granting the possibility of operation at highly dusty or highly humid / cloudy conditions, which has so far been a burdensome challenge in this scientific field. For achieving such a goal, a lightweight measurement system was constructed, based on an optical sensor with the addition of a novel diffusion drying channel design, and then accommodated on two different UASs, one rotorcraft (known as the MASC-MC) and one fixed-wing aircraft (of type MASC-3). A series of laboratory experiments inside a fog tank showed that the new drying channel provided effective drying (from 95 - 96 % to 41 % relative humidity) for at least 30 min. Comparison of the sensor on the MASC-MC with high-end instrumentation at a governmental air pollution station in central Germany, gave promising results for particulate matter (PM) measurements under humid conditions. Vertical profiling through a low-level stratus cloud showcased the reliability of the system in determining cloud base accurately, as well as water vapour and liquid content inside the cloud, by employing a dual-measurement technique of identical sensors only differing on the addition of the drying channel. This technique of simoultaneous PM measurements with two sensors but a dryer on just one, was also used for the development of a new mathematical method for determining aerosol particle hygroscopic properties and air mass origin, based on the differences between ambient and dry airflow content. A similar system with the same optical sensor and drying channel was adopted for mineral dust measurements above Cyprus with the MASC-3, during a Saharan dust event in April, 2022. The scientific payload of the MASC-3 allowed for probing meteorological parameters (wind vector, turbulent kinetic energy, potential temperature and mixing ratio) with the addition of aerosol particle number concentrations and dust charge. The measurements successfuly captured the whole extent of the Saharan dust layer between 1600 and 2600 m above sea level (a.s.l), with a concentration peak of $100 \cdot \mathrm{cm}^{-3}$. Corresponding charge measurements indicated a charging effect from the aircraft body, which was handled through the development of a correction based on the observed linear relationship between dust charge and concentrations. Corrected dust charge profiles had peaks of 3 $\mathrm{pC} \cdot \mathrm{m}^{-3}$ mainly at the dust cloud edges, and they matched expected present charge amounts as a result of ion attachment processes. This illustrates that the dust was charged mainly due to ion attachment and not from a tribo-electric process. These are the first in-situ measurements with a UAS inside either clouds or Saharan dust, that can provide information such as moisture and droplet concentrations in the first case, or individual dust charge in the latter case. The developed sensor systems could be highly useful for follow-up research that would require UAS in-situ observations under the aforementioned atmospheric conditions.

# Zussammenfassung

Luftverschmutzung spielt in allen Aspekten der modernen Welt eine Rolle. Seit dem letzten Jahrhundert ist es so wichtig wie nie zuvor, die Mechanik und das Verhalten von Aerosolpartikeln in der Atmosphäre besser zu verstehen. Ziel dieser Arbeit war es, kleine Sensorsysteme für zeitlich begrenzte Aerosolmessungen mit einem kleinen unbemannten Flugsystem (UAS) zu entwickeln, das die Möglichkeit bietet, bei hoher Staubkonzentration oder sehr feuchten/bewölkten Bedingungen zu messen, was bisher eine große Herausforderung darstellte. Um dieses Ziel zu erreichen, wurde ein leichtes Messsystem konstruiert, das auf einem optischen Sensor mit einem neuartigen Diffusionstrocknungskanal basiert, und das auf zwei verschiedenen UAS untergebracht wurde, einem Multikopter (MASC-MC) und einem Starrflügler (MASC-3). Eine Reihe von Laborexperimenten in einem Nebeltank zeigte, dass der neue Trocknungskanal eine effektive Trocknung für mindestens 30 min ermöglichte (von 95 - 96 % auf 41 % relative Luftfeuchtigkeit). Ein Vergleich des Sensors auf dem MASC-MC mit High-End-Instrumenten einer staatlichen Messeinrichtung für Luftqualität in Mitteldeutschland ergab vielversprechende Ergebnisse bei der Messung von Feinstaub (PM) unter feuchten Bedingungen. Vertikale Profilmessungen durch eine niedrige Stratuswolke zeigten die Zuverlässigkeit des Systems bei der genauen Bestimmung der Wolkenbasis sowie des Wasserdampf- und Flüssigkeitsgehalts innerhalb der Wolke, indem eine Doppelmesstechnik mit identischen Sensoren eingesetzt wurde, die sich nur durch die Nutzung des Diffusionstrockners unterscheiden. Diese Technik der gleichzeitigen PM-Messung mit zwei Sensoren, bei der nur einer der Sensoren mit einem Trockner ausgestattet ist, wurde auch für die Entwicklung einer neuen mathematischen Methode zur Messung der hygroskopischen Eigenschaften von Aerosolpartikeln und zur Bestimmung des Ursprungs der Luftmasse verwendet, die auf den Unterschieden im Aerosolpartikelgehalt von Umgebungs- und Trockenluftstrom beruht. Ein ähnliches System mit demselben optischen Sensor und Trocknungskanal wurde für Mineralstaubmessungen über Zypern mit dem MASC-3 während eines Saharastaubereignisses im April 2022 eingesetzt. Die wissenschaftliche Nutzlast des MASC-3 ermöglichte die Untersuchung meteorologischer Parameter (Windvektor, turbulente kinetische Energie, potenzielle Temperatur und Mischungsverhältnis), ergänzt durch die Messung der Aerosolpartikelkonzentration und der Elektrischen Ladung des Staubs. Die Messungen erfassten erfolgreich die gesamte Ausdehnung der Saharastaubschicht zwischen 1600 und 2600 m über dem Meeresspiegel (a.s.l.), mit einem Konzentrationsmaximum von $100 \cdot \mathrm{cm}^{-3}$. Entsprechende Messungen der elektrischen Ladung wiesen auf einen Aufladungseffekt durch den Flugzeugkörper hin, der durch die Entwicklung einer Korrektur auf der Grundlage der beobachteten linearen Beziehung zwischen elektrischer Ladung und Staubkonzentration behandelt wurde. Die korrigierten Staubladungsprofile wiesen Spitzen von 3 $\mathrm{pC} \cdot \mathrm{m}^{-3}$ auf, vor allem an den Rändern der Staubwolke, und stimmen mit den erwarteten Ladungsmengen, basierend auf ein Prozess der Aufnahme von Ionen, überein. Dies zeigt, dass der Staub hauptsächlich durch Aufnahme von Ionen und nicht durch einen triboelektrischen Prozess elektrisch aufgeladen wurde. Dies sind die ersten In-situ Messungen mit einem UAS in Wolken oder Saharastaub, die sowohl Informationen zu Feuchtigkeit und Tröpfchenkonzentration als auch zur elektrischen Ladung von Staub liefern können. Die entwickelten Sensorsysteme können für zukünftige Forschungsprojekte, die In-situ-Beobachtungen mit UAS unter den oben genannten atmosphärischen Bedingungen erfordern, sehr nützlich sein.

# Acknowledgements

There is a number of people who contributed directly and indirectly to the eventual fruition of this work. Their support and assistance during this time is greatly appreciated and I am thankful to have come across them.

Firstly, I would like to thank my two supervisors Dr. habil. Andreas Platis and Prof. Dr. Jens Bange, who encouraged me to pursue this topic, placed a lot of trust in me and my ideas, and contributed with valuable insights along the way. I am grateful for the scientific freedom I was provided, the professionalism and the interaction within and outside of the workplace that I experienced during my years of work in Tübingen. I would also like to thank Prof. Dr. Jean Sciare, who was very eager and positive in looking over my work as an external supervisor. I am also thankful for the support of Dr. Frank Beyrich and the German Meteorological Service, during our experimental campaigns at the field site of Falkenberg. Moreover, I deeply appreciate the guidance and contributions of Dr. Keri Nicoll to parts of the scientific outcomes of this work, with whom I collaborated closely the last few months of my doctorate. I could not have achieved this without your expertise and diligence.

Secondly, sincere thanks to the Atmospheric Physics group: Martin, Kjell, Yann, Ines, Hasan, Jakob and Moritz, for the warm welcome and mentoring during the first months of my arrival in Germany. Also, I appreciate the collective supportive spirit of the Train2Wind team: Matteo, Gabriela, Yongtan and Mosaab, as we commenced and traversed the journey closely together. Thanks to fellow physicists and friends Giannis and Stamatis, for the numerous spirited scientific (and not only) discussions that provided to me a breath of fresh air amidst the tumult of academic life. My enormous gratitude goes towards my lifelong friends Haralambos and Maria, whose aid was not of a work-related nature, but nonetheless proved indispensable in helping me towards completion. I sincerely value the support from a fellow PhD candidate, Giulia, during the whole time we have been in Germany potently pursuing this common goal, each with their own hardships.

Lastly, I am forever thankful and would not be the person I am today, without my parents and brother. Everything I do, I do it through them.

# Abbreviations

**ABL** Atmospheric Boundary Layer

**AERONET** Aerosol Robotic Network

**AOD** Aerosol Optical Depth

**CAD** Computer-Aided Design

**CALIPSO** Cloud-Aerosol Lidar and Infrared Pathfinder Satellite Observations

**CCN** Cloud Condensation Nuclei

**CPC** Condensantional Particle Counter

**DWD** German Meteorological Service (Deutscher Wetterdienst)

**E-field** Electric Field

**EARLINET** The European Aerosol Research Lidar Network

**GF** Growth Factor

**GEC** Global Electric Circuit

**GEOS FP** Goddard Earth Observing System Forward Processing

**GCR** Galactic Cosmic Rays

**H-TDMA** Hygroscopic Tandem Differential Mobility Analyzer

**HYSPLIT** Hybrid Single-Particle Lagrangian Integrated Trajectory

**INS** Inertial Navigation System

**LiDAR** LIght Detection And Ranging

**MASC-3** Multipurpose Airborne Sensor Carrier

**MASC-MC** Multipurpose Airborne Sensor Carrier-Multicopter

**NOAA** National Oceanic and Atmospheric Administration

**NPF** New Particle Formation

**OAS** Optical Aerosol Spectrometer

**OPC** Optical Particle Counter

**PG** Potential Gradient

**PM** Particulate Matter

**PNC** Particle Number Concentration

**RH** Relative Humidity

**SEVIRI** Spinning Enhanced Visible and Infrared Imager

**SFR** Sample Flow Rate

**TAS** True Air Speed

**TKE** Turbulent Kinetic Energy

**UAS** Uncrewed Aircraft System

**USRL** Unmanned Systems Research Laboratory

**VDR** Volume Depolarization Ratio

**WHO** World Health Organization

# Contents

# Chapter 1

# List of Publications

This dissertation is the outcome of accumulated work on three peer-reviewed publications. All three manuscripts have been published in scientific journals, as noted below.

## 1.1 Peer-reviewed publications as first author

I **Savvakis V.**, Schön M., Bramati M., Bange J., Platis A. (2024) Small-scale diffusion dryer on an optical particle counter for high humidity measurements with an uncrewed aerial system, *Journal of Atmospheric and Oceanic Technology*. American Meteorological Society. 41(3): 205-219.

II **Savvakis V.**, Schön M., Bramati M., Bange J., Platis A. (2024) Calculation of aerosol particle hygroscopic properties from OPC derived PM2.5 data, *Meteorologische Zeitschrift*. Advances in Atmospheric Sciences. 33(2): 145-157.

III **Savvakis V.**, Schön M, Nicoll K., Ryder C., Pappeta A., Kezoudi M., Bange J., Platis A. (2024) In-situ observations of charged Saharan dust from an uncrewed aircraft system. *Aerosol Science and Technology*. London: Taylor & Francis. 58(11): 1249-1266.

## 1.2 Peer-reviewed publications as co-author

I Bramati M., Schön M., Schulz D., **Savvakis V.**, Wang Y., Platis A., Bange J. (2024). A versatile calibration method for rotary-wing UAS as wind measurement systems, *Journal of Atmospheric and Oceanic Technology*. 41(1): 25 - 43.

II Büchau Y. G., Mashni H., Bramati M., **Savvakis V.**, Schäfer I., Jung S., Miranda-Garcia G., Hardt D., Bange J. (2024) PARMESAN: Meteorological Timeseries and Turbulence Analysis Backed by Symbolic Mathematics. *Journal of Open Source Software*. 9(94): 6127.

III Schön M., **Savvakis V.**, Bramati M., Kezoudi M., Platis A., Bange J., OPC-Pod: A New Sensor Payload to Measure Aerosol Particles for Small Uncrewed Aircraft Systems (2024). *Journal of Atmospheric and Oceanic Technology*. American Meteorological Society. 41(5): 499 - 513.

IV Boventer J., Bramati M., **Savvakis V.**, Beyrich F., Kayser M., Platis A., Bange J. (2024). Validation of Doppler Wind LiDAR measurements with an Uncrewed Aerial System (UAS) in the daytime atmospheric boundary layer. *Journal of Atmospheric and Oceanic Technology*. American Meteorological Society.

V Bramati M., **Savvakis V.**, Beyrich F., Bange J., Platis A. (2024). In-situ uncrewed aircraft measurements of turbulent kinetic energy over heterogeneous terrain, *Journal of Atmospheric and Oceanic Technology*. American Meteorological Society. *Under revision*.

## 1.3 Conference participations

- **Savvakis V.**, Bramati M., Schön M., Mashni H., Platis A., Bange J. (talk) Identifying aerosol concentrations in wind farms using unmanned aerial systems. European Academy of Wind Energy (EAWE) PhD Seminar. 2nd to 5th of November, 2021. Porto, Portugal.
- **Savvakis V.**, Bramati M., Schön M., Platis A., Bange J. (talk) Sea salt concentrations estimation in off-shore wind parks. Wind Energy Science Conference (WESC). 23rd to 26th of May, 2023. Glasgow, Scotland.
- **Savvakis V.**, Bramati M., Schön M., Platis A., Bange J. (talk) Small diffusion dryer on an optical particle counter for aerosol monitoring with an uncrewed aerial system. International Society for Atmospheric Research using Remotely piloted Aircraft (ISARRA). 1st to 4th of August, 2023. Bergen, Norway.
- **Savvakis V.**, Bramati M., Schön M., Bange J., Platis A. (poster) Small-scale diffusion drying channel for aerosol particle measurements with an uncrewed aerial system. European Aerosol Conference (EAC). 2nd to 8th of September, 2023. Malaga, Spain.
- **Savvakis V.**, Schön M., Nicoll K., Bramati M., Bange J., Platis A. (poster) In-situ Saharan dust observations over the Eastern Mediterranean with an uncrewed aircraft system. European Geosciences Union (EGU). 14th to 19th of April, 2024. Vienna, Austria.
- **Savvakis V.**, Schön, M., Bramati, M., Bange, J., and Platis, A. (talk) In-situ measurements of Saharan dust concentrations and charge over Cyprus with an uncrewed aircraft system. European Meteorological Society (EMS). 2nd to 5th of September, 2024. Barcelona, Spain.

# Chapter 2

# Introduction

## 2.1 Fundamentals of aerosol science

Every breathing organism pollutes. According to the World Health Organization (WHO), nine out of ten people globally inhale impure air, and pollution is estimated to be accountable for nine million (one out of six) deaths per year (Fuller et al., 2022). One of the pollutants that are most important for concern regarding public health is Particulate Matter (PM), which is defined as the total amount of solid or liquid mass of aerosol particles suspended in the air, and can be single or aggregates of multiple element molecules (Vallero, 2014). Aerosols (etymology: "aero" - from the Ancient Greek word "$\alpha\acute{\eta}\rho$" = air, and "sol" - the first syllable in the world *solution*) are omnipresent in the atmosphere, have various sources with a wide variety of direct and indirect effects to the environment. For that, there has been a tremendous increase of interest in understanding aerosol characterization and mechanics, which stands as a daring challenge that branches out to several scientific fields.

The literature related to the detrimental effects of high amounts of PM on human health is vast (Arfin et al., 2023). Apart from that, there are significant atmospheric impacts that require our attention. Aerosols directly affect the Earth's radiative balance by scattering and absorption of incoming solar radiation (Yu et al., 2006). They are also often instrumental in cloud formation as they can act as Cloud Condensation Nuclei (CCN) (Spracklen et al., 2008), and their interaction with clouds and resulting precipitation has also been thoroughly studied (Hobbs, 1993; Devara and Manoj, 2013). Similarly to CCN, they can be activated for ice nucleation and contribute to ice forming in cases when it would not be expected to occur (Santachiara et al., 2010). Thick aerosol presence also decreases visibility, which often has adverse effects on urban center transportations and has been linked to aviation disasters (Moses and Akinyemi, 2017). An often overlooked but pivotal aspect connected to climate change is the so-called "global dimming" caused by long range transport and lifetime of particles (Wild, 2009). Temperature changes due to the higher scattering of radiation from these particles has been shown to have regional-scale repercussions over lands and oceans, with non-straightforward implications on the climatic balance when coupled to the larger phenomenon of global warming (Ramanathan, 2007). To comprehend the magnitude of these effects, one should dive into the composition of major aerosols, as well as their possible sources or sinks in the atmosphere.

Sources of aerosol generation are generally divided in two main categories: natural and anthropogenic. Natural sources include sea spray, wind-carried dust, volcanic activity, or biogenic aerosols (e.g. pollen, spores, bacteria, etc). Important anthropogenic sources refer to emissions

due to human activity, i.e. fossil fuel combustion, biomass burning, agriculture etc. (Chin and Kahn, 2009). Aerosols are also labeled as primary (directly emitted into the air) or secondary (a result of gas-to-particle conversion), depending on their formation process (Tomasi and Lupi, 2017). Their lifetime is contingent to their chemical structure and size, averaging from days to a few weeks in the troposphere (Pandis et al., 1995). Particles are then removed from the atmosphere either by deposition on the ground, referred to as dry deposition, or by precipitation droplet scavenging, referred to as wet deposition (Zannetti, 1990). Fig. 2.1 shows the global coverage of major aerosols on an indicative day. With different colouring for each one, the image displays: black carbon from agricultural burning or wildfire smoke (deep red color), sea salt (light blue) and mineral dust from the Sahara desert (light purple).

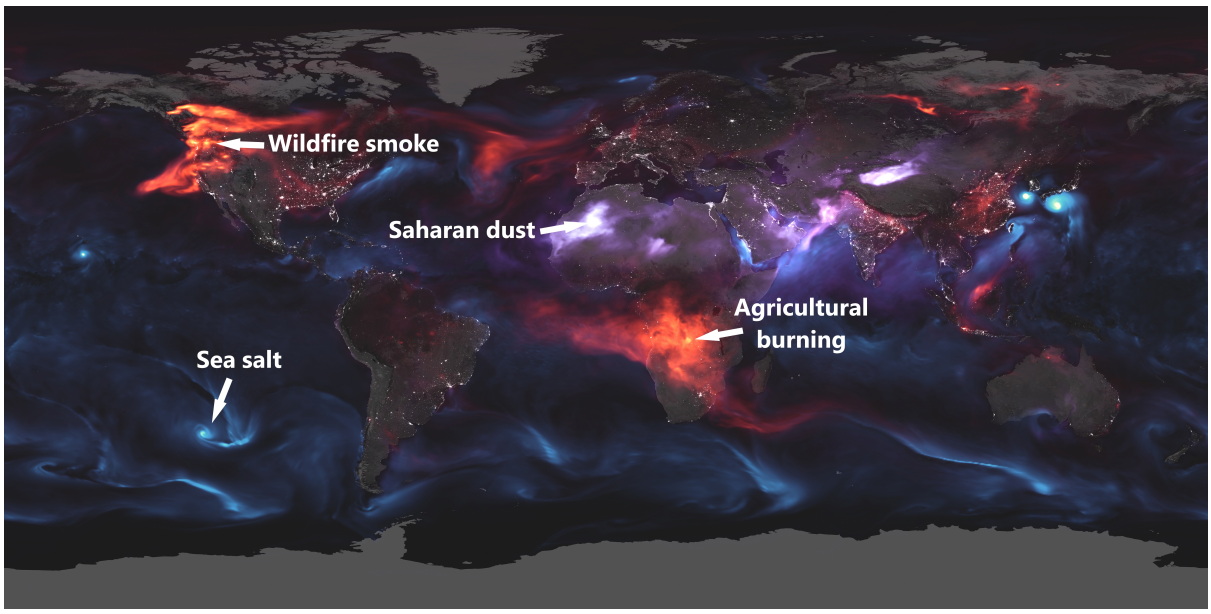


Figure 2.1: *"Just another day on aerosol earth." Model output of the Goddard Earth Observing System Forward Processing (GEOS FP), by the NASA Earth Observatory. Reproduced with permission.*

The most essential aspect of an aerosol is its size, which directly influences the physical laws that affect it, as well as its behavior and transport in the atmospheric air. Spherical aerosols are represented by their characteristic diameter, and non-spherical aerosols are described by the conceptual "equivalent" diameter, which is the diameter a spherical particle with the same physical properties as the one under inspection would have, if it were spherical (Kulkarni et al., 2011). Consequently, particles are most often assumed spherical and their size is described by their characteristic diameter. Atmospheric aerosols cover a size spectrum of a new nm, up to hundreds of μm in diameter (Thomas and Charvet, 2017), and their size distribution is one of the most heavily analysed subject matters related to aerosols (Willeke and Whitby, 1975). The size distribution is lognormal (i.e. skewed towards smaller sizes) in nature (Jaenicke and Davies, 1976), and represents the spatial variability of a specific particle property over the total covered size range. These properties most commonly are: particle number, area, volume or mass (John et al., 2011). Based on their volume size distribution, aerosol particles consist of three distinct size modes (Whitby, 1978): the nuclei / Aitken mode (sizes up to 0.1 μm), the accumulation mode (sizes from 0.1 to 2 μm) and the coarse mode (sizes above 2 μm).

The PM subtypes that relate to common pollutants are also expressed on the basis of the size of the aerosols of interest: $PM_1$ includes particles with an equivalent aerodynamic diameter up

to 1 μm, $PM_{2.5}$ includes particles up to 2.5 μm, and $PM_{10}$ particles up to 10 μm in diameter (WHO, 2021). PM, as defined above, is a quantity of mass concentration and has units of $\mu g \cdot m^{-3}$. Following the mindset of a size distribution, particle concentration is another means for describing aerosol amount of one of its properties in space (= over a unit of volume). For example, Particle Number Concentration (PNC) is the amount of particle number over a basic volume of air, and mass concentration is the amount of the total mass over the same basic volume of air, hence the units of mass over volume above (Kulkarni et al., 2011). Similarly, particle area and volume concentrations can be evaluated when deemed necessary.

There's extensive scholarly research and ongoing technological advances on aerosol monitoring standards and instrumentation (Vincent, 2007). One of the tools to obtain particle concentrations and size distributions is through optical sensing, and by exploiting instruments such as a Condensantional Particle Counter (CPC), an Optical Particle Counter (OPC) or an Optical Aerosol Spectrometer (OAS). These sensors, while having intricacies exclusive to each one, all operate under the same physical principle of Mie scattering (Drake and Gordon, 1985), which is a consequence of light's interaction with airborne particles. In an OPC, a laser beam illuminates a certain volume (i.e. the sampling volume), where the aerosol-borne air stream passes through. As particles cross the laser beam, photons scatter in all directions and then are redirected towards a photodectector that produces a voltage spike. This voltage spike is connected to the size of the aerosol particle, and all the different voltage responses / particle sizes are converted to a size distribution by populating discrete size channels (Colbeck and Lazaridis, 2014). Following that, the sensors usually introduce certain assumptions of sphericity, particle density, complex refractive index, and internally calculate PM values from the raw bin counts that have been recorded during each measurement period. Recently, OPCs have been substantially down-scaled and to meet the need of either ground based or airborne measurements at as many locations as possible, and low-cost alternatives are constantly being developed and assessed (Alfano et al., 2020).

## 2.2 Hygroscopic growth

Aerosol particles commonly found in the atmosphere exhibit a relative size growth behavior after interacting with surrounding water vapour at given Relative Humidity (RH) levels. This effect is called hygroscopic growth and it is characterized by a certain amount of water uptake by the aerosol particles, when conditions are humid enough (Swietlicki et al., 1999). Hygroscopic growth results in an increase of particle apparent size, as water vapour is adsorbed and a water layer is formed around the aerosol's solid core, resulting in a larger aerodynamic diameter of the wet aerosol compared to just its dry counterpart (Sorjamaa and Laaksonen, 2007). A visualisation of this phenomenon can be seen in Fig. 2.2.

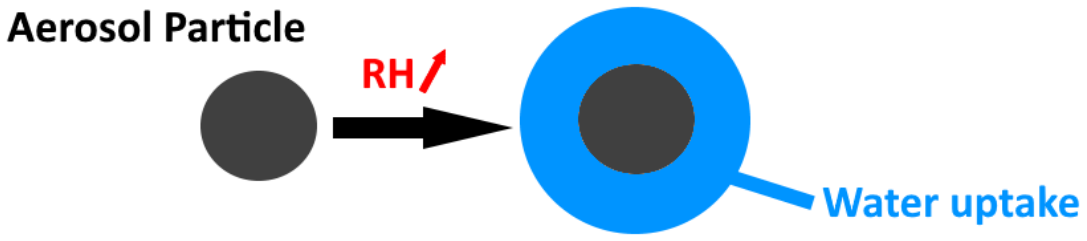


Figure 2.2: *The effect of hygroscopic growth on relative particle size.*

To quantify hygroscopic growth, a dimensionless parameter called the hygroscopic Growth Factor (GF) is defined, which is the ratio between the aerodynamic diameter of the aerosol at given humid conditions ($d_w$), over its aerodynamic diameter in dry conditions ($d_d$):

$$\mathrm{GF} = \frac{d_w}{d_d} \tag{2.1}$$

The level at which hygroscopicity is evident at various aerosols depends strongly on their chemical composition, with studies already performed on commonly met airborne particles, such as ammonium sulphate (Hämeri et al., 2000) or sodium chloride (Biskos et al., 2006). Inorganic salts such as the aforementioned ones, have been observed to undergo a hysteresis effect at varying RH conditions in the air, meaning that they adsorb or release water vapour at different rates when RH either increases or decreases. At dry conditions, RH may rise and the aerosol will not attract water vapour until a critical RH point, which is named the deliquescence point of the aerosol. At humid conditions, the aerosol may lose water vapour even below its deliquescence point, before crystallizing back to a completely dry particle, at a different critical point, which is named the efflorescence point. Hysteresis is therefore, the phenomenon of the deliquescence and efflorescence points of a particle being non-identical. An example of this is given in Fig. 2.3 for ammonium sulphate, whose growth curve has been determined experimentally (Lei et al., 2018), as it has a known deliquescence point at 80 % RH (Brooks et al., 2002), and an efflorescence point at 35 % RH (Di Antonio et al., 2018).

In case the aerosol is a composite of multiple elements, then its hygroscopic growth is also not described singularly. If particle structure is known, the resulting hygroscopic behavior takes all different components into account by weighting them with respect of their different singular hygroscopicities, and then considering their fraction amounts in the aerosol (Pariyothon et al., 2023). Various implications are culminated when considering active hygroscopicity on the aerosol particles. For instance, a correlation between New Particle Formation (NPF) and increased hygroscopic activity with a distinctive diurnal cycle has been observed in a previous works (Lance et al., 2013). Also, the affected interaction between the particle and incoming radiation, is also expressed in terms of altering light absorption (Michel Flores et al., 2012) and scattering coefficients of the aerosols (Tang, 1996), at conditions of high humidity. In relation to the ongoing battle against climate change, it has been shown that hygroscopically grown sulphates provide more efficient cooling in the lower stratosphere, where RH levels are higher (Krishnamohan et al., 2020). The consequence of hygroscopic growth on particle lung deposition has also been investigated (Vu et al., 2015).

Initial studies of the interaction of aerosol particles with present water vapour was done by using the electrodynamic balance between parallel rings, along with Raman spectrometry to identify small droplet behavior (Davis et al., 1990). The currently most established method for hygroscopicity analysis includes a Hygroscopic Tandem Differential Mobility Analyzer (H-TDMA) (Swietlicki et al., 2008). On the contrary, optical sensing techniques do not provide information on particle composition or water uptake. For example, optical sensors such as OPCs base their measurements on the apparent size of the sampled aerosols, and it is then quintessential to account for this size discrepancy when performing PM measurements, as what is of interest there is the mass of the dry aerosols and not the water vapour content in the air. The issue has so far been tackled with various approaches, and is the subject of this cumulative dissertation's first and second publication (Sect. 3.1 and 3.2).

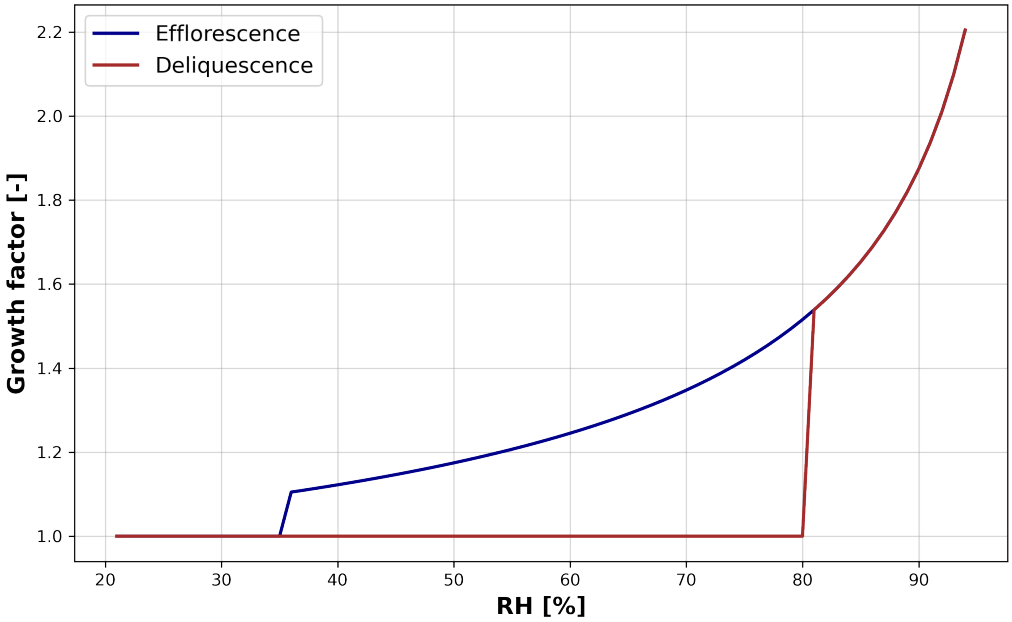


Figure 2.3: *Hygroscopic behavior of ammonium sulphate, at a RH range from 20 to 95 %. The growth factor equals to 1 when the particle has not adsorbed any water vapour. Starting from dry conditions, the growth factor will follow the deliquescence line (dark red) until 80 %, where there is a sudden jump and the particle grows significantly due to attracted air moisture. Then, when conditions become less humid, the growth factor follows the efflorescence line (blue), overlapping with the deliquescence everywhere except from 80 to 35 %. The particle becomes dry again below the efflorescence jump point. The figure has been reproduced with the same procedure described in Di Antonio et al. (2018).*

## 2.3 Mineral dust phenomenology

Airborne mineral dust from arid regions such as the Saharan desert is one of the largest natural PM sources on the planet. According to Varga et al. (2014), more than one billion tons of mineral dust from various sources are released in the air yearly. The same author notes that the amount of tons transported from Sahara through the Mediterranean basin is at the order of magnitude of $10^5$. It has been shown that such concentrations strongly influence the climate and atmosphere of the Mediterranean (Moulin et al., 1998).

As with any type of aerosol that scatters and absorbs incoming radiation, a direct effect of Saharan dust in the atmosphere is the perturbation of the radiative balance (Saidou Chaibou et al., 2020). Saharan dust can interfere with processes in clouds, due to the particles' CCN potential (Karydis et al., 2011; Kumar et al., 2011). Moreover, its interaction with numerous trace gases has shown a potentially significant impact on atmospheric chemistry (Bauer et al., 2004). The lifetime of airborne dust also affects its optical properties, and this in turn can have further radiative effect (Haywood et al., 2001) or induce changes on surface albedo (Ryder et al., 2013). It has been observed how Saharan dust high calcium carbonate ($CaCO_3$) content can raise pH levels in precipitation water, which leads to the so-called "red rain" (Loye-Pilot

et al., 1986). Since it is a vital factor for PM level increase, it has been linked to air pollution with further adverse human health impacts and mortality (Karanasiou et al., 2012; Kotsyfakis et al., 2019).

It is evidently difficult to define general morphological characteristics of mineral dust, but the majority of samples is seemingly comprised of silicates (e.g. quartz) and clay minerals (Scheuvens and Kandler, 2014). While the particles are most often non-spherical (Kalashnikova and Sokolik, 2004), the least error-prone method for side-stepping this when using optical sensing techiques, is the assumption of particle sphericity with an aerodynamic equivalent diameter (Reid et al., 2003). In numerous experimental studies that have been performed, Saharan dust has been shown to have a wide size distribution range, from a few nm up to larger than 100 μm (Ryder et al., 2019), but at times the particles were distributed around the range of a few microns (Gini et al., 2022). Different approaches in identifying the chemical and physical composition of dust have been analyzed (Formenti et al., 2010), yet due to the immense complexity that arises from particle shape, composition, age and large size range, accurate dust characterization proves to be a Herculean task.

The earliest study on sand and dust storms dates back to the 1940's (Hubert, 1943). First measurements of the dust's radiative effects and its transport in Europe were published four decades later (Carlson and Caverly, 1977; Prodi and Fea, 1979). Currently, surface level observations are mainly achieved with stations that provide long-term measurements (Cowie, 2014). Other than that, both remote and in-situ sensing techniques have been exploited for better tracking of dust events. For instance, the Aerosol Robotic Network (AERONET) provides a crucial chain grid of aerosol data from numerous sun / sky photometer stations that operate for the last 35 years (Holben et al., 1998). Vertically integrated Aerosol Optical Depth (AOD) profiles at different wavelengths and their corresponding Ångstrom exponents are indicators of coarse dust particles, which can also be identified among other aerosol types. Remote sensors such as LIght Detection And Ranging (LiDAR) systems are also extensively used for multiple reasons including dust trailing, in Europe more prominently with the The European Aerosol Research Lidar Network (EARLINET) (Pappalardo et al., 2014). Dust sources are examined with Earth-orbiting satellites, such as the Cloud-Aerosol Lidar and Infrared Pathfinder Satellite Observations (CALIPSO) (Winker et al., 2009) (operating since 2006) or by collecting spectral imaging data from the Spinning Enhanced Visible and Infrared Imager (SEVIRI) (Derrien and Le Gléau, 2005), on the Meteostat MSG (operating since 2003).

These satellites contribute significantly to dust transport models with input datasets that are valuable for reanalysis, for example as in Di Tomaso et al. (2022). The dust load is then assessed from AOD levels over vertical chunks, which however neglect changes of aerosol size distributions and concentrations inside the dust layer itself. This has led to inaccurate simulations when compared to remote or in-situ measurements (Chouza et al., 2016; Gasteiger et al., 2017; Ansmann et al., 2017; O'Sullivan et al., 2020), and underscores the crucial necessity for more comprehensive in-situ data sets with sufficient vertical range, which can be obtained with airborne platforms. There have been recent works related to Saharan dust measurements with crewed (Haywood et al., 2001; Highwood et al., 2003; Tanré et al., 2003; Petzold et al., 2009; Ryder et al., 2015; Liu et al., 2018), and uncrewed aircrafts (Renard et al., 2016; Schrod et al., 2017; Mamali et al., 2018). Nevertheless, crewed aircrafts may often disturb sampled air and data collection that demands high resolution (i.e. turbulence). The overarching link between meteorological conditions, turbulent structures, dust concentrations and accumulated charge density (see Sect. 2.4), explored *in-situ*, is still missing.

## 2.4 Space charge

In his famous *Lectures on Physics*, Richard Feynman opened his talk on atmospheric electricity by saying there is a 200 V difference between the height of your feet, and the height of your nose (Feynman et al., 1964). Of course, he was vividly referring to a quantification of the Earth's Electric Field (E-field), which can also be expressed as a vertical Potential Gradient (PG) of 100 $\mathrm{V \cdot m^{-1}}$ in the lower atmosphere and at undisturbed weather conditions (Chalmers, 2013). While the famous physics mastermind stated a constant value, the E-field actually undergoes a diurnal variation caused by thunderstorm and cloud precipitation activity, known as the Carnegie curve (Harrison, 2013). Charge transfer through this worldwide E-field produces a potential difference that sustains a vertical conduction current $J_c \approx 10^{-12}\mathrm{Am^{-2}}$, which exists globally and bridges the positively charged ionosphere with the planet's surface (Wilson et al., 1929; Chalmers, 2013). The interconnected system of electrical flows across the Earth's atmosphere, also more widely known as the Global Electric Circuit (GEC), was introduced by C.T.R. Wilson after a series of observations on thunderstorms (Wilson, 1921), and has been extensively studied since (Rycroft et al., 2000).

The fact that the Earth's atmosphere is a weak conductive medium stems from the presence of charged cluster ions in the ionosphere, which are generated due to the influx of Galactic Cosmic Rays (GCR) from further outside the solar system. Additional ionization occurs near the surface due to the decay of natural radioactive elements from the ground, such as radon (Rycroft et al., 2008). One can obtain the PG by simply dividing $J_c$ with a certain conductivity $\sigma$, which in this case, is the conductivity of the atmospheric air (Aplin, 2006). Small ion concentrations and mobility directly affects the $\sigma$ factor, which is in turn alters the resulting PG / E-field fluctuations (Gringel, 1986) locally. According to Gauss' law, electric charge emanates from the divergence of the E-field, specifically:

$$\nabla \cdot \mathbf{E} = \frac{\rho}{\varepsilon_0} \tag{2.2}$$

where $\mathbf{E}$ is the E-field in three dimensions, $\varepsilon_0$ is the permittivity in a vacuum and $\rho$ is the net electric charge per unit volume, which from here on will be referred to as space charge. As the directionality of the GEC and especially the E-field gradient is predominantly in the vertical axis, i.e. from higher altitudes towards the surface (Aplin and Harrison, 2013), of most interest is to convert Eq. 2.2 to one dimension:

$$\frac{dE(z)}{dz} = \frac{\rho(z)}{\varepsilon_0} \tag{2.3}$$

In the form of Eq. 2.3, the Gauss' law describes the distribution of space charge $\rho$ in relation to changes in the E-field with respect to altitude $z$, e.g. within the Atmospheric Boundary Layer (ABL). In the ABL, space charge can have a range from less than one to 80 - 100 pC $\mathrm{m^{-3}}$ (Nicoll et al., 2018) and can be transported by turbulent processes at convective conditions (i.e. the term "convective generator"), which is another important parameter that affects the GEC (Morozov, 2006). In areas of high aerosol particle or droplet concentrations, a scavenging procedure of the small ions by the larger particles can take place, which reduces $\sigma$ locally, and in turn increases PG and $\rho$ (Rycroft et al., 2008). Specifically, the small ions can get attached to the particles and transfer their charge on them, creating an electrical step jump at the boundaries between an aerosol layer and the aerosol-free air above and below it. Assuming an aerosol layer (e.g. a cloud, fog, or dust cloud) with reduced $\sigma$ compared to its surroundings, the passing of $J_c$ through it results in further changes in the E-field and is therefore another source of space

charge, which is eventually accumulated at the layer's boundaries. So far, observations of this phenomenon at the borders of clouds, have been thoroughly analyzed (Zhou and Tinsley, 2007; Harrison et al., 2020). In such cases, $\rho$ is a function of $d\sigma/dz$ and is expressed by the following formula (Nicoll and Harrison, 2016; Harrison et al., 2017):

$$\rho = \varepsilon_0 J_c \left(\frac{1}{\sigma^2}\right) \frac{d\sigma}{dz} \tag{2.4}$$

Eq. 2.4 reveals the parameters affecting aerosol charge, which are the magnitude of $J_c$ vertically, the conductivity $\sigma$ as well as its gradient in the same direction. It has been shown that ongoing microphysics in clouds are significantly influenced by charge on their boundaries (Harrison et al., 2015). A theoretical representation of the effect of a cloud layer on the vertical distribution of the basic electrical properties can be seen in Fig. 2.4. In essence, conductivity lowers inside the cloud due to ion scavenging from cloud droplets, which in turns increases PG and space charge is compiled at the edges, where $d\sigma/dz$ is highest.

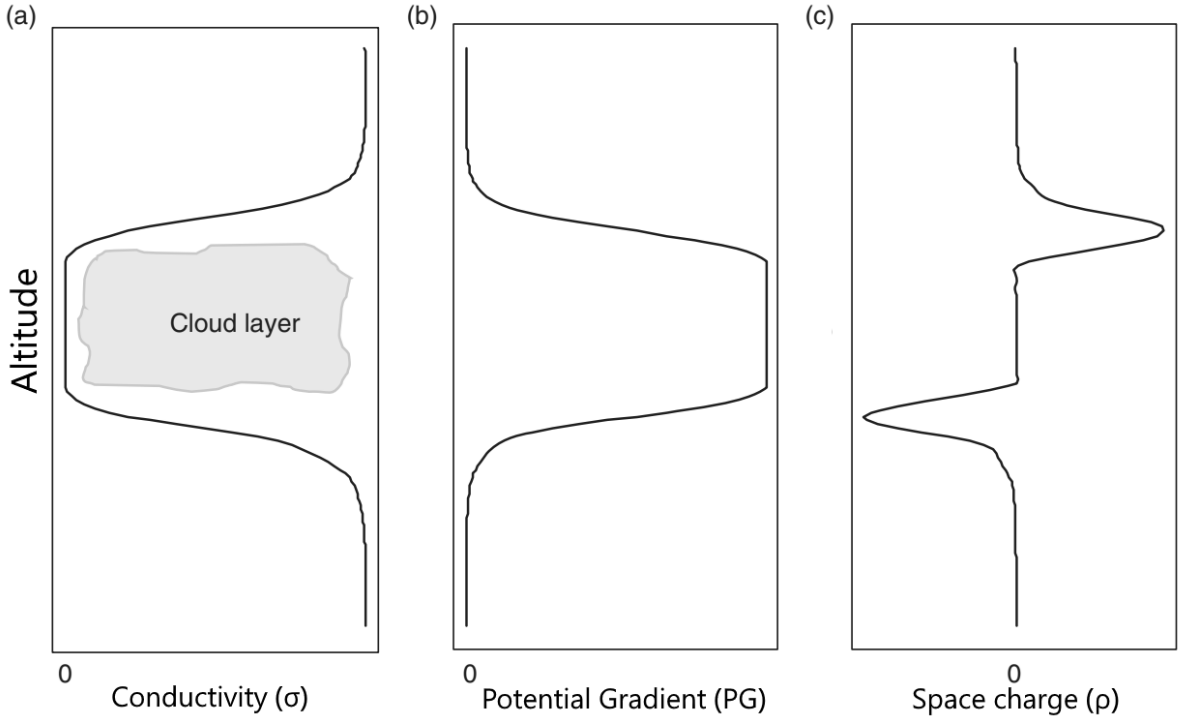


Figure 2.4: *Basic example of vertical profiles of three basic properties, at the presence of a cloud (units are arbitrary). (a) The conductivity, (b) the potential gradient, (c) the space charge. Reproduced from Nicoll and Harrison (2016) with permission.*

In conditions of dense aerosol presence, such as a mineral dust layer, high charging has been repeatedly observed, e.g. in Yair et al. (2016). This is due to similar physical procedures as in clouds, with the addition of another phenomenon named "triboelectrification" (Ferguson, 2010), which is a self-charging process from the dust particles themselves. Therefore, dust particle charging in the atmosphere is known to be a product of two main processes, namely ion-particle attachment and triboelectrification (Mallios et al., 2021). Airborne observations of charged Saharan dust is the topic of the third publication that comprises this dissertation (Sect. 3.3).

## 2.5 Uncrewed aircraft measurements

The utilization of Uncrewed Aircraft System (UAS) for atmospheric research has been on the rise in recent years, particularly for aerosol particle measurements, among other pollutants. A few distinct advantages of using miniaturized platforms such as UAS are their ability to be employed at complex, hard-to reach areas (urban or rural), their cost-effectiveness compared to bigger, crewed aircrafts, and the possibility of near-surface vertical profiling and data acquisition at multiple locations, unlike stationary towers or air pollution stations. This has led to a simultaneous development of UAS use for atmospheric measurements, as well as a tendency for miniaturization of the scientific payload, to dimensionally meet the needs for operation on an airborne platform.

Apart from meteorological parameters, airborne aerosol measurements with UAS have been under development the last two decades. Among other studies, fixed-wing systems have been used for profiling particles in the ABL (Corrigan et al., 2008; Altstädter et al., 2015; Schrod et al., 2017; Mamali et al., 2018; Harm-Altstädter et al., 2023). Additionally, small rotary-wing UAS have been used for air quality research (Alvarado et al., 2017; Gu et al., 2018; Bretschneider et al., 2022). This type of UAS has also been used for gas and particle measurements above volcanoes (Stix et al., 2018), pollen quantification (Crazzolara et al., 2019), and particulate matter levels assessment (Mayuga et al., 2018; Wang et al., 2020; Jumaah et al., 2021). Under these motives and on the foundation of instruments such as an OPC for PM data acquisition, small-sized payloads are built and evaluated for the improvement of airborne atmospheric research (Bezantakos et al., 2018; Girdwood et al., 2020). Autonomous pollution level monitoring with multiple UAS has been employed as well, as input for software-based air quality index (Rohi et al., 2020).

Two UASs were used in this cumulative work: the rotary-wing Multipurpose Airborne Sensor Carrier-Multicopter (MASC-MC), and a fixed-wing aircraft referred to as the Multipurpose Airborne Sensor Carrier (MASC-3), both operated by the Atmospheric Physics group at the department of Earth Sciences of the university of Tübingen, Germany. Each UAS featured scientific payload specifically designed for its own platform, for measurements of meteorological parameters as well as aerosol particles with lightweight, miniaturized instrumentation. More detailed description can be found in the following two subsections.

### 2.5.1 MASC-MC

The MASC-MC is a rotary-wing UAS based on the Spreading Wings S900 frame by the well-known Chinese company DJI. It is a hexacopter (= six rotors) with a 900 mm rotor distance, an approximate height of 1.2 m and weight of 3.8 kg. Onboard the platform is an autopilot apparatus (PixHawk 2.1 Cube Orange) and the system is controlled through that and open source firmware (Arducopter v. 4.0.5). Flight missions are simulated beforehand on a ground computer, with appropriate software (Mission Planner), and they are pre-loaded on the autopilot system for autonomous operations. The UAS pilot is usually responsible for take-off and landing, as well as monitoring ongoing missions with little to no interference. Attitude and flight parameters are recorded on the system during flight at a frequency of 10 Hz, and pairs of 6S Lithium-Polymer batteries (weight of 3 kg, capacity of 12000 mAh each) provide flight endurance of 20 - 25 min, depending on the conditions.

An array of six miniaturized sensors (one under each rotor arm) provides meteorological measurements (temperature, humidity and air pressure) at a frequency of 1 Hz. The UAS is

encased in two styrofoam domes of a 50 cm diameter, which cover all the electronics and different components except the six rotors. This converts its overall shape to an approximate sphere. Air sampling for PM measurements is located at the top of the upper dome, which has a 4 cm circular opening connected to the inlet of an OPC sensor system mounted on the UAS platform. This sensor system hosts an OPC of type N3 (Alphasense, United Kingdom) with an adjusted diffusion drying channel, connected to a small computer (Raspberry Pi 3b+) for data acquisition at 1 Hz. The OPC-N3 has a size range from 0.35 to 40 µm across 24 size channels and a weight of 100 g. Aspiration is provided using a micro-fan at the exhaust of the OPC, and the connections are airtight in a way that the airflow first passes through the dryer and then across the sampling area of the OPC.

The total weight of the MASC-MC, including the batteries and sensor load, is at 7.3 kg. Standard ascent rate of 1.5 m $s^{-1}$ gives a maximum altitude range of about 800 - 900 m. The UAS has been employed in a few scientific studies before, e.g. for a sensor-free horizontal wind estimation method (Bramati et al., 2024) or measurements of pollen with an impactor (Crazzolara et al., 2019). A picture of the system in flight can be seen in Fig. 2.5.

Figure 2.5: *The MASC-MC, which is an altered version of the DJI S900 commercial frame, in operation. The autopilot system, batteries and sensor electronics are located inside the two styrofoam domes, while an opening at the upper dome's top allows for aerosol particle sampling. Photo by Martin Schön.*

### 2.5.2 MASC-3

The MASC-3 (shown in Fig. 2.6) is the third generation the MASC (Wildmann et al., 2014), a small fixed-wing aircraft designed for atmospheric research with a focus on turbulence measurements. The mass of the aircraft, including a standard 1.5 kg scientific payload, is about 8 kg. It has a length of 2.1 m and a wing span of 4 m, with an endurance of up to 2.5 h.

Similarly to the MASC-MC, the MASC-3 operates with the assistance of a Pixhawk 2.1 Cube Orange autopilot, and its automated missions are executed through Mission Planner. Data acquisition is achieved by logging onboard the aircraft at a frequency of 100 Hz. This includes the three-dimensional wind vector with a five-hole probe and the aircraft's Inertial Navigation System (INS), temperature with a finewire platinum thermometer, alongside a slower digital temperature and humidity sensor (SHT31 - sampled at 12 Hz) (Rautenberg et al., 2019). The configuration at the given temporal resolution provides accurate measurements of meteorological parameters, as well as turbulence parameters such as the Turbulent Kinetic Energy (TKE). Sensors are located at the nose of the aircraft, so flight and attitude effects on the measurements are minimal (Rautenberg et al., 2019). The nominal cruising speed of the MASC-3 is at 18.5 m $s^{-1}$.

Additionally to the sensors described above, two oval-shaped Pods are installed on each wing of the aircraft. One Pod (referred to as the OPC-Pod) is dedicated to aerosol particle measurements (Schön et al., 2024), with a modified OPC-N3 that samples the airflow based on passive aspiration, taking advantage of the aircraft speed and its aerodynamic shape (Mashni et al., 2023). The system also features a drying chamber and operates at a frequency of 1 Hz. The second Pod (referred to as the Charge-Pod) provides measurements of space charge, with an appropriately designed charge sensor at a frequency of 10 Hz. The Pod sensors' measurement principles and evaluation on the MASC-3 have been described in other publications (Schön et al., 2022a, 2024).

Including the two Pods, the total payload of the UAS is approximately 2 kg. As a whole, this aircraft stands as a unique UAS capable of capturing aerosol concentrations, related charge on these aerosols, and meteorological conditions at high resolution, along with information on turbulence. In this configuration, the maximum altitude that has been achieved with it was 5700 m and so far, it has been employed in several atmospheric research studies, e.g. in Mauz et al. (2019); zum Berge et al. (2021); Schön et al. (2022b).

Figure 2.6: *The MASC-3 in flight, with its scientific payload mounted in the front and both Pods on the wings. Photo by Christos Keleshis.*

## 2.6 Objectives

Numerous topics have been introduced in Chapter 2, and all of them include knowledge that is essential for the achievement of a common goal: precise aerosol measurements with a UAS. While this practice has gained traction the recent years, there are several unresolved questions for achieving the possibility of reproducible aerosol monitoring at different weather conditions, and expertise is required at an array of fields. The aim of the different work parts of this dissertation was to address a set of rather specific issues, related to airborne aerosol particle measurements.

On the ground, methods of drying sampled aerosols are widely used, as the necessity dictates so, yet there is no equivalent system small or light enough for a UAS. At the same time, commonly used low-cost OPCs rarely include a drying component, which is an overall fragile point in the ever-growing sensor industry. Lastly, research including in-situ measurements of the effect of atmospheric electricity on the lifetime and behavior of dust particles, is essentially non-existent. Based on these outlines, the following goals were set:

1. Development of a small-sized, cost-effective OPC sensor system including a novel drying procedure with appropriate dimensions for employment on a small UAS, and its evaluation in outdoor conditions

2. Postulation of a new mathematical method for asserting levels of hygroscopicity in the sampled aerosol, solely by acquiring PM data from OPC sensors and the plausibility of assessing the air mass content or origin from its hygroscopic behavior

3. Simultaneous aerosol concentrations and space charge measurements with a UAS during a Saharan dust event and an analysis of the relationship between the two in conjunction with ongoing meteorological conditions

Resolving the points above required the design of new, task-specific components for the assembly of sensors and electronics, rigorous experiments in the lab and in the real environment, and extensive algorithm development for acquiring and analysing the data. Accordingly, the Results are presented in Chapter 3, and the Discussion and Outlook follow in Chapters 4 and 5.

# Chapter 3

# Results

This chapter provides a concise overview of the key findings included in this dissertation, which are further elaborated in the attached peer-reviewed publications (see Sect. A.1 - A.3).

## 3.1 Objective I - UAS aerosol particle measurements using an OPC with a small-sized diffusion dryer

For accurate aerosol particle measurements under humid conditions, it is necessary for the airflow to be sufficiently dried before passing through the sampling volume of a sensor such as an OPC. As explained in Sect. 2.2, disregard of the moisture in the airflow leads to erroneous OPC readings, due to the effect of hygroscopic growth on the apparent size of the aerosol particles (Swietlicki et al., 2008). The motivation of this work was the construction of an OPC adjustable small-sized, lightweight drying system for short-term measurements with a UAS, and its subsequent validation at high humidity conditions in the laboratory, as well in an outdoor environment.

Low-cost OPCs without treatment of the water vapour in the air prior to sampling have been observed to have significant bias on PNC levels (Jayaratne et al., 2018) and PM concentrations (Vogt et al., 2021), at conditions of high humidity. So far, post-processing mathematical corrections on the data have been applied (Crilley et al., 2018; Di Antonio et al., 2018) or usage of heated inlets on the sensors (Magi et al., 2020). However, these inlets may have thermal losses and would require a power supply to operate, while RH-based mathematical corrections are based on aerosol particle composition assumptions, and are limited to an RH range that doesn't include near saturation or saturation conditions. Furthermore, hygroscopicity also affects the optical properties of the aerosols (Tang and Munkelwitz, 1994), which is not taken into account in the aforementioned post-processing formulations. To solve the negative effect of hygroscopic growth on PM measurements more adequately, it is therefore preferable to employ a drying component on an OPC that is sustainable (i.e. not requiring external power or energy) and reduces RH to levels of 40 % or lower, before sampling takes place.

Recent works related to applying low-cost drying on the airflow for sampling with optical sensors focused on laboratory conditions and featured larger and heftier drying channels (Masic et al., 2020; Samad et al., 2021; Chacón-Mateos et al., 2022). A study that included airborne

aerosol particle measurements with a crewed aircraft, also featured a bigger dryer with considerable weight (Platis et al., 2016). Such dimensions are unfavorable for employment on a UAS, where size and weight are crucial for balanced flights, endurance and data acquisition. Experiments with a rotary-wing UAS and a non-drying OPC-N3 onboard noted the necessity of a dryer's addition for accurate measurements in humid conditions (Samad et al., 2022). This emphasizes the importance of designing a downscaled, lighter and inexpensive drying channel for airborne operation.

In this publication, a small-sized diffusion drying channel was designed and evaluated in laboratory and outdoor conditions, for the purposes of employment on an OPC onboard the MASC-MC (Sect. 2.5.1). Initially, the performance of the dryer in effectively reducing water vapour was investigated in a self-constructed fog chamber, by taking RH measurements before and after the airflow has passed through it. Then, the dryer was adjusted to a sensor system including an OPC-N3 on the platform of the MASC-MC, and hovering flights near an established governmental air pollution station (Mannheim-Nord, Mannheim, Germany) were conducted under highly humid conditions (88 - 94 % RH), where the data from the UAS were compared to the high-end OAS Fidas Frog 200 (Palas, Germany), which has the same measurement principle like an OPC for PM measurements. Apart from the laboratory experiments and the comparison against a reference instrument, the UAS also performed vertical profiles through a low-stratus cloud at a rural location near Lindenberg, Germany, where the German Meteorological Service (Deutscher Wetterdienst) (DWD) maintains the 98-m high Falkenberg meteorological tower. Detection of the cloud base was compared to a ceilometer (CHM 15k NIMBUS - Lufft GmbH, Germany) operating at the location, and the changes in PM levels through the cloud were investigated.

This dryer is based on the principle of diffusion drying, which is widely used alongside optical sensors for PM measurements in air pollution stations around the world. In essence, the airflow passes through a cylinder where its liquid content diffuses to a dessicant, reducing its RH along the way from the dryer's inlet to its exhaust. It consists of two co-axial tubes, from which the inner one is perforated, and in between them the absorbent material is placed. In this case, blue silica gel beads were chosen, as they are color coded (blue: dry beads, purple: wet beads), making it convenient to distinguish when the material has saturated with water vapour. Once it is saturated, the beads can be dried back by exposure to a temperature of 70 - 80 $^{\circ}$ C, for a short amount of time. This makes the dryer more sustainable than alternatives, which would require constant power to operate. The dimensional specifications are given in Table 3.1:

Table 3.1: Dimensions and material used for the design of the drying channel. Taken from Savvakis et al. (2024c).

| | **Inner tube** | **Outer tube** |
|---|---|---|
| Inner diameter [mm] | 6.2 | 20 |
| Outer diameter [mm] | 6.5 | 23 |
| Material | Liquid Resin | Poly Lactic Acid (PLA) |
| Length [mm] | 120 | 99 |

The design of both tubes was done with Computer-Aided Design (CAD) software and then 3-D printed. For the inner tube, where wall smoothness is essential, the technique of masked stereolithography was used with cured liquid resin as the material, since the resulting product

has high horizontal and vertical resolution. Its hole openings are distributed in equal distances and have a diameter of 1.6 mm, covering the whole length of the dryer. As abrupt changes in tube diameter can result in particle losses (Muyshondt et al., 1996), the tube's inner diameter is 6.2 mm, to match the parent inlet of the OPC-N3. Another source of particle loss can be due to static electricity (Liu et al., 1985), so the printed tubes were sprayed with graphite paint as a coating for conductivity of the material. The total weight of this dryer, including the silica beads, is approximately 50 g.

Since the only modification done on the OPC-N3 was the addition of an extra tubing component, its effect on the resulting flow rate through the system from the sensor's micro-fan was examined by taking PM measurements with and without the dryer. Specifically, three cases of having a dryer attached, replacing it with a regular, non-perforated tube of the same length, or having neither of the two attached, was considered to look at how much the data output would be affected in each case. Apart from the effect on $PM_1$, $PM_{2.5}$, and $PM_{10}$, the change in Sample Flow Rate (SFR) was also inspected. Results from consecutive short-term measurement periods can be seen in Fig. 3.1.

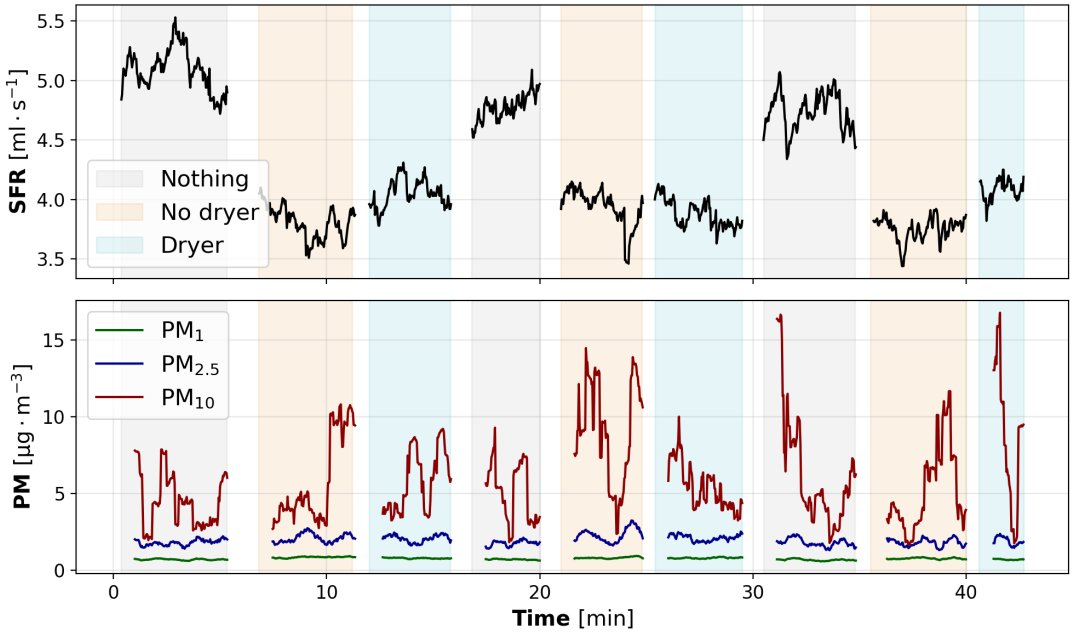


Figure 3.1: *SFR and PM types for the three measurement cases: no dryer attached (gray areas), a regular tube attached (orange areas) and a dryer attached (cyan areas). The time series covers approximately 45 minutes and the gaps indicate parts' adjustments between the different cases, which were removed from the data analysis. Taken from Savvakis et al. (2024c).*

When nothing was attached to the OPC-N3, the SFR had a mean value of $4.8 \pm 0.2$ ml $\cdot$ s$^{-1}$ and were close to the typical value provided by the manufacturer, namely around 5 ml $\cdot$ s$^{-1}$. SFR then had a lower value for the cases when a regular tube or a drying tube was attached, with mean values of $3.9 \pm 0.2$ ml $\cdot$ s$^{-1}$ and $4 \pm 0.1$ ml $\cdot$ s$^{-1}$, respectively.

This change, however, had little impact to the PM output of the OPC, which exhibited little to no identifiable differences between the three cases. Specifically, the measured $PM_1$ and $PM_{2.5}$ hardly varied across all measurements, being slightly lower during the cases when an extra tube was attached to the sensor. This reduction was at the second decimal of the PM value

(0.72 $\mu g \cdot m^{-3}$ and 0.79 $\mu g \cdot m^{-3}$ for $PM_1$, 1.87 $\mu g \cdot m^{-3}$ and 1.98 $\mu g \cdot m^{-3}$ for $PM_{2.5}$), which is a deviation smaller than the indicated accuracy of the sensor by the manufacturer. The three different cases also had no identifiable effect on $PM_{10}$ either. A previous study with a longer self-made dryer noted a deviation of just 2 % on the flow rate of their OPC system (Chacón-Mateos et al., 2022), which for these experiment was at varying values but up to 17 %, yet the PM data in Fig. 3.1 suggest no alteration of the measurements due to the dryer alone.

To consider the effectiveness of the dryer at humid conditions, it was first used in a self-constructed fog tank. The tank features an airtight plastic container with water and an ultrasonic humidifier. When the humidifier is in operation, visible fog forms in the tank, which is a result of decoupled liquid droplets at the surface of the water due to mechanical oscillations produced by emitted high frequency signals. The constructed dryer is then placed horizontaly, connecting the fog tank with a second, smaller box of ambient air, and a micro-pump at the same power as the OPC-N3's fan ensures a flow with a direction from the fog tank, through the dryer and then in the ambient air box. Two miniaturised meteorological sensors (SHT31 - Sensirion, Switzerland) collect RH data in the fog tank and in the ambient air box, capturing the water vapour reduction as the air passes from a highly humid / saturating environment to one with initially dry air. The setup is visualised in Fig 3.2.

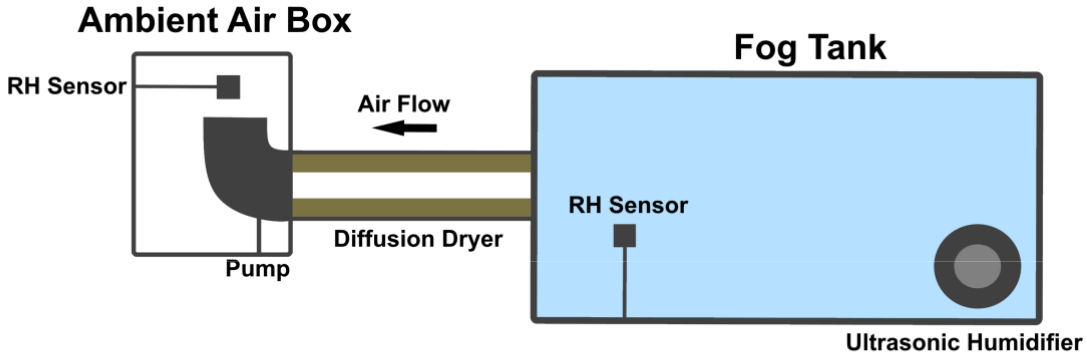


Figure 3.2: *Sketch of the experimental setup during the evaluation of the dryer in the laboratory, at the self-constructed fog tank. The pump draws air from the fog tank, which first passes from the dryer and then RH measurements in the ambient air box, are compared to RH measurements inside the induced fog. Taken from Savvakis et al. (2024c).*

These experiments were split into two sections, one with the dryer in place and one with a regular tube, and a time series of the two RH levels (in the fog tank, and in the ambient air box) was compared for quantifying the drying performance during a short amount of time. Since the aim is to provide drying at least as long as the endurance of the MASC-MC, employment is intended for short-term airborne measurements, rather than longer-term data collection from stationary sources (e.g. towers, stations etc). The results can be seen in Fig. 3.3.

Looking at Fig. 3.3a and once the pump is turned on, there is an evident reduction of RH from 95 % inside the ambient air box, down to 41 % in the ambient air box, for a total of almost 35 minutes, due to the drying from the dryer in place. In the equivalent experiment with an absent dryer (Fig. 3.3b), there is virtually no RH difference between the two containers as there is no drying component included in the setup. Generally, RH levels of around 40 % are considered low enough for the hygroscopic growth effect to be negligible and the airflow to be considered as dry (Held and Mangold, 2021), which is also a boundary that has been

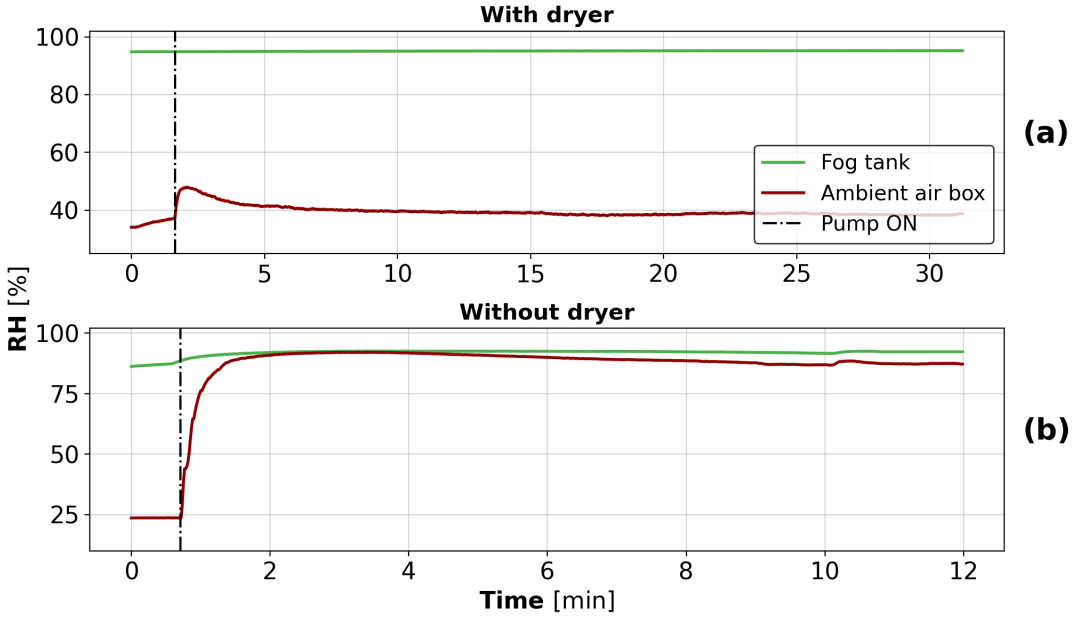


Figure 3.3: *RH measurements during the fog tank experiments, split into two different measurement sections. In both cases, the dark red line is the measurement in the ambient air box, the green line is the measurement inside the fog tank, and the vertical dashed line shows the time of turning the micro-pump on. (**a**) Experiment with a dryer. (**b**) Experiment without the dryer. Taken from Savvakis et al. (2024c).*

put forth in other experimental studies with low-cost OPCs and self-made dryers (Bezantakos et al., 2018). Moreover, the constructed dryer provides drying for at least 30 minutes, which is a longer time duration than the 20 minute flight endurance of the MASC-MC. As a result, the conclusion can be taken that it is appropriate for short-term use with the UAS for airborne measurements, even at humid conditions as high as almost at saturation.

Such airborne measurements were performed and compared against the OAS Fidas Frog 200, a high-end instrument commonly used as reference for validation studies (Bílek et al., 2021; Vogt et al., 2021), which operated at the roof of the Mannheim-Nord air pollution station in Mannheim, Germany. The MASC-MC performed four consecutive hovering flights at a low altitude of approximately 7 m, the same as the level above the ground where the stationary sensor collects data. The measurements took place on the 14th of February, 2022 with the following strategy: each pair of flights first featured the dryer and then it was removed, so that a difference in PM concentrations due to the hygroscopic growth effect could be identified. Apart from that, comparison of both cases with or without a dryer was done against the Fidas 200, to assess the overall accuracy of the system while in flight. Figure 3.4 shows the RH and PM measurements with the MASC-MC, in relation to the reference instrument.

RH levels had a mean value of 94 % during flights 1 and 2 in the morning, and 88 % during flights 3 & 4 in the afternoon. During both flight pairs, there is a clear overestimation in all PM measurements when there was no dryer in place with the OPC, compared to the Fidas 200. When the dryer was included in the OPC configuration, PM measurements were at the same order of magnitude as the reference, except the slight underestimation of 8 - 13 % in $PM_1$. This difference could be expected due to the lower cut-off boundary the Fidas 200 has in its lowest size channel, which includes aerosol particles as small as 150 nm in diameter, whereas the

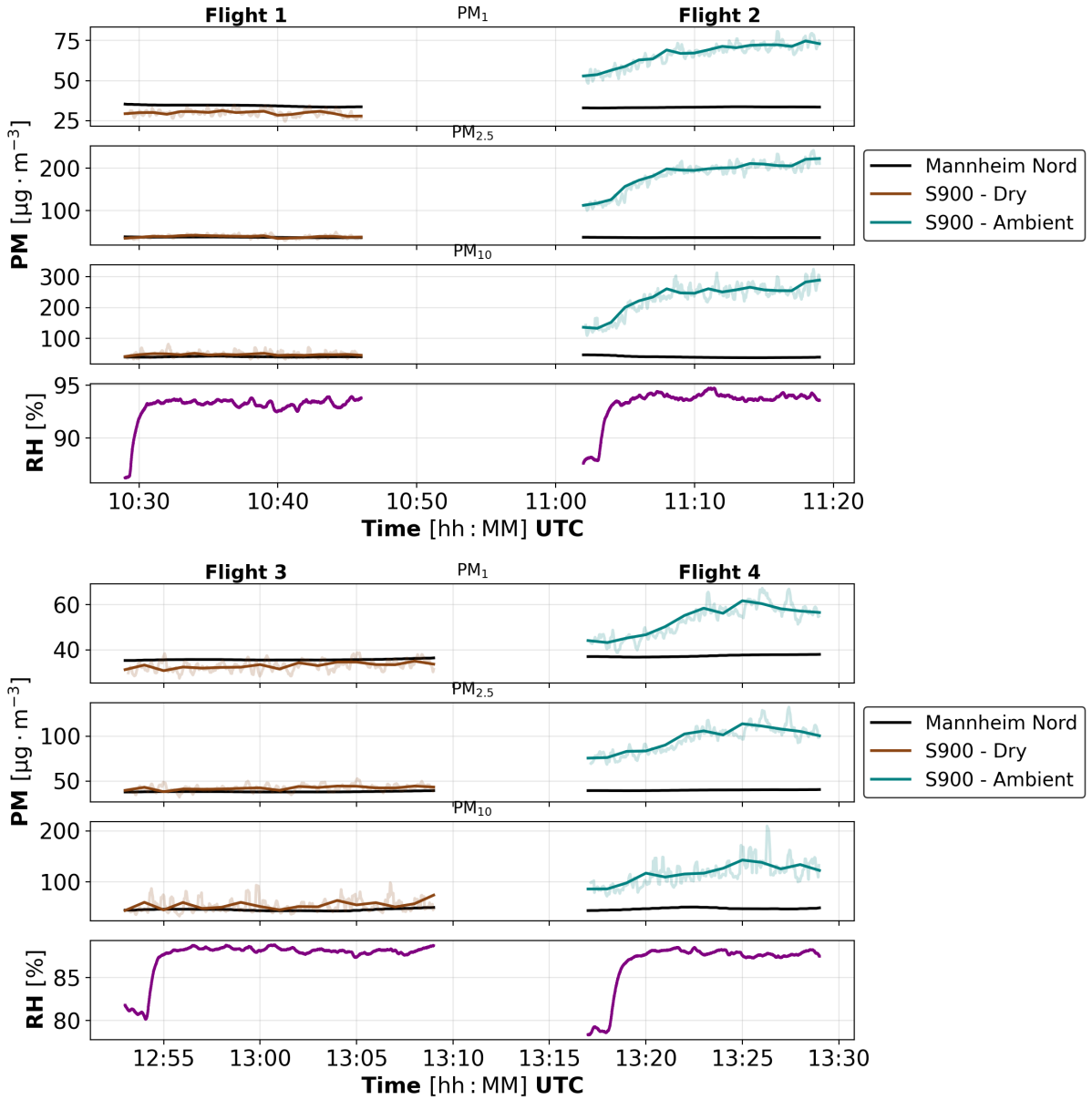


Figure 3.4: *Measurements at the Mannheim-Nord measurement station. The black lines show the data from the reference Fidas 200, brown lines indicate the flights with a present dryer, and the blue lines indicate the follow-up flights without a dryer. RH levels during the times were collected from SHT31 sensors onboard, and are shown on the bottom subplots. From the PM measurements with the UAS, the solid lines are 1 minute mean averages, and the less opaque lines of the same colors are non-averaged. Taken from Savvakis et al. (2024c).*

lowest size channel of the OPC-N3 is at a diameter of 350 nm. This means that the Fidas 200 sums aerosol particles from a wider size range for its resulting $PM_1$ value, than the OPC-N3. Largest overestimations during the flights without a dryer were recorded in the morning flights with higher humidity, and specifically for $PM_{10}$ (about 480 % higher). Since the flight pairs were performed consecutively with exactly the same UAS and setup, differing solely on the use of a dryer, these differences can be attributed to a strong hygroscopic growth effect during these highly humid conditions, which was evidently mitigated by the active drying component.

On November 22nd 2022, the MASC-MC was employed for vertical profiling through a low-altitude stratus cloud during conditions of high humidity at the boundary layer field site Falkenberg in Lindenberg, Germany. The UAS ascended at a rate of 1.5 m/s up to 200 m during the morning and afternoon, with a similar strategy as in the Mannheim-Nord evaluation experiment, by consecutively using and not using the dryer. The focus of the measurements was to identify the cloud base, quantify liquid water droplets as well as amounts of present water vapour prior to saturation, and the cloud ceiling. The first two flights were done in the early morning (07:50 UTC) when the cloud was low in altitude and visible by eye, and flights 3 & 4 in the afternoon (14:00 UTC) when the cloud was not present in the same vertical extent. Results from the vertical profiles are shown in Fig. 3.5.

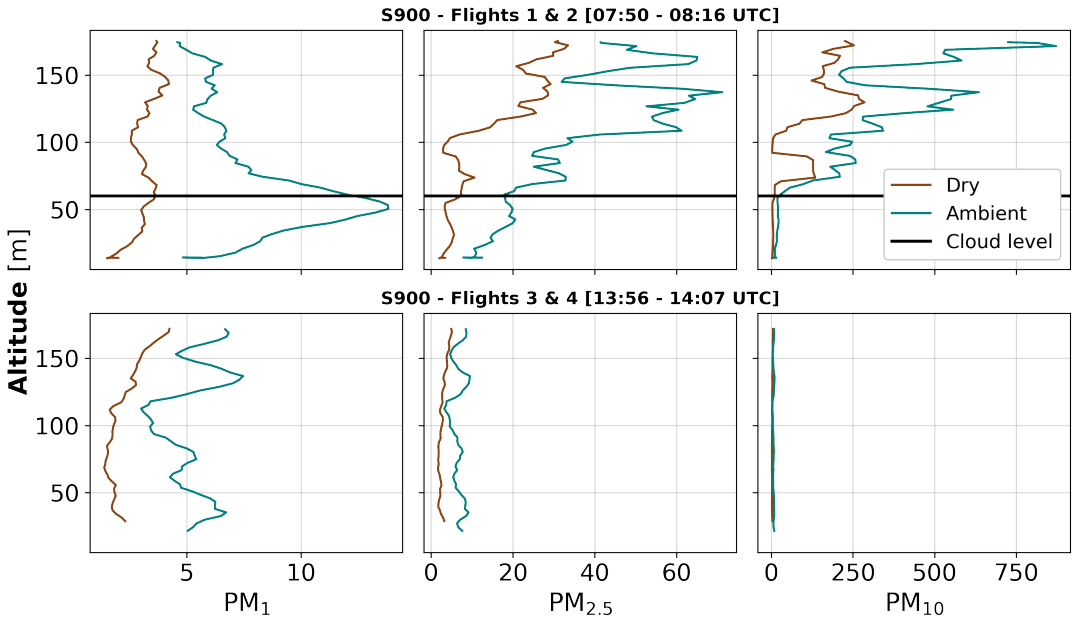


Figure 3.5: *Vertical profiling near the Falkenberg meteorological tower. "Ambient" flights refer to the cases when no dryer was used for the measurements, and "dry" refers to the same profiles but with a dryer in place. A vertical black line in flights 1 & 2 shows the cloud layer base, as recorded by the ceilometer CHM-15k at the location. Units for the three PM values are* $\mu g \cdot m^{-3}$. *Taken from Savvakis et al. (2024c).*

During the morning flights, a distinct rise in $PM_{2.5}$ and $PM_{10}$ can be noted from an altitude of 65 m upwards, which was the same altitude that the ceilometer CHM-15k recorded the cloud base during the time of the vertical profiles. On the contrary, during the afternoon, when there was no present cloud throughout the altitude up to 180 m, PM concentrations remained low. The difference between flights with (i.e. "dry") and without (i.e. "ambient") the drying channel

indicate the presence of liquid droplets throughout the cloud, as well as present water vapour that has not yet condensated. A recent study that used an OPC-N3 on a building roof in fog conditions suggested how the sensor captured both fog droplets and non-condensated particles just with water uptake (Nurowska et al., 2023), which is also demonstrated with the vertical profiles shown in Fig. 3.5. Evidently, the dryer only partially dried the airflow under these conditions, where liquid droplets and highly wetted aerosols existed in the cloud. These in-situ measurements showcase how this low-cost lightweight system could adequately be used for detecting cloud layer vertical extent. While the cloud base was clearly identified, it is proposed that the cloud top was also captured at the PM decrease at the top of the vertical layer in flights 1 & 2 in Fig. 3.5, however due to considerations of rotor icing, the UAS did not ascend to higher altitudes during that day.

## 3.2 Objective II - PM measurements for calculating hygroscopic characteristics and identifying air mass origin

This chapter's topic elaborates on taking advantage of the previously developed dryer for simultaneous optical sensor measurements with and without it, to calculate hygroscopicity parameters based on the PM differences between the ambient and dried airflow. It is well established that most of aerosols attract water vapour from the environment and undergo hygroscopic growth, when conditions are increasingly humid (Svenningsson et al., 2006; Davies et al., 2021). The order of magnitude of hygroscopic growth is also directly related to aerosol type, with studies investigating the phenomenon on e.g. ammonium sulphate (Hämeri et al., 2001) or sea salt (Zieger et al., 2017). A main instrument for measurements of aerosol particle water uptake is the H-TDMA (Swietlicki et al., 2008), but other approaches have been based on combining scattering data from a LiDAR sensor and aircraft RH data (Feingold and Morley, 2003), or particle collection with impactors (Hitzenberger et al., 1997). The idea to co-relate dried and non-dried measurements with hygroscopicity previously compared the differences in size distributions of the two (Hegg et al., 2006), or analysed changes in particle spectral densities and concentrated on error sources such as refractive index and particle shape (Snider and Petters, 2008). Often, the aforementioned instruments or analysis methods require expensive instrumentation and high optical size resolution, to provide detailed size distributions for the aerosols. On the other hand, PM values are most commonly available among all kinds of optical sensors, regardless of the cost. The purpose of this study was to use PM data from sensors with and without a dryer, and develop a formula to calculate aerosol particle hygroscopicity parameter $\kappa$ and GF from the two measurement types. Furthermore, an assessment of the air mass origin could be made, by looking at the different hygroscopic levels of the airflow, being either continental- or marine-sourced.

GF is defined as the ratio between an aerosol's wet diameter at humid conditions ($d_w$), and its dry diameters at non-humid conditions ($d_d$), as given in Eq. 2.1. By introducing the hygroscopicity parameter $\kappa$, the equation tha relates GF to different RH conditions is (Petters and Kreidenweis, 2007):

$$\mathrm{GF} = \left(1 + \kappa \cdot \frac{a_w}{1 - a_w}\right)^{\frac{1}{3}} \tag{3.1}$$

In Eq. 3.1, $a_w$ is the so-called water activity, which equals to RH / 100 when the Kelvin effect is negligible (Fitzgerald, 1975). Studies have shown that $\kappa$ = 1.1 for sea salt (which is mostly what marine air masses consist of) (Zieger et al., 2017), and $\kappa$ = 0.61 for ammonium sulphate, which is commonly met in continental, polluted air masses (Di Antonio et al., 2018). Moreover, the efflorescence point of the two compounds has been noted at RH = 35 % for ammonium sulphate Di Antonio et al. (2018), and RH = 45.6 % for sea salt (Gupta et al., 2015). It is important to note that sea salt usually consists of a number of salts and has a more perplexed hygroscopic behavior, than one described by a single $\kappa$ value. Yet, for the purposes of this study, the assumption that sea salt consists solely of sodium chloride was made, as it has been observed to have comparable hygroscopicity (Tang et al., 1997). A novel mathematical equation was developed for this study, that progresses from the GF definition, by assuming

aerosol spherical size and taking advantage of the relationship between particle mass, density and volume (Savvakis et al., 2024a):

$$\mathrm{GF} = \left(1 + \frac{\rho_d \cdot \mathrm{PM}_{\mathrm{water}}}{\rho_{\mathrm{water}} \cdot \mathrm{PM}_d}\right)^{\frac{1}{3}} \tag{3.2}$$

By using two OPCs that only differ on the drying component, the OPC with a dryer measures the dry airflow (i.e. $\mathrm{PM}_d$), and the OPC without a dryer measures the ambient airflow (i.e. $\mathrm{PM}_w$). The aerosol water content is then calculated from the simple subtraction: $\mathrm{PM}_{\mathrm{water}} = \mathrm{PM}_w - \mathrm{PM}_d$. It is therefore possible to calculate GF at given RH conditions, with the developed Eq. 3.2, and by combining the measurements from the two OPCs. Data were collected during spring of 2021 and autumn of 2022, at two different locations: in Norderney island, Germany (coordinates: 53.7193, 7.2141) nearshore of the North Sea, and at the port city of Rødby, Denmark (coordinates: 54.6343, 11.4123), near shore the Baltic Sea. The purpose of the study was to use two OPCs with and without a drying channel, to measure $\mathrm{PM}_d$ and $\mathrm{PM}_w$ and then calculate hygroscopic properties of the aerosols based on Eq. 3.2, and then compare it to the theoretical values expected at certain RH conditions, based on Eq. 3.1.

On eight different measurement days, Table 3.2 shows the measurement times, back trajectory indication from Hybrid Single-Particle Lagrangian Integrated Trajectory (HYSPLIT) and the OPC configuration used for the experiments (Savvakis et al., 2024a)., based on Fig. 3.6 - 3.7. Furthermore, PM data from an OPC with a dryer are mentioned as "Dry", while ones without a dryer are mentioned as "Ambient". For each case, the air mass was labeled as marine if originating from the sea, and urban if originating from land, by using 24-hour back trajectory simulations from the HYSPLIT model by the National Oceanic and Atmospheric Administration (NOAA) (Stein et al., 2015), which can be seen in Fig. 3.6 for the cases of marine based samples and Fig. 3.7 for the cases of urban based samples. From each OPC or when using the OAS Fidas Fly 100, only the $\mathrm{PM}_{2.5}$ sensor output was considered for this study, and differences between $\mathrm{PM}_w$ and $\mathrm{PM}_d$ essentially stem from the hygroscopic growth effect, and indicate the water uptake of the measured aerosols. From Fig. 3.6 - 3.7, most notable are the red lines, which correspond to an altitude of 10 m, which were closest to what each OPC captured on the ground. Based on the method described above, GF and $\kappa$ was calculated from the collected data and are shown in Fig. 3.8 and Table 3.3 .

Table 3.2: Date, location, starting and ending time of data collection for all measurements (Savvakis et al., 2024a).

| **Date** | **Location** | **Ambient** | **Dry** | **Start - End UTC** | **Air mass** |
|---|---|---|---|---|---|
| 17 Apr 21 | Norderney | OPC-N2 | OPC-N2+dryer | 07:09 - 08:12 | Marine |
| 16 Sep 22 | Rødby-Land | OPC-N3 | Fidas Fly 100 | 16:40 - 19:14 | Marine |
| 17 Sep 22 | Rødby-Land | OPC-N3 | Fidas Fly 100 | 07:17 - 09:16 | Marine |
| 21 Sep 22 | Rødby-Vessel | OPC-N3 | OPC-N3+dryer | 11:38 - 12:34 | Marine |
| 19 Apr 21 | Norderney | OPC-N2 | OPC-N2+dryer | 09:42 - 10:44 | Urban |
| 19 Sep 22 | Rødby-Land | OPC-N3 | Fidas Fly 100 | 17:15 - 19:12 | Urban |
| 22 Sep 22 | Rødby-Vessel | OPC-N3 | OPC-N3+dryer | 12:27 - 13:15 | Urban |
| 23 Sep 22 | Rødby-Land | OPC-N3 | OPC-N3+dryer | 10:30 - 11:15 | Urban |

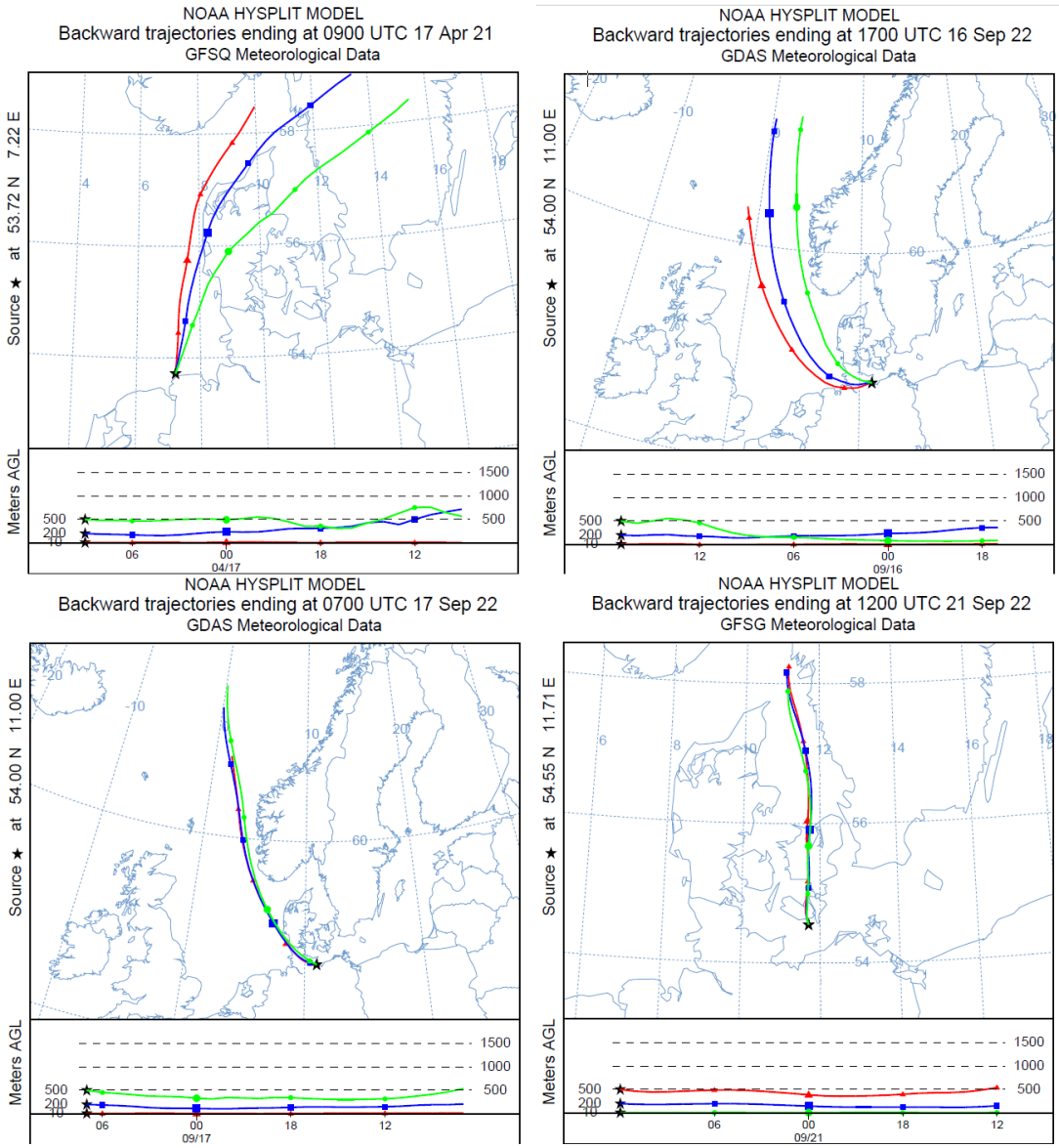


Figure 3.6: *24-hour back trajectories from the NOAA HYSPLIT model, for the cases when air was originating from the sea (Savvakis et al., 2024a).*

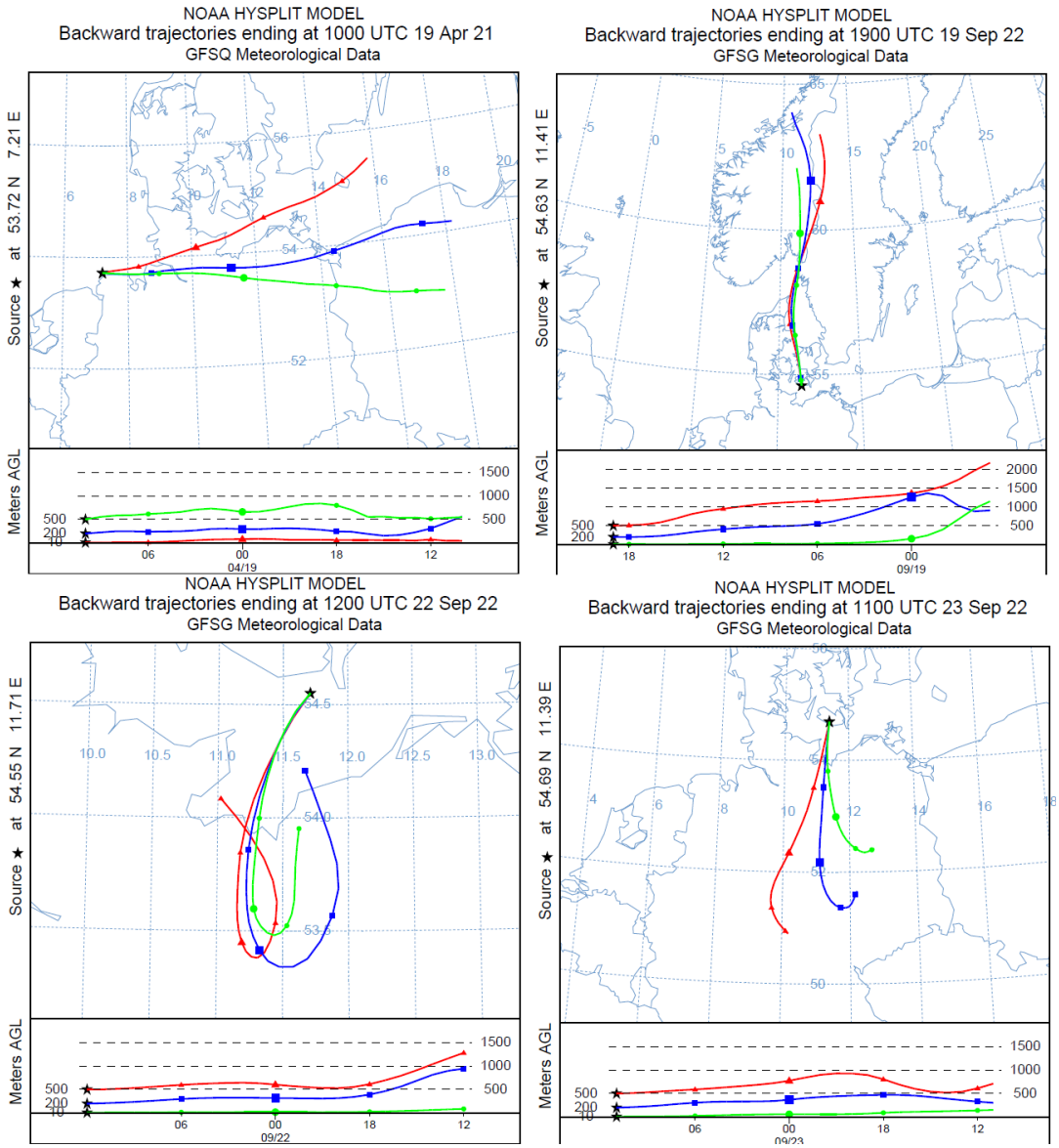


Figure 3.7: *24-hour back trajectories from the NOAA HYSPLIT model, for the cases when air was originating from land (Savvakis et al., 2024a).*

In Fig. 3.8, each point represents a different measurement period, here depicted as water activity instead. It is demonstrated how the calculated GF (from Eq. 3.2) matches the expected growth curve (from 3.1) of a given aerosol particle, depending on the source of the sampled air mass (from Fig. 3.6 - 3.7). Two different particle densities are used, namely ammonium sulphate density $\rho_{as} = 1.77\ g \cdot cm^{-3}$ and sea salt density $\rho_{ss} = 2.1\ g \cdot cm^{-3}$, as the two characteristic compounds of either urban or marine aerosol sources, and the results align only when the appropriate density is used. This result confirms the air mass origin depiction met by the back trajectory simulations, as different hygroscopic growth is effective when different aerosols comprise the sampled air (either above the sea - predominantly sea salt, or above land - polluted).

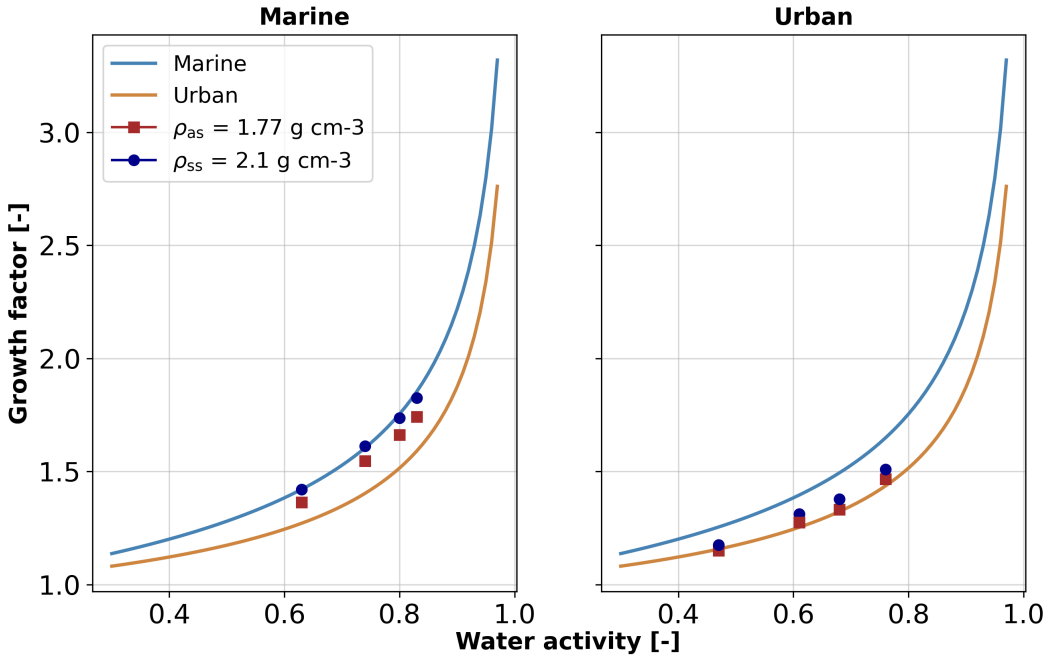


Figure 3.8: *Calculation of hygroscopic growth factor using Eq. 3.2 at certain RH conditions of each measurement period. The two densities of ammonium sulphate and sea salt were both used, and the resulting points are plotted on the expected growth curve for each compound. The figure is split in two cases, one when the air mass had a marine origin (top) and one that had a continental origin (bottom). Taken from Savvakis et al. (2024a).*

If a non-appropriate density value is used, the resulting GF matches neither line, and this technique indicates the kind of aerosol particles the OPC was measuring, which is information not inherently available from these sensors. Furthermore, $\kappa$ was also determined from the calculated GF based on the presented method, and can be found in Table 3.3. From the fourth and fifth column of Table 3.3, it is evident that the result matches the expected $\kappa$ value (1.1 for sea salt, and 0.61 for ammonium sulphate), only with the appropriate GF calculation. As $PM_{2.5}$ values were used for this publication, aerosol particles up to an aerodynamic diameter of 2.5 μm were considered, a size range that exceeds conventional hygroscopicity studies, which are focused on sub-micron and nanometer sized aerosols (Swietlicki et al., 2008). With the

Table 3.3: Calculation of hygroscopic growth factor using Eq. 3.2 at certain RH conditions of each measurement period. The two densities of ammonium sulphate and sea salt were both used, and the resulting points are plotted on the expected growth curve for each compound. The figure is split in two cases, one when the air mass had a marine origin (left) and one that had a continental origin (right) (Savvakis et al., 2024a).

| **Date** | **GF** ($\rho_{ss}$) | **GF** ($\rho_{as}$) | $\kappa$ ($\rho_{ss}$) | $\kappa$ ($\rho_{as}$) | $\overline{RH}$ [%] | $\kappa_{ss}$ |
|---|---|---|---|---|---|---|
| 17 Apr 21 | $1.83 \pm 0.08$ | $1.74 \pm 0.08$ | $1.0 \pm 0.1$ | $0.9 \pm 0.2$ | 83 | 1.1 |
| 16 Sep 22 | $1.61 \pm 0.07$ | $1.55 \pm 0.06$ | $1.1 \pm 0.2$ | $1.0 \pm 0.2$ | 74 | 1.1 |
| 17 Sep 22 | $1.74 \pm 0.06$ | $1.65 \pm 0.05$ | $1.1 \pm 0.1$ | $0.9 \pm 0.1$ | 80 | 1.1 |
| 21 Sep 22 | $1.4 \pm 0.1$ | $1.3 \pm 0.1$ | $1.1 \pm 0.1$ | $0.9 \pm 0.1$ | 63 | 1.1 |
| | | | | | | $\kappa_{as}$ |
| 19 Apr 21 | $1.38 \pm 0.09$ | $1.33 \pm 0.08$ | $0.8 \pm 0.1$ | $0.6 \pm 0.1$ | 68 | 0.61 |
| 19 Sep 22 | $1.5 \pm 0.1$ | $1.4 \pm 0.1$ | $0.8 \pm 0.2$ | $0.6 \pm 0.2$ | 76 | 0.61 |
| 22 Sep 22 | $1.17 \pm 0.05$ | $1.15 \pm 0.06$ | $0.7 \pm 0.1$ | $0.6 \pm 0.1$ | 47 | 0.61 |
| 23 Sep 22 | $1.31 \pm 0.05$ | $1.27 \pm 0.05$ | $0.8 \pm 0.1$ | $0.7 \pm 0.1$ | 61 | 0.61 |

hygroscopic growth effect more apparent in these ranges, the method would consequently be tested with $PM_1$ as well, always using identical sensors that sample the same air and only differ on the dryer presence. Further examination of hygroscopic growth on specific size bins, would require raw bin counts from each OPC, and calculation of PM per bin, instead of summation of bins for the currently established PM types. This could shed some light on the hygroscopic growth effect at specific size ranges, and then it could be compared with similar approaches of other studies (Hegg et al., 2006), that used particle size distribution differences between dried and non-dried measurements.

## 3.3 Objective III - In-situ simoultaneous measurements of Saharan dust concentrations and electric charge with a UAS

As discussed in Sect. 2.3, Saharan dust is one of the primary aerosol sources in the Mediterranean basin as well as the European continent. This dust can also be electrically charged, through a process called ion-particle attachment, which describes how charged ions are attached to the dust particles and generate charge on them (Mallios et al., 2022). Additional self-charging can occur a process called triboelectrification, i.e. the collision of the particles with each other and the resulting charge that arises from their friction (Kamra, 1972). Related measurements have been attempted as early as the beginning of the previous millenium (Rudge, 1913), and it is a topic of ongoing research (Zhang and Zhou, 2020).

The triboelectric effect is prominent during the lofting proces of the dust, and can affect electromagnetic wave propagation (Zhou et al., 2005), as well as the lifetime of the dust particles in the air (Esposito et al., 2016). Charged particles decrease overall optical depth due to vertical alignment (known as the "Venetian blind effect") (Ulanowski et al., 2007), which is currently disregarded by retrieval methods of remote sensing instruments. Triboelectrification has also been identified in dust devils (Franzese et al., 2018). Moreover, aerosols in the coarse mode or larger have been observed to remain airborne for longer time periods than what is predicted by dust transport modeling simulations (Maring et al., 2003) or measured by crewed aircrafts (Ryder et al., 2013). This may be connected to the E-field forces counteracting the gravitational force, thus contributing to the more extended transport of the bigger particles.

Surface measurements have been performed with E-field mills for studying the electrical properties of dust storms (Yair et al., 2016; Katz et al., 2018), and the advection of charged dust in higher atmospheric layers (Daskalopoulou et al., 2021). Alternatively, small charge sensors have been mounted on balloons for vertical airborne measurements of space charge through layers of Saharan dust, e.g. by (Nicoll and Harrison, 2010; Harrison et al., 2018; Mallios et al., 2023). On the contrary, there is a considerable research gab when it comes to such in-situ measurements with crewed or uncrewed aircraft, due to the overwhelming charging produced by the E-field of the platform itself, which is larger than the charge of the dust. This issue has been stated in sparse studies related to factors affecting crewed aircraft flight through dust layers and their implications on data collection related to electricity (Perala, 2009; Lekas, 2019). The authors of these works noted significant charging from the aircraft body, especially considering large crewed planes with considerably bigger dimensions, weight and speed than a small UAS. This begs the question, whether accurate space charge measurements would be possible with a small UAS, minimally affected by self-charging.

This work includes concurrent aerosol PNC and space charge measurements using a UAS of type MASC-3 during a Saharan dust event over Cyprus, during the first week of April, 2022. The aircraft has been described in Sect. 2.5.2, and also in previous publications (Rautenberg et al., 2019; Mauz et al., 2019). The dust event was analyzed first using satellite imagery two days prior to the measurements, and originated from North West Africa, and over Algeria. Apart from its regular scientific payload, the MASC-3 featured additional miniaturised sensors for the aerosol and space charge measurements. Specifically, it hosted an OPC-Pod, described in detail by Schön et al. (2024), and a Charge-Pod, as described in Schön et al. (2022a). The OPC-Pod is an oval-shaped measurement system based on an OPC-N3, modified for passive aspiration (Mashni et al., 2023), and with a small diffusion dryer (Savvakis et al., 2024c). The

Charge-Pod is based on a small charge sensor, developed and described in detail by Nicoll and Harrison (2009), and evaluated on the MASC-3 in Schön et al. (2022a). Vertical profiles with an ascent speed of 1.5 $m \cdot s^{-1}$ up to 2.8 km altitude were performed by the MASC-3 on April 6th, 2022 at the Unmanned Systems Research Laboratory (USRL). The USRL is an airfield near Orounda, Cyprus operated by the Cyprus Institute, and described in Kezoudi et al. (2021a). Measurements from the UAS were compared with remote sensors at the day of flights, and the magnitude of the aircraft charge effect was assessed and hanlded through the development of a mathematical correction for the measured data.

Results from the SEVIRI Dust RGB instruments are shown in Fig. 3.9, which reveal the initial altitude rise of the dust plume and its transport across the Mediterranean towards Cyprus. Specifically, first indications appear on April 4th at the areas of West Morocco and Algeria, and the dust plume (magenta colour) spread further and moved, alongside high altitude cirrus clouds (black colour) on the evening of April 4th and morning of April 5th. Later on, the dust is shown to arrive everywhere around Cyprus in the evening of April 5th, with a spread that is seemingly evenly distributed above the country.

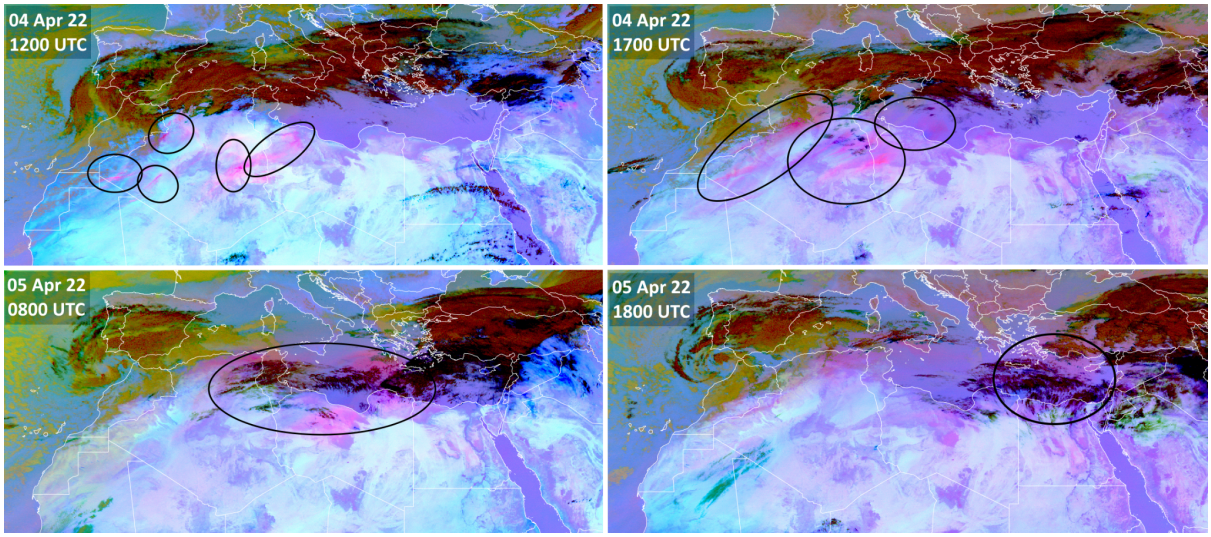


Figure 3.9: *Initial appearance and evolution of the dust layer measured on the 6th of April, starting from two days earlier, as captured by the SEVIRI Dust RGB instrument operating on Meteostat-8. The black circles show the uplift (April 4th, upper left), transport (April 4th and 5th, upper right and bottom left) and arrival (evening of April 5th, bottom right) of the dust layer in the Cyprus area (Savvakis et al., 2024b).*

During the day of measurements, Volume Depolarization Ratio (VDR) at 532 nm wavelength, calculated backscatter and extinction coefficients according to Klett (1981), from a CE376 LiDAR operating in Nicosia, is shown in Fig. 3.10. The instrument identified a large peak from 2300 to 2600 m and a smaller peak at about 1750 altitude, as demonstrated clearly by the backscatter and extinction coefficient profiles (Fig. 3.10b and 3.10c), which suggests the presence of a Saharan dust layer (back tracked as in Fig. 3.9) in this altitude range. VDR shows a drop at 2700 m, which is followed by the two coefficients, also indicating the top boundary of the specific dust layer. It is noteworthy to mention here, that the vertical profiles from the CE376 in Fig. 3.10 start at an altitude of 1.2 km, because that is the overlap region of this particular LiDAR, and readings only above that height are reasonable.

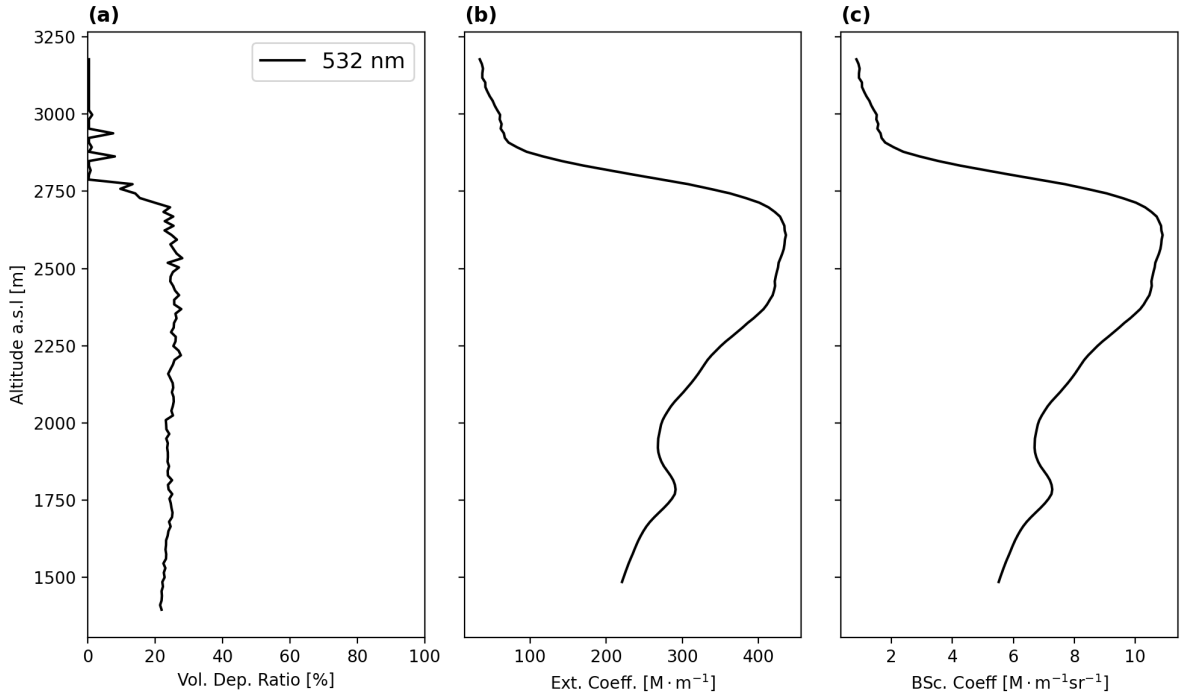


Figure 3.10: *Observations from the CE376 LiDAR in Nicosia, on April 6th at 10:00 UTC. At that time, the MASC-3 was in the air performing its first vertical profile (Savvakis et al., 2024b).*

Results from the two MASC-3 flights are showcased in Fig. 3.11, which includes vertical profiles of meteorological parameters, aerosol PNC in the whole range of the OPC-Pod (from 3 to 40 μm) and the voltage responses of the Charge-Pod. Firstly, given the times of the day when the flights took place (morning and noon), a lower than expected ABL is visible, located below 1000 m altitude for flight 1 as well as flight 2 (Fig. 3.11a and 3.11e). Such a narrow ABL extent is related to the presence of a thick dust cloud above, and the ABL height is located lower than about 1200 m normally expected at the location, during a convective spring day. The same figures also showed overall low moisture levels in the air during the flights, only up to 8 $g \cdot kg^{-1}$ across the whole vertical extent for both flights. Naturally, higher TKE values were measured inside the ABL due to vertical mixing, and values up to 0.2 $m^2 \cdot s^{-2}$ inside the dust layer (Fig. 3.11b and 3.11f). Small bumps in TKE could be observed even inside the Saharan dust, where the wind shear and aerosol vertical gradient is strongest. Wind speeds were always above 6 $m \cdot s^{-1}$, with higher values above the ABL and in higher altitudes (Fig. 3.11b and 3.11f).

As with the CE376 LiDAR profiles in Fig. 3.10, similar PNC peaks were captured by the OPC-Pod on the MASC-3 (Fig. 3.11c and 3.11g). PNC levels between 40 - 50 $cm^{-3}$ were measured below the Saharan dust layer height, but distinct aerosol rise resided at altitudes of 2000 - 2500 m in both fligths, with flight 1 having two PNC peaks equivalent to the backscatter and extinction coefficient peaks from the CE376. As then shown in the spectral images of the SEVIRI, dust was spread everywhere above Cyprus, so it can be concluded that the LiDAR and MASC-3 measurements were in agreement in identifying the location of the dust layer, which also clearly ended at 2600 m (where PNC was reduced to almost zero). The Charge-Pod had a similar response to the aerosol change, showing higher voltage values at the same altitude

peaks (Fig. 3.11d and 3.11h). Higher variation of charge was, as expected, found inside the ABL, which is consistent with previous studies (Nicoll et al., 2018; Schön et al., 2022a). Also, balloon OPC measurements of Saharan dust above Cyprus by Kezoudi et al. (2021b) showed concentrations around 50 $cm^{-3}$ inside the dust layer, but also at a smaller size range (only up to 13.6 µm) compared to the OPC-Pod.

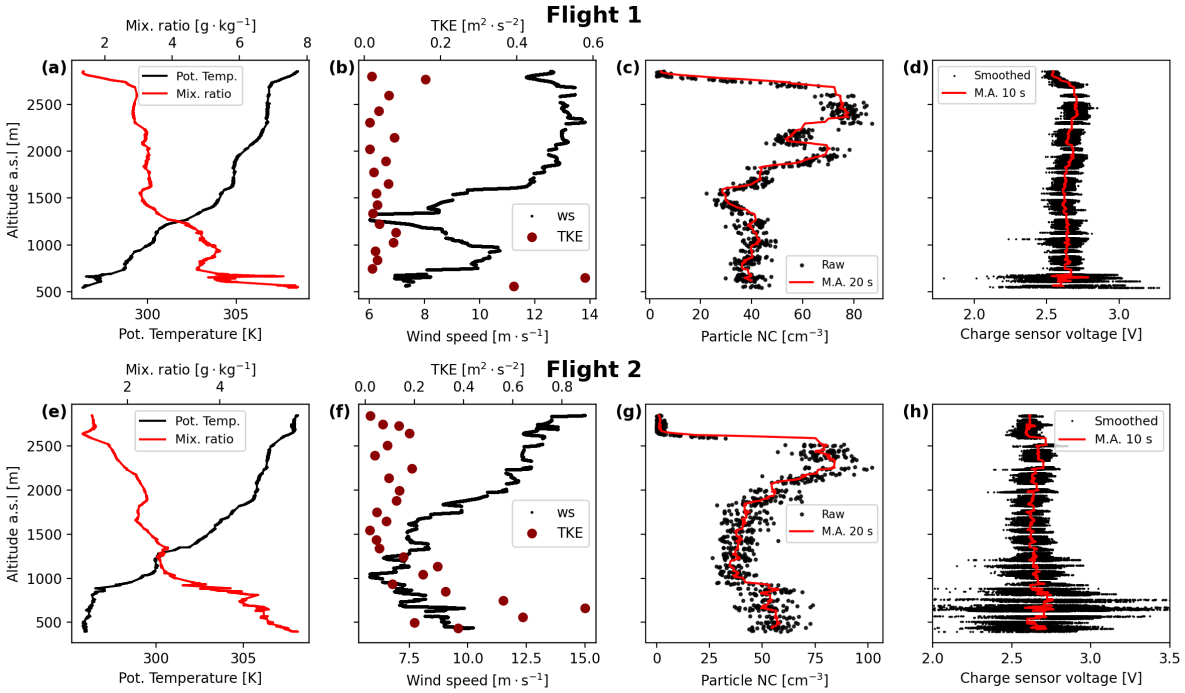


Figure 3.11: *Flights 1 and 2 with the MASC-3, profiling meteorological parameters, aerosol particles and charge sensor voltage vertically across an altitude range of 450 and 2800 m. In the figure: (a) mixing ratio g and potential temperature θ, (b) wind speed and TKE, (c) PNC, (d) charge voltage. The same quantities are plotted from (e) to (h) for flight 2. (Savvakis et al., 2024b).*

Following that, the conversion of charge voltages to dimensions of physical space charge was applied according to the process explained in Nicoll and Harrison (2016); Schön et al. (2022a) and the results are shown in Fig. 3.12. By looking at Fig. 3.12a and Fig. 3.12d, most of the aerosols measured by the OPC-Pod were below 2.5 µm in diameter, covering about 97 % of the total measured aerosols. Then, space charge has a clear rise inside the dust layer that reaches 5 $pC \cdot m^{-3}$ at the dust peaks, yet a strong correlation between PNC change and measured charge can be observed, which implies a potential effect of the aircraft platform to the measurements, specifically due to triboelectrification between the aircraft and the particles, and not because of the particles' own charge.

While aircraft charge is present in the measurements, it is significantly lower than what has been observed before for larger, crewed aircrafts (Lekas, 2019). This is also due to the beneficial construction and placement of the OPC-Pod on the wing of the MASC-3, which aims for mitigation of the effect (Schön et al., 2022a). The configuration minimizes the aircraft effective area impacting the dust as it flies through it, which has been shown to have a significant effect in the production of aircraft charging (Perala, 2009; Lekas et al., 2014). Cruising speed

is another factor that affects the measurements as shown for crewed aircrafts in Perala (2009), which our experiments, the True Air Speed (TAS) and the ascent rate were constant at about 19 $\mathrm{m \cdot s^{-1}}$ and 2 $\mathrm{m \cdot s^{-1}}$ respectively in the case of the UAS flights, considerably slower than regular aircraft speed. For these reasons, and according to the assertions detailed in Perala (2009), a correction was developed based on the evident linear relationship between PNC and space charge, in the dust cloud for each flight.

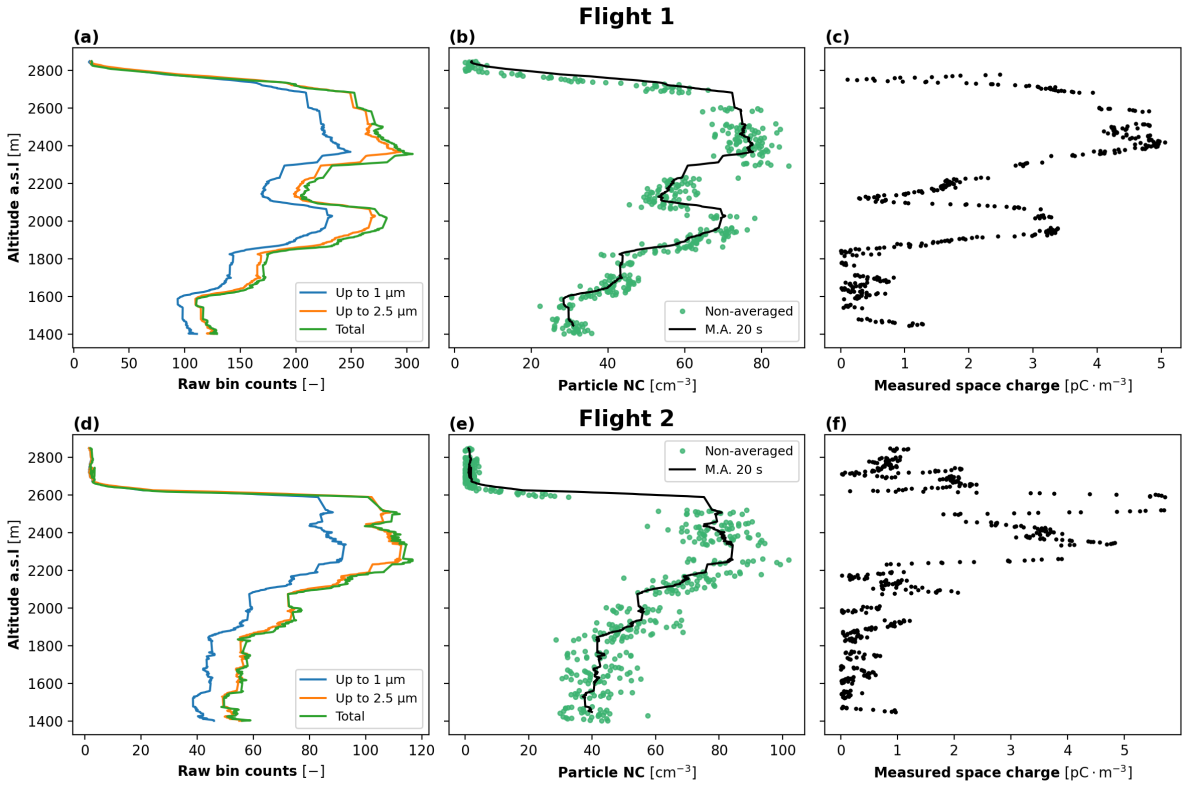


Figure 3.12: *Aerosol particles and measured space charge for flights 1 and 2 with the MASC-3. (a) number of aerosol particles up to 1, 2.5* µm*, as well as total bin counts, (b) PNC as shown in Fig. 3.11, (c) measured space charge from the Charge-Pod voltages. The same quantities are plotted from (d) to (f) for flight 2 (Savvakis et al., 2024b).*

The correction is based on a fitted line equation that is a product of linear regression, when assuming PNC as the independent and space charge the dependent variable. This line equation is built on a certain slope and intercept that is also calculated from the linear regression, and predicted space charge $\rho_{\mathrm{pred}}$ is then calculated based on the slope, intercept and measured PNC data. When $\rho_{\mathrm{pred}}$ is known, the corrected space charge $\rho_{\mathrm{corr}}$ is obtained by the difference between the measured space charge $\rho_{\mathrm{meas}}$ and $\rho_{\mathrm{pred}}$:

$$\rho_{\mathrm{corr}} = \rho_{\mathrm{meas}} - \rho_{\mathrm{pred}} \tag{3.3}$$

Eq. 3.3 is essentialy the residual, or what we consider as the real dust charge variation, excluding the charge originating from the aircraft's movement. Based on this procedure, which is also explained in more detail in Savvakis et al. (2024b), corrected space charge profiles are shown in Fig. 3.13.

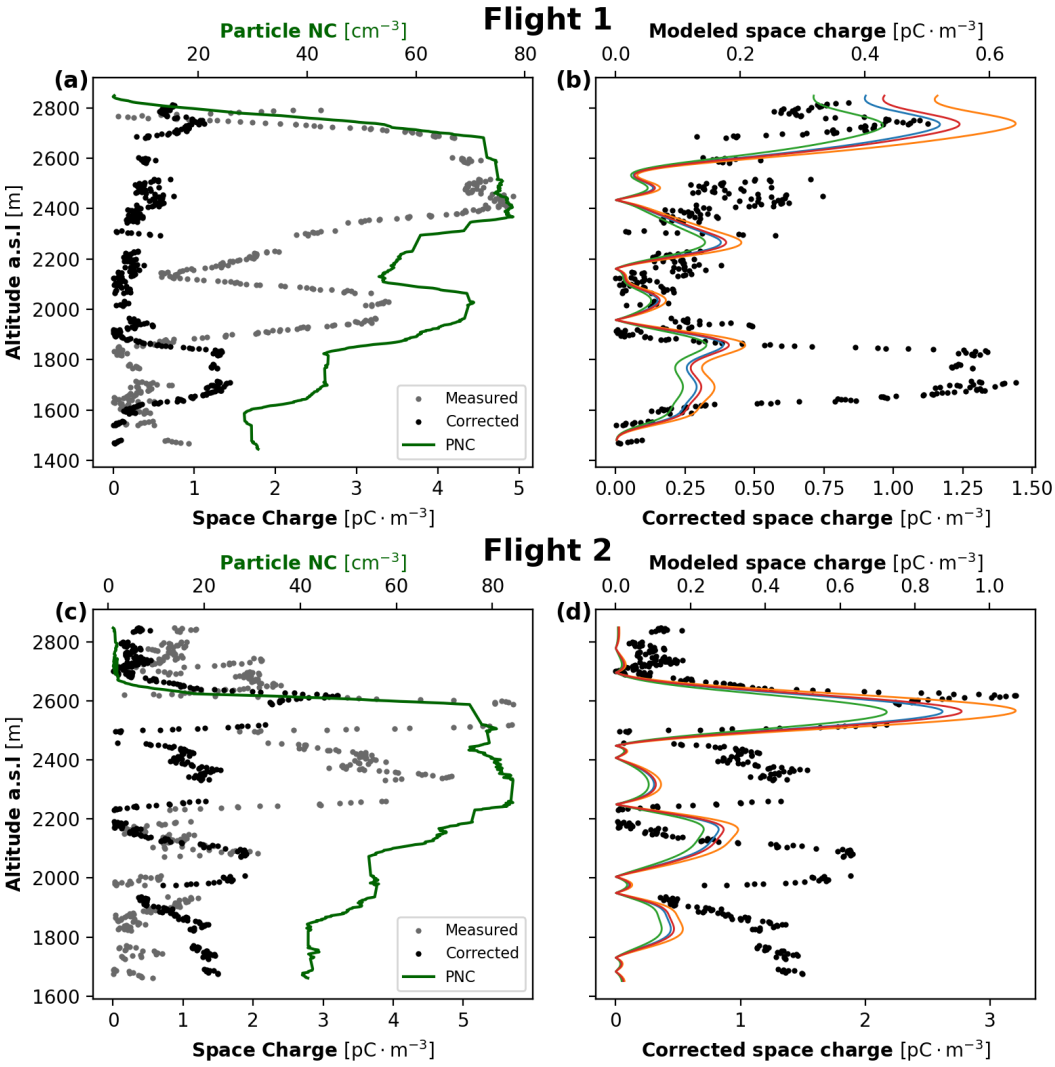


Figure 3.13: *Combined MASC-3 measurements from its two flights, after the aircraft charge correction has been applied. Specifically: (a) measured, corrected space charge and PNC on a double axis, (b) corrected and modeled space charge on the double axis. The same quantities are plotted from (c) to (d) for flight 2 (Savvakis et al., 2024b).*

Figure 3.13 provides the main body of the results of the MASC-3 flights in a compact way. Specifically, the linearity between PNC and space charge is obvious, especially in flight 1 (Fig. 3.13a), but a bit less clear in flight 2 (Fig. 3.13b). An additional important parameter that has been added in the plot is the expected space charge in these aerosol particle concentrations, calculated theoretically and founded on what amount of charge would be present at the area mainly due to ion-particle attachment. This modeled charge is based on a series of assumptions that initiate with Eq. 2.3, and thoroughly described in Nicoll and Harrison (2016); Savvakis et al. (2024b). The comparison between corrected and modeled charge shows close agreement inside the dust cloud with generally low values, between almost zero to 0.8 - 1 pC $\cdot$ m$^{-3}$. Higher peaks can be found at the dust layer top and bottom boundaries in both flights (up to 3 pC $\cdot$ m$^{-3}$), which is what is expected from theory and has been demonstrated before in clouds (Harrison et al., 2018, 2020), and also explained in Sect. 2.4 of this dissertation.

# Chapter 4

# Discussion

## 4.1 On airborne operations at humid conditions

So far, there have been multiple different approaches for diminishing the effect of hygroscopic growth on aerosol particle measurements, e.g. dillution drying, heated inlets and others. One of these approaches has also been drying by diffusion, which is the principle of operation of the dryer described in Sect. 3.1. Commercial dryes of this kind are usually large in dimensions, and heavy in weight, as they are intended for long term use on air pollution stations or meteorological towers. These products are unfavorable for UAS measurements that require miniaturised components, and this need has been accommodated by building not only a smaller version of a costly, large diffusion dryer, but also with lighter 3-D material, without compromising its efficiency (Fig. 3.3). Of course, this dryer is appropriate only for short-term measurements, before its effect wears out due to saturation of the dessicant, but its ease of reproducibility and dimensional convenience allows for multiple products to be readily available for repeated measurements. The results shown in Savvakis et al. (2024c) are therefore a reasonable next step to recent studies related to low-cost accurate PM data with self-constructed dryers, which has so far been tested in the lab (Bezantakos et al., 2018; Chacón-Mateos et al., 2022).

In this configuration, the extra tubings had a small effect on SFR measured by the OPC-N3, but this did not significantly affect the resulting PM measurements (Savvakis et al., 2024c), however it may be a point of consideration if longer dryers are intended to be added to a given optical sensor. As most OPCs have a built in aspiration system (e.g. a microfan, or a small pump), the addition of an extra dryer must always be decided in relation to the sensor's optimal flow rate operation range. As shown in Fig. 3.4, all PM types were significantly closer to the reference measurements when the dryer was in place during the hovering test flights with the MASC-MC, which at the same time overly overestimated PM without the dryer. Under humid conditions and when void of a drying method, this overestimation has been repeatedly reported before with low-end OPCs such as the OPC-N2/N3 (Badura et al., 2018; Samad et al., 2021; Vogt et al., 2021). New, previously unavailable information from in-situ measurements can also be retracted when using the UAS through cloud or fog layers, by taking advantage the dryer's effect compared to ambient, non-dryed air sampling. Figure 3.5 showcases that not only the cloud layer base can be accurately found when performing vertical profiles with this sensor system, but also that the comparison of dry (with a dryer) and ambient (without a dryer) measurements from the OPC reveal water vapour and liquid droplet concentrations inside the cloud, since the overestimation during ambient measurements is only

due to hygroscopic growth, when identical OPCs are used.

At this point, two more potential aspects related to aerosol monitoring and UAS operation in humid conditions, may be important for further developing this system. One is the alteration of aerosol particle optical properties due to adsorption of water vapour (Tang and Munkelwitz, 1994), which becomes important when using OPC which are pre-calibrated for dry particles and assuming dry complex refractive index and constant density $\rho$. The work in this dissertation does not address this directly, but the measurements do support insights given on droplet size and water content through the cloud, which has not been addressed before in this way (as shown in Fig. 3.3). Furthermore, UAS flights in highly humid conditions or through cloud, would require additional catering of the UAS platform to handle zero and sub-zero temperatures, as rotor icing (an extremely dangerous complication) did occur in our flights.

## 4.2 On hygroscopicity assessment based on PM data

The factors contributing to the total effect of hygroscopic growth of aerosol particles are multiple (particle size, age and composition) and therefore, fully characterising it would require sophisticated instrumentation. Through experiments and principles of physical chemistry, it would then be made possible to identify aerosol state and water uptake at humid conditions. The approach presented in Sect. 3.2 aims to acquire the same information in a more elementary manner, and through means (such as a low-cost OPCs, and self-made drying channel) that are often less specialised, less expensive and more accessible than sensors focused solely on hygroscopicity (Swietlicki et al., 2008).

For that reason, this approach should only be regarded an approximation, which can still offer reasonable results for hygroscopic properties, as shown e.g in Fig. 3.8. For example, sea salt's complex composition results in a more complicated hygroscopic behavior than one described with the efflorescence and deliquescence points of pure sodium chloride (Fig. 2.3). However, as demonstrated in Tang et al. (1997), the latter is the most common element of the former, and the two have comparable hygroscopic nature, which makes the method in Sect. 3.2 and Eq. 3.1 - 3.2, sensible. Table 3.3 showed how the calculated GF and $\kappa$ for sea salt matched their expected values well at various RH conditions, and this was further supported by the back tracking trajectories of the sampled air masses (Fig. 3.6).

A set of assumptions need to be carefully considered when applying these formulas, and especially at cases of continental air, which can have complicated particle mixtures due to different aerosol sources. Different studies have proposed different $\kappa$ values for mixed polluted air (Crilley et al., 2018; Cheung et al., 2020). The value selected for this work's measurements was the one of pure ammonium sulphate, in accordance to the motives in Di Antonio et al. (2018), yet a range of $\kappa$ values (e.g from 0.3 to 0.7) should be considered for different experiment conditions. The same temperament should be kept for the selection of particle density, yet the proposed method is less sensitive to that than the main hygroscopicity parameters, and that's why GF had little variance with different $\rho$ compared to different $\kappa$ in the results of Sect. 3.2. Ultimately, this method can be used as an PM based alternative to what was done in Hegg et al. (2006), who used differences in ambient / dry size distributions for hygroscopic property calculations. PM is a more common aerosol sensor output, even of the ones who include little to no information on size distributions (i.e. having a couple or only a handful of size channels).

With the usage of two optical sensors with just one drying channel, air mass origin was predicted correctly in the broad dualistic case of either urban or marine source. When focusing on more specific cases of continental air, the procedure should be adjusted accordingly and

based on the aforementioned range of $\kappa$. While this method is not intended for stricter aerosol source apportionment or composition identification, similar assumptions of what the density of the expected aerosols would be, should still provide accurate results at least for the hygroscopic properties of the aerosol mixture, within the error margin of the used sensors.

## 4.3 On UAS dust charge measurements

A Saharan air layer roughly extending from 1500 to 2500 m a.s.l was measured during the MASC-3 flights over Cyprus on April 6th, 2022. As seen in Fig. 3.11a and 3.11e, the vertical profiles of mixing ratio and potential temperature suggest a shallow boundary layer up to 900 m a.s.l, an intermediate layer up to 1500 m a.s.l and then a new air layer, populated with Saharan dust, from that atlitude up to 2500 m a.s.l. While the upper edge of the layer is distinct from the PNC measurements (Fig. 3.11c and 3.11g), the lower edge was less pronounced, but distinct local maxima were identified at altitudes that were also in alignment with the outputs of the SEVIRI Dust RGB product (Fig. 3.9), and the LiDAR instruments nearby the flight location (Fig. 3.10).

The measured charge after the linear fitting correction was applied was small, with peaks between 1 - 3 $\mathrm{pC} \cdot \mathrm{m}^{-3}$ at the horizontal edges of the layer (Fig. 3.13), similarly to how charging is distributed in clouds (Harrison et al., 2020). The charge also shows a variability that is partially expected from theory, considering the charge that these aerosol concentrations would have due ion-particle attachment processes, which indicates that the dust particles were charged at the location from ion-particle attachment, rather than due to a triboelectric process. It is also unlikely that this low charge would counteract gravitational settling, which has been speculated in other cases of aerosol long range transport of especially bigger particles (Van Der Does et al., 2018), but these findings are in agreement with theoretical studies on the expected dust charge after long range transport (Mallios et al., 2022). Quite higher amounts of charge have been measured closer to the source of lofting (Silva et al., 2016; Yair et al., 2016), yet other measurements at elevated levels have undulated at magnitudes similar to our observations (Nicoll et al., 2010; Nicoll, 2012).

The estimated charge calculation based on the set of equations described in Sect. 2.4 corresponds to the amount of ion charge (and not the total charge, when there is dust present as well), which may be a reason for the difference between modeled and measured charge structures shown in Fig. 3.13. However, Fig. 3.13 is not intended for direct comparison between the two vertical profiles, but rather to acquire an understanding of the orders of magnitude of each quantity, and to reveal the dominant vertical charge structures (clearly depicted at the layer edges). A more thorough solution of the aforementioned equations, e.g. as in Mallios et al. (2022), could provide with a more defined vertical profile of modeled charge, and it's the difference between the two (ion charge calculated from theory, and total charge measured by our UAS) that provides an approximation of the dust particle charge.

There may be certain limitations in the aircraft charge correction that was developed for the flights through the dust layer. The linear relationship between PNC and space charge ($r^2 = 0.91$ and $r^2 = 0.75$ for flights 1 and 2, respectively) support the motivation behind a fitting based on linear regression, yet higher order polynomial corrections may need to be investigated in case of different dust events or aircraft platforms. Conclusively, the measurements presented in Sect. 3.3 and explained thoroughly in Savvakis et al. (2024b), stand as the first successful observations of dust charge with an aircraft, which has not been achieved before due to the induced E-field of the aircraft body.

# Chapter 5

# Conclusions and Outlook

Within the scopes of this work, a miniaturised diffusion drying channel was developed for usage with a small OPC on a UAS of type MASC-MC with the intention of performing repeatable measurements at humid or saturated conditions (e.g. fog or clouds). Two OPC systems of the same kind were then employed for parallel measurements, with only one having a dryer installed, to calculate parameters of the hygroscopic identity of the sampled aerosol particles. Apart from the experiments related to the new diffusion dryer, the OPC system was modified further and installed on a UAS of type MASC-3 for profiling a Saharan dust layer over Cyprus, simultaneously measuring aerosol concentrations, space charge and meteorological parameters (wind, humidity, potential temperature and turbulent kinetic energy). The major conclusions that can be drawn based on this research, considering the outlined initial objectives, are as follows:

- Inside a fog container with RH levels close to 100 %, the self-constructed dryer was effective in drying the airflow for 35 min, longer than the flying time of the MASC-MC
- Vertical profiles with the MASC-MC through a a low-altitude stratus cloud identified cloud layer base at the same altitude as a high-end ceilometer installed at the measurement location, supporting the proposition to use such sensor systems in these conditions
- Simultaneous measurements with two identical OPCs, one with a drying channel and one without, revealed additional information regarding liquid droplets and water vapour through the cloud, based on the difference between ambient and dried data outputs, due to hygroscopic growth
- This same method was also used for validly calculating aerosol particle hygroscopic properties based on the definition of the growth factor GF, and air mass origin in different cases of marine or continental air was made possible to be determined
- During a Saharan dust event in Cyprus, the first ever in-situ measurements of the vertical distribution of dust concentrations and electric charge were achieved with the MASC-3 after successfuly identifying and correcting raw data for the aircraft-induced charge
- The MASC-3 flights showed a weakly charged (up to $\mathrm{pC} \cdot \mathrm{m}^{-3}$) dust layer that extended for about 1000 m to almost 3000 m a.s.l, with most charge on the layer boundaries and at comparable amounts to what would be predicted from theory because of the effect of ion-particle attachment

- The agreement between theoretically calculated and measured charge profiles suggests on-site charging of the dust particles due to ion-particle attachment rather than triboelectrification, which is in agreement with previous modeling studies related to the different magnitudes of these effects

Either at humid or dusty conditions and building the outcomes of the presented work, further investigation (in terms of calculational as well as experimental endeavors) would potentially amount to more solidified insight on airborne aerosol behavioral mechanics. The proposed dual-OPC measurement, which principally isolates and quantifies the hygroscopic growth effect, can be used for obtaining the origin and hygroscopic nature of the aerosol particles, and would prove highly valuable for instantaneous, direct examination of fog and clouds. This examination would not necessarily be limited in particle / droplet number concentrations, but a next step could be taken in unraveling the differences in size distributions of the droplets and the non-dried particles, as well as calculating hygroscopic growth parameters per size channel, as well as from PM data.

Furthermore, future experimental flights with the MASC-3 through multiple Saharan dust layers at different altitudes, close and far away of their source, would provide unique datasets of dust charge that would allow for the investigation of the underlying mechanisms affecting the dust's lifetime in the air. With the developed payload designed for UAS, these in-situ measurements of dust and electric charge could reveal completely new information about the dust's presence in the atmosphere, potentially addressing the intriguing mystery of long range transport that has been attributed to charging mechanisms, but so far only as speculation and without direct observational data. As a whole, these results contribute to improving UAS operational procedures for aerosol particle observations in humid environments as well as Saharan dust events. Hence, what has foundationally been established here can be used as a cornerstone for subsequent, relevant reseach and expand our present understanding and knowledge within these fields of atmospheric science.

# Bibliography


Alfano, B., Barretta, L., Del Giudice, A., De Vito, S., Di Francia, G., Esposito, E., Formisano, F., Massera, E., Miglietta, M. L., and Polichetti, T. (2020). A review of low-cost particulate matter sensors from the developers' perspectives. *Sensors*, 20(23):6819.

Altstädter, B., Platis, A., Wehner, B., Scholtz, A., Wildmann, N., Hermann, M., Käthner, R., Baars, H., Bange, J., and Lampert, A. (2015). ALADINA–an unmanned research aircraft for observing vertical and horizontal distributions of ultrafine particles within the atmospheric boundary layer. *Atmos. Meas. Tech.*, 8(4):1627–1639.

Alvarado, M., Gonzalez, F., Erskine, P., Cliff, D., and Heuff, D. (2017). A methodology to monitor airborne PM10 dust particles using a small unmanned aerial vehicle. *Sensors*, 17(2):343.

Ansmann, A., Rittmeister, F., Engelmann, R., Basart, S., Jorba, O., Spyrou, C., Remy, S., Skupin, A., Baars, H., Seifert, P., et al. (2017). Profiling of Saharan dust from the Caribbean to western Africa–Part 2: Shipborne lidar measurements versus forecasts. *Atmospheric Chemistry and Physics*, 17(24):14987–15006.

Aplin, K. L. (2006). Atmospheric electrification in the solar system. *Surveys in Geophysics*, 27(1):63–108.

Aplin, K. L. and Harrison, R. G. (2013). Lord Kelvin's atmospheric electricity measurements. *History of Geo-and Space Sciences*, 4(2):83–95.

Arfin, T., Pillai, A. M., Mathew, N., Tirpude, A., Bang, R., and Mondal, P. (2023). An overview of atmospheric aerosol and their effects on human health. *Environmental Science and Pollution Research*, pages 1–23.

Badura, M., Batog, P., Drzeniecka-Osiadacz, A., and Modzel, P. (2018). Evaluation of low-cost sensors for ambient PM2.5 monitoring. *J. Sens.*, 2018.

Bauer, S., Balkanski, Y., Schulz, M., Hauglustaine, D., and Dentener, F. (2004). Global modeling of heterogeneous chemistry on mineral aerosol surfaces: Influence on tropospheric ozone chemistry and comparison to observations. *Journal of Geophysical Research: Atmospheres*, 109(D2).

Bezantakos, S., Schmidt-Ott, F., and Biskos, G. (2018). Performance evaluation of the cost-effective and lightweight Alphasense optical particle counter for use onboard unmanned aerial vehicles. *Aerosol Sci. Technol.*, 52(4):385–392.

Biskos, G., Malinowski, A., Russell, L., Buseck, P., and Martin, S. (2006). Nanosize effect on the deliquescence and the efflorescence of sodium chloride particles. *Aerosol Science and Technology*, 40(2):97–106.

Bramati, M., Schön, M., Schulz, D., Savvakis, V., Wang, Y., Bange, J., and Platis, A. (2024). A versatile calibration method for rotary-wing UAS as wind measurement systems. *Journal of Atmospheric and Oceanic Technology*, 41(1):25–43.

Bretschneider, L., Schlerf, A., Baum, A., Bohlius, H., Buchholz, M., Düsing, S., Ebert, V., Erraji, H., Frost, P., Käthner, R., et al. (2022). MesSBAR—Multicopter and instrumentation for air quality research. *Atmosphere*, 13(4):629.

Brooks, S. D., Wise, M. E., Cushing, M., and Tolbert, M. A. (2002). Deliquescence behavior of organic/ammonium sulfate aerosol. *Geophysical Research Letters*, 29(19):23–1.

Bílek, J., Bílek, O., Maršolek, P., and Buček, P. (2021). Ambient air quality measurement with low-cost optical and electrochemical sensors: An evaluation of continuous year-long operation. *Environments*, 8(11).

Carlson, T. N. and Caverly, R. S. (1977). Radiative characteristics of Saharan dust at solar wavelengths. *Journal of geophysical Research*, 82(21):3141–3152.

Chacón-Mateos, M., Laquai, B., Vogt, U., and Stubenrauch, C. (2022). Evaluation of a low-cost dryer for a low-cost optical particle counter. *Atmos. Meas. Tech.*, 15(24):7395–7410.

Chalmers, J. A. (2013). *Atmospheric Electricity: International Series of Monographs in Natural Philosophy*, volume 11. Elsevier.

Cheung, H. C., Chou, C. C.-K., Lee, C. S. L., Kuo, W.-C., and Chang, S.-C. (2020). Hygroscopic properties and cloud condensation nuclei activity of atmospheric aerosols under the influences of asian continental outflow and new particle formation at a coastal site in eastern asia. *Atmospheric Chemistry and Physics*, 20(10):5911–5922.

Chin, M. and Kahn, R. (2009). *Atmospheric aerosol properties and climate impacts*, volume 2. US Climate Change Science Program.

Chouza, F., Reitebuch, O., Benedetti, A., and Weinzierl, B. (2016). Saharan dust long-range transport across the Atlantic studied by an airborne Doppler wind lidar and the MACC model. *Atmospheric Chemistry and Physics*, 16(18):11581–11600.

Colbeck, I. and Lazaridis, M. (2014). *Aerosol Science*. Wiley Online Library.

Corrigan, C., Roberts, G., Ramana, M., Kim, D., and Ramanathan, V. (2008). Capturing vertical profiles of aerosols and black carbon over the Indian Ocean using autonomous unmanned aerial vehicles. *Atmospheric Chemistry and Physics*, 8(3):737–747.

Cowie, S. M. (2014). *Characterising dust emission events from long-term surface observations in northern Africa*. PhD thesis, University of Leeds.

Crazzolara, C., Ebner, M., Platis, A., Miranda, T., Bange, J., and Junginger, A. (2019). A new multicopter-based unmanned aerial system for pollen and spores collection in the atmospheric boundary layer. *Atmospheric Measurement Techniques*, 12(3):1581–1598.

Crilley, L. R., Shaw, M., Pound, R., Kramer, L. J., Price, R., Young, S., Lewis, A. C., and Pope, F. D. (2018). Evaluation of a low-cost optical particle counter (Alphasense OPC-N2) for ambient air monitoring. *Atmos. Meas. Tech.*, 11(2):709–720.

Daskalopoulou, V., Mallios, S. A., Ulanowski, Z., Hloupis, G., Gialitaki, A., Tsikoudi, I., Tassis, K., and Amiridis, V. (2021). The electrical activity of Saharan dust as perceived from surface electric field observations. *Atmospheric Chemistry and Physics*, 21(2):927–949.

Davies, J. F., Price, C. L., Choczynski, J., and Kohli, R. K. (2021). Hygroscopic growth of simulated lung fluid aerosol particles under ambient environmental conditions. *Chemical Communications*, 57(26):3243–3246.

Davis, E. J., Buehler, M. F., and Ward, T. L. (1990). The double-ring electrodynamic balance for microparticle characterization. *Review of Scientific Instruments*, 61(4):1281–1288.

Derrien, M. and Le Gléau, H. (2005). MSG/SEVIRI cloud mask and type from SAFNWC. *International Journal of Remote Sensing*, 26(21):4707–4732.

Devara, P. and Manoj, M. (2013). Aerosol–cloud–precipitation interactions: A challenging problem in regional environment and climate research. *Particuology*, 11(1):25–33.

Di Antonio, A., Popoola, O. A., Ouyang, B., Saffell, J., and Jones, R. L. (2018). Developing a relative humidity correction for low-cost sensors measuring ambient particulate matter. *Sensors*, 18(9):2790.

Di Tomaso, E., Escribano, J., Basart, S., Ginoux, P., Macchia, F., Barnaba, F., Benincasa, F., Bretonnière, P.-A., Buñuel, A., Castrillo, M., et al. (2022). The MONARCH high-resolution reanalysis of desert dust aerosol over northern Africa, the middle East and Europe (2007–2016). *Earth system science data*, 14(6):2785–2816.

Drake, R. and Gordon, J. (1985). Mie scattering. *American Journal of Physics*, 53(10):955–962.

Esposito, F., Molinaro, R., Popa, C., Molfese, C., Cozzolino, F., Marty, L., Taj-Eddine, K., Di Achille, G., Franzese, G., Silvestro, S., et al. (2016). The role of the atmospheric electric field in the dust-lifting process. *Geophysical Research Letters*, 43(10):5501–5508.

Feingold, G. and Morley, B. (2003). Aerosol hygroscopic properties as measured by lidar and comparison with in situ measurements. *Journal of Geophysical Research: Atmospheres*, 108(D11).

Ferguson, D. (2010). A basic triboelectric series for heavy minerals from inductive electrostatic separation behaviour. *Journal of the Southern African Institute of Mining and Metallurgy*, 110(2):75–78.

Feynman, R. P., Leighton, R. B., and Sands, M. (1964). Electricity in the atmosphere. *The Feynman Lectures on Physics*, 2.

Fitzgerald, J. W. (1975). Approximation formulas for the equilibrium size of an aerosol particle as a function of its dry size and composition and the ambient relative humidity. *Journal of Applied Meteorology and Climatology*, 14(6):1044–1049.

Formenti, P., Schuetz, L., Balkanski, Y., Desboeufs, K., Ebert, M., Kandler, K., Petzold, A., Scheuvens, D., Weinbruch, S., and Zhang, D. (2010). Recent progress in understanding physical and chemical properties of mineral dust. *Atmos. Chem. Phys. Discuss*, 10(12):31187–31251.

Franzese, G., Esposito, F., Lorenz, R., Silvestro, S., Popa, C. I., Molinaro, R., Cozzolino, F., Molfese, C., Marty, L., and Deniskina, N. (2018). Electric properties of dust devils. *Earth and Planetary Science Letters*, 493:71–81.

Fuller, R., Landrigan, P. J., Balakrishnan, K., Bathan, G., Bose-O'Reilly, S., Brauer, M., Caravanos, J., Chiles, T., Cohen, A., Corra, L., et al. (2022). Pollution and health: A progress update. *The Lancet Planetary Health*, 6(6):e535–e547.

Gasteiger, J., Groß, S., Sauer, D., Haarig, M., Ansmann, A., and Weinzierl, B. (2017). Particle settling and vertical mixing in the Saharan air layer as seen from an integrated model, lidar, and in situ perspective. *Atmospheric Chemistry and Physics*, 17(1):297–311.

Gini, M., Manousakas, M., Karydas, A., and Eleftheriadis, K. (2022). Mass size distributions, composition and dose estimates of particulate matter in Saharan dust outbreaks. *Environmental Pollution*, 298:118768.

Girdwood, J., Smith, H., Stanley, W., Ulanowski, Z., Stopford, C., Chemel, C., Doulgeris, K.-M., Brus, D., Campbell, D., and Mackenzie, R. (2020). Design and field campaign validation of a multi-rotor unmanned aerial vehicle and optical particle counter. *Atmospheric Measurement Techniques*, 13(12):6613–6630.

Gringel, W. (1986). Electrical structure from 0 to 30 kilometers. *The Earth's Electrical Environment*, pages 166–182.

Gu, Q., R. Michanowicz, D., and Jia, C. (2018). Developing a modular unmanned aerial vehicle (UAV) platform for air pollution profiling. *Sensors*, 18(12):4363.

Gupta, D., Eom, H.-J., Cho, H.-R., and Ro, C.-U. (2015). Hygroscopic behavior of NaCl–MgCl 2 mixture particles as nascent sea-spray aerosol surrogates and observation of efflorescence during humidification. *Atmospheric Chemistry and Physics*, 15(19):11273–11290.

Hämeri, K., Laaksonen, A., Väkevä, M., and Suni, T. (2001). Hygroscopic growth of ultrafine sodium chloride particles. *Journal of Geophysical Research: Atmospheres*, 106(D18):20749–20757.

Hämeri, K., Väkevä, M., Hansson, H.-C., and Laaksonen, A. (2000). Hygroscopic growth of ultrafine ammonium sulphate aerosol measured using an ultrafine tandem differential mobility analyzer. *Journal of Geophysical Research: Atmospheres*, 105(D17):22231–22242.

Harm-Altstädter, B., Bärfuss, K., Bretschneider, L., Schön, M., Bange, J., Käthner, R., Krejci, R., Mazzola, M., Park, K., Pätzold, F., et al. (2023). Spatial distribution and variability of boundary layer aerosol particles observed in Ny-ålesund during late spring in 2018. *Aerosol Research Discussions*, 2023:1–41.

Harrison, R., Nicoll, K., and Ambaum, M. (2015). On the microphysical effects of observed cloud edge charging. *Quarterly Journal of the Royal Meteorological Society*, 141(692):2690–2699.

Harrison, R. G. (2013). The carnegie curve. *Surveys in Geophysics*, 34(2):209–232.

Harrison, R. G., Nicoll, K. A., and Aplin, K. L. (2017). Evaluating stratiform cloud base charge remotely. *Geophysical Research Letters*, 44(12):6407–6412.

Harrison, R. G., Nicoll, K. A., Mareev, E., Slyunyaev, N., and Rycroft, M. J. (2020). Extensive layer clouds in the global electric circuit: their effects on vertical charge distribution and storage. *Proceedings of the Royal Society A*, 476(2238):20190758.

Harrison, R. G., Nicoll, K. A., Marlton, G. J., Ryder, C. L., and Bennett, A. J. (2018). Saharan dust plume charging observed over the UK. *Environmental Research Letters*, 13(5):054018.

Haywood, J. M., Francis, P. N., Glew, M. D., and Taylor, J. P. (2001). Optical properties and direct radiative effect of Saharan dust: A case study of two saharan dust outbreaks using aircraft data. *Journal of Geophysical Research: Atmospheres*, 106(D16):18417–18430.

Hegg, D., Covert, D. S., Crahan, K., Jonsson, H., and Liu, Y. (2006). Measurements of aerosol size-resolved hygroscopicity at sub and supermicron sizes. *Geophysical research letters*, 33(21).

Held, A. and Mangold, A. (2021). Measurement of fundamental aerosol physical properties. In *Springer Handbook of Atmospheric Measurements*, pages 535–565. Springer.

Highwood, E. J., Haywood, J. M., Silverstone, M. D., Newman, S. M., and Taylor, J. P. (2003). Radiative properties and direct effect of saharan dust measured by the C-130 aircraft during saharan dust experiment (SHADE): 2. terrestrial spectrum. *Journal of Geophysical Research: Atmospheres*, 108(D18).

Hitzenberger, R., Berner, A., Dusek, U., and Alabashi, R. (1997). Humidity-dependent growth of size-segregated aerosol samples. *Aerosol Science and Technology*, 27(2):116–130.

Hobbs, P. V. (1993). Aerosol-cloud interactions. In *International Geophysics*, volume 54, pages 33–73. Elsevier.

Holben, B. N., Eck, T. F., Slutsker, I. a., Tanré, D., Buis, J., Setzer, A., Vermote, E., Reagan, J. A., Kaufman, Y., Nakajima, T., et al. (1998). AERONET—a federated instrument network and data archive for aerosol characterization. *Remote sensing of environment*, 66(1):1–16.

Hubert, H. (1943). A summary of knowledge of the sand and dust storms of French west Africa. *Bulletin of the American Meteorological Society*, 24(6):243–246.

Jaenicke, R. and Davies, C. (1976). The mathematical expression of the size distribution of atmospheric aerosols. *Journal of Aerosol Science*, 7(3):255–259.

Jayaratne, R., Liu, X., Thai, P., Dunbabin, M., and Morawska, L. (2018). The influence of humidity on the performance of a low-cost air particle mass sensor and the effect of atmospheric fog. *Atmos. Meas. Tech.*, 11(8):4883–4890.

John, W. et al. (2011). Size distribution characteristics of aerosols. *Aerosol measurement*, 3:41–54.

Jumaah, H. J., Kalantar, B., Halin, A. A., Mansor, S., Ueda, N., and Jumaah, S. J. (2021). Development of UAV-based PM2.5 monitoring system. *Drones*, 5(3):60.

Kalashnikova, O. and Sokolik, I. (2004). Modeling the radiative properties of nonspherical soil-derived mineral aerosols. *Journal of Quantitative Spectroscopy and Radiative Transfer*, 87(2):137–166.

Kamra, A. (1972). Measurements of the electrical properties of dust storms. *Journal of Geophysical Research*, 77(30):5856–5869.

Karanasiou, A., Moreno, N., Moreno, T., Viana, M., de Leeuw, F., and Querol, X. (2012). Health effects from Sahara dust episodes in Europe: Literature review and research gaps. *Environment international*, 47:107–114.

Karydis, V., Kumar, P., Barahona, D., Sokolik, I., and Nenes, A. (2011). On the effect of dust particles on global cloud condensation nuclei and cloud droplet number. *Journal of Geophysical Research: Atmospheres*, 116(D23).

Katz, S., Yair, Y., Price, C., Yaniv, R., Silber, I., Lynn, B., and Ziv, B. (2018). Electrical properties of the 8–12th September, 2015 massive dust outbreak over the Levant. *Atmospheric Research*, 201:218–225.

Kezoudi, M., Keleshis, C., Antoniou, P., Biskos, G., Bronz, M., Constantinides, C., Desservettaz, M., Gao, R.-S., Girdwood, J., Harnetiaux, J., et al. (2021a). The unmanned systems research laboratory (USRL): a new facility for UAV-based atmospheric observations. *Atmosphere*, 12(8):1042.

Kezoudi, M., Tesche, M., Smith, H., Tsekeri, A., Baars, H., Dollner, M., Estellés, V., Bühl, J., Weinzierl, B., Ulanowski, Z., Müller, D., and Amiridis, V. (2021b). Measurement report: Balloon-borne in situ profiling of Saharan dust over Cyprus with the UCASS optical particle counter. *Atmospheric Chemistry and Physics*, 21(9):6781–6797.

Klett, J. D. (1981). Stable analytical inversion solution for processing LIDAR returns. *Applied optics*, 20(2):211–220.

Kotsyfakis, M., Zarogiannis, S. G., and Patelarou, E. (2019). The health impact of Saharan dust exposure. *International journal of occupational medicine and environmental health*, 32(6):749–760.

Krishnamohan, K., Bala, G., Cao, L., Duan, L., and Caldeira, K. (2020). The climatic effects of hygroscopic growth of sulfate aerosols in the stratosphere. *Earth's Future*, 8(2):e2019EF001326.

Kulkarni, P., Baron, P. A., and Willeke, K. (2011). Introduction to aerosol characterization. *Aerosol measurement: principles, techniques, and applications*, 3.

Kumar, P., Sokolik, I. N., and Nenes, A. (2011). Measurements of cloud condensation nuclei activity and droplet activation kinetics of fresh unprocessed regional dust samples and minerals. *Atmospheric Chemistry and Physics*, 11(7):3527–3541.

Lance, S., Raatikainen, T., Onasch, T. B., Worsnop, D. R., Yu, X.-Y., Alexander, M. L., Stolzenburg, M., McMurry, P., Smith, J. N., and Nenes, A. (2013). Aerosol mixing state, hygroscopic growth and cloud activation efficiency during MIRAGE 2006. *Atmospheric Chemistry and Physics*, 13(9):5049–5062.

Lei, T., Zuend, A., Cheng, Y., Su, H., Wang, W., and Ge, M. (2018). Hygroscopicity of organic surrogate compounds from biomass burning and their effect on the efflorescence of ammonium sulfate in mixed aerosol particles. *Atmospheric Chemistry and Physics*, 18(2):1045–1064.

Lekas, T. I. (2019). Electrostatic charging of an aircraft due to airborne dust particles impacts. *CEAS Aeronautical Journal*, 10:903–908.

Lekas, T. I., Kushta, J., Solomos, S., and Kallos, G. (2014). Some considerations related to flight in dusty conditions. *Journal of Aerospace Operations*, 3(1):45–56.

Liu, B., Pui, D., Rubow, K., and Szymanski, W. (1985). Electrostatic effects in aerosol sampling and filtration. *Ann. Occup. Hyg.*, 29(2):251–269.

Liu, D., Taylor, J. W., Crosier, J., Marsden, N., Bower, K. N., Lloyd, G., Ryder, C. L., Brooke, J. K., Cotton, R., Marenco, F., et al. (2018). Aircraft and ground measurements of dust aerosols over the west African coast in summer 2015 during ICE-D and AER-D. *Atmospheric Chemistry and Physics*, 18(5):3817–3838.

Loye-Pilot, M., Martin, J., and Morelli, J. (1986). Influence of Saharan dust on the rain acidity and atmospheric input to the Mediterranean. *Nature*, 321(6068):427–428.

Magi, B. I., Cupini, C., Francis, J., Green, M., and Hauser, C. (2020). Evaluation of PM2.5 measured in an urban setting using a low-cost optical particle counter and a Federal Equivalent Method Beta Attenuation Monitor. *Aerosol Sci. Technol.*, 54(2):147–159.

Mallios, S., Daskalopoulou, V., Spanakis-Misirlis, V., Hloupis, G., and Amiridis, V. (2023). Novel measurements of desert dust electrical properties: A multi-instrument approach during the ASKOS 2022 campaign. *Environmental Sciences Proceedings*, 26(1):22.

Mallios, S. A., Daskalopoulou, V., and Amiridis, V. (2022). Modeling of the electrical interaction between desert dust particles and the Earth's atmosphere. *Journal of Aerosol Science*, 165:106044.

Mallios, S. A., Papangelis, G., Hloupis, G., Papaioannou, A., Daskalopoulou, V., and Amiridis, V. (2021). Modeling of spherical dust particle charging due to ion attachment. *Frontiers in Earth Science*, 9:709890.

Mamali, D., Marinou, E., Sciare, J., Pikridas, M., Kokkalis, P., Kottas, M., Binietoglou, I., Tsekeri, A., Keleshis, C., Engelmann, R., et al. (2018). Vertical profiles of aerosol mass concentration derived by unmanned airborne in situ and remote sensing instruments during dust events. *Atmospheric Measurement Techniques*, 11(5):2897–2910.

Maring, H., Savoie, D., Izaguirre, M., Custals, L., and Reid, J. (2003). Mineral dust aerosol size distribution change during atmospheric transport. *Journal of Geophysical Research: Atmospheres*, 108(D19).

Mashni, H., Knaus, H., Platis, A., and Bange, J. (2023). Development of an airfoil-based passive volumetric air sampling and flow control system for fixed-wing uas. *Bulletin of Atmospheric Science and Technology*, 4(1):6.

Masic, A., Bibic, D., Pikula, B., Blazevic, A., Huremovic, J., and Zero, S. (2020). Evaluation of optical particulate matter sensors under realistic conditions of strong and mild urban pollution. *Atmos. Meas. Tech.*, 13(12):6427–6443.

Mauz, M., Rautenberg, A., Platis, A., Cormier, M., and Bange, J. (2019). First identification and quantification of detached-tip vortices behind a wind energy converter using fixed-wing unmanned aircraft system. *Wind Energy Science*, 4(3):451–463.

Mayuga, G. P., Favila, C., Oppus, C., Macatulad, E., and Lim, L. H. (2018). Airborne particulate matter monitoring using uavs for smart cities and urban areas. In *TENCON 2018-2018 IEEE Region 10 Conference*, pages 1398–1402. IEEE.

Michel Flores, J., Bar-Or, R., Bluvshtein, N., Abo-Riziq, A., Kostinski, A., Borrmann, S., Koren, I., Koren, I., and Rudich, Y. (2012). Absorbing aerosols at high relative humidity: Linking hygroscopic growth to optical properties. *Atmospheric Chemistry and Physics*, 12(12):5511–5521.

Morozov, V. (2006). The influence of convective current generator on the global current. *Nonlinear Processes in Geophysics*, 13(2):243–246.

Moses, E. E. and Akinyemi, M. (2017). A short review on the effects of aerosols on visibility impairment. In *Journal of Physics: Conference Series*, volume 852, page 012006. IOP Publishing.

Moulin, C., Lambert, C., Dayan, U., Masson, V., Ramonet, M., Bousquet, P., Legrand, M., Balkanski, Y., Guelle, W., Marticorena, B., et al. (1998). Satellite climatology of african dust transport in the Mediterranean atmosphere. *Journal of Geophysical Research: Atmospheres*, 103(D11):13137–13144.

Muyshondt, A., McFarland, A. R., and Anand, N. K. (1996). Deposition of aerosol particles in contraction fittings. *Aerosol Sci. Technol.*, 24(3):205–216.

Nicoll, K. (2012). Measurements of atmospheric electricity aloft. *Surveys in Geophysics*, 33(5):991–1057.

Nicoll, K. and Harrison, R. (2009). A lightweight balloon-carried cloud charge sensor. *Review of Scientific Instruments*, 80(1).

Nicoll, K. and Harrison, R. (2010). Experimental determination of layer cloud edge charging from cosmic ray ionisation. *Geophysical Research Letters*, 37(13).

Nicoll, K., Harrison, R., and Ulanowski, Z. (2010). Observations of saharan dust layer electrification. *Environmental Research Letters*, 6(1):014001.

Nicoll, K. and Harrison, R. G. (2016). Stratiform cloud electrification: comparison of theory with multiple in-cloud measurements. *Quarterly Journal of the Royal Meteorological Society*, 142(700):2679–2691.

Nicoll, K., Harrison, R. G., Silva, H., Salgado, R., Melgao, M., and Bortoli, D. (2018). Electrical sensing of the dynamical structure of the planetary boundary layer. *Atmospheric Research*, 202:81–95.

Nurowska, K., Mohammadi, M., Malinowski, S., and Markowicz, K. (2023). Applicability of the low-cost opc-n3 optical particle counter for microphysical measurements of fog. *Atmos. Meas. Tech.*, 16(9):2415–2430.

O'Sullivan, D., Marenco, F., Ryder, C. L., Pradhan, Y., Kipling, Z., Johnson, B., Benedetti, A., Brooks, M., McGill, M., Yorks, J., et al. (2020). Models transport Saharan dust too low in the atmosphere: a comparison of the MetUM and CAMS forecasts with observations. *Atmospheric chemistry and physics*, 20(21):12955–12982.

Pandis, S. N., Wexler, A. S., and Seinfeld, J. H. (1995). Dynamics of tropospheric aerosols. *The Journal of Physical Chemistry*, 99(24):9646–9659.

Pappalardo, G., Amodeo, A., Apituley, A., Comeron, A., Freudenthaler, V., Linné, H., Ansmann, A., Bösenberg, J., D'Amico, G., Mattis, I., et al. (2014). EARLINET: towards an advanced sustainable european aerosol lidar network. *Atmospheric Measurement Techniques*, 7(8):2389–2409.

Pariyothon, J., Bualert, S., Choomanee, P., Rungratanaubon, T., Thongyen, T., Fakkaew, N., Phuetfoo, C., Phupijit, J., Szymanski, W. W., et al. (2023). Hygroscopic growth factors of sub-micrometer atmospheric aerosols at four selected sites in Thailand. *Aerosol and Air Quality Research*, 23:220374.

Perala, R. (2009). A critical review of precipitation static research since the 1930's and comparison to aircraft charging by dust. *Electro Magnetic Applications Inc*, 7655.

Petters, M. and Kreidenweis, S. (2007). A single parameter representation of hygroscopic growth and cloud condensation nucleus activity. *Atmospheric Chemistry and Physics*, 7(8):1961–1971.

Petzold, A., Rasp, K., Weinzierl, B., Esselborn, M., Hamburger, T., DöRNBRACK, A., Kandler, K., SchuüTZ, L., Knippertz, P., Fiebig, M., et al. (2009). Saharan dust absorption and refractive index from aircraft-based observations during SAMUM 2006. *Tellus B: Chemical and Physical Meteorology*, 61(1):118–130.

Platis, A., Altstädter, B., Wehner, B., Wildmann, N., Lampert, A., Hermann, M., Birmili, W., and Bange, J. (2016). An observational case study on the influence of atmospheric boundary-layer dynamics on new particle formation. *Bound.-Layer Meteorol.*, 158(1):67–92.

Prodi, F. and Fea, G. (1979). A case of transport and deposition of saharan dust over the Italian peninsula and southern Europe. *Journal of Geophysical Research: Oceans*, 84(C11):6951–6960.

Ramanathan, V. (2007). Global dimming by air pollution and global warming by greenhouse gases: Global and regional perspectives. In *Nucleation and Atmospheric Aerosols: 17th International Conference, Galway, Ireland, 2007*, pages 473–483. Springer.

Rautenberg, A., Schön, M., Zum Berge, K., Mauz, M., Manz, P., Platis, A., van Kesteren, B., Suomi, I., Kral, S. T., and Bange, J. (2019). The multi-purpose airborne sensor carrier MASC-3 for wind and turbulence measurements in the atmospheric boundary layer. *Sensors*, 19(10):2292.

Reid, J. S., Jonsson, H. H., Maring, H. B., Smirnov, A., Savoie, D. L., Cliff, S. S., Reid, E. A., Livingston, J. M., Meier, M. M., Dubovik, O., et al. (2003). Comparison of size and morphological measurements of coarse mode dust particles from Africa. *Journal of Geophysical Research: Atmospheres*, 108(D19).

Renard, J.-B., Dulac, F., Berthet, G., Lurton, T., Vignelles, D., Jégou, F., Tonnelier, T., Jeannot, M., Couté, B., Akiki, R., et al. (2016). LOAC: a small aerosol optical counter/sizer for ground-based and balloon measurements of the size distribution and nature of atmospheric particles–part 2: First results from balloon and unmanned aerial vehicle flights. *Atmospheric Measurement Techniques*, 9(8):3673–3686.

Rohi, G., Ofualagba, G., et al. (2020). Autonomous monitoring, analysis, and countering of air pollution using environmental drones. *Heliyon*, 6(1).

Rudge, W. D. (1913). Atmospheric electrification during South African dust storms. *Nature*, 91(2263):31–32.

Rycroft, M., Israelsson, S., and Price, C. (2000). The global atmospheric electric circuit, solar activity and climate change. *Journal of Atmospheric and Solar-Terrestrial Physics*, 62(17-18):1563–1576.

Rycroft, M. J., Harrison, R. G., Nicoll, K. A., and Mareev, E. A. (2008). An overview of Earth's global electric circuit and atmospheric conductivity. *Planetary Atmospheric Electricity*, pages 83–105.

Ryder, C., McQuaid, J. B., Flamant, C., Rosenberg, P., Washington, R., Brindley, H., Highwood, E., Marsham, J., Parker, D., Todd, M., et al. (2015). Advances in understanding mineral dust and boundary layer processes over the sahara from Fennec aircraft observations. *Atmospheric Chemistry and Physics*, 15(14):8479–8520.

Ryder, C. L., Highwood, E. J., Rosenberg, P. D., Trembath, J., Brooke, J. K., Bart, M., Dean, A., Crosier, J., Dorsey, J., Brindley, H., et al. (2013). Optical properties of saharan dust aerosol and contribution from the coarse mode as measured during the fennec 2011 aircraft campaign. *Atmospheric Chemistry and Physics*, 13(1):303–325.

Ryder, C. L., Highwood, E. J., Walser, A., Seibert, P., Philipp, A., and Weinzierl, B. (2019). Coarse and giant particles are ubiquitous in Saharan dust export regions and are radiatively significant over the Sahara. *Atmospheric Chemistry and Physics*, 19(24):15353–15376.

Saidou Chaibou, A. A., Ma, X., and Sha, T. (2020). Dust radiative forcing and its impact on surface energy budget over west Africa. *Scientific reports*, 10(1):12236.

Samad, A., Alvarez Florez, D., Chourdakis, I., and Vogt, U. (2022). Concept of using an unmanned aerial vehicle (UAV) for 3D investigation of air quality in the atmosphere-Example of measurements near a roadside. *Atmosphere*, 13(5):663.

Samad, A., Melchor Mimiaga, F. E., Laquai, B., and Vogt, U. (2021). Investigating a low-cost dryer designed for low-cost PM sensors measuring ambient air quality. *Sensors*, 21(3).

Santachiara, G., Di Matteo, L., Prodi, F., and Belosi, F. (2010). Atmospheric particles acting as ice forming nuclei in different size ranges. *Atmospheric Research*, 96(2-3):266–272.

Savvakis, V., Schön, M., Bramati, M., Bange, J., and Platis, A. (2024a). Calculation of aerosol particle hygroscopic properties from opc derived pm2.5 data. *Meteorologische Zeitschrift*, 33(2):145–157.

Savvakis, V., Schön, M., Nicoll, K. A., Ryder, C. L., Papetta, A., Kezoudi, M., Marenco, F., Bange, J., and Platis, A. (2024b). In-situ observations of charged saharan dust from an uncrewed aircraft system. *Aerosol Science and Technology*, 58(11):1249–1266.

Savvakis, V., Schön, M., Bramati, M., Bange, J., and Platis, A. (2024c). Small-scale diffusion dryer on an optical particle counter for high-humidity aerosol measurements with an uncrewed aircraft system. *Journal of Atmospheric and Oceanic Technology*, 41(3):205 – 219.

Scheuvens, D. and Kandler, K. (2014). On composition, morphology, and size distribution of airborne mineral dust. *Mineral dust: A key player in the Earth system*, pages 15–49.

Schrod, J., Weber, D., Drücke, J., Keleshis, C., Pikridas, M., Ebert, M., Cvetković, B., Nickovic, S., Marinou, E., Baars, H., et al. (2017). Ice nucleating particles over the Eastern Mediterranean measured by unmanned aircraft systems. *Atmospheric Chemistry and Physics*, 17(7):4817–4835.

Schön, M., Nicoll, K. A., Büchau, Y. G., Chindea, S., Platis, A., and Bange, J. (2022a). Fair-weather atmospheric charge measurements with a small UAS. *Journal of Atmospheric and Oceanic Technology*, 39(11):1799–1813.

Schön, M., Savvakis, V., Kezoudi, M., Platis, A., and Bange, J. (2024). OPC-Pod: A new sensor payload to measure aerosol particles for small uncrewed aircraft systems. *Journal of Atmospheric and Oceanic Technology*, 41(5):499 – 513.

Schön, M., Suomi, I., Altstädter, B., van Kesteren, B., zum Berge, K., Platis, A., Wehner, B., Lampert, A., and Bange, J. (2022b). Case studies of the wind field around Ny-ålesund, Svalbard, using unmanned aircraft.

Silva, H., Lopes, F., Pereira, S., Nicoll, K., Barbosa, S., Conceição, R., Neves, S., Harrison, R. G., and Pereira, M. C. (2016). Saharan dust electrification perceived by a triangle of atmospheric electricity stations in southern portugal. *Journal of Electrostatics*, 84:106–120.

Snider, J. R. and Petters, M. D. (2008). Optical particle counter measurement of marine aerosol hygroscopic growth. *Atmospheric Chemistry and Physics*, 8(7):1949–1962.

Sorjamaa, R. and Laaksonen, A. (2007). The effect of $H_20$ adsorption on cloud drop activation of insoluble particles: a theoretical framework. *Atmospheric Chemistry and Physics*, 7(24):6175–6180.

Spracklen, D. V., Carslaw, K. S., Kulmala, M., Kerminen, V.-M., Sihto, S.-L., Riipinen, I., Merikanto, J., Mann, G. W., Chipperfield, M. P., Wiedensohler, A., et al. (2008). Contribution of particle formation to global cloud condensation nuclei concentrations. *Geophysical Research Letters*, 35(6).

Stein, A., Draxler, R. R., Rolph, G. D., Stunder, B. J., Cohen, M. D., and Ngan, F. (2015). NOAA's HYSPLIT atmospheric transport and dispersion modeling system. *Bulletin of the American Meteorological Society*, 96(12):2059–2077.

Stix, J., de Moor, J. M., Rüdiger, J., Alan, A., Corrales, E., D'Arcy, F., Diaz, J. A., and Liotta, M. (2018). Using drones and miniaturized instrumentation to study degassing at Turrialba and Masaya volcanoes, central America. *Journal of Geophysical Research: Solid Earth*, 123(8):6501–6520.

Svenningsson, B., Rissler, J., Swietlicki, E., Mircea, M., Bilde, M., Facchini, M., Decesari, S., Fuzzi, S., Zhou, J., Mønster, J., et al. (2006). Hygroscopic growth and critical supersaturations for mixed aerosol particles of inorganic and organic compounds of atmospheric relevance. *Atmospheric Chemistry and Physics*, 6(7):1937–1952.

Swietlicki, E., Hansson, H. C., Hämeri, K., Svenningsson, B., Massling, A., Mcfiggans, G., Mcmurry, P. H., Petäjä, T., Tunved, P., Gysel, M., Topping, D., Weingartner, E., Baltensperger, U., Rissler, J., Wiedensohler, A., and Kulmala, M. (2008). Hygroscopic properties of submicrometer atmospheric aerosol particles measured with H-TDMA instruments in various environments—a review. *Tellus B: Chem. Phys. Meteorol.*, 60(3):432–469.

Swietlicki, E., Zhou, J., Berg, O. H., Martinsson, B. G., Frank, G., Cederfelt, S.-I., Dusek, U., Berner, A., Birmili, W., Wiedensohler, A., et al. (1999). A closure study of sub-micrometer aerosol particle hygroscopic behaviour. *Atmospheric Research*, 50(3-4):205–240.

Tang, I. and Munkelwitz, H. (1994). Water activities, densities, and refractive indices of aqueous sulfates and sodium nitrate droplets of atmospheric importance. *J. Geophys. Res. Atmos.*, 99(D9):18801–18808.

Tang, I. N. (1996). Chemical and size effects of hygroscopic aerosols on light scattering coefficients. *Journal of Geophysical Research: Atmospheres*, 101(D14):19245–19250.

Tang, I. N., Tridico, A., and Fung, K. (1997). Thermodynamic and optical properties of sea salt aerosols. *Journal of Geophysical Research: Atmospheres*, 102(D19):23269–23275.

Tanré, D., Haywood, J., Pelon, J., Léon, J., Chatenet, B., Formenti, P., Francis, P., Goloub, P., Highwood, E., and Myhre, G. (2003). Measurement and modeling of the Saharan dust radiative impact: Overview of the Saharan dust experiment (SHADE). *Journal of Geophysical Research: Atmospheres*, 108(D18).

Thomas, D. and Charvet, A. (2017). An introduction to aerosols.

Tomasi, C. and Lupi, A. (2017). Primary and secondary sources of atmospheric aerosol. *Atmospheric Aerosols: Life Cycles and Effects on Air Quality and Climate*, pages 1–86.

Ulanowski, Z., Bailey, J., Lucas, P., Hough, J., and Hirst, E. (2007). Alignment of atmospheric mineral dust due to electric field. *Atmospheric Chemistry and Physics*, 7(24):6161–6173.

Vallero, D. A. (2014). *Fundamentals of air pollution*. Academic press.

Van Der Does, M., Knippertz, P., Zschenderlein, P., Giles Harrison, R., and Stuut, J.-B. W. (2018). The mysterious long-range transport of giant mineral dust particles. *Science advances*, 4(12):eaau2768.

Varga, G., Újvári, G., and Kovács, J. (2014). Spatiotemporal patterns of saharan dust outbreaks in the Mediterranean basin. *Aeolian Research*, 15:151–160.

Vincent, J. H. (2007). *Aerosol sampling: science, standards, instrumentation and applications*. John Wiley & Sons.

Vogt, M., Schneider, P., Castell, N., and Hamer, P. (2021). Assessment of low-cost particulate matter sensor systems against optical and gravimetric methods in a field co-location in Norway. *Atmosphere*, 12(8).

Vu, T. V., Delgado-Saborit, J. M., and Harrison, R. M. (2015). A review of hygroscopic growth factors of submicron aerosols from different sources and its implication for calculation of lung deposition efficiency of ambient aerosols. *Air Quality, Atmosphere & Health*, 8:429–440.

Wang, D., Wang, Z., Peng, Z.-R., and Wang, D. (2020). Using unmanned aerial vehicle to investigate the vertical distribution of fine particulate matter. *International Journal of Environmental Science and Technology*, 17:219–230.

Whitby, K. T. (1978). The physical characteristics of sulfur aerosols. In *Sulfur in the Atmosphere*, pages 135–159. Elsevier.

WHO (2021). *WHO global air quality guidelines: particulate matter (PM2.5 and PM10), ozone, nitrogen dioxide, sulfur dioxide and carbon monoxide*. World Health Organization.

Wild, M. (2009). Global dimming and brightening: A review. *Journal of Geophysical Research: Atmospheres*, 114(D10).

Wildmann, N., Hofsäß, M., Weimer, F., Joos, A., and Bange, J. (2014). MASC–a small remotely piloted aircraft (RPA) for wind energy research. *Advances in Science and Research*, 11(1):55–61.

Willeke, K. and Whitby, K. T. (1975). Atmospheric aerosols: Size distribution interpretation. *Journal of the Air Pollution Control Association*, 25(5):529–534.

Wilson, C. et al. (1929). Some thundercloud problems. *Journal of the Franklin Institute*, 208(1):1–12.

Wilson, C. T. R. (1921). Iii. investigations on lighting discharges and on the electric field of thunderstorms. *Philosophical Transactions of the Royal Society of London. Series A, Containing Papers of a Mathematical or Physical Character*, 221(582-593):73–115.

Winker, D. M., Vaughan, M. A., Omar, A., Hu, Y., Powell, K. A., Liu, Z., Hunt, W. H., and Young, S. A. (2009). Overview of the CALIPSO mission and CALIOP data processing algorithms. *Journal of Atmospheric and Oceanic Technology*, 26(11):2310–2323.

Yair, Y., Katz, S., Yaniv, R., Ziv, B., and Price, C. (2016). An electrified dust storm over the Negev desert, Israel. *Atmospheric Research*, 181:63–71.

Yu, H., Kaufman, Y., Chin, M., Feingold, G., Remer, L., Anderson, T., Balkanski, Y., Bellouin, N., Boucher, O., Christopher, S., et al. (2006). A review of measurement-based assessments of the aerosol direct radiative effect and forcing. *Atmospheric Chemistry and Physics*, 6(3):613–666.

Zannetti, P. (1990). Dry and wet deposition. *Air Pollution Modeling: Theories, Computational Methods and Available Software*, pages 249–262.

Zhang, H. and Zhou, Y.-H. (2020). Reconstructing the electrical structure of dust storms from locally observed electric field data. *Nature communications*, 11(1):5072.

Zhou, L. and Tinsley, B. A. (2007). Production of space charge at the boundaries of layer clouds. *Journal of Geophysical Research: Atmospheres*, 112(D11).

Zhou, Y.-H., Shu He, Q., and Jing Zheng, X. (2005). Attenuation of electromagnetic wave propagation in sandstorms incorporating charged sand particles. *The European Physical Journal E*, 17:181–187.

Zieger, P., Väisänen, O., Corbin, J. C., Partridge, D. G., Bastelberger, S., Mousavi-Fard, M., Rosati, B., Gysel, M., Krieger, U. K., Leck, C., et al. (2017). Revising the hygroscopicity of inorganic sea salt particles. *Nature Communications*, 8(1):1–10.

zum Berge, K., Schoen, M., Mauz, M., Platis, A., van Kesteren, B., Leukauf, D., El Bahlouli, A., Letzgus, P., Knaus, H., and Bange, J. (2021). A two-day case study: Comparison of turbulence data from an unmanned aircraft system with a model chain for complex terrain. *Boundary-Layer Meteorology*, 180:53–78.

# Appendix A

# First author peer-reviewed publications

## A.1 Publication I

# Small-Scale Diffusion Dryer on an Optical Particle Counter for High-Humidity Aerosol Measurements with an Uncrewed Aircraft System

VASILEIOS SAVVAKIS,[a] MARTIN SCHÖN,[a] MATTEO BRAMATI,[a] JENS BANGE,[a] AND ANDREAS PLATIS[a]

[a] *Department of Geosciences, Eberhard Karls Universität Tübingen, Tübingen, Germany*

(Manuscript received 19 July 2023, in final form 21 November 2023, accepted 2 January 2024)

ABSTRACT: The negative effects of relative humidity to measurements of particulate matter (PM) due to hygroscopic growth are often not inherently handled by low-cost optical particle counters (OPCs). This study presents a new approach in constructing a miniaturized diffusion dryer, for use with an OPC mounted on an uncrewed aircraft system (UAS), namely, the DJI S900 (weight of 7.5 kg and flight endurance of 20 min) for short-term measurements under humid conditions. In this work, an OPC of type N3 (Alphasense) was employed alongside the dryer, with experiments both in the laboratory and outdoors. Evaluation of the dryer's performance in a fog tank showed effective drying from almost saturated air to 41% relative humidity for 35 min, which is longer than the endurance of the UAS, and therefore sufficient. Changes in the flow rate through the OPC-N3 with the dryer showed a 17% reduction compared to an absent dryer, but the measured PM values remained unaffected. Airborne measurements were taken from four hovering flights near a governmental air pollution station (Mannheim-Nord, Germany) under humid conditions (88%–93%) where the system gave agreeable concentrations when the dryer was in place, but significantly overestimated all PM types without it. At a rural area near the Boundary Layer Field Site Falkenberg (Lindenberg, Germany), operated by the German Meteorological Service (DWD), vertical profiles inside a low-altitude cloud showed sharp increase in concentrations when the UAS entered the cloud layer, demonstrating its capability to accurately detect the layer base.

KEYWORDS: Cloud droplets; In situ atmospheric observations; Unpiloted aerial systems; Aerosol hygroscopicity; Aerosols/particulates

## 1. Introduction

Being a vital constituent of the atmosphere, aerosol particles have been a scientific topic of interest for decades. It is well established that suspended particles in the atmospheric air have detrimental effects on human health (Davidson et al. 2005; Anderson et al. 2012). At the same time, particulate matter (PM) directly and indirectly interacts with the environment, affecting cloud formation and precipitation (Lohmann and Feichter 2005; Andreae and Rosenfeld 2008), the solar radiation budget (Charlson et al. 1992), the evolution of the atmospheric boundary layer (Li et al. 2017), and global warming (Chen et al. 2021). Monitoring of aerosol concentrations is usually attained with properly equipped measurement stations at key locations of urban centers or rural areas, but concentrations often vary on a much smaller spatial scale. This has led to the industrial development of mobile, cost-effective aerosol sensors (Rai et al. 2017), which can be employed in a more flexible manner, improving the spatial resolution of the measurements at desired areas.

As aerosol measurement systems get dimensionally downscaled, the possibility arises to install them on uncrewed aircraft systems (UASs) for more dynamic data acquisition in the horizontal and vertical direction. Fixed-winged aircraft systems have already been used for related research before, for example, measuring vertical profiles of aerosols and black carbon (Corrigan et al. 2008), ice nucleating particles in the lower part of the troposphere (Schrod et al. 2017), Saharan dust episodes (Mamali et al. 2018), or ultrafine particles within the atmospheric boundary layer (ABL) (Altstädter et al. 2015). However, such aircraft often require a large space for takeoff and landing and are generally more expensive than multirotor UAS, which can be employed easier for purposes related to, e.g., urban air quality. Alvarado et al. (2017) employed a small UAS with an OPC-N2 (predecessor of the N3) and also did indoor tests of the rotor effect to the placement of its sampling probe. Air pollution tracking with multirotor UAS is also under development, for example, in studies by Weber et al. (2017), Gu et al. (2018), and Bretschneider et al. (2022). Currently, there are multirotor UAS being used solely for meteorological measurements, for example, by Brosy et al. (2017).

When performing aerosol particle measurements, it is critical to consider the influence of relative humidity (RH), because of the hygroscopic growth effect, which describes the relative growth of a particle's size as a result of water uptake from the environment (Swietlicki et al. 2008). It has also been observed that hygroscopic growth is affected by the mixing state of the aerosol particles (Cruz and Pandis 2000), and hygroscopic particles can produce different levels of light scattering based on their chemical composition (Tang 1996). Water uptake by the aerosol particle increases its apparent size, which translates to erroneous readings by a sensor like an OPC. Therefore, measurements of a dry airflow are necessary for accurate PM observations. This issue has been previously assessed either by applying thermal treatment to the OPC's inlet (Irwin et al. 2013; Magi et al. 2020), or by introducing RH-related mathematical corrections to the raw data

*Corresponding author*: Vasileios Savvakis, vasileios.savvakis@uni-tuebingen.de

DOI: 10.1175/JTECH-D-23-0093.1

during the postprocessing of the analysis (Di Antonio et al. 2018; Crilley et al. 2018). Nevertheless, using heated inlets to the sensors is often energy demanding and would require a complicated arrangement to avoid heat losses, whereas the accuracy of the postprocessing corrections decreases when conditions are close to saturation, and they undergo certain sets of assumptions of particle chemical composition for the value of the hygroscopicity factor $\kappa$. Furthermore, since ambient RH conditions not only affect the size of the aerosols due to hygroscopic growth, but also their optical properties (Tang and Munkelwitz 1994), the usage of optical-based sensors such as OPCs becomes even more challenging, as demonstrated by Rosati et al. (2015). Since an OPC assumes a refractive index that is typically of a dry particle, this complexity shows how a drying method prior to sampling could prove more physically meaningful than a postprocessing correction based on inaccurate responses from the sensor's optical detector.

On that account, increased relative humidity causes aerosol–water interactions that have consequences on PM measurements, and has been a recent topic of concern. In the laboratory as well as at ambient conditions, the performance of the low-cost sensor Plantower PMS1003A was evaluated and the results (Jayaratne et al. 2018) showed major increases in particle number concentrations (PNC) during fog events (28% rise of the total number of particles, and 50% rise for particles bigger than 2.5 $\mu$m), compared to a particle mass monitor, which featured a charcoal dryer at its inlet. A particle sensor system including the OPC-N3 also showed significant positive bias as RH increased toward 90% (Vogt et al. 2021). Later on, a first attempt to accommodate an inexpensive drying channel on the OPC-N3, which was based on applying voltage to provide thermal energy for moisture extraction, showed improved results for the sensor compared to the same instrument without the dryer (Samad et al. 2021).

Research on creating low-cost drying chambers for OPCs has taken its first steps, for example, by Chacón-Mateos et al. (2022), who constructed one heated drying chamber of 50 cm length for an OPC-R1 (Alphasense 2019). That study limited itself to laboratory testing and the chamber itself, apart from being energy consuming, would not be dimensionwise convenient for portable operation in a real environment. At the same time, such long extra compartments should be chosen wisely considering the strength of the OPC's internal fan, which becomes less and less efficient the longer the extra tube is. $PM_{2.5}$ average total bias of 30% was observed for the OPC sensor MASQ under conditions of mild and high pollution in Sarajevo, Bosnia and Herzegovina, over a period of six months between December 2019 and May 2020, which was partly due to hygroscopic growth (Masic et al. 2020). In that study, the spectrometer GRIMM 11-D operated with a self-made diffusion dryer (8 cm external diameter, with 1 kg of silica gel) and it performed much better compared to the reference instrument (an expensive beta attenuation monitor). Since measurements were meant for a longer period of time, the constructed dryer was bigger in dimensions and significantly heavier in weight, than a potential minidiffusion drying chamber for a low-cost OPC, which has not been thoroughly tested yet. On the implementation of drying component for airborne measurements, a recent study using a multirotor UAS with an unmodified OPC-N3 notes the sensitivity of the sensor at higher humidity levels during their measurements as an issue that needs to be addressed preferably prior to postprocessing (Samad et al. 2022). Another study by Platis et al. (2016), featured aerosol particle measurements with a large, fixed-wing UAS and drying-equipped instrumentation, yet the payload of the aircraft as well as the sensor system was significantly higher. This stresses the necessity of lightweight and less costly alternatives. Furthermore, increased strictness in aviation regulations when it comes to uncrewed operations raises the difficulty of using large platforms in certain areas and especially urban centers, which also calls for the development of miniaturized UAS and scientific payloads.

In this study, we present a fully self-constructed particle measurement system that includes meteorological sensors and an OPC with a diffusion drying chamber, designed with computer-aided design (CAD) software, and at the appropriate fitting dimensions for placement as an extension of the instrument's inlet. The system operates as a scientific payload for a multirotor UAS, specifically the S900 by DJI (China). As commercial diffusion dryers are often fairly expensive, constructed at specific dimensions, as well as overly heavy for use on a low-end OPC, an easily reproduced, economical alternative is suggested here, which provides structural flexibility for experiment or sensor specific requirements. The construction supports an OPC-N3, which was used for this study, or another OPC with similar dimensions. A new approach for the drying chamber's construction has been used, which consists of 3D printed internal and external tubes instead of commonly used material like copper or stainless steel, and blue silica gel in between to act as the desiccant for diffusion drying. The dryer is easily removable in case wet particles in humid conditions are of interest to be measured.

Using an airtight container with liquid water and an ultrasonic humidifier, fog was created in a controlled environment in the laboratory where the dryer's capacity of moisture removal from the airflow was tested by measuring RH inside and outside of the fog tank, i.e., before and after the air sample has passed through the chamber that hosts the desiccant. Further experiments collecting airborne data were conducted outdoors, at two locations in Germany: in the city of Mannheim next to a governmental air pollution station under highly humid conditions, and at a field site near Lindenberg (Brandenburg), performing vertical profiles through a low-altitude stratus cloud. Consecutive flights with and without the dryer were performed, to analyze differences due to water uptake and to assess the accuracy of the system on the UAS against reference sensors. With these experiments, both in laboratory conditions as well as outdoors in a realistic environment, how well the drying chamber extracts water vapor from the airflow, as well as the performance of the low cost OPC system as a whole against the reference instrument, was examined. The duration of the drying has to be effective for a time period longer than the flight endurance of the UAS, i.e., at least 20 min long. The main goal of this particular drying channel in this configuration is to achieve a reduction of relative humidity to around 40%, for at least the duration of the UAS's flight endurance, which can be described as a dry flow where

TABLE 1. Dimensions and material used for the design of the drying chamber.

| | Inner tube | Outer tube |
|---|---|---|
| Inner diameter (mm) | 6.2 | 20 |
| Outer diameter (mm) | 6.5 | 23 |
| Material | Liquid resin | Polylactic acid (PLA) |
| Length (mm) | 120 | 99 |

the hygroscopic growth effect is negligible (Held and Mangold 2021). Such a dryer is therefore intended for short-term measurements on a UAS platform, instead of longer-term use on a stationary sampling station.

## 2. Methods

### a. *Measurement system*

The OPC-N3 (cost of less than EUR 500 at the time of purchase) is used for aerosol particle measurements at a size range of 0.3–40 $\mu$m through 24 discrete size bins. The sensor's weight is approximately 105 g including its fan and it has a typical sampling flow rate of 280 mL min$^{-1}$, and total flow rate of 5.5 L min$^{-1}$. As with all OPCs, the sampled airstream goes through a laser beam that is hosted inside the sensor, and scattered light intensity is used to determine particle size, a method that is theoretically described in physics with Mie scattering theory (Drake and Gordon 1985). The diode laser used in the instrument has a wavelength of 658 nm, and a spherical particle shape with a complex refractive index $n = 1.5 + 0i$ and density $\rho = 1.65$ g cm$^{-3}$ is assumed internally by the instrument. It should be noted that the sensor itself has an internal calculation for its sampling flow rate (SFR), based on the concept of time of flight of particles traveling through the volume illuminated by the detection laser. The item comes precalibrated by the manufacturer, using mono dispersed polystyrene latex particles, and does not have a built-in battery, but instead requires a power supply between 4.8 and 5.2 V for operation.

For the atmospheric conditions during the time of measurements, an array of 6 miniaturized meteorological sensors (SHT31, Sensirion) is on board the UAS for temperature and humidity measurements. Each sensor is placed below each rotor arm of the S900 (see section 2c for more details on the UAS platform), inside a cylindrical radiation shield with enough airflow through the front and back openings, but not in direct contact with sunlight. The OPC-N3 runs through the use of a companion computer (Raspberry Pi 3b) at a sampling rate of 1 s, with a real-time clock (RTC) for an accurate measurement time stamp and an independent power supply that provides an endurance of approximately 2 h, thus facilitating several UAS flights if needed. The total weight of all components including the dryer amounts to 450 g, which makes it a compact and lightweight payload for UAS operations with multirotor systems such as the S900.

### b. *Drying channel design and construction*

The drying channel's conceptual basis is diffusion drying and consists of two coaxial cylinders with different diameters,

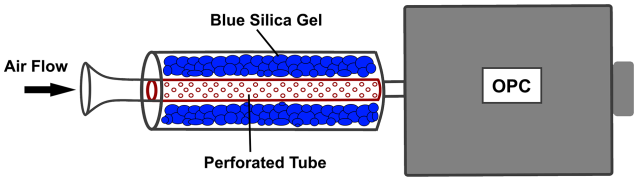


FIG. 1. Basic sketch of the diffusion drying chamber (arbitrary dimensions). The air goes through the chamber in the inner, perforated, UV resin printed tube, where blue silica gel extracts the water vapor from the flow. When exiting the chamber, the air is dry enough to be sampled at the OPC's sensing area.

where the desiccant is placed in between and dries the airflow for as long as it passes through the chamber. Two different techniques of additive manufacturing were chosen for each tube, as the inner tube should be perforated, nonporous on its solid surface, and as smooth as possible to produce the least roughness induced turbulence and particle loss possible. For that, masked stereolithography apparatus (MSLA) printing was used (resin printer model Phrozen Sonic Mini), which provides products of high precision ($X$–$Y$-plane resolution of 35 $\mu$m, $Z$-axis resolution of 10 $\mu$m) with an LED-based printing technique. The result is significantly lighter than commonly used parts of other diffusion dryers, like stainless steel. The inner diameter of the tube was chosen to match the diameter of the OPC-N3's own inlet, so that there are no sudden changes in diameter between the different tubings of the system, as that can be another source of particle loss (Muyshondt et al. 1996). Holes of 1.6 mm were designed first following a circular pattern on one side of the dryer, and then expanding the same pattern along its length, while keeping the distances of each hole with its neighboring constant, creating a perforated cylinder with a homogeneous distribution of openings. The outer tube was created with a Prusa I3 MK3, a fused deposition modeling (FDM) open source 3D printer, first released in 2020. Details of the drying chamber that was tested are shown in Table 1.

Commercially available blue silica gel was chosen as a desiccant (Wisedry). This silica consists of small almost spherical beads, which are color coded based on the amount of moisture they have absorbed, with deep blue showing completely dry silica and light pink/purple showing saturated silica. Reactivation can be achieved by heating up the beads for a short period of time, making the whole dryer reusable and sustainable. Including the blue silica, its weight is 50 g, considerably lighter than most current alternatives, which grants the possibility for short-term measurement use. A drawing of the drying chamber and its position on the OPC's inlet is shown in Fig. 1. The printed inner tubes were coated with graphite paint spray to ensure conductivity of the material, which is necessary to avoid aerosol particle losses due to static (Liu et al. 1985).

The presented construction approach accommodates a number of advantages: dimensions or number of products can be decided on demand, as the material cost per dryer is minimal. Its weight allows for usage on a UAS, which requires lightweight scientific payload. On the contrary to bigger,

heavier commercial diffusion dryers, where the desiccant alone can often weigh more than 1–2 kg, this dryer stands as an equivalent, miniaturized version that utilizes the same physical process for drying but built more compact, in a way that is ideal for short-term UAS measurements. Its length of 12 cm takes the strength of the OPC-N3's internal microfan into consideration, as a tubing part that is too long can nullify the provided aspiration and stall the sensor's measurement process. While exchanging the fan with a stronger pump can be a way to circumvent this problem for cases of longer drying systems, the OPC-N3 was kept intact in this study to maintain the total weight as low as possible. A hyperbolic surfaced inlet is attached on the upper end of the drying chamber to accelerate the airflow inside the drying chamber, thus increasing the sample flow rate (SFR) closer to its typical value stated by the manufacturer. Its shape is based on a previous study by Crazzolara et al. (2019), who used the same UAS platform as in this work for measurements of pollen.

### c. *Multirotor UAS*

The measurement system described in section 2a operates on a multirotor UAS, the S900 by DJI. The S900 is a multirotor UAS with 6 rotor arms and a span of 900 mm (hence the name) from rotor to rotor. Lithium-polymer batteries that grant an endurance from 15 to 25 min depending on the combination, are used for the flights. The platform, including the batteries and the scientific load, weighs about 7.5 kg and has a maximum cruising speed of 14 m $s^{-1}$, while its ascending/descending speed is maintained at 1.5 m $s^{-1}$. The OPC system is located in the middle of the platform of the UAS, as close as possible to its center of gravity for more stable flying. Two Styrofoam dome parts are placed on top and below the platform, leaving only the rotors on the outside. More details regarding all the information around the operation of the UAS have been noted by Bramati et al. (2024).

An opening at the middle point of the top Styrofoam dome at exactly the same diameter as the outer part of the bell-shaped inlet of the OPC system provides air samples from the environment for PM measurements. The opening is covered by circular cover on top at a distance of 4 cm, to counteract direct effects by the rotor-induced downwash of the UAS and for protection from dirt falling directly into the inlet (much like the cover shields in stationary air pollution measurement locations). A picture of the UAS with the measurement system fixed on it, along with the two Styrofoam domes, can be seen in Fig. 2.

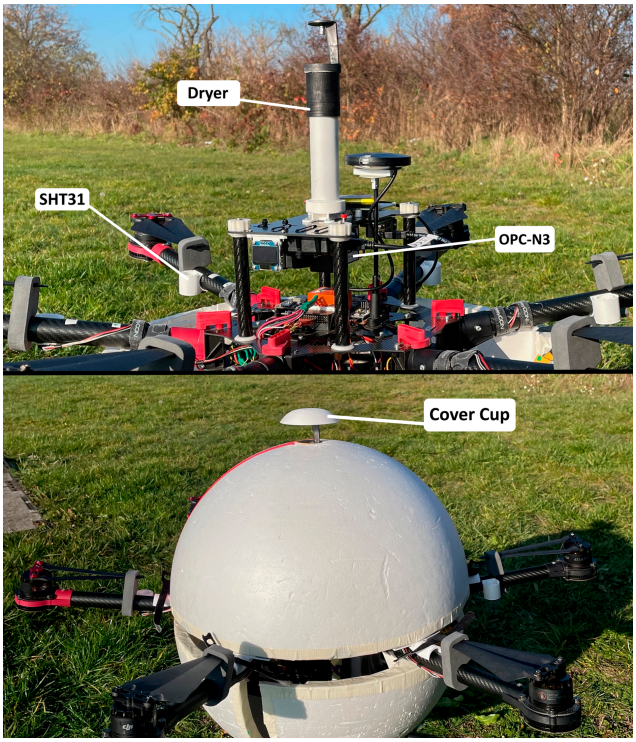


FIG. 2. The DJI S900, with the OPC measurement system installed on it. The dryer stands in the middle of the construction and aspiration is in the vertical downward direction, first through the dryer channel and then toward the sampling volume of the OPC-N3. Six SHT31 sensors are placed around the platform under each rotor arm. The OPC-N3 is located at the bottom of the supporting table, which is mounted on the main body of the UAS. Once the upper Styrofoam dome is in place, air sampling happens through the opening on top, which has a cover cup protection above it.

## 3. Experimental setup

### a. *Laboratory experiments*

Initially, we investigated the effect of the bell-shaped inlet and the extra tube attached to the OPC-N3's inlet on the SFR and, consequently, the PM values. This was achieved by doing short-duration measurements in laboratory conditions, where the air is generally ventilated and low on aerosol particles, consecutively with and without the drying channel, but also with nothing attached to the sensor at all. Differences were first observed between the three cases and how that translated to the output particle concentrations and the recorded SFR by the system. Following that, the same procedure was followed but this time by removing and replacing only the bell inlet, to see the changes on the same parameters. In this way, it was possible to discover if major measuring discrepancies arise just by the drying channel itself, and how much the output would deviate compared to the same sensor, unmodified.

The drying channel's performance was then evaluated in a self-constructed fog tank. The fog tank consists of an airtight plastic container box, half full of water and an ultrasonic humidifier dipped inside it. In essence, a conversion of electricity to high-frequency signals produces bubbles at the top of the humidifier, which are then hurled toward the surface and produce a strong mechanical oscillation that decouples liquid droplets from the water, resulting in the creation of fog that goes along the airflow above. Small circular openings were made for ventilation around the upper part of the container, as well as a hole at the appropriate size to fit the OPC inlet/drying channel inner tube diameter, from where fog samples were extracted for testing the channel's performance under heavily humid conditions (above 95%).

While having an enclosed fog tank at saturated conditions, RH was observed before and after the dryer. One end of the

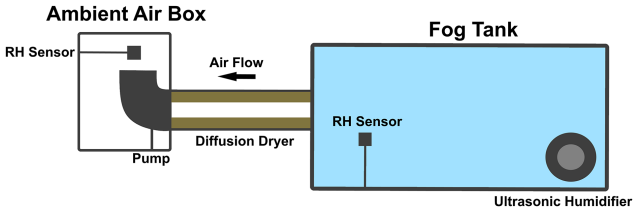


FIG. 3. Description of the drying chamber testing in a self-constructed fog tank. Fog is produced with an ultrasonic humidifier in an enclosed container, raising the relative humidity levels close to saturation. An SHT31 sensor measures the humidity in the fog tank, and the air is then drawn using a small pump, first through the diffusion dryer, into a second box with ambient air where a second SHT31 sensor is located, which measures the humidity after the humid air passes along the drying chamber.

dryer was placed in the tank's opening of the same diameter, and the other end was in a second, smaller box of ambient air levels of moisture. On that side, an external micropump was placed to ensure a steady airflow from the fog tank through the dryer and into the additional box, similar in power to the strength of the OPC-N3's fan. Two SHT31 sensors were placed on each side of the dryer, one inside the tank and one in the extra compartment, and RH was measured with a tank full of produced fog from the humidifier. In that way, the difference between the humidity levels of the air between a saturated fog environment and the same air after it has passed through the dryer could be inspected.

Figure 3 shows a sketch of the experimental process. As the flight time of the S900 is limited to 25 min, the effect of the dryer was tested for about 35 min to assure whether or not drying will be effective for a whole flight duration. At the same time, the same setup was also tested without a dryer in place, for obtaining the humidity differences in the ambient air box between the two cases and quantify the drying efficiency.

### b. *High-humidity measurements*

On 14 February 2023, an OPC system as described in section 2 was employed on board the S900 at urban conditions (Mannheim, Germany) next to a governmental air pollution station that collects data, among others, of aerosol particles. The name of the station is Mannheim-Nord (WGS84 east: 8°27′55.01″, WGS84 north: 49°32′38.68″) and is operated by the State Department of Environment Baden-Württemberg: Landesanstalt für Umwelt Baden-Württemberg (LUBW). On the station, a Fidas 200 (Palas) is installed, which is a high-end optical aerosol spectrometer (OAS) that provides information on $PM_1$, $PM_{2.5}$, $PM_4$, and $PM_{10}$. The Fidas 200 is an established measurement system that has also been used as a reference before (Chakraborty et al. 2020; Bílek et al. 2021; Vogt et al. 2021) For taking care of hygroscopic growth at higher humidity levels, the sensor also features its own drying procedure installed by the manufacturer, namely, the Intelligent Aerosol Drying System (IADS).

Two sets of hovering flights were performed next to the station (Fig. 4) and at an altitude of approximately 5 m (to match the height of the station's sensor inlet at the roof) in the

FIG. 4. The S900 in flight (right) next to Mannheim-Nord station (left). The sensors, including the aerosol particle measurements from the Fidas 200, are located at the roof of the station. The distance between the S900 and the station was maintained between 7 and 12 m for safety reasons, and for the UAS downwash to leave the station's measurements unaffected.

morning (between 1029 and 1119 UTC) and in the afternoon (between 1253 and 1329 UTC) of that day: with the OPC-N3 and a drying chamber, and then without it, consecutively. Specific details of the short four flights can be found in Table 2.

Humidity conditions at the time of the comparison was high (above 85% in both cases—third column in Table 2) and the relative difference between dried/nondried measurements was analyzed, along with the accuracy of the system with its dryer and while in flight, against the reference instrumentation. Data from the station were available for every 10 s. For the UAS data, an initial resampling to 10 s was done from measurements every 2 s, and then further resampling to 1 min was performed as that is a commonly used averaging time for PM sensors, and to get a clearer trend of the concentrations compared to the Fidas 200.

Mean values with standard deviations of $PM_1$, $PM_{2.5}$, and $PM_{10}$ were calculated for the data from the flights, and then compared with the reference, as well as the root-mean-square error (RMSE) differences between the two for each flight case (with a dryer, referred to as "dry," and without a dryer, referred to as "ambient"). Particle number and volume concentration size distributions were then calculated to determine size-specific effects of hygroscopic growth within the range that amounts up to $PM_{10}$, i.e., for aerosol particles up to 10 $\mu$m.

TABLE 2. Takeoff and landing times during the flights on 14 Feb 2023 near Mannheim-Nord station. The RH conditions at the time were collected by the SHT31 sensors on board and the flights for measurements with or without the dryer are also noted.

| | Takeoff time (UTC) | Landing time (UTC) | RH (%) | Dryer |
|---|---|---|---|---|
| Flight 1 | 1129 | 1146 | 93.2 | Yes |
| Flight 2 | 1202 | 1219 | 93.8 | No |
| Flight 3 | 1253 | 1309 | 88.4 | Yes |
| Flight 4 | 1317 | 1329 | 88.1 | No |

TABLE 3. Takeoff and landing times during the flights on 22 Nov 2022, at the Boundary Layer Field Site Falkenberg. Flights for measurements with or without the dryer are noted.

| | Takeoff UTC | Landing UTC | Dryer |
|---|---|---|---|
| Flight 1 | 0750 | 0756 | Yes |
| Flight 2 | 0809 | 0816 | No |
| Flight 3 | 1356 | 1404 | Yes |
| Flight 4 | 1407 | 1416 | No |

### c. *Cloud measurements*

Prior to that, the UAS had been used for further measurements at high-humidity conditions at the Boundary Layer Field Site (GM) Falkenberg (WGS84 east: 14°7, WGS84 north: 52°10′, elevation of 73 m above sea level), in Lindenberg, Germany, operated by the German Meteorological Service [Deutscher Wetterdienst (DWD)]. Among a series of operations at the field site, there is a 99-m-high meteorological tower taking measurements of quantities like temperature, relative humidity, air pressure, wind speed and direction, at different heights. Four vertical profiles up to an altitude of 180 m above ground level were performed on 22 November 2022 at the site, in the same philosophy as in the comparison with Mannheim-Nord, two sets of data collection with and without a dryer on the OPC. Table 3 shows the flight specifics.

Temperature and RH profiles at heights 10, 40, 60, and 80 m were taken from Vaisala HMP45D sensors in an aspirated radiation shield (Young 43408), which are the sensors installed on the meteorological tower. During the flights 1 and 2 (first and second rows in Table 3) in the morning, a low altitude stratus cloud was present and visible at an altitude of approximately 65 m above ground. At the location, there is also an operating ceilometer (CHM 15k "NIMBUS," Lufft GmbH, Germany) that captures cloud altitude heights and extent, which was used to verify that altitude during the time of the early day operations. The UAS performed a vertical profile below it and through the layer until about 180 m above ground level. For flights 3 and 4 (third and fourth rows in Table 3), the cloud layer had disappeared but conditions were still very humid and close to saturation. A similar vertical profile was performed to observe the PM measurement of the OPC-N3 with and without a drying chamber, inside the cloud layer and afterward in its absence. As the UAS ascends at a vertical speed of 1.5 m $s^{-1}$ to 180 m, the vertical profiles only lasted a few minutes, which are enough for it to rise at that altitude and return on the ground.

## 4. Results

### a. *Effect of the dryer on SFR and PM*

The outcome of the sample flow rate SFR difference measured by the OPC in case of present or absent drying channel can be seen in Fig. 5. When nothing is attached to the OPC, the SFR is higher and closer to its typical value as stated by the manufacturer, here measured at 4.76 ± 0.25 mL $s^{-1}$, the mean value among the three measurement periods under this setup. SFR is reduced when either a tube or a dryer of same length is attached by about 0.8 mL $s^{-1}$, measured at 3.92 ± 0.17 mL $s^{-1}$ and 3.97 ± 0.13 mL $s^{-1}$, respectively. This change in SFR has a small impact on the output of $PM_1$, where a value of 0.72 ± 0.18 $\mu$g $m^{-3}$ was measured without anything attached, but 0.79 ± 0.18 $\mu$g $m^{-3}$ with a tube and 0.78 ± 0.18 $\mu$g $m^{-3}$ with a dryer. A similar change is observed for $PM_{2.5}$, where 1.87 ± 1.0 $\mu$g $m^{-3}$ was measured without

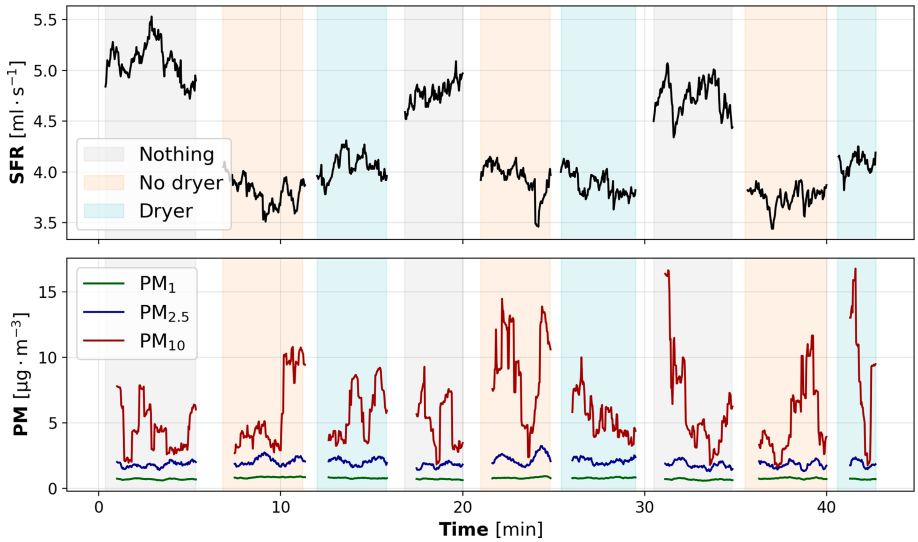


FIG. 5. Recorded SFR and the three PM values for a time of 43 min in laboratory conditions for the dryer test case. Each colored area at the top graph indicate measurement times where there was no tube attached to the OPC-N3's inlet (area in gray), a tube but not a dryer was attached (area in brown), or the dryer was attached (area in cyan). Small gaps in between the different measurement stages indicate the time for adjusting or removing the dryer, and were excluded from the analysis.

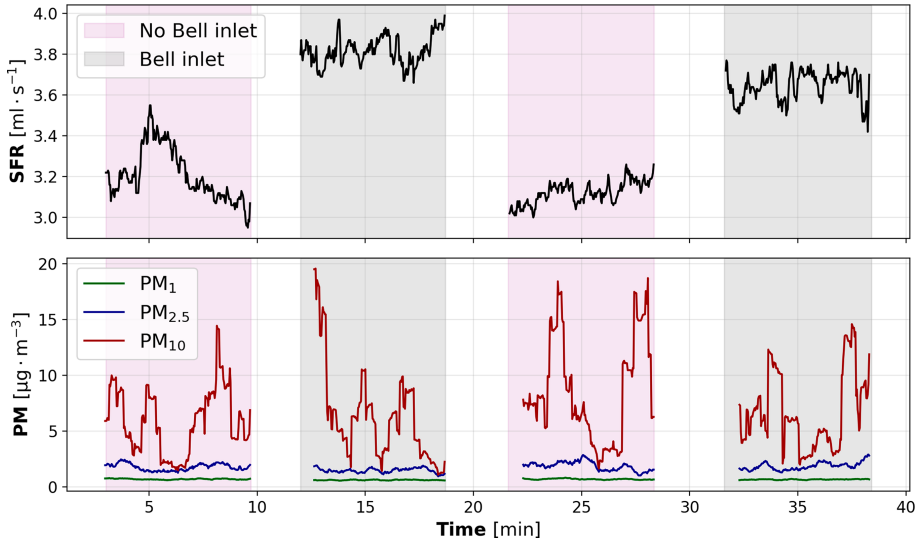


FIG. 6. Recorded SFR and the three PM values for a time of 37 min in laboratory conditions for the bell-shaped inlet test case. Each colored area at the top graph indicate measurement times where there was no bell inlet attached to the OPC-N3's extra tube (area in red), or it was attached (area in gray). Units for the three PM values are $\mu g\ m^{-3}$.

anything attached, but 1.98 ± 1.1 $\mu g\ m^{-3}$ with a tube and 1.98 ± 1.1 $\mu g\ m^{-3}$ with a dryer. No significant effect of the tubing/dryer on $PM_{10}$ can be identified in Fig. 5 (mean values of 6.0, 5.85 and 6.56 $\mu g\ m^{-3}$, respectively).

A similar approach was followed for looking at the differences between a bell-shaped inlet in place, and an absent one. The results are seen in Fig. 6. The difference between the case of an attached bell and absent bell for the SFR is 0.55 mL $s^{-1}$, with measured 3.18 ± 0.25 mL $s^{-1}$ and 3.91 ± 0.25 mL $s^{-1}$ for each case, respectively. The PM values were comparable: 0.69 ± 0.18 $\mu g\ m^{-3}$ and 0.64 ± 0.17 $\mu g\ m^{-3}$ for $PM_1$, 1.84 ± 1.2 $\mu g\ m^{-3}$ and 1.82 ± 1.0 $\mu g\ m^{-3}$ for $PM_{2.5}$, and 7.21 $\mu g\ m^{-3}$ and 6.86 $\mu g\ m^{-3}$ for $PM_{10}$. It can also be clearly seen that the bell-shaped inlet indeed increases the flow through the dryer, reaching a value that is closer to what the sensor would have while in operation without any extra component. Differences on the PM values with or without the dryer fall on the second decimal of the mean value, yet the standard deviation is at least one order of magnitude bigger. This makes the effect of the dryer to the flow through the OPC negligible and can therefore be assumed that there is no significant alteration, caused by the extra channel and inlet attached to it, to the operation with its parent microfan.

### b. *Evaluation in the fog tank*

The experiments in the fog tank included RH measurements of the airflow first from inside the saturated container, and then after the airflow has passed through the dryer in an ambient air box. When the humidifier is on, RH levels in the tank (measured by the SHT31 inside it) reach 95%–100%, and condensation is visible in the form of fog which provides an environment similar to highly humid or foggy conditions outdoors.

Experiments in the fog tank consists of two distinct cases:

1) humid conditions using the dryer (95% humidity inside the tank, present fog but no active humidifier)
2) humid conditions (as above) without the dryer

As it can be observed in Fig. 7a, highly humid air of 95% RH is present in the fog tank, which is then dried by the drying chamber down to 41%, which shows moisture being removed and the airflow being sufficiently dry for an aerosol measurement with the OPC. A short kick is recognized the moment the pump is turned on, which is balanced by the active blue silica that constantly retains the RH level at the ambient air box low. At the same time, RH in the fog tank is almost constantly at 95% with very low variance. At exactly the same conditions but with no drying chamber connecting the tank and the dryer box (Fig. 7b), the humidity, as expected, does not reduce significantly, but remains the same in the two measurement boxes. A 4% difference in relative humidity is observed after 8 min of run time even in the case of no drying chamber used (Fig. 7b). This is a result of the operation of the micropump itself, which slowly raises the temperature in the ambient air box, which in turn reduces the humidity locally.

### c. *Airborne measurements*

#### 1) COMPARISON WITH REFERENCE URBAN STATION

Results from the comparison between Mannheim-Nord station and the UAS hovering flights in the station, explained in section 3b, are shown in Fig. 8. A distinct difference can be seen between measurements with the drying chamber and without it. It is clear that under such high-humidity conditions, the OPC with its installed drying channel lowers the concentrations and is in acceptable statistical agreement with the reference station for all three PM types. At times with no present dryer, the overestimation is significant. Table 4

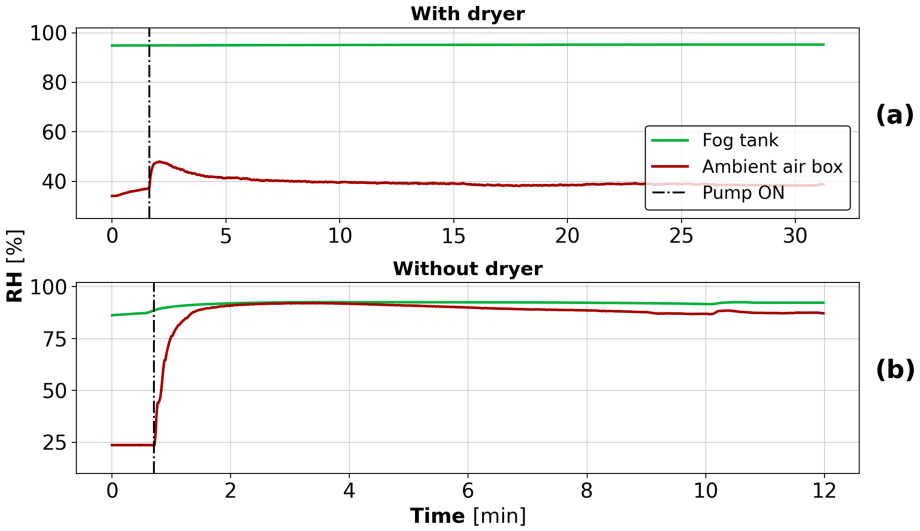


FIG. 7. Two different examples of relative humidity measurements at the fog tank, using the constructed drying channels. (a) Fog is present in the fog tank creating high-humidity conditions, but the humidifier is then turned off. The dashed vertical black line indicates the moment when the pump is turned on, beginning the suctioning of wet air through the drying chamber. (b) The conditions are the same as in the first case, but this time there is no drying chamber but a simple copper tube connecting the two boxes.

contains the mean values and standard deviations calculated for each flight, along with mean values from the reference Fidas 200.

During the morning, and at an average RH level of 93.6%, the nondrying OPC on the UAS heavily overestimates the concentrations, as $PM_1$ is 83%, $PM_{2.5}$ is 397%, and $PM_{10}$ is 481% higher than the equivalent values of the reference instrument. On the contrary, during the UAS flight with the drying OPC, results are on the same order of magnitude. Specifically, the airborne OPC underestimates $PM_1$ by 13%, slightly overestimates $PM_{2.5}$ by 3% and measures slightly higher $PM_{10}$ concentrations too, with an 11% difference from the reference instrument. The standard deviations are higher when no dryer is present as well, and the same behavior remains during the afternoon with RH levels at 86.5%, with significant overestimations during the "ambient" flights (41%, 141%, and 144% for $PM_1$, $PM_{2.5}$, and $PM_{10}$). Measurements during the drying OPC flight show similarity with the morning case, as $PM_1$ is underestimated by 8%, but $PM_{2.5}$ and $PM_{10}$ are overestimated by 10% and 20%. The results from these four flights show that the dryer provides effective drying at such humid conditions. The average RMSE for the "dry" cases was 3.7 $\mu g\ m^{-3}$ for $PM_1$, compared to 25.95 $\mu g\ m^{-3}$ during the "ambient" cases. The same calculation was 3.4 $\mu g\ m^{-3}$ compared to 107 $\mu g\ m^{-3}$ for $PM_{2.5}$, and 9.5 $\mu g\ m^{-3}$ compared to 138.2 $\mu g\ m^{-3}$ for $PM_{10}$.

Figure 9 shows the size distributions of the number and volume concentrations from the flights. Both distributions show a larger difference between "dry" and "ambient" case between 1 and 4 $\mu$m, while the same is less obvious for smaller or bigger aerosols in this size range. The distributions also do not follow a completely similar trend because of this, as the aforementioned size ranges seem to get more affected by water uptake due to hygroscopic growth.

During the airborne measurements, the flow rate through the OPC was determined from the sensor output, as in section 4a. For the first flight, the mean SFR was 3.21 mL $s^{-1}$, while it was slightly lower during the second flight, at 2.95 mL $s^{-1}$. This indicates that the flight conditions affect the flow rate through the OPC system further than on the ground, which is expected due to the rotor movement in the vicinity. Nevertheless, calculated PM values are still not negatively affected from this flow rate decrease during the "dry" measurements, as seen from Fig. 8 and Table 4.

### 2) VERTICAL PROFILES INSIDE A CLOUD

Figure 10 contains the results from consecutive vertical profiling flights, with and without a dryer on the OPC-N3, taken on 22 November 2022 at Falkenberg tower. All flights show measurements only during the ascent of the UAS, to avoid potential downwash effects from its rotors on the PM data of the sensor. A sharp increase in concentrations can be noticed exactly at the bottom altitude level of the cloud layer (measured by the CHM-15k ceilometer), for $PM_{2.5}$ and $PM_{10}$, during the morning flights, in both the dried and nondried measurements. For $PM_1$, concentrations do not indicate the cloud layer, which is expressed in the bigger sizes with the larger PM types. During the afternoon (flights 3 and 4 in Fig. 10), all concentrations are considerably lower than in the morning as there is no cloud present at the covered altitude range.

Temperature and humidity up to 99 m from the Falkenberg tower at the location are shown in the upper panel of Fig. 11. The temperature closer to the ground was slightly below 0°C in the morning, and the RH levels were also higher than in the afternoon. It can be seen that as early as 0750 UTC, measured RH at the tower was at saturation at three altitudes (20, 60, and 99 m), while later at 1400 UTC, RH was generally

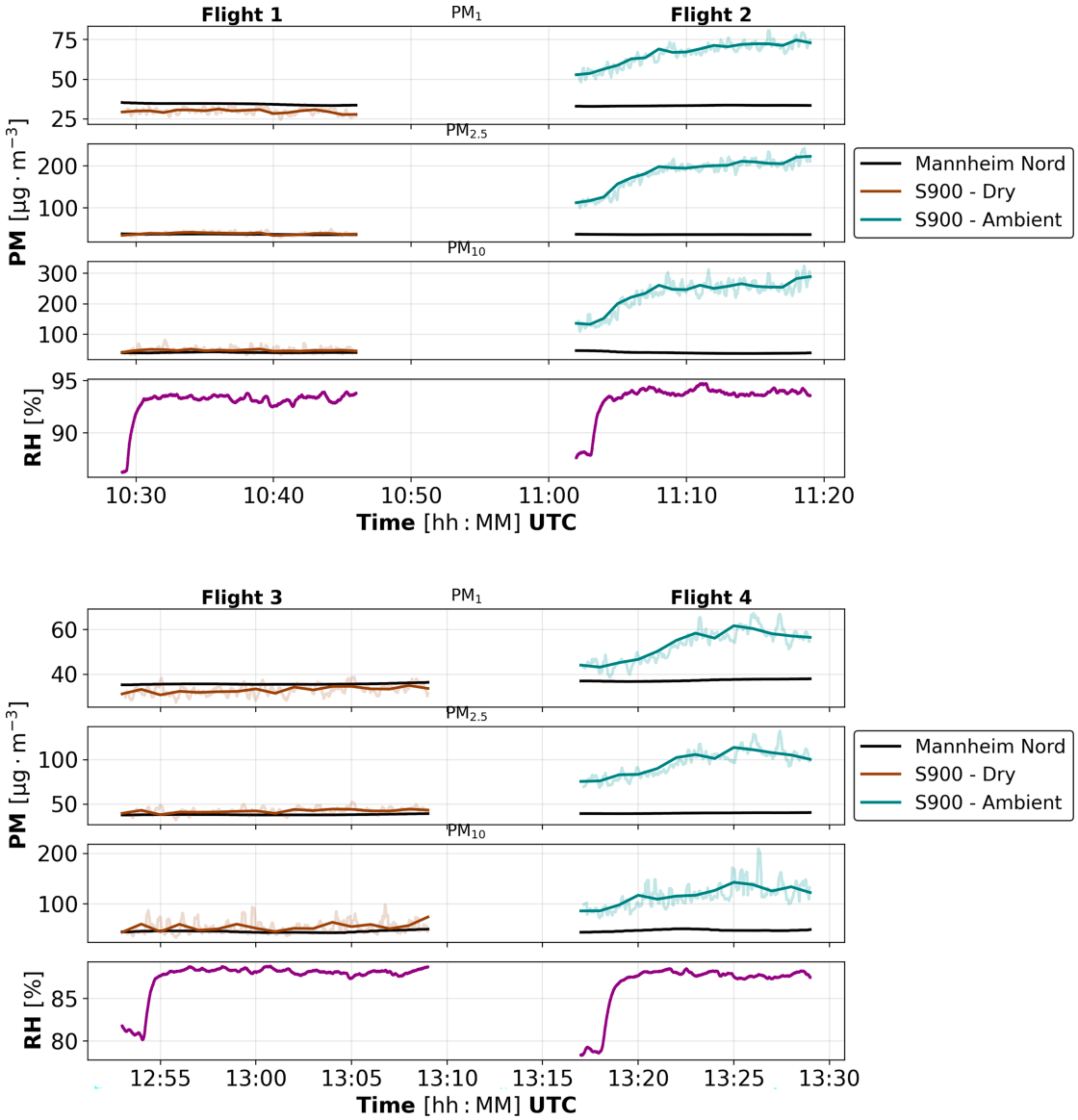


FIG. 8. Measurements at Mannheim-Nord station during the morning (flights 1–2) and afternoon (flights 3–4) of 14 Feb 2023. Two consecutive flights with (i.e. "dry" case) a dryer on the OPC system and without (i.e. "ambient" case) it, for the cases of the three PM types. Measured RH from the SHT31 is shown at the bottom plot, and the solid black line shows the reference measurements from the Fidas 200 at the station. The solid S900 lines indicate 1 min resampled averages, and the less opaque lines of the same colors indicate the nonaveraged data.

high at all altitudes, with a value below 96% only at 40 m and at saturation at 99 m. At these extremely humid conditions during these flights, a comparison between "dry" and "ambient" measurements from the OPC system on the UAS show, apart from an evident indication of the vertical extent of the cloud layer, the general hygroscopic growth effect on the aerosol particles that have not yet condensed into cloud droplets.

TABLE 4. Mean values and standard deviations for each PM type, and for each flight. Flights 1 and 3 include the dryer and flights 2 and 4 do not. Near the measurements from the S900 are shown the PM levels measured by the Fidas 200 at the Mannheim-Nord station. All PM values have units of $\mu g\ m^{-3}$.

| | S900 $PM_1$ | S900 $PM_{2.5}$ | S900 $PM_{10}$ | Ref $PM_1$ | Ref $PM_{2.5}$ | Ref $PM_{10}$ |
|---|---|---|---|---|---|---|
| Flight 1 (dry) | 30 ± 1.0 | 38.3 ± 2.2 | 45.8 ± 2.5 | 34.4 | 37.0 | 41 |
| Flight 2 (ambient) | 66.5 ± 6.7 | 184.7 ± 33.9 | 233.9 ± 46 | 33.4 | 36.3 | 40.2 |
| Flight 3 (dry) | 33.0 ± 1.2 | 42.1 ± 1.7 | 54.4 ± 6.6 | 35.7 | 38.2 | 45.2 |
| Flight 4 (ambient) | 53.3 ± 6.3 | 96.8 ± 12.8 | 116 ± 17.4 | 37.7 | 39.9 | 47.5 |

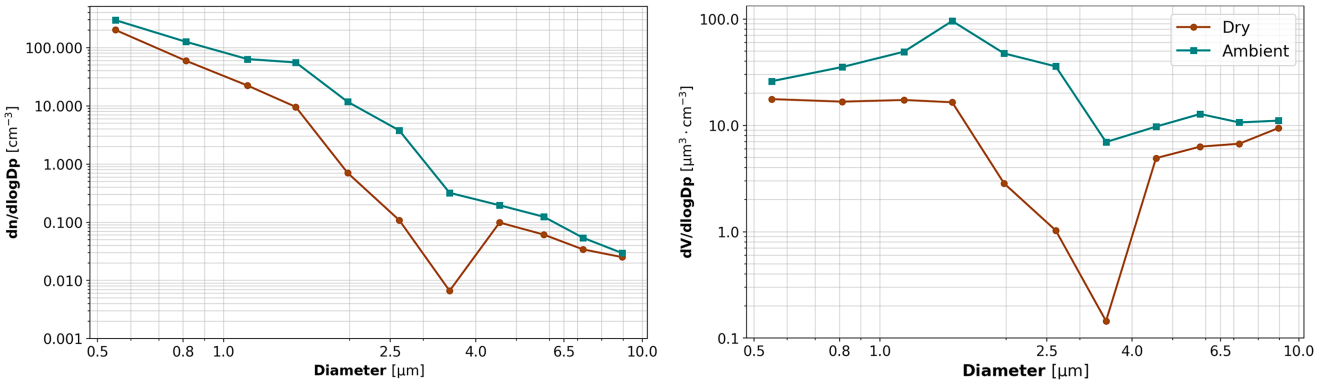


FIG. 9. Calculated (left) aerosol particle number and (right) volume size distributions between 0.5 and 9 $\mu$m.

## 5. Discussion

### a. *Experiments in the laboratory*

The effect of the dryer, at these dimensions and configuration, on the flow rate of the OPC-N3, was first examined in the laboratory by measuring SFR and PM levels while having the extra components in place or not. From Figs. 5 and 6, there is a recognizable difference in SFR levels when either a tube, a dryer, or a bell-shaped inlet is in place, compared to when the sensor is running without anything fixed to it. As the microfan preinstalled in the instrument was built to provide a certain pressure drop, the change is expected, yet from the results it seems that it does not negatively affect the final output of the sensor. Differences between the PM levels due to the dryer alone lie on an order of magnitude that is smaller than the accuracy of the sensors, and SFR levels do not drop drastically in a way that they would completely negate the aspiration of the OPC-N3. Chacón-Mateos et al. (2022) noted that the inner diameter of the low-cost 50 cm dryer of that study for an OPC-R1 was chosen so that the flow rate through the sensor does not have a deviation bigger than 2% compared to the case of an absent dryer. In our case, the deviation is higher on the ground measurements, at about 17%, but it is demonstrated that the PM readings are essentially the same under the

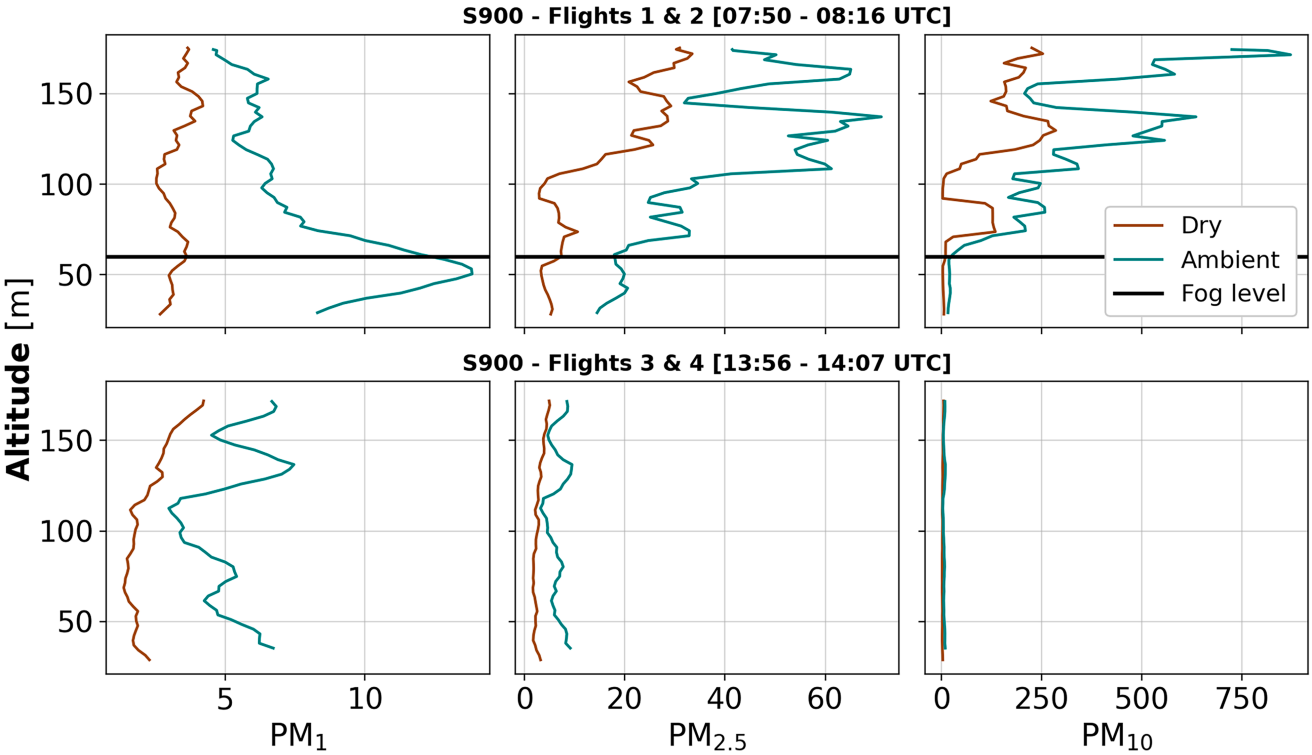


FIG. 10. Measurements inside a low-stratus cloud at Falkenberg tower. The first two flights took place in the morning when the cloud layer was quite low, starting at an altitude of 65 m, as recorded by the installed CHM-15k at the site. (top) Its level is indicated with the black horizontal line for flights 1 and 2. (bottom) In the afternoon (flights 3 and 4), the cloud was not anymore at the same altitude range. The three PM types are depicted under the two cases of using a dryer (i.e., dry) and not using one (i.e., ambient). Units for the three PM values are $\mu$g m$^{-3}$.

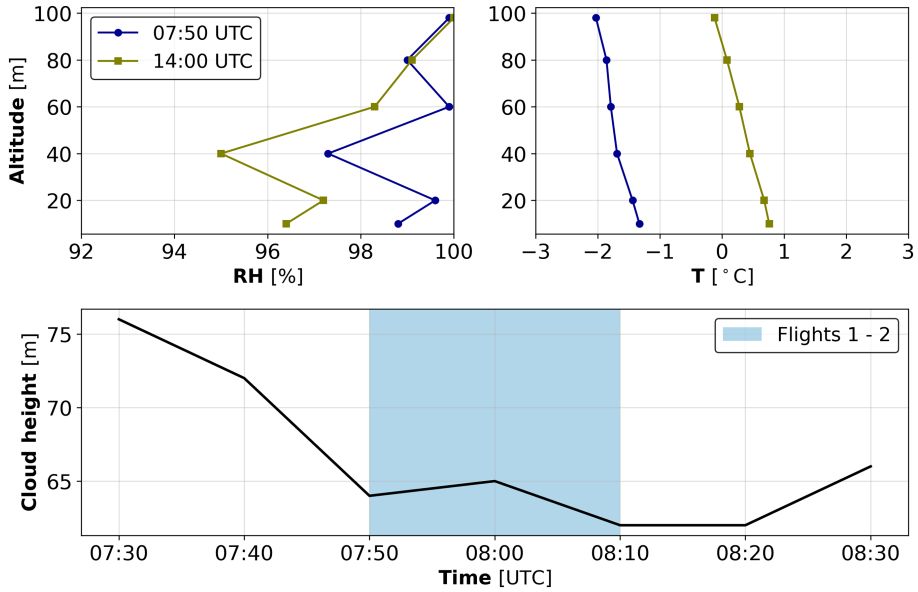


FIG. 11. Humidity and temperature during the time of measurement flights of the UAS, taken from the sensor instrumentation at Falkenberg tower. (top) The two lines correspond to the two points during that day when the vertical profiles where performed, one in the morning and one in the afternoon. (bottom) The cloud layer height, observed by the ceilometer, is shown for a time period of 1 h. The time of flights of the UAS are also indicated in shaded blue, starting from the first vertical profile at 0750 UTC.

different conditions. From this outcome, it is considered that the specific dryer does not interfere with the sensor's operation to an extent that it would result in false PM measurements.

The dryer was employed in a container where fog was produced through an ultrasonic humidifier dipped in water. Miniaturized meteorological sensors (SHT31) recorded the relative humidity inside the fog tank and in the air after the drying chamber to compare differences between the water vapor levels of the airflow before and after it passed through the blue silica tube (as depicted in Figs. 3 and 7). Figure 7a shows the performance of the drying chamber when in contact with air that has an average level of 95% relative humidity. It seems that after the microfan (to assure an airflow through the system) is turned on, relative humidity after passing the dryer is lowered down to approximately 40%, which is an acceptable level to consider the air as dried, and have also been considered a safe standard for other aerosol measurement studies of the same topic, for example, in the drying chamber by Bezantakos et al. (2018). Without any drying chamber, there is no significant RH drop (this case is the equivalent of using the OPC at a humid environment without a drying method). The duration of the fog tank test amounts for a time of more than 30 min, longer than the flight endurance of the UAS on which the OPC system is intended to be used. As the dryer is easily reproducible, multiple units can be used for multiple flights and it becomes vital that the dryer is effective for at least one flight, which is achieved here as shown in Fig. 7.

### b. *Outdoor measurements*

For the urban experiments near Mannheim-Nord, the OPC-N3 with a dryer on the UAS agree well with the monitoring station using a certified Fidas 200. The underestimation of $PM_1$ is an anticipated result as the Fidas 200 has a lowest detectable size boundary of 0.18 $\mu$m, which is lower than the one of the OPC-N3 at 0.35 $\mu$m. This means that the Fidas 200 is able to detect even smaller aerosol particles, which are all eventually amounted for the final $PM_1$ value it records. Thus, the difference between the $PM_1$ values between the two systems could be explained by the fact that particles between 0.18 and 0.35 $\mu$m were detected by the Fidas 200 but not by the OPC-N3. This discrepancy is most evident in that PM type but not in the bigger sizes, as the OPC-N3 $PM_{2.5}$ outputs were in agreement with the Fidas 200. $PM_{10}$ was overestimated even with in the case of the "dry" measurements, which is a result that has been noted before for the OPC-N3 (Vogt et al. 2021). In that evaluation study, which compared a few low-cost sensors and an OPC-N3, relative humidity problems were also identified for that specific instrument and a difficulty to measure larger particles was also pointed out. The authors noted how all the low-cost sensors did not reach a high agreement with their reference instrumentation for bigger sizes. However, our study focuses on the relative difference between "dry" and "ambient" measurements and from that perspective, the installed dryer evidently dried the airflow effectively for the duration of the flights. Noteworthy is that the overestimation of "dry" measurements increased from the morning to the afternoon, despite the decrease in RH, which may be due to the lowering efficiency of the desiccant, exposed to such high-humidity conditions, as hours passed by.

Numerous studies have already pointed out the measurement overestimation of low-cost OPCs at high-humidity

conditions. For example, Samad et al. (2021) found that an OPC-N3 without a drying chamber measured almost double the PM amounts compared to the same sensor with its installed drying chamber, at a laboratory test in a climate chamber at high-humidity conditions. Badura et al. (2018) arrived at similar conclusions were drawn in a longer-term experiment of $PM_{2.5}$ measurements in real-life conditions for an OPC-N2 (which suffers from the same issue as the OPC-N3 when it comes to humidity), when measurement conditions were under RH of 80% or more. Samad et al. (2022) noted $PM_{2.5}$ overestimation at certain times during their UAS flights compared to the reference, which were attributed to the RH conditions at the time. In the case of the Mannheim experiments, also with airborne measurements, there is significant overestimation from the system when no dryer was attached, as seen in Fig. 8 and at the PM mean value calculations at Table 4. This can be attributed to the same reason, as the flights with the dryer show concentrations much closer to the reference values to the Fidas 200. There is a lower level of overestimation in the "ambient" afternoon flights compared to the flights in the morning, which shows how much a reduction of RH from close to 95% to a bit less than 90% can affect PM measurements on an OPC without a component to remove the water vapor from the airflow.

Size distributions of number and volume concentrations in Fig. 9 also show different water uptake at different sizes, which is likely a result of the specific particle chemical composition at the given time of measurements. Such a result supports the notion of not applying postprocessing solutions to collected nondried measurements, as hygroscopic growth can be different throughout different aerosol size modes, but also chemical composition and type. Since such information cannot be retracted solely from an optical sensor such as the OPC-N3, it is difficult to assess the reasons behind size-specific hygroscopic growth differences. A previous study including crewed aircraft flights was done by Hegg et al. (2007), where different hygroscopic growth factors at different altitudes, but also at different sizes between 0.5 and 3.2 $\mu$m, were observed. The authors of that work stated that particles differed in composition across the covered size range, which is presumably the case for our measurements too. Another hygroscopicity study for particles up to 10 $\mu$m in size revealed higher hygroscopic growth factors in the micron range and up to 5 $\mu$m for RH = 91% (Eichler et al. 2008), which was a comparable result to the depicted distribution in Fig. 9. It has been shown that there is a proportionality of hygroscopic growth factors for continental submicron- and micron-sized aerosols (Zhang et al. 2014), which may imply the presence of particles from other sources during the Mannheim measurements, which were more hygroscopic in the micron range. This emphasizes the effect of particle mixing and composition on the resulting growth due to water uptake.

During the vertical profiling flights at Falkenberg tower, a low-altitude cloud was over the area during the morning of 22 November 2022, but later dissipated during the day and was gone in the afternoon, while RH conditions remained high (Fig. 11). The ceilometer recorded a cloud layer altitude between 62 m (at 0810 UTC) and 65 m (at 0800 UTC) in the area, and Fig. 10 clearly shows a significant rise in $PM_{10}$ as the UAS entered the cloud at that altitude. At the same time, the RH sensors on the tower seem to be at saturation at their highest altitude of 99 m. This indicates that measuring at such conditions with two identical OPCs that only differ on the presence of a dryer could accurately show the altitude of a cloud ceiling when standard RH sensors have slower response time or get saturated. From Fig. 10, it can also be observed that the PM concentrations under the cloud level were relatively low, and on the same order of magnitude as the concentrations during the afternoon flights for the whole vertical profile, showcasing how the PM difference above 65 m between the two sets of flights, comes from the cloud only present in the morning. It is important to note that the SFR during the vertical profiles was lower than in the laboratory tests (section 4a) as well as the hovering flights at Mannheim (section 4c), ranging from 1 to 1.5 mL $s^{-1}$, indicating how the UAS and atmospheric conditions affected the flow rate through the sensor. This SFR change however did not decrease the measurement accuracy, as the OPC data also showed generally low raw bin counts, i.e., sampling less volume of air, but also less particles than what it would, at a higher SFR. This can be realized from the high PM levels especially for $PM_{10}$ during the morning flights (Fig. 10), where peaks reached 250 $\mu$g $m^{-3}$ during the flight with a dryer, and 750 $\mu$g $m^{-3}$ during the flight without it.

As water droplets have different optical properties than dry aerosol particles, the implications regarding their interaction with an optical sensor such as an OPC-N3 were not within the objectives of this work, which only assesses the drying procedure. However, a recent study by Nurowska et al. (2023) examined the usage of an OPC-N3 specifically for fog measurements in detail, and the authors concluded that the sensor measures fog droplets, as well as aerosol particles that are wetted from water vapor in the environment (i.e., hygroscopically grown). In our morning vertical profiles (flights 1 and 2 in Fig. 10), both "dry" and "ambient" measurements rise above the 65 m mark for $PM_{2.5}$ and $PM_{10}$, which leads to the conclusion that the constructed dryer was able to only partially dry the sampled air when liquid water was present. Hence, it is more appropriate for measurements at high-humidity conditions, when condensation has not occurred yet. Still, the base height of the cloud was accurately detected, and the difference between the two profiles can give an indication of the amount of noncondensed aerosol particles across the layer. Later on in the day (flights 3 and 4 in Fig. 10), concentrations are significantly lower and more comparable to how they were during the morning below the cloud layer, i.e., showing that the cloud has passed. We assume that the vertical extent of the cloud was in the lower part of the atmosphere and just some tens of meters above the highest point of the UAS at that time, when considering the potentially major decrease that started evolving at the very top of the $PM_{2.5}$ and $PM_{10}$ vertical profiles during the morning flights. However, ascent was not continued due to considerations about rotor icing at such cold temperatures (already 0°C at ground level), which would severely compromise the flying operations.

## 6. Conclusions

A compact, lightweight diffusion drying channel was built and tested with an OPC-N3 on a UAS for short-term measurements in highly humid conditions. Its dimensions and weight provide for a flexible and sustainable solution for UAS data collection, which requires components smaller and lighter than their ground-based counterparts. The effect of the dryer was tested in a fog tank where drying from almost saturated to 40% RH was achieved for at least half an hour. The dryer's length (12 cm) and attached bell-shaped inlet on top also did not significantly interfere with the sensor's aspiration process, which stems from the use of a microfan. More meticulous analysis of the flow inside the dryer and potential particle loss through its inner chamber will be the focus of a future, separate study.

In this work, the question was approached by looking at the final SFR levels through the OPC-N3 and the corresponding PM values, which remained reasonable. This was also further evaluated during hovering flights near the reference station Mannheim-Nord at conditions of high humidity, where effective drying was demonstrated by comparing measurements with and without the dryer, against the tower's instrumentation as reference. The rotor-induced downwash of this specific UAS platform (S900 + Styrofoam encasing) is also another point of a follow-up study, which will indicate more clearly the ideal placement of the sensor or dryer. However, the adjustability of such a system is high, as it is self-designed and can be modified further for future experiments. While the effect of the rotor flow to the resulting sampling flow through the inlet and dryer was not directly inspected, the resulting SFR values during flight still gave reasonable values for the PM concentrations, as it is apparent from the comparison with the reference, Fidas 200.

Vertical profiles inside a low-altitude cloud revealed that the OPC-N3 can accurately detect the cloud layer base, which was aligned with the indication from the ceilometer. When used in combination with a dual measurement with and without a dryer, it can give further information on the amount of fog droplets and humidified aerosols. An OPC can potentially record a sharp change in concentrations when the cloud was encountered, and therefore pinpoint cloud ceiling with high accuracy. For future work, a more compact UAS, suited for measurements in cold and icy conditions, with two mounted OPCs for capturing ambient and dry concentrations simultaneously, is being developed and will be further used with a drying channel as described currently. Furthermore, replacement of the parent microfan with a steady pump can accommodate for less flow rate undulations, but with careful consideration of the weight limits related to UAS operations. This small dryer showcased that it can provide adequate drying for short-term measurements even in highly humid air, and could prove useful in many future UAS activities that include miniaturized aerosol particle sensors such as OPCs.

*Acknowledgments.* We thank the Baden-Württemberg State Institute for the Environment (LUBW) for providing the data from Mannheim-Nord station for the comparisons conducted in the paper. Furthermore, we appreciate data provided by DWD from the Falkenberg site and specifically the help of Dr. Frank Beyrich during our flight activities and the hospitality during our stay in Lindenberg for the experimental campaign. This work is partly funded by the European Union Horizon 2020 research and innovation program under Grant Agreement 861291 as part of the Train2Wind Marie Skłodowska-Curie Innovation Training Network (https://www.train2wind.eu/). Partial funding was also acquired from the Federal Ministry for Education and Research for Project Funding (NABF) by the German Weather Service (DWD) in Germany, under grant agreement with a reference: 4819EMF01. The authors of the manuscript declare no conflicts of interest.

*Data availability statement.* Raw sensor outputs, processing and data acquisition scripts can be shared from the article's lead author, along with necessary clarifications, upon reasonable request.

## REFERENCES

Alphasense, 2019: User manual: OPC-R1 optical particle counter. Alphasense Doc., 33 pp.

Altstädter, B., and Coauthors, 2015: ALADINA—An unmanned research aircraft for observing vertical and horizontal distributions of ultrafine particles within the atmospheric boundary layer. *Atmos. Meas. Tech.*, **8**, 1627–1639, https://doi.org/10.5194/amt-8-1627-2015.

Alvarado, M., F. Gonzalez, P. Erskine, D. Cliff, and D. Heuff, 2017: A methodology to monitor airborne $PM_{10}$ dust particles using a small unmanned aerial vehicle. *Sensors*, **17**, 343, https://doi.org/10.3390/s17020343.

Anderson, J. O., J. G. Thundiyil, and A. Stolbach, 2012: Clearing the air: A review of the effects of particulate matter air pollution on human health. *Med. Toxicol.*, **8**, 166–175, https://doi.org/10.1007/s13181-011-0203-1.

Andreae, M. O., and D. Rosenfeld, 2008: Aerosol–cloud–precipitation interactions. Part 1. The nature and sources of cloud-active aerosols. *Earth-Sci. Rev.*, **89**, 13–41, https://doi.org/10.1016/j.earscirev.2008.03.001.

Badura, M., P. Batog, A. Drzeniecka-Osiadacz, and P. Modzel, 2018: Evaluation of low-cost sensors for ambient $PM_{2.5}$ monitoring. *J. Sens.*, **2018**, 5096540, https://doi.org/10.1155/2018/5096540.

Bezantakos, S., F. Schmidt-Ott, and G. Biskos, 2018: Performance evaluation of the cost-effective and lightweight Alphasense optical particle counter for use onboard unmanned aerial vehicles. *Aerosol Sci. Technol.*, **52**, 385–392, https://doi.org/10.1080/02786826.2017.1412394.

Bílek, J., O. Bílek, P. Maršolek, and P. Buček, 2021: Ambient air quality measurement with low-cost optical and electrochemical sensors: An evaluation of continuous year-long operation. *Environments*, **8**, 114, https://doi.org/10.3390/environments8110114.

Bramati, M., M. Schön, D. Schulz, V. Savvakis, Y. Wang, J. Bange, and A. Platis, 2024: A versatile calibration method for rotary-wing UAS as wind measurement systems. *J. Atmos. Ocean. Technol.*, **41**, 25–43, https://doi.org/10.1175/JTECH-D-23-0010.1.

Bretschneider, L., and Coauthors, 2022: MesSBAR—Multicopter and instrumentation for air quality research. *Atmosphere*, **13**, 629, https://doi.org/10.3390/atmos13040629.

Brosy, C., K. Krampf, M. Zeeman, B. Wolf, W. Junkermann, K. Schäfer, S. Emeis, and H. Kunstmann, 2017: Simultaneous multicopter-based air sampling and sensing of meteorological variables. *Atmos. Meas. Tech.*, **10**, 2773–2784, https://doi.org/10.5194/amt-10-2773-2017.

Chacón-Mateos, M., B. Laquai, U. Vogt, and C. Stubenrauch, 2022: Evaluation of a low-cost dryer for a low-cost optical particle counter. *Atmos. Meas. Tech.*, **15**, 7395–7410, https://doi.org/10.5194/amt-15-7395-2022.

Chakraborty, R., J. Heydon, M. Mayfield, and L. Mihaylova, 2020: Indoor air pollution from residential stoves: Examining the flooding of particulate matter into homes during real-world use. *Atmosphere*, **11**, 1326, https://doi.org/10.3390/atmos11121326.

Charlson, R. J., S. E. Schwartz, J. M. Hales, R. D. Cess, J. A. Coakley Jr., J. E. Hansen, and D. J. Hofmann, 1992: Climate forcing by anthropogenic aerosols. *Science*, **255**, 423–430, https://doi.org/10.1126/science.255.5043.423.

Chen, S.-L., S.-W. Chang, Y.-J. Chen, and H.-L. Chen, 2021: Possible warming effect of fine particulate matter in the atmosphere. *Commun. Earth Environ.*, **2**, 208, https://doi.org/10.1038/s43247-021-00278-5.

Corrigan, C. E., G. C. Roberts, M. V. Ramana, D. Kim, and V. Ramanathan, 2008: Capturing vertical profiles of aerosols and black carbon over the Indian Ocean using autonomous unmanned aerial vehicles. *Atmos. Chem. Phys.*, **8**, 737–747, https://doi.org/10.5194/acp-8-737-2008.

Crazzolara, C., M. Ebner, A. Platis, T. Miranda, J. Bange, and A. Junginger, 2019: A new multicopter-based unmanned aerial system for pollen and spores collection in the atmospheric boundary layer. *Atmos. Meas. Tech.*, **12**, 1581–1598, https://doi.org/10.5194/amt-12-1581-2019.

Crilley, L. R., M. Shaw, R. Pound, L. J. Kramer, R. Price, S. Young, A. C. Lewis, and F. D. Pope, 2018: Evaluation of a low-cost optical particle counter (Alphasense OPC-N2) for ambient air monitoring. *Atmos. Meas. Tech.*, **11**, 709–720, https://doi.org/10.5194/amt-11-709-2018.

Cruz, C. N., and S. N. Pandis, 2000: Deliquescence and hygroscopic growth of mixed inorganic–organic atmospheric aerosol. *Environ. Sci. Technol.*, **34**, 4313–4319, https://doi.org/10.1021/es9907109.

Davidson, C. I., R. F. Phalen, and P. A. Solomon, 2005: Airborne particulate matter and human health: A review. *Aerosol Sci. Technol.*, **39**, 737–749, https://doi.org/10.1080/02786820500191348.

Di Antonio, A., O. A. M. Popoola, B. Ouyang, J. Saffell, and R. L. Jones, 2018: Developing a relative humidity correction for low-cost sensors measuring ambient particulate matter. *Sensors*, **18**, 2790, https://doi.org/10.3390/s18092790.

Drake, R. M., and J. E. Gordon, 1985: Mie scattering. *Amer. J. Phys.*, **53**, 955–962, https://doi.org/10.1119/1.14011.

Eichler, H., and Coauthors, 2008: Hygroscopic properties and extinction of aerosol particles at ambient relative humidity in south-eastern China. *Atmos. Environ.*, **42**, 6321–6334, https://doi.org/10.1016/j.atmosenv.2008.05.007.

Gu, Q., D. R. Michanowicz, and C. Jia, 2018: Developing a modular unmanned aerial vehicle (UAV) platform for air pollution profiling. *Sensors*, **18**, 4363, https://doi.org/10.3390/s18124363.

Hegg, D. A., D. S. Covert, H. Jonsson, and P. A. Covert, 2007: An instrument for measuring size-resolved aerosol hygroscopicity at both sub- and super-micron sizes. *Aerosol Sci. Technol.*, **41**, 873–883, https://doi.org/10.1080/02786820701506955.

Held, A., and A. Mangold, 2021: Measurement of fundamental aerosol physical properties. *Springer Handbook of Atmospheric Measurements*, T. Foken, Ed., Springer, 535–565.

Irwin, M., Y. Kondo, N. Moteki, and T. Miyakawa, 2013: Evaluation of a heated-inlet for calibration of the SP2. *Aerosol Sci. Technol.*, **47**, 895–905, https://doi.org/10.1080/02786826.2013.800187.

Jayaratne, R., X. Liu, P. Thai, M. Dunbabin, and L. Morawska, 2018: The influence of humidity on the performance of a low-cost air particle mass sensor and the effect of atmospheric fog. *Atmos. Meas. Tech.*, **11**, 4883–4890, https://doi.org/10.5194/amt-11-4883-2018.

Li, Z., and Coauthors, 2017: Aerosol and boundary-layer interactions and impact on air quality. *Natl. Sci. Rev.*, **4**, 810–833, https://doi.org/10.1093/nsr/nwx117.

Liu, B. Y., D. Y. Pui, K. L. Rubow, and W. W. Szymanski, 1985: Electrostatic effects in aerosol sampling and filtration. *Ann. Occup. Hyg.*, **29**, 251–269, https://doi.org/10.1093/annhyg/29.2.251.

Lohmann, U., and J. Feichter, 2005: Global indirect aerosol effects: A review. *Atmos. Chem. Phys.*, **5**, 715–737, https://doi.org/10.5194/acp-5-715-2005.

Magi, B. I., C. Cupini, J. Francis, M. Green, and C. Hauser, 2020: Evaluation of $PM_{2.5}$ measured in an urban setting using a low-cost optical particle counter and a federal equivalent method beta attenuation monitor. *Aerosol Sci. Technol.*, **54**, 147–159, https://doi.org/10.1080/02786826.2019.1619915.

Mamali, D., and Coauthors, 2018: Vertical profiles of aerosol mass concentration derived by unmanned airborne in situ and remote sensing instruments during dust events. *Atmos. Meas. Tech.*, **11**, 2897–2910, https://doi.org/10.5194/amt-11-2897-2018.

Masic, A., D. Bibic, B. Pikula, A. Blazevic, J. Huremovic, and S. Zero, 2020: Evaluation of optical particulate matter sensors under realistic conditions of strong and mild urban pollution. *Atmos. Meas. Tech.*, **13**, 6427–6443, https://doi.org/10.5194/amt-13-6427-2020.

Muyshondt, A., A. R. McFarland, and N. K. Anand, 1996: Deposition of aerosol particles in contraction fittings. *Aerosol Sci. Technol.*, **24**, 205–216, https://doi.org/10.1080/02786829608965364.

Nurowska, K., M. Mohammadi, S. Malinowski, and K. Markowicz, 2023: Applicability of the low-cost OPC-N3 optical particle counter for microphysical measurements of fog. *Atmos. Meas. Tech.*, **16**, 2415–2430, https://doi.org/10.5194/amt-16-2415-2023.

Platis, A., B. Altstädter, B. Wehner, N. Wildmann, A. Lampert, M. Hermann, W. Birmili, and J. Bange, 2016: An observational case study on the influence of atmospheric boundary-layer dynamics on new particle formation. *Bound.-Layer Meteor.*, **158**, 67–92, https://doi.org/10.1007/s10546-015-0084-y.

Rai, A. C., P. Kumar, F. Pilla, A. N. Skouloudis, S. Di Sabatino, C. Ratti, A. Yasar, and D. Rickerby, 2017: End-user perspective of low-cost sensors for outdoor air pollution monitoring. *Sci. Total Environ.*, **607–608**, 691–705, https://doi.org/10.1016/j.scitotenv.2017.06.266.

Rosati, B., G. Wehrle, M. Gysel, P. Zieger, U. Baltensperger, and E. Weingartner, 2015: The white-light humidified optical particle spectrometer (WHOPS)—A novel airborne system to characterize aerosol hygroscopicity. *Atmos. Meas. Tech.*, **8**, 921–939, https://doi.org/10.5194/amt-8-921-2015.

Samad, A., F. E. Melchor Mimiaga, B. Laquai, and U. Vogt, 2021: Investigating a low-cost dryer designed for low-cost PM sensors measuring ambient air quality. *Sensors*, **21**, 804, https://doi.org/10.3390/s21030804.

——, D. Alvarez Florez, I. Chourdakis, and U. Vogt, 2022: Concept of using an unmanned aerial vehicle (UAV) for 3D investigation of air quality in the atmosphere—Example of measurements near a roadside. *Atmosphere*, **13**, 663, https://doi.org/10.3390/atmos13050663.

Schrod, J., and Coauthors, 2017: Ice nucleating particles over the eastern Mediterranean measured by unmanned aircraft systems. *Atmos. Chem. Phys.*, **17**, 4817–4835, https://doi.org/10.5194/acp-17-4817-2017.

Swietlicki, E., and Coauthors, 2008: Hygroscopic properties of submicrometer atmospheric aerosol particles measured with H-TDMA instruments in various environments—A review. *Tellus*, **60B**, 432–469, https://doi.org/10.1111/j.1600-0889.2008.00350.x.

Tang, I. N., 1996: Chemical and size effects of hygroscopic aerosols on light scattering coefficients. *J. Geophys. Res.*, **101**, 19 245–19 250, https://doi.org/10.1029/96JD03003.

——, and H. R. Munkelwitz, 1994: Water activities, densities, and refractive indices of aqueous sulfates and sodium nitrate droplets of atmospheric importance. *J. Geophys. Res.*, **99**, 18 801–18 808, https://doi.org/10.1029/94JD01345.

Vogt, M., P. Schneider, N. Castell, and P. Hamer, 2021: Assessment of low-cost particulate matter sensor systems against optical and gravimetric methods in a field co-location in Norway. *Atmosphere*, **12**, 961, https://doi.org/10.3390/atmos12080961.

Weber, K., G. Heweling, C. Fischer, and M. Lange, 2017: The use of an octocopter UAV for the determination of air pollutants—A case study of the traffic induced pollution plume around a river bridge in Duesseldorf, Germany. *Int. J. Educ.*, **2**, 63–66.

Zhang, X., P. Massoli, P. K. Quinn, T. S. Bates, and C. D. Cappa, 2014: Hygroscopic growth of submicron and supermicron aerosols in the marine boundary layer. *J. Geophys. Res. Atmos.*, **119**, 8384–8399, https://doi.org/10.1002/2013JD021213.

## A.2 Publication II

Meteorol. Z. (Contrib. Atm. Sci.), Early Access DOI 10.1127/metz/2024/1198


Early Access Article

# Calculation of aerosol particle hygroscopic properties from OPC derived PM2.5 data

Vasileios Savvakis*, Martin Schön, Matteo Bramati, Jens Bange and Andreas Platis

Eberhard Karls Universität Tübingen, Germany

(Manuscript received March 20, 2023; in revised form December 26, 2023; accepted January 1, 2024)

**Abstract**

Hygroscopic growth of aerosol particles due to increasing relative humidity in the atmosphere is characterized by their hygroscopicity parameter $\kappa$ and their hygroscopic growth factor GF. A technique to calculate the two using $PM_{2.5}$ data from two optical counting sensors is examined. Only one of the two instruments is equipped with a drying channel, and therefore differences between ambient and dry air concentrations can be observed when both are working simultaneously. Based on the definition of the hygroscopic growth factor as the ratio between an aerosol particle's wet and dry diameter, a relationship including PM values is reached through the assumption of particle spherical shape and basic geometry. Aerosol particles from marine and urban sources were sampled during a week of measurements in two locations, in Norderney, Germany during April 2021 and in Rødby, Denmark, during September 2022. Calculated GF and $\kappa$ values were related to the origin of the air mass using back trajectory modeling (NOAA HYSPLIT) and by comparing the results to their expected values and fits on theoretical growth curves. It was found that $\kappa = 0.6 \pm 0.1$ when continental air was sampled (agreeing with ammonium sulphate's $\kappa = 0.61$) and $\kappa = 1.1 \pm 0.1$ when marine air was sampled (agreeing with sea salt's same value). The GF estimates also matched their respective expected values within a deviation of $1\sigma$. For the measurements in Rødby, particle number size distributions for the cases of marine sourced concentrations showed a peak at 1 to 2 µm, which is similar to previous studies of Baltic sea aerosol particle size distribution and structure.

**Keywords:** hygroscopic growth, hygroscopicity parameter, optical particle counter, marine aerosol, urban aerosol

## 1 Introduction

The vast majority of aerosol particles grow in apparent size due to water uptake from the environment in conditions of increasing moisture in the air (Svennings-son et al., 2006; Laskina et al., 2015; Davies et al., 2021). This phenomenon, often called hygroscopicity, is characteristic of aerosol particle chemical composition (Gysel et al., 2007; Tang et al., 2019). Among others, studies have been conducted related to the hygroscopic growth of diesel soot (Weingartner et al., 1997), mineral dust (Kaaden et al., 2009), ammonium sulphate (Hämeri et al., 2000), pollen (Griffiths et al., 2012), sea salt (Ming and Russell, 2001; Zieger et al., 2017) as well as pure sodium chloride (Hämeri et al., 2001; Biskos et al., 2006).

For aerosol particle concentrations monitoring, optical particle counters (OPCs) are widely used as they usually cover a sufficient size range for air quality assessment and can provide information on particulate matter (PM) types like $PM_1$, $PM_{2.5}$ and $PM_{10}$. While high end instrumentation of this type often features internal treatment of the hygroscopic growth effect by employment of drying methods, low-cost OPCs do not inherently deal with the issue. As a result, relative humidity (RH) related mathematical corrections have been developed for adjusting the data during post-processing (Di Antonio et al., 2018; Crilley et al., 2020; Malings et al., 2020). They rely on certain assumptions about the characteristics of the sampled air mass, which remains unknown. To give information on aerosol size, OPCs work on the principle of Mie scattering theory (Drake and Gordon, 1985; Bohren and Huffman, 2008), and aerosol identification is not directly possible. Deeper insight on aerosol particle type could be achieved, if instruments with and without a drying component operate at the same time and analysis is performed based on their output difference, which comes from evident hygroscopicity at humid conditions.

In the sub-micrometer range, aerosol particle humidification has been studied most commonly by using a Hygroscopic Tandem Differential Mobility Analyzer (H-TDMA) (Swietlicki et al., 2008; Kitamori et al., 2009), which was developed following the influential work of Liu et al. (1978), who first introduced the concept. For larger size ranges, other methods that have been attempted include directly collecting particles with a cascade impactor, e.g. Hitzenberger et al. (1997); Turšič et al. (2006), or combining in-situ RH and aerosol data from an aircraft, and a vertical scan-

*Corresponding author: Vasileios Savvakis, Eberhard Karls Universität Tübingen, Department of Geosciences, Schnarrenbergstraße 96, 72076 Tübingen, Germany, e-mail: vasileios.savvakis@uni-tuebingen.de

ning LIDAR for estimation of the scattering enhancement factor $f$ for up to sizes of 3 µm (Feingold and Morley, 2003). Hegg et al. (2006) first presented a hygroscopicity study using airborne OPC data, which extended up to 3.5 µm, by comparing particle size distributions from a highly humid air sample (around 90 % RH) and one at a drier state (around 50 %), both collected with the two OPCs on board an aircraft on the east coast of California, United States. In their work, both marine and polluted aerosol sources were examined and it was verified that marine aerosols are generally more hygroscopic than ones found in urban centers. A similar approach of aircraft based OPC measurements, one featuring a drying chamber and one operating without it, was conducted by Snider and Petters (2008), who investigated aerosol spectral densities and derived growth factor (GF) values from the dried / non-dried data, by addressing possible sources of uncertainty like particle shape, refractive index and aerosols being chemical solutions of different components. Additional studies using direct PM data for inspecting hygroscopicity have focused on the changes in scattering enhancement due to increased moisture and have been related to visibility (Zhao et al., 2019; Molnár et al., 2020; Won et al., 2021).

The objective of this work is to investigate how accurately the hygroscopic GF can be calculated from direct PM readings, for example $PM_{2.5}$, based on a set of calculations starting from the formula definition of GF. Previous studies have followed different approaches after conceiving the concept, and used measurements from manned airborne platforms or direct aerosol particle collection. This method is still based on solely two sensors with the same measurement principle, and the use of their direct PM output. One of the two should feature a drying chamber, either self-constructed as a modification to a sensor that doesn't have one (Savvakis et al., 2024), or internally adjusted by the manufacturer as an extra component. Measurements of $PM_{2.5}$ can be collected from one sensor with a drying chamber at the same time with another sensor without a drying chamber, and based on the observed differences, a GF value can be calculated. Previous related studies have approached this problem by analysing aerosol particle size distributions and the differences between wet / dry case, however a PM value is generally more accessible and more foundational regarding particulate matter. As many low-cost sensors do not have a high number of size bins that is required for an accurate size distribution, such an analysis is often not possible. In this paper, we examine whether calculating hygroscopic properties of aerosol particles and unveiling details on the origin of the sampled air mass, is possible solely from PM data, a universally shared sensor output. The description of the parameters and derived formulas is described in Section 2.1, and then results from the measurements in two locations, in the North Sea (Norderney island), and the Baltic Sea (Rødby port), where the method and analysis was applied, are presented in Section 3.

# 2 Materials and methods

## 2.1 Theory

### 2.1.1 Hygroscopic growth

For an aerosol particle, GF is defined via the ratio between its wet diameter in ambient conditions and its dry diameter under conditions of low RH, below its efflorescence point:

$$\mathrm{GF} = \frac{d_w(\mathrm{RH})}{d_d} \tag{2.1}$$

According to Eq. (2.1), this ratio will be above unity when $d_w > d_d$, essentially when conditions are humid enough for the aerosol particle to adsorb water vapor from its surroundings. At dry conditions, $d_w = d_d$ and therefore, GF = 1. A formula has been developed for calculating GF only as a function of RH and by introducing a hygroscopicity parameter $\kappa$, first introduced and analysed by Petters and Kreidenweis (2007):

$$\mathrm{GF} = \left(1 + \kappa \cdot \frac{a_w}{1 - a_w}\right)^{\frac{1}{3}} \tag{2.2}$$

In Eq. (2.2), $a_w$ is the so-called water activity, which is defined as the dimensionless ratio between the water vapor pressure of water in the solution and the vapor pressure of pure water, i.e. RH over the Kelvin effect. For deriving Eq. (2.2), the Kelvin effect has been omitted, as it is only important for aerosol particles of sizes in the nanometer range (Fitzgerald, 1975; Snider and Petters, 2008). Therefore, in this case $a_w$ is reduced to:

$$a_w = \frac{\mathrm{RH}}{100} \tag{2.3}$$

In the past, potential values for the hygroscopicity parameter $\kappa$, at urban and marine environments, have been thoroughly examined. Marine air predominantly consists of sea salt with $\kappa = 1.1$ (Zieger et al., 2017; Hagan and Kroll, 2020). Urban air masses can be more mixed, and following the conceptual approach of Di Antonio et al. (2018), $\kappa = 0.61$ can be considered as a reasonable value for a typical polluted environment with the assumption that it consists mainly of ammonium sulphate. By considering an efflorescence point of RH = 35 % (or $a_w = 0.35$) for ammonium sulphate (Di Antonio et al., 2018) and RH = 45.6 % (or $a_w = 0.456$) for sea salt (Gupta et al., 2015), the GF relationship to increased RH for all possible cases can be calculated by using Eq. (2.2)–(2.3) and the aforementioned $\kappa$ values. Figure 1 shows the result for the two different compounds. Since $\kappa$ is higher for sea salt than for ammonium sulphate, its GF curve is also higher in Figure 1, i.e. a sea salt particle attracts more water vapor than an ammonium sulphate particle at the same RH conditions. Sea salt can have multiple salts and a consequently more complex hygroscopic nature that would

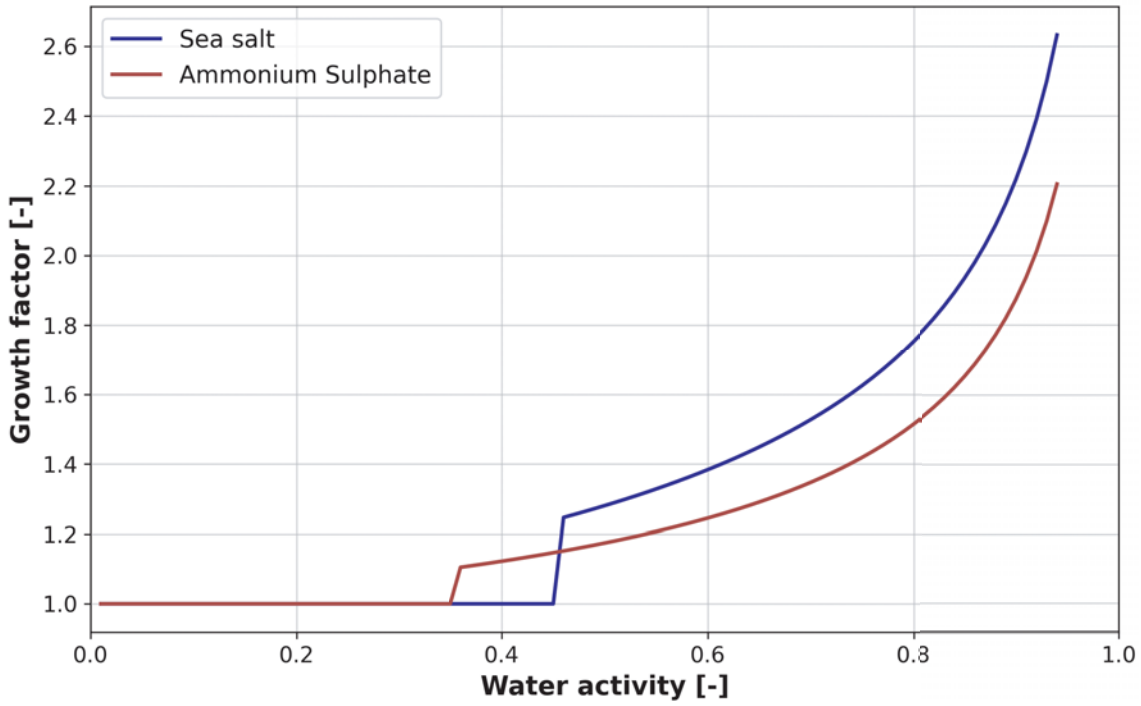


**Figure 1:** Growth factors for values of $a_w$ between 0.2 and 0.95, produced by using Eq. (2.2) and by taking into account the two efflorescence points for ammonium sulphate (35 %) and sea salt (45.6 %). Below these boundaries, the RH conditions are low enough for the aerosol particle to not attract any water vapor, hence its growth factor is equal to unity.

not be described by a singular efflorescence point. This means that measured sea salt may still contain water content below the 45.6 % point depicted in Figure 1. Nevertheless, for the purposes of this study, the efflorescence point of sodium chloride was considered for the case of sea salt, as its preeminent component, and with similar hygroscopic behavior (Tang et al., 1997).

### 2.1.2 Calculation of GF from PM measurements

Based on Eq. (2.1), the following steps can be made to attain an expression with PM types starting from $d_w$ and $d_d$, by assuming that the aerosol particles are spherical, and therefore of a known volume formula:

$$\begin{aligned} \mathrm{GF} = \frac{d_w}{d_d} &= \left(\frac{V_w}{V_d}\right)^{\frac{1}{3}} = \left(\frac{V_d + V_{\mathrm{water}}}{V_d}\right)^{\frac{1}{3}} \\ &= \left(1 + \frac{V_{\mathrm{water}}}{V_d}\right)^{\frac{1}{3}} = \left(1 + \frac{\frac{\mathrm{PM}_{\mathrm{water}}}{\rho_{\mathrm{water}}}}{\frac{\mathrm{PM}_d}{\rho_d}}\right)^{\frac{1}{3}} \\ \Rightarrow \mathrm{GF} &= \left(1 + \frac{\rho_d \cdot \mathrm{PM}_{\mathrm{water}}}{\rho_{\mathrm{water}} \cdot \mathrm{PM}_d}\right)^{\frac{1}{3}} \end{aligned} \tag{2.4}$$

In the final expression (Eq. (2.4)), $\rho_{\mathrm{water}}$ is the density of water, $\mathrm{PM}_{\mathrm{water}}$ is the mass of the water layer around the aerosol particle, $\mathrm{PM}_d$ its solid (i.e. real) size and $\rho_d$ is the density of the dry particle. The calculation above assesses that the total PM value of a wet aerosol particle exists as a meta-stable solution between dry core and water uptake, meaning that the two layers neighbor but do not mix, hence the concept of adsorption (Sorjamaa and Laaksonen, 2007). As principles of physical chemistry can make clear statements about aerosol state and composition (that for example, sea salt is an aqueous well-mixed solution), this procedure represents an approximation. Based on that, $\mathrm{PM}_{\mathrm{water}}$ is estimated as:

$$\mathrm{PM}_{\mathrm{water}} = \mathrm{PM}_w - \mathrm{PM}_d \tag{2.5}$$

where $\mathrm{PM}_w$ is the ambient PM measurement and $\mathrm{PM}_d$ is the dry PM measurement. These two quantities, and in return $\mathrm{PM}_{\mathrm{water}}$ from Eq. (2.5), correspond to an OPC measurement without and with a drying chamber, respectively.

When calculating GF in this way, the dry particle density $\rho_d$ is still required, which demands knowledge on the type of particles measured. However, theoretical densities of different elements are known in literature and can be tested through Eq. (2.4). Since the difference between $\mathrm{PM}_w$ and $\mathrm{PM}_d$ in a specific measurement time is dependent on the type of air being sampled, only the appropriate particle density value will match its corresponding GF curve from Figure 1. A verdict of the air mass type during the measurements can then be drawn by using only PM data from the two OPCs and the theoretical GF curve shown in Figure 1, which here displays two components representative of urban polluted (ammonium sulphate) and marine (sea salt) air content.

**Table 1:** Date, location, starting and ending time of data collection for all measurements. For each case, the air mass gets a classification as either "Marine" which corresponds to an origin from the sea, or "Urban" for an origin from land, according to the 24-hour back trajectories done with HYSPLIT and shown in Figure 2–3. "Dry" refers to PM data from an OPC with a drying chamber, i.e. $PM_d$, and "Ambient" to PM data from an OPC without a drying chamber, i.e. $PM_w$.

| Date | Location | Ambient | Dry | Start UTC | End UTC | Air mass [HYSPLIT] |
|---|---|---|---|---|---|---|
| 17 Apr 21 | Norderney | OPC-N2 | OPC-N2+dryer | 07:09 | 08:12 | Marine |
| 16 Sep 22 | Rødby-Land | OPC-N3 | Fidas Fly 100 | 16:40 | 19:14 | Marine |
| 17 Sep 22 | Rødby-Land | OPC-N3 | Fidas Fly 100 | 07:17 | 09:16 | Marine |
| 21 Sep 22 | Rødby-Vessel | OPC-N3 | OPC-N3+dryer | 11:38 | 12:34 | Marine |
| 19 Apr 21 | Norderney | OPC-N2 | OPC-N2+dryer | 09:42 | 10:44 | Urban |
| 19 Sep 22 | Rødby-Land | OPC-N3 | Fidas Fly 100 | 17:15 | 19:12 | Urban |
| 22 Sep 22 | Rødby-Vessel | OPC-N3 | OPC-N3+dryer | 12:27 | 13:15 | Urban |
| 23 Sep 22 | Rødby-Land | OPC-N3 | OPC-N3+dryer | 10:30 | 11:15 | Urban |

## 2.2 Instrumentation

Two low-cost OPCs were employed, the OPC of type N2 (Alphasense, 2015) and N3 (Alphasense, 2019), which are both very similar in terms of dimensions and operation. The sensors feature their own micro-fan for active aspiration and cover a range of 0.38–17 µm with 16 size channels (OPC-N2) and 0.35–40 µm with 24 size channels (OPC-N3), and provide output of PM data based on raw size channel bins and their own internal algorithms. Both the OPC-N2 and OPC-N3 have an operational range of 0–95 % RH, according to the manufacturer. Furthermore, the optical aerosol spectrometer (OAS) Fidas Fly 100 (Palas, Karlsruhe, Germany) was also used, a high-end instrument with similar operational philosophy that covers a size range of 0.18 to 18 µm through 264 channels. Since the OPC-N2/N3 do not include a technique for drying the sampled air, they were used for measurements of ambient air, i.e. including moisture, while the Fidas Fly 100 was used for capturing dry PM concentrations, as it features its own internal dilution dryer, the Intelligent Aerosol Drying System (IADS).

Humidity was measured with the miniaturised T/RH sensor named SHT31 (Sensirion, Switzerland), which operated simultaneously along the OPCs. The SHT31 comes pre-calibrated and operates at the whole RH range, with a response time of 8 s and typical error of 2 % for humidity (Sensirion, 2016). Its measurement principle is based on capacitive humidity sensing, i.e. RH is determined from the capacitance change of a dielectric material between two electrodes, as a response to moisture absorption. At times, only the two low-cost OPCs operated for intercomparison, and in this case self-constructed diffusion drying channels were installed on one of the sensors only. Details on the setup of each measurement time period can be found in Table 1. Both instruments' function, along with the RH sensor, was supported by the use of a companion computer (Raspberry Pi 3b*), which handled the data acquisition and saving of the output files at a frequency of 1 Hz. The OPC-N2/N3 and the Fidas Fly include embedded algorithms for the calculation of PM types from raw bin counts, and only direct $PM_{2.5}$ readings were taken for the calculations of this study.

## 2.3 Measurement locations

The first measurement location was at the north side of Norderney island, Germany (coordinates: 53.7229, 7.2116) for two days in April (17th and 19th), 2021 and the second location was outside of the town of Rødby, Denmark and near Hyldtofte Østersøbad beach (coordinates: 54.6385, 11.4158), lasting one week in September, 2022. Both locations are in maritime environment (North and Baltic Sea), granting the chance of sampling marine based air, and the experimental periods were chosen to cover spring and autumn. During days of southerly winds, air masses from the land (e.g. Germany or Poland respectively) can arrive in both these spots, carrying continental sourced aerosol particles. The difference between maritime / urban air can be seen in their hygroscopic behavior. Similar but not identical rates of hygroscopic growth should become visible under humid conditions between these two cases, as the included elements have different values for $\kappa$, as seen in the two characteristic lines of Figure 1. Measurements were taken for time periods of 30 minutes to 2 hours throughout the span of the week in the morning or late evening of the day, for capturing the higher humidity conditions at night. Alongside the two main sensors, RH data was collected through an SHT31 (Sensirion, Switzerland) miniaturised meteorological sensor working in parallel, which operated at a sampling rate of 2 s, the same as the OPC-N2/N3 and Fidas Fly 100. The total of all measurement periods are summarised in Table 1. 24-hour back trajectories of the air mass at the time of measurements were acquired through the NOAA Hybrid Single-Particle Lagrangian Integrated Trajectory (HYSPLIT) model (Stein et al., 2015) at three different altitudes above sea level: 10, 200 and 500 m, to track the source of the measured aerosol particles, be it of marine or urban origin. The back trajectories can be seen in Figure 2a–3.

For each measurement day, $PM_{2.5}$ data were collected from the ambient air using an instrument without a drying chamber (third column in Table 1) and the

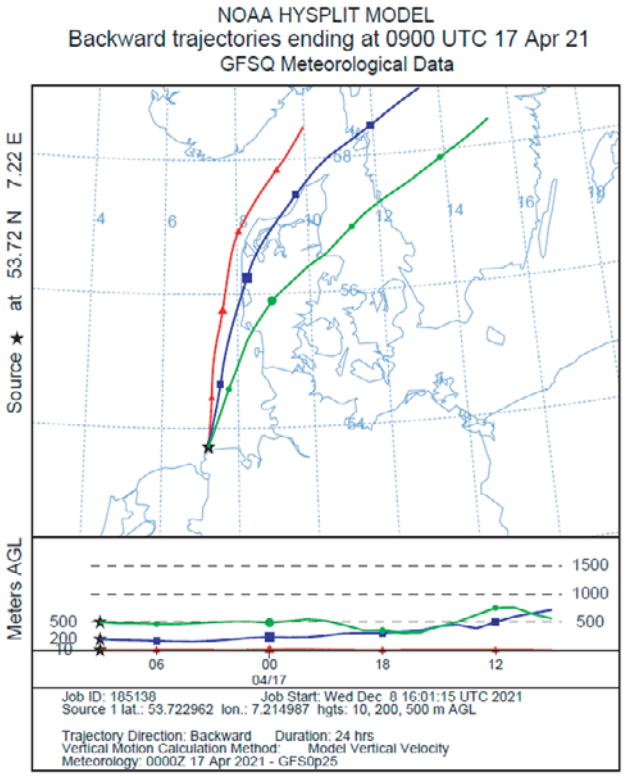


(a) 17th of April, 2021 (Norderney).

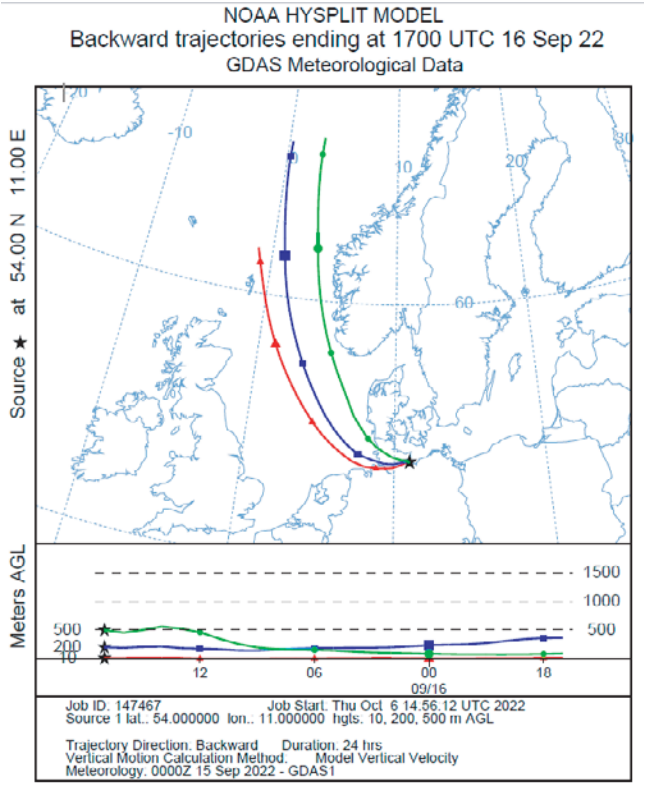


(b) 16th of September, 2022 (Rødby).

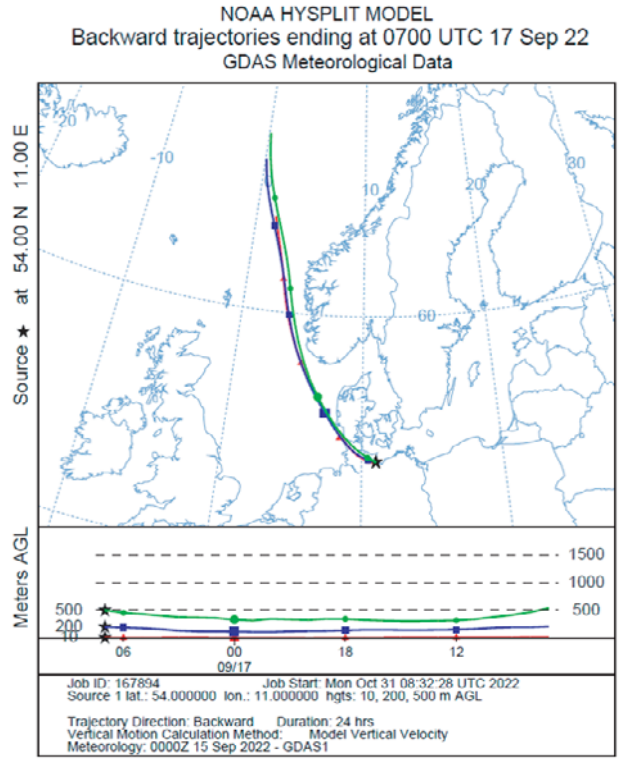


(c) 17th of September, 2022 (Rødby).

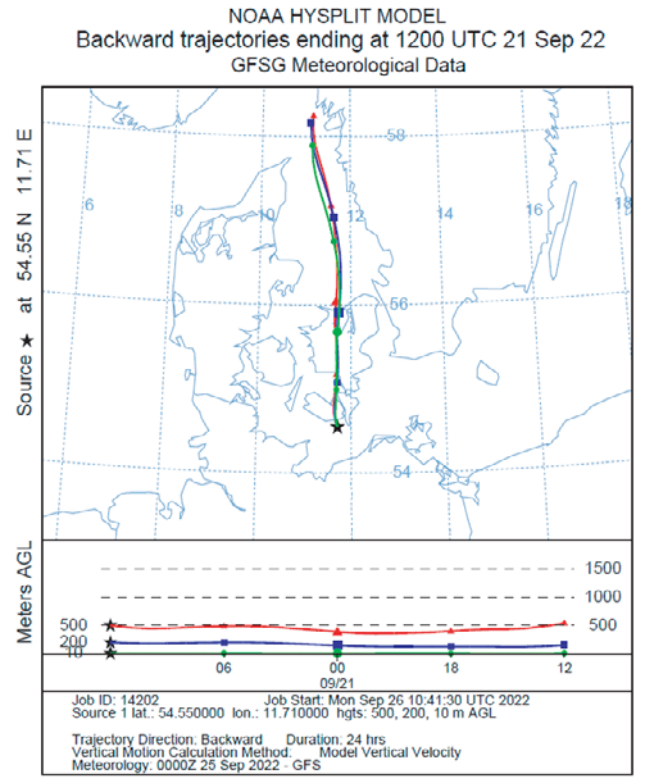


(d) 21st of September, 2022 (Rødby).

**Figure 2:** Air mass 24-hour back trajectories for the cases of a marine aerosol source. The black star denotes the measurement location, which is also captioned below each figure, and the three lines indicate the origin of the air mass at three different altitudes, 10 m (light green), 200 m (dark blue) and 500 m (red).

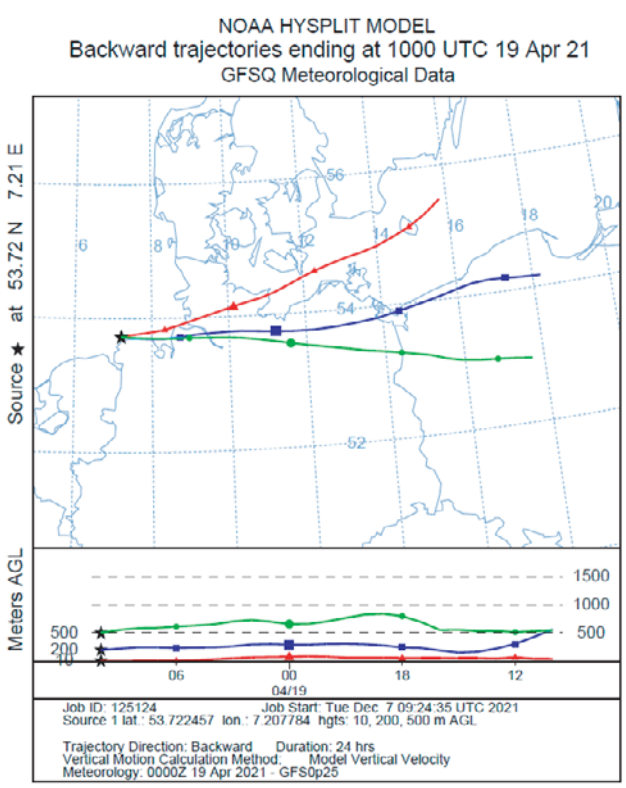


(a) 19th of April, 2021 (Norderney).

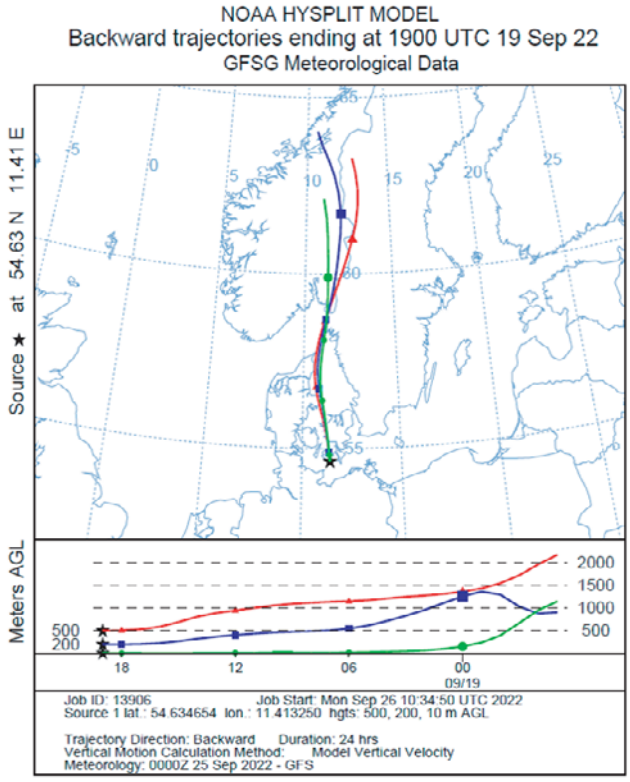


(b) 19th of September, 2022 (Rødby).

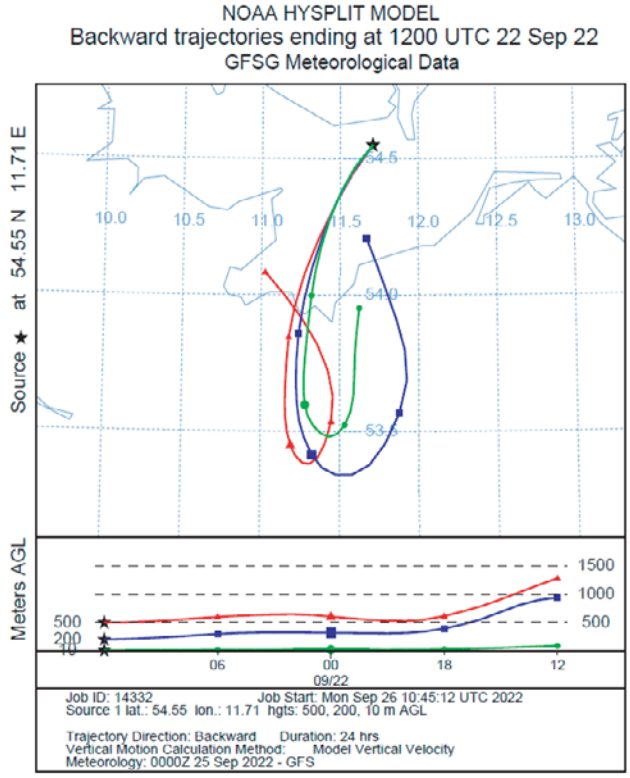


(c) 22nd of September, 2022 (Rødby).

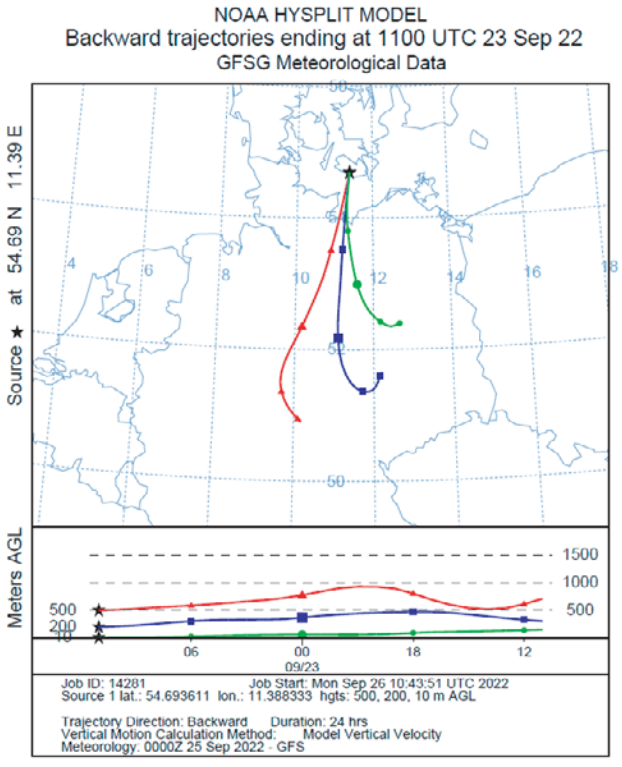


(d) 23rd of September, 2022 (Rødby).

**Figure 3:** Air mass 24-hour back trajectories for the cases of an urban aerosol source. The black star denotes the measurement location, which is also captioned below each figure, and the three lines indicate the origin of the air mass at three different altitudes, 10 m (light green), 200 m (dark blue) and 500 m (red).

dried air (fourth column in Table 1). The hygroscopicity parameter $\kappa$ and growth factor GF were calculated according to the procedure described in Section 2.1, using RH measurements from the SHT31. $PM_{water}$ is calculated with Eq. (2.5), and using $PM_w$ and $PM_d$ according to Table 1. Then, GF is calculated from Eq. (2.4) by using two values for particle density, $\rho_{as} = 1.77\,g \cdot cm^{-3}$ for ammonium sulphate and $\rho_{ss} = 2.1\,g \cdot cm^{-3}$ for sea salt. Afterwards, Eq. (2.2) is solved for $\kappa$ by using the newly calculated growth factors. For each measurement period, 1-min mean values of all the related parameters were computed from the raw sensor outputs. A mean value of GF and $\kappa$ was then calculated across the whole measurement period, and the uncertainty of the measurement was determined by calculating the corresponding standard deviation. Results were then compared to the growth factor curve in Figure 1 and the established $\kappa$ values of each element. The governing difference between $PM_d$ and $PM_w$ dictates the outcome, because it reflects the hygroscopic behavior of the aerosol particle that is actually measured. Since the air mass type is known from HYSPLIT and shown in Figure 2–3, the method to identify it from PM data, as described in Section 2.1, is possible to be tested. To test the efficiency of the drying system when inter-comparing OPC-N3 and Fidas Fly 100, three OPCs were in operation for one of the measurement days, including the reference instrument and one OPC-N3 with a drying chamber, and one without. In this way, it could be investigated whether differences between ambient and dry measurements were solely because of the hygroscopic growth effect.

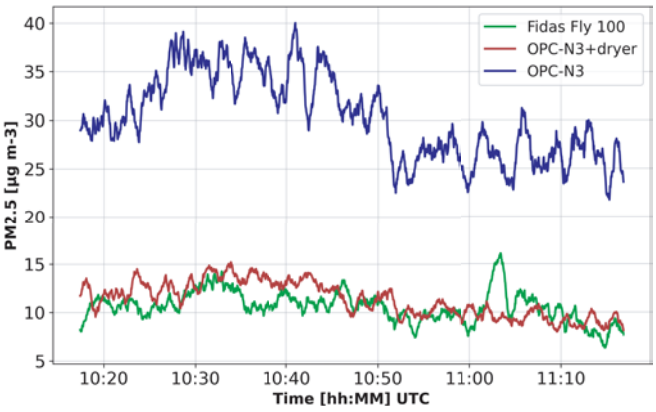


**Figure 4:** $PM_{2.5}$ time series for September 17th. The three OPCs included a reference instrument with a drying method (Fidas Fly 100 – green line), the OPC-N3 with a self-constructed diffusion drying chamber (dark red line) and an unmodified OPC-N3 that featured no drying (blue line).

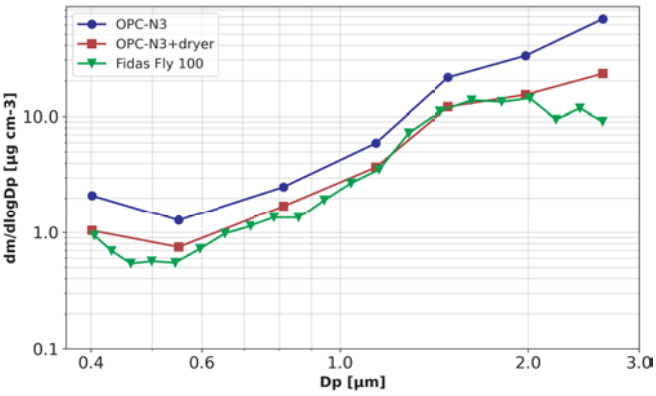


**Figure 5:** Particle mass size distributions for September 17th. The three OPCs included a reference instrument with a drying method (Fidas Fly 100 – green line), the OPC-N3 with a self-constructed diffusion drying chamber (dark red line) and an unmodified OPC-N3 that featured no drying (blue line).

## 3 Results

For the 17th of September 2022, the results of the $PM_{2.5}$ time series and mass distributions can be seen in Figure 4–5. A clear overestimation is evident for the case of the unmodified OPC-N3, which recorded almost three times higher $PM_{2.5}$ than the reference instrument (Figure 4). Similar is the case for the overestimation of the particle mass size distribution shown in Figure 5, demonstrating the effect of hygroscopic growth at humid conditions. For the case of the modified OPC-N3 with an added diffusion dryer, $PM_{2.5}$ is in better agreement with the reference instrument, with an overestimation of 21 % between 10:25–10:45 UTC. As observed at the mass distributions (Figure 5), there is a general consistency between OPC-N3 with a dryer and Fidas Fly 100, with an 16 % overestimation of the former up to sizes of 0.8 µm. Between the smaller sizes of 0.4–0.55 µm, the two instruments are in agreement at the points where they have exactly the same size boundary. The two instruments match well from 1 to 2 µm, and an overestimation of the OPC-N3 can be seen above 2 µm, with a maximum difference at the last size bin, which is however above 2.5 µm and therefore not accounted for when calculating $PM_{2.5}$. There is a distinct peak for a period of two minutes from the Fidas Fly 100 at 11:03 UTC, most likely from measuring particles smaller than what the OPC-N3 can detect. Figures 4–5 show comparable results between the Fidas Fly 100 and the OPC-N3 with its own drying method, and both were used for capturing $PM_d$ at different measurement periods, as described in Table 1.

Calculated GF, $\kappa$ and the expected $\kappa$ values, according to Sections 2.1 & 2.3, are shown in Table 2. The computations for each day were based on time series equivalent to Figure 4, with $PM_d$ being the measurements from the OPC-N2/N3+dryer or Fidas Fly 100, and $PM_w$ were the measurements from the unmodified OPC-N2/N3. Columns 2–4 of Table 2 show the calculations for GF and $\kappa$. They are based on two different particle densities, sea salt ($\rho_{ss}$) and for ammonium sulphate ($\rho_{as}$), that reflect marine and urban background air respectively. A known $\kappa$ for these two elements, from

**Table 2:** Calculated GF, $\kappa$ using two particle densities ($\rho_{ss}$: density of sea salt, $\rho_{as}$: density of ammonium sulphate), and the average RH levels during the times of each measurement, for each data time period.

| **Date** | **GF ($\rho_{ss}$)** | **GF ($\rho_{as}$)** | **$\kappa(\rho_{ss})$** | **$\kappa(\rho_{as})$** | $\overline{RH}$ [%] | $\kappa_{ss}$ (Zieger et al., 2017) |
|---|---|---|---|---|---|---|
| 17 Apr 21 | $1.83 \pm 0.08$ | $1.74 \pm 0.08$ | $1.0 \pm 0.1$ | $0.9 \pm 0.2$ | 83 | 1.1 |
| 16 Sep 22 | $1.61 \pm 0.07$ | $1.55 \pm 0.06$ | $1.1 \pm 0.2$ | $1.0 \pm 0.2$ | 74 | 1.1 |
| 17 Sep 22 | $1.74 \pm 0.06$ | $1.65 \pm 0.05$ | $1.1 \pm 0.1$ | $0.9 \pm 0.1$ | 80 | 1.1 |
| 21 Sep 22 | $1.4 \pm 0.1$ | $1.3 \pm 0.1$ | $1.1 \pm 0.1$ | $0.9 \pm 0.1$ | 63 | 1.1 |
| | | | | | | $\kappa_{as}$ (Di Antonio et al., 2018) |
| 19 Apr 21 | $1.38 \pm 0.09$ | $1.33 \pm 0.08$ | $0.8 \pm 0.1$ | $0.6 \pm 0.1$ | 68 | 0.61 |
| 19 Sep 22 | $1.5 \pm 0.1$ | $1.4 \pm 0.1$ | $0.8 \pm 0.2$ | $0.6 \pm 0.2$ | 76 | 0.61 |
| 22 Sep 22 | $1.17 \pm 0.05$ | $1.15 \pm 0.06$ | $0.7 \pm 0.1$ | $0.6 \pm 0.1$ | 47 | 0.61 |
| 23 Sep 22 | $1.31 \pm 0.05$ | $1.27 \pm 0.05$ | $0.8 \pm 0.1$ | $0.7 \pm 0.1$ | 61 | 0.61 |

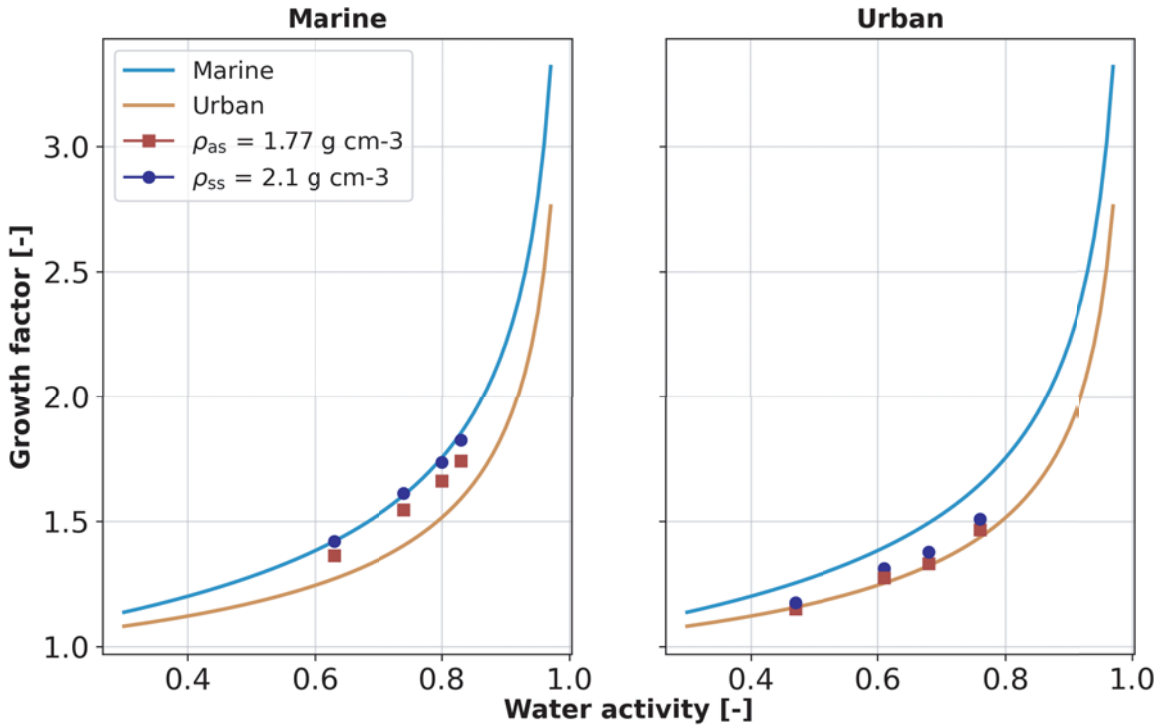


**Figure 6:** Growth factor curves as in Figure 1, but now limited to a range between $a_w$ of 0.3 and 1. Each data point in the plot represents a different measurement day, and results are split in two categories, the cases when marine or urban air was present, according to Table 1. The average RH level is taken from the SHT31 measurements and shown in Column 6 of Table 2, as it is converted to water activity with Eq. (2.3). Two points per RH are shown, which are related to two growth factors, one using $\rho_{as}$ and one from $\rho_{ss}$.

previous studies on the subject, is also shown and the two air mass origins are separated as in Table 1. It can be noted that when HYSPLIT displays air from the sea (Figure 2), calculated $\kappa$ matches the expected value for sea salt perfectly, only when using with the appropriate particle density. The same holds for the case of air from land, as it can be seen in Figure 3. When unsuitable particle densities are inserted, the resulting $\kappa$ is not close to either expected value.

This is a first hint of understanding the type of air mass that is sampled, starting only from PM data, and the point is further illustrated by applying the calculated GF values (columns 2 and 3 in Table 2) on the growth rate plots of Figure 1, which can be seen in Figure 6.

The same phenomenon is apparent from the data points in Figure 6, where each one is the outcome of each measurement time period from Tables 1 and 2. GF values fall on a different growth curve depending of the sampled background air, regardless of the choice of particle density.

A closer look for the study case in Rødby, where aerosol particle number size distributions are calculated from the raw data for both ambient and dry air samples during these days, is shown in Figure 7. The distributions vary slightly between the first and second part of the experiments, as different air masses were measured in each time. Distributions from the 16th and 17th show a bump between 1 and 2 µm, which is smoothed out dur-

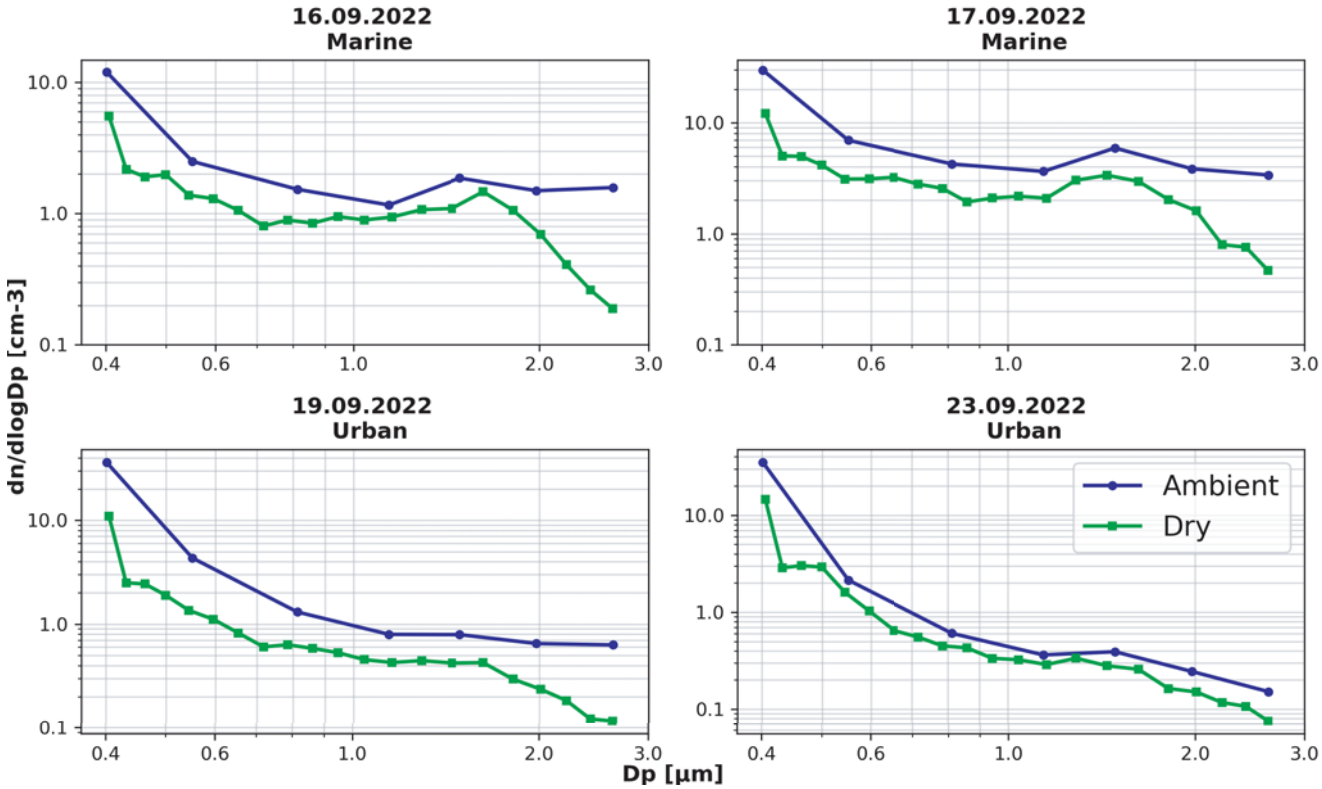


**Figure 7:** Particle number distributions for 4 measurement days, from the OPC-N3 (measuring ambient air) and the Fidas Fly 100 (measuring dry air). The distributions range from 0.4 to 3 µm particle geometric mean diameter size.

ing the cases with air from land, on the 19th and 23rd of September in Figure 7. The hygroscopic growth effect is evident everywhere, as number concentrations from the Fidas Fly 100 are lower across all bins in this size range.

Figure 2 shows simulations of the air mass back trajectories 24 hours prior to the measurements at the area of Rødby. It can be seen that for the 16th and 17th of September, the origins of the air mass are from the Northwest in the North Sea at all three presented altitudes, hardly passing any land until their arrival at Rødby. At the same time, for the 19th of September, the air mass came from a clearer northerly direction passing inland Norway and Sweden, and on the 23rd of September the source of the air mass can be tracked to the South, inside Germany. These two different air mass origins suggest a similar conclusion like Table 2 and Figure 6, which show an analogous resulting hygroscopicity parameter and growth factor that can be distinguished in each situation.

## 4 Discussion

The method proposed in this paper aims for estimating hygroscopic properties of aerosol particles, specifically the growth factor GF and hygroscopicity parameter $\kappa$, from $PM_{2.5}$ data and by taking advantage of the fundamental definition of GF, as it is stated with Eq. (2.1). As it can be identified in Table 2, the calculated $\kappa$ for sea salt through Eq. (2.2) & (2.4) resulted in $\kappa_{ss} = 1.1$ when using the appropriate particle density, which is in agreement with a recent study that suggested the same value for numerical models (Zieger et al., 2017). For ammonium sulphate, $\kappa_{as} = 0.6$ is also aligned with previous studies on the element or a mixed urban aerosol with it as a dominant component (Svenningsson et al., 2006; Di Antonio et al., 2018), where values ranged between 0.61 and 0.62. It is important to remark that the hygroscopic growth curves for Figure 1 were produced by using the literature numbers for $\kappa$, yet the procedure to estimate them with our data begins from the difference of dry and wet PM measurements. This works as an affirmation to the already established values.

Prior to the calculation of $\kappa$, GF was found from Eq. (2.4) through $PM_{2.5}$ readings from the two sensors. A range of different RH levels was ongoing during the measurements, from 47 to 83 %, which allowed for a GF computation for different points on the curves of Figure 1. With the use of the applicable particle density, points for each measurement day agree with the expected growth factor of the given particle, basically showing that these kind of aerosol particles were being sampled that day. If the inappropriate particle density is used, the result is still closer to the correct growth curve related to the sampled air mass. As different densities are being tested, the results in GF and $\kappa$ from Table 2

indicate that when using the expected particle density, both $\kappa$ and GF match their anticipated values but if a non-appropriate particle density is used, neither $\kappa$ or GF have any relevance with any of the two components. For example, for the case of the 19th of September, GF ($\rho_{as}$) = 1.4 matches the brown curve in Figure 6 at the average RH amount of the time of measurements, but the value GF ($\rho_{ss}$) = 1.5 doesn't match the blue curve, and the same can be seen for $\kappa$: 0.6 is close to the expected value if ammonium sulphate is the measured aerosol particle (when using $\rho_{as}$), while 0.8 is neither correct for sea salt or ammonium sulphate. This demonstrates that GF will be calculated correctly, when the appropriate density is inserted in Eq. (2.4), but if a different value (i.e. considering the growth of a certain particle type, but using a density of another), the resulting GF will still be in the vicinity of the correct curve and $\kappa$ will match neither. Outcomes when using an appropriate value for density match their GF curves, and the following calculation of $\kappa$ agrees with previously known values.

The results of this study are supported by the 24-hour back trajectories for each day, which show the same situation when it comes to the origin of the air mass. When an air mass from the sea is sampled (Figure 2a–2d), the proper $\kappa$ and GF values are in turn calculated and agree with theory, but when the air mass originates from land (Figure 3a–3d), the hygroscopic properties are closer to what one would expect from an air sample that contains ammonium sulphate and not sea salt. A difference between these two is also clear from the particle number size distributions in Figure 7, which shows a slightly different structure between the first and last two days of the measurement period. The small "hill" identified in the first two days at sizes between 1 and 2 µm, represents a size distribution from water in the North and Baltic Sea, and it is reminiscent to other studies that have computed such size distributions in the area, predominantly occupied by sea salt from breaking waves, e.g. in Clarke et al. (2003). Specifically for the case in Figure 2a, while air masses higher above do pass from land, at 10 m altitude (red colored line) the trajectory shows a path only above water, which justifies how the ground measurements captured hygroscopic properties that are more similar to a marine based aerosol source. For that case, since higher altitude layers contain continental air mass which is less hygroscopic, the resulting $\kappa = 1 \pm 0.1$ is lower but still within the margin of the expected value of pure sea salt, which gives the verdict of an air sample mainly comprised of sea salt, yet mixed with non-marine air as well. On the last two days of the experiments in Rødby, the air mass originates from Scandinavia and Germany, more related to a mixed / polluted environment with its applicable size distribution. An extensive study on the chemical composition of $PM_{2.5}$ in north Taiwan for a year in 2016–2017 by Cheung et al. (2020), found $\kappa$ values up to 0.56 related to an urban polluted environment with various pollutants. This work's result of $\kappa = 0.6$ matches better the hygroscopicity parameter of ammonium sulphate only ($\kappa = 0.61$), and it can be concluded that the air masses originating from land contained such aerosol particles for sizes up to 2.5 µm.

The method proposed aims for a direct way to estimate hygroscopic properties of aerosol particles, specifically the growth factor GF and hygroscopicity parameter $\kappa$, from direct sensor $PM_{2.5}$ data and by taking advantage of the fundamental definition of GF, as it is stated with Eq. (2.1). The assumption of particle spherical shape is maintained in this process, but it is a generally accepted notion that is taken into account when it comes to most aerosol particle analysis or PM calculation by instruments such as an OPC. A discrepancy in the measurements could lie in the fact that each sensor usually assumes its own complex refractive index for particle characterization, for this the OPC-N3 considers a value of $n = 1.5 + 0i$ (Alphasense, 2019) and for the Fidas Fly 100 in its standard mode it is $n = 1.59 + 0i$. For the specific experiments, $PM_1$ was avoided because of the difference in the sensors' lower bin size: 0.18 µm for the Fidas Fly 100 and 0.35 µm for the OPC-N3. This remains as a potential indirect comparison error. Hegg et al. (2006) noted a slight difference in GF values between aerosol particles in the sub-micrometer and micrometer range at certain RH conditions, while $PM_{2.5}$ of course considers all aerosol particles up to an aerodynamic diameter of 2.5 µm. Nevertheless, results from the current study showed that the calculation steps described in Section 2.1 can provide an accurate estimation for $\kappa$ and GF, as it can be concluded when looking at the air mass back trajectories in Figure 2, and combining them with the points in Figure 6 and contents of Table 2. When comparing an OPC-N3 with a drying channel and the Fidas Fly 100, results were in agreement with each other as seen in Figure 4–5. This demonstrates how the overestimation of the unmodified OPC-N3 compared to either the OPC-N3 + dryer or reference instrument, is widely due to the effect of RH on the apparent size of the sampled aerosol particles.

## 5 Conclusions

A concise method is presented for the calculation of GF and $\kappa$ using $PM_{2.5}$ from two aerosol particle optical sensors. One of them features a drying system and one does not, and the difference between ambient and dried PM concentrations are used through Eq. (2.1) to calculate GF and $\kappa$. Eq. (2.2), which relates GF and different RH levels through $\kappa$ only (Petters and Kreidenweis, 2007; Di Antonio et al., 2018), is used for connecting all parameters together and plotting theoretical growth curves for specific elements (Figure 1). Using measurements on an island in the North Sea (Norderney, Germany) and at the coast of South Denmark and near the Baltic Sea, these aerosol particle hygroscopic properties were calculated by using an OPC-N2/N3 (with and without a drying chamber) and a Fidas Fly 100 (with a drying chamber). Results showed that $\kappa = 0.6 \pm 0.1$ when

the measured air mass had an urban origin, indicating aerosol particles predominantly with ammonium sulphate, a typical component of polluted air. When measuring air from the sea, the hygroscopicity parameter was found to be $\kappa = 1.1 \pm 0.1$, which agrees with the value expected for abundant sea salt in the sample.

Accordingly, growth factors matched their appropriate curves with a distinction between the two cases (marine and urban aerosol) for various RH levels, which were all above the efflorescence points of both sea salt and ammonium sulphate, hence the presence of hygroscopic growth. The origin of the air masses was tracked by simulating back trajectories from the NOAA HYSPLIT model 24 hours before the measurements, which show the times when the air mass was of urban or marine source and agree with the hygroscopic growth differences expected for sea salt and ammonium sulphate. Particle number size distributions also show a notable difference, with the case of marine aerosol from the Baltic and North Sea, a small peak in number concentrations is seen at sizes of 1–2 µm.

As strictly defining the chemical composition of aerosol particles would require a cascade impactor, this method provides insight on aerosols through their hygroscopic properties at least to the level of air mass origin. This also extends the size range where such properties are studied, as mostly the hygroscopic growth effect is present in ranges often much lower that what typical OPCs cover, aerosol particle sizes with an aerodynamic diameter at the order of magnitude from few to few hundreds of nanometers. By combining ambient and dry PM data collection, a sensor otherwise blind to particle composition and air mass origin, can be used to provide such information by taking advantage of the hygroscopic growth effect. As low-cost OPCs without the inclusion of a drying chamber have been under development during the last few years for air quality research, our method could prove useful when expensive instrumentation, specifically for hygroscopic growth analysis, is unavailable.

## Acknowledgements

The authors would like to thank the off-shore Wind Park company RWE for their hospitality on the maintenance vessels of the off-shore wind park Rodsand II during September 2022, where parts of the acquired measurements were obtained. We would also like to thank the Train2Wind Innovation Network for the collaboration and partial financial support of this project.

## Declaration of competing interest

The authors declare that they have no conflict of interest.

## Data availability statement

Data, post-processing scripts, and data acquisition scripts can be provided from the corresponding author upon reasonable request.

## Funding

This work is partly funded by the European Union Horizon 2020 research and innovation program under grant agreement no. 861291 as part of the Train2Wind Marie Sklodowska-Curie Innovation Training Network (https://www.train2wind.eu/)

## Appendix

### A Diffusion dryer

The diffusion dryer attached on the low-cost OPCs of this study was a self-constructed dryer, and subject of another publication (Savvakis et al., 2024). A short description and details of dimensions are given here.

#### A.1 Specifications

The drying channel is based on the concept of diffusion drying, and consists of two co-axial tubes. The inner tube is perforated while the outer tube is solid, and in between a dessicant is placed, in this case blue silica beads. The inner tube has the same diameter as the inlet of the OPC-N2 or OPC-N3, and it is attached to it in a way that the connection is airtight. All the components have been designed with Computer Aided Design (CAD) programming and 3-D printed.

Characteristics of the dryer can be found the following table, taken from Savvakis et al. (2024):

| | **Inner tube** | **Outer tube** |
|---|---|---|
| Inner diameter [mm] | 6.2 | 20 |
| Outer diameter [mm] | 6.5 | 23 |
| Material | Liquid Resin | Poly Lactic Acid (PLA) |
| Length [mm] | 120 | 99 |

### List of Abbreviations

| | |
|---|---|
| GF | Growth factor |
| H-TDMA | Hygroscopic Tandem Differential Mobility Analyzer |
| HYSPLIT | Hybrid Single-Particle- Langrangian Integrated Trajectory |
| IADS | Intelligent Aerosol Drying System |
| OAS | Optical aerosol spectrometer |
| OPC | Optical particle counter |
| PM | Particulate matter |
| PNC | Particle number concentration |
| RH | Relative humidity |

## References

Alphasense, L., 2015: User Manual: OPC-N2 Optical Particle Counter. https://www.manualslib.com/manual/1540841/Alphasense-Opc-N2.html (Accessed on December 12th, 2022).

Alphasense, L., 2019: User Manual: OPC-N3 Optical Particle Counter.. https://www.alphasense.com/wp-content/uploads/2019/03/OPC‑N3.pdf (Accessed on October 14th, 2022).

Biskos, G., A. Malinowski, L. Russell, P. Buseck, S. Martin, 2006: Nanosize effect on the deliquescence and the efflorescence of sodium chloride particles. – Aerosol Sci. Technol. **2**, 97–106, DOI: 10.1080/02786820500484396.

Bohren, C.F., D.R. Huffman, 2008: Absorption and scattering of light by small particles – John Wiley & Sons.

Cheung, H.C., C.C.K. Chou, C.S.L. Lee, W.C. Kuo, S.C. Chang, 2020: Hygroscopic properties and cloud condensation nuclei activity of atmospheric aerosols under the influences of Asian continental outflow and new particle formation at a coastal site in Eastern Asia. – Atmos. Chem. Phys. **10**, 5911–5922, DOI: 10.5194/acp-20-5911-2020.

Clarke, A., V. Kapustin, S. Howell, K. Moore, B. Lienert, S. Masonis, T. Anderson, D. Covert, 2003: Sea-salt size distributions from breaking waves: Implications for marine aerosol production and optical extinction measurements during SEAS. – J. Atmos. Ocean. Technol. **10**, 1362–1374, DOI: 10.1175/1520-0426(2003)020<1362:SSDFBW>2.0.CO;2.

Crilley, L.R., A. Singh, L.J. Kramer, M.D. Shaw, M.S. Alam, J.S. Apte, W.J. Bloss, L. Hildebrandt Ruiz, P. Fu, W. Fu, others, 2020: Effect of aerosol composition on the performance of low-cost optical particle counter correction factors. – Atmos. Measur. Techniq. **3**, 1181–1193.

Davies, J.F., C.L. Price, J. Choczynski, R.K. Kohli, 2021: Hygroscopic growth of simulated lung fluid aerosol particles under ambient environmental conditions. – Chemical Commun. **26**, 3243–3246, DOI: 10.1039/D1CC00066G.

Di Antonio, A., O.A. Popoola, B. Ouyang, J. Saffell, R.L. Jones, 2018: Developing a relative humidity correction for low-cost sensors measuring ambient particulate matter. – Sensors **9**, 2790, DOI: 10.3390/s18092790.

Drake, R., J. Gordon, 1985: Mie scattering. – Amer. J. Phys. **10**, 955–962, DOI: 10.1119/1.14011.

Feingold, G., B. Morley, 2003: Aerosol hygroscopic properties as measured by lidar and comparison with in situ measurements. – J. Geophys. Res. Atmos. **D11**, DOI: 10.1029/2002JD002842.

Fitzgerald, J.W., 1975: Approximation formulas for the equilibrium size of an aerosol particle as a function of its dry size and composition and the ambient relative humidity. – J. Appl. Meteor. Climatol. **6**, 1044–1049, DOI: 10.1175/1520-0450(1975)014<1044:AFFTES>2.0.CO;2.

Griffiths, P., J.S. Borlace, P. Gallimore, M. Kalberer, M. Herzog, F. Pope, 2012: Hygroscopic growth and cloud activation of pollen: A laboratory and modelling study. – Atmos. Sci. Lett. **4**, 289–295, DOI: 10.1002/asl.397.

Gupta, D., H.J. Eom, H.R. Cho, C.U. Ro, 2015: Hygroscopic behavior of NaCl–MgCl 2 mixture particles as nascent seaspray aerosol surrogates and observation of efflorescence during humidification. – Atmos. Chem. Phys. **19**, 11273–11290, DOI: 10.5194/acp-15-11273-2015.

Gysel, M., J. Crosier, D. Topping, J. Whitehead, K. Bower, M. Cubison, P. Williams, M. Flynn, G. McFiggans, H. Coe, 2007: Closure study between chemical composition and hygroscopic growth of aerosol particles during TORCH2. – Atmos. Chem. Phys. **24**, 6131–6144, DOI: 10.5194/acp-7-6131-2007.

Hagan, D.H., J.H. Kroll, 2020: Assessing the accuracy of low-cost optical particle sensors using a physics-based approach. – Atmos. Measur. Techniq. **11**, 6343–6355, DOI: 10.5194/amt-13-6343-2020.

Hämeri, K., M. Väkevä, H.C. Hansson, A. Laaksonen, 2000: Hygroscopic growth of ultrafine ammonium sulphate aerosol measured using an ultrafine tandem differential mobility analyzer. – J. Geophys. Res. Atmos.**D17**, 22231–22242.

Hämeri, K., A. Laaksonen, M. Väkevä, T. Suni, 2001: Hygroscopic growth of ultrafine sodium chloride particles. – J. Geophys. Res. Atmos. **D18**, 20749–20757, DOI: 10.1029/2000JD900220.

Hegg, D., D.S. Covert, K. Crahan, H. Jonsson, Y. Liu, 2006: Measurements of aerosol size-resolved hygroscopicity at sub and supermicron sizes. – Geophys.Res. Lett. **21**, DOI: 10.1029/2006GL026747.

Hitzenberger, R., A. Berner, U. Dusek, R. Alabashi, 1997: Humidity-dependent growth of size-segregated aerosol samples. – Aerosol Sci. Technol. **21**, 116–130, DOI: 10.1080/02786829708965461.

Kaaden, N., A. Massling, A. Schladitz, T. Müller, K. Kandler, L. Schütz, B. Weinzierl, A. Petzold, M. Tesche, S. Leinert, others, 2009: State of mixing, shape factor, number size distribution, and hygroscopic growth of the Saharan anthropogenic and mineral dust aerosol at Tinfou, Morocco. – Tellus B: Chem. Phys. Meteor. **1**, 51–63, DOI: 10.1111/j.1600-0889.2008.00388.x.

Kitamori, Y., M. Mochida, K. Kawamura, 2009: Assessment of the aerosol water content in urban atmospheric particles by the hygroscopic growth measurements in Sapporo, Japan. – Atmos. Env. **21**, 3416–3423, DOI: 10.1016/j.atmosenv.2009.03.037.

Laskina, O., H.S. Morris, J.R. Grandquist, Z. Qin, E.A. Stone, A.V. Tivanski, V.H. Grassian, 2015: Size matters in the water uptake and hygroscopic growth of atmospherically relevant multicomponent aerosol particles. – J. Phys. Chem. A **19**, 4489–4497.

Liu, B., D. Pui, K. Whitby, D.B. Kittelson, Y. Kousaka, R. McKenzie, 1978: The aerosol mobility chromatograph: a new detector for sulfuric acid aerosols. – In: Sulfur in the atmosphere, Elsevier, 99–104.

Malings, C., R. Tanzer, A. Hauryliuk, P.K. Saha, A.L. Robinson, A.A. Presto, R. Subramanian, 2020: Fine particle mass monitoring with low-cost sensors: Corrections and long-term performance evaluation. – Aerosol Sci. Technol. **2**, 160–174, DOI: 10.1080/02786826.2019.1623863.

Ming, Y., L.M. Russell, 2001: Predicted hygroscopic growth of sea salt aerosol. – J. Geophys. Res. Atmos. **D22**, 28259–28274, DOI: 10.1029/2001JD000454.

Molnár, A., K. Imre, Z. Ferenczi, G. Kiss, A. Gelencsér, 2020: Aerosol hygroscopicity: Hygroscopic growth proxy based on visibility for low-cost PM monitoring. – Atmos. Res. **236**, 104815, DOI: 10.1016/j.atmosres.2019.104815.

Petters, M., S. Kreidenweis, 2007: A single parameter representation of hygroscopic growth and cloud condensation nucleus activity. – Atmos. Chem. Phys. **8**, 1961–1971, DOI: 10.5194/acp-7-1961-2007.

Savvakis, V., M. Schön, M. Bramati, B. Jens, A. Platis, 2024: Small-scale diffusion dryer on an optical particle counter for high humidity aerosol measurements with an uncrewed aircraft system. – accepted by J. Atmos. Ocean. Technol.

Sensirion, S., 2016: Sensor datasheet: SHT31.. https://sensirion.com/media/documents/213E6A3B/63A5A569/Datasheet_SHT3x_DIS.pdf (Accessed on November 22nd, 2023).

Snider, J.R., M.D. Petters, 2008: Optical particle counter measurement of marine aerosol hygroscopic growth. – Atmos. Chem. Phys. **7**, 1949–1962, DOI: 10.5194/acp-8-1949-2008.

Sorjamaa, R., A. Laaksonen, 2007: The effect of $H_20$ adsorption on cloud drop activation of insoluble particles: a theoretical framework. – Atmos. Chem. Phys. **24**, 6175–6180, DOI: 10.5194/acp-7-6175-2007.

Stein, A.F., R.R. Draxler, G.D. Rolph, B.J.B. Stunder, M.D. Cohen, F. Ngan, 2015: NOAA's HYSPLIT

atmospheric transport and dispersion modeling system. – Bull. Amer. Meteor. Soc.**12**, 2059–2077, DOI: 10.1175/BAMS-D-14-00110.1.

Svenningsson, B., J. Rissler, E. Swietlicki, M. Mircea, M. Bilde, M. Facchini, S. Decesari, S. Fuzzi, J. Zhou, J. Mønster, others, 2006: Hygroscopic growth and critical supersaturations for mixed aerosol particles of inorganic and organic compounds of atmospheric relevance. – Atmos. Chem. Phys. **7**, 1937–1952, DOI: 10.5194/acp-6-1937-2006.

Swietlicki, E., H.C. Hansson, K. Hämeri, B. Svenningsson, A. Massling, G. McFiggans, P. McMurry, T. Petäjä, P. Tunved, M. Gysel, others, 2008: Hygroscopic properties of submicrometer atmospheric aerosol particles measured with H-TDMA instruments in various environments – a review. – Tellus B: Chem. Phys. Meteor. **3**, 432–469, DOI: 10.1111/j.1600-0889.2008.00350.x.

Tang, I.N., A. Tridico, K. Fung, 1997: Thermodynamic and optical properties of sea salt aerosols. – J. Geophys. Res. Atmos. **D19**, 23269–23275.

Tang, M., C.K. Chan, Y.J. Li, H. Su, Q. Ma, Z. Wu, G. Zhang, Z. Wang, M. Ge, M. Hu, others, 2019: A review of experimental techniques for aerosol hygroscopicity studies. – Atmos. Chem. Phys. **19**, 12631–12686, DOI: 10.5194/acp-19-12631-2019.

Turšič, J., B. Podkrajšek, I. Grgić, P. Ctyroky, A. Berner, U. Dusek, R. Hitzenberger, 2006: Chemical composition and hygroscopic properties of size-segregated aerosol particles collected at the Adriatic coast of Slovenia. – Chemosphere **7**, 1193–1202, DOI: 10.1016/j.chemosphere.2005.08.040.

Weingartner, E., H. Burtscher, U. Baltensperger, 1997: Hygroscopic properties of carbon and diesel soot particles. – Atmos. Env. **15**, 2311–2327, DOI: 10.1016/S1352-2310(97)00023-X.

Won, W.S., R. Oh, W. Lee, S. Ku, P.C. Su, Y.J. Yoon, 2021: Hygroscopic properties of particulate matter and effects of their interactions with weather on visibility. – Sci. Rep. **1**, 1–12, DOI: 10.1038/s41598-021-95834-6.

Zhao, P., J. Ding, X. Du, J. Su, 2019: High time-resolution measurement of light scattering hygroscopic growth factor in Beijing: A novel method for high relative humidity conditions. – Atmos. Env. **215**, 116912, DOI: 10.1016/j.atmosenv.2019.116912.

Zieger, P., O. Väisänen, J.C. Corbin, D.G. Partridge, S. Bastelberger, M. Mousavi-Fard, B. Rosati, M. Gysel, U.K. Krieger, C. Leck, others, 2017: Revising the hygroscopicity of inorganic sea salt particles. – Nature Comm. **1**, 1–10, DOI: 10.1038/ncomms15883.

## A.3 Publication III

Aerosol Science and Technology

ISSN: (Print) (Online) Journal homepage: www.tandfonline.com/journals/uast20

# *In-situ* observations of charged Saharan dust from an uncrewed aircraft system

**Vasileios Savvakis, Martin Schön, Keri A. Nicoll, Claire L. Ryder, Alkistis Papetta, Maria Kezoudi, Franco Marenco, Jens Bange & Andreas Platis**

**To cite this article:** Vasileios Savvakis, Martin Schön, Keri A. Nicoll, Claire L. Ryder, Alkistis Papetta, Maria Kezoudi, Franco Marenco, Jens Bange & Andreas Platis (11 Jul 2024): *In-situ* observations of charged Saharan dust from an uncrewed aircraft system, Aerosol Science and Technology, DOI: 10.1080/02786826.2024.2372399

**To link to this article:** https://doi.org/10.1080/02786826.2024.2372399



Published online: 11 Jul 2024.

AEROSOL SCIENCE AND TECHNOLOGY
https://doi.org/10.1080/02786826.2024.2372399



# *In-situ* observations of charged Saharan dust from an uncrewed aircraft system

Vasileios Savvakis[a], Martin Schön[a], Keri A. Nicoll[b], Claire L. Ryder[b], Alkistis Papetta[c], Maria Kezoudi[c], Franco Marenco[c], Jens Bange[a], and Andreas Platis[a]

[a]Department of Geosciences, University of Tübingen, Tübingen, Germany; [b]Department of Meteorology, University of Reading, Reading, United Kingdom; [c]Climate and Atmosphere Research Center, The Cyprus Institute, Nicosia, Cyprus

**ABSTRACT**

Mineral dust from the Sahara desert can travel long distances at high altitudes, perturbing the energy budget of the atmosphere. Charging of dust has been observed to occur near the surface through triboelectric charging during dust lofting, potentially affecting particle coagulation, fall speeds, and the lofting process itself. Apart from near-surface studies, measurements at elevated dust layers, where charge may play a role in particle long-range transport, are rare. This study presents new observations from an uncrewed aircraft system (UAS) of type MASC-3, through an elevated Saharan dust layer over Cyprus on 6 April 2022. The dust layer ranged from 1500 to 2500 meters above sea level (a.s.l), with maximum particle number concentrations (PNC) of 80–100 $cm^{-3}$, primarily consisting of particles up to 2.5 μm in size. Measurements showed elevated charge within the dust layer, with magnitude proportional to PNC. It was concluded that there was a small influence of aircraft charge on the measurements, which was handled by developing a PNC-based correction factor. Corrected charge within the dust layer ranged from 0.2 to 3 pC $m^{-3}$, with most of the charge at the upper and lower dust layer boundaries. The magnitude and location of the charge was consistent with predictions of ion-particle attachment. This suggests that most of the measured charge did not originate from the lofting process, but dust particles were charged on site through ion-particle attachment processes.

**ARTICLE HISTORY**
Received 14 March 2024
Accepted 11 June 2024

**EDITOR**
Nicole Riemer

**GRAPHICAL ABSTRACT**

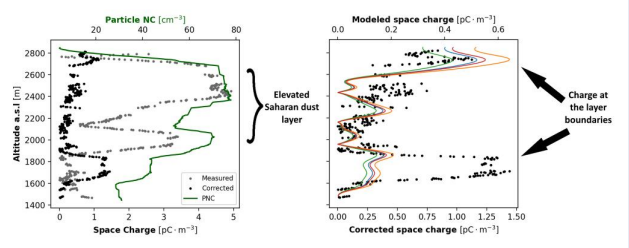


## 1. Introduction

A major source of mineral dust is North Africa, and specifically the Sahara desert (Stuut, Smalley, and O'Hara-Dhand 2009). Its predominant channel of transport across all seasons of the year is the Mediterranean sea (Israelevich et al. 2012), but it occasionally follows a curved path around the east side of the Atlantic. The amount of dust transported north from the Sahara is in the order of magnitude of hundreds of thousands of tons (Varga, Újvári, and Kovács 2014), with a wide array of environmental effects (Goudie and Middleton 2001). For instance, its interaction with incoming radiation through absorption and scattering can disturb the atmospheric energy budget and influence the total heating or cooling of the atmosphere (Carlson and Benjamin 1980). This radiative effect of dust loading has been extensively studied as it frequently affects the whole of the

CONTACT Vasileios Savvakis vasileios.savvakis@uni-tuebingen.de Department of Geosciences, University of Tübingen, Schnarrenbergstraße 94-96, 72076 Tübingen, Germany.

Mediterranean basin, and especially central and eastern parts (Soupiona et al. 2020).

Electrification of dust particles is known to result from the process of triboelectrification (Kamra 1972), whereby particles collide with each other, exchanging charge. Triboelectrification of dust occurs readily during dust lofting, including dust storms (Rudge 1913) and dust devils ((Franzese et al. 2018). The separation of positive and negative charge gives rise to large electric fields (E-fields) in the order of kV $m^{-1}$ (Williams et al. 2009; Katz et al. 2018). This can affect processes such as lofting of particles from the ground (Esposito et al. 2016), as well as the propagation of electromagnetic waves during dust storms (Zhou, Shu He, and Jing Zheng 2005). Dust electrification studies have typically been conducted from the surface using electric field mills in dense dust storm events (Yair et al. 2016; Zhang, Bo, and Zheng 2017; Katz et al. 2018). Such ground based instrumentation has also been used to characterize charging in advected elevated layers of Saharan dust transported over long distances (Silva et al. 2016; Harrison et al. 2018; Daskalopoulou et al. 2021).

In comparison to surface observations, measurements of the electrical properties of dust above the surface are few. Gringel and Muhleisen (1978) measured a conductivity decrease by a factor of two, associated within a Saharan dust layer from a balloon platform, whilst Nicoll, Harrison, and Ulanowski (2010) used a balloon borne space charge sensor and aerosol number concentration counter to detect weakly charged Saharan dust over the Cape Verde Isles. A similar space charge sensor has more recently been flown by Mallios et al. (2023) through dust events, alongside a miniature electric field mill, also from a balloon platform. Another study with a miniaturized optical sensor on a balloon platform during a Saharan dust event in Minorca island (Spain) during the summer of 2013, also obliquely indicated dust particle charge due to the sensitivity of the employed instrument to electromagnetic field alterations (Renard et al. 2018).

Although there have been abundant measurements of dust particle concentrations and sizes from crewed aircraft and uncrewed aircraft systems (UASs) (Haywood et al. 2001; Tanré et al. 2003; Johnson and Osborne 2011; Granados-Muñoz et al. 2016; Schrod et al. 2017; Mamali et al. 2018; Ryder et al. 2019), dust particle charge measurements from aircraft are exceptionally rare in literature. This is likely due to the triboelectric charging effect of the dust on the body of aircraft, which generates large E-fields and overwhelms the measurement of dust particle charge (Lekas 2019). Previous laboratory research has been performed on the charge acquired by aircraft due to dust (Perala 2009), finding values of 5–10 μA $m^{-2}$ of charging rate per effective area, at speeds of 180 m $s^{-1}$ (640 km per hour, typical cruising speed for a large jet aircraft). A dependence of charge on the speed of the aircraft, area of the aircraft body impacted by dust, and the dust particle concentration was found.

For the study presented here, we employed a UAS with a wing span of 4 m, i.e., an order of magnitude smaller than a typical crewed aircraft (e.g., a BAE-146), flying at a cruising speed approximately 6–10 times slower than crewed aircraft and with significantly less weight. Therefore, although some charging of the aircraft body is expected whilst flying through dust, it is likely to be many orders of magnitude less than on a crewed aircraft. The effect of aircraft charge on the measurements is discussed and accounted for in Section 3.3.

Although dust electrification has been known about since the measurements of Rudge (1913) there has been a drive in recent decades to understand the mechanisms of dust electrification and to better quantify the variability of the charge carried by dust particles, e.g., in Zhang and Zhou (2020). This is partly in response to potential impacts of dust electrification on a number of atmospheric processes important for climate. These include vertical alignment (polarization) of dust particles in high altitude dust layers in the atmospheric E-field (Ulanowski et al. 2007), known as the "Venetian blind effect," which may alter the cross-sectional area covered by particles and decreases optical depth, something that is not currently accounted for in remote-sensing retrievals of aerosols or sun photometers (Ulanowski et al. 2008). It has also been hypothesized that in elevated dust layers, the atmospheric E-field may also act as a counterbalance to the gravitational force for aerosol particles in the coarser modes, thus allowing large aerosol particles to stay aloft and be transported over longer distances. Dust transport models often underestimate the transport range of coarse particles (Ginoux et al. 2001; Maring et al. 2003; Van Der Does et al. 2018), and the existence of coarse/giant mode particles transported over distances longer than what predicted by conventional theory, has been reported in studies using measurements from balloons (Renard et al. 2018) as well as crewed aircraft (Ryder et al. 2013; Marenco et al. 2018; Adebiyi and Kok 2020; O'Sullivan et al. 2020). The lack of particle charge and

E-field observations in elevated dust layers has so far been a barrier to progress in this area, and it is therefore important to acquire more direct measurements through Saharan dust layers. Capturing vertically extended space charge and aerosol concentrations, could contribute to better understanding the aforementioned effects and how to incorporate them in currently used models.

This work aims to address these objectives by presenting new, simultaneous aerosol concentration and charge measurements from a fixed wing UAS, specifically the Multipurpose Airborne Sensor Carrier (MASC-3) (Mauz et al. 2019; Rautenberg et al. 2019), during a Saharan dust event that occurred over Cyprus in April, 2022. This has been the first attempt of using a UAS equipped with a scientific payload for both space charge and aerosol particles, as well as meteorological (wind vector, temperature, humidity) and turbulent quantities like the turbulent kinetic energy (TKE), to perform vertical profiles within a Saharan dust layer and investigate their relationship. Details of the aircraft and instrumentation are discussed in Section 2. Section 3.1 discusses the transport of the dust, based on a 48-h back trajectory simulation prior to the day of measurements, spectral images from satellites and remote-sensing instrumentation at the vicinity of the aircraft flights. Measurements of meteorological, aerosol and charge vertical profiles through the dust layer are shown in Section 3.2 and a method to account for charge acquired on the aircraft body discussed in Section 3.3, along with vertical profiles of corrected charge. A description of the theoretical model to estimate the expected dust charge at the given conditions, is explained in Section 3.4. The discussion and conclusions then follow in Sections 4 and 5.

## 2. Materials and methods

### 2.1. UAS instrumentation

A fixed-wing, uncrewed aircraft of type MASC-3 (Mauz et al. 2019; Rautenberg et al. 2019), was employed for the flights described in our study. The UAS has a maximum take-off weight of 8 kg, endurance of 1.5 h, and a wingspan of 4 m. During flight missions, a speed of about 18.5 m $s^{-1}$ is kept constant by the autopilot system (PixHawk 2.1 Cube Orange). A 1.5 kg sensor system at the nose of the aircraft provides high resolution data of meteorological and turbulent variables (air temperature, humidity, 3-D wind vector, TKE), which are stored onboard the platform at a frequency of 100 Hz. The autopilot also allows for accurate, pre-planned, automatic flight missions. The aircraft's location, attitude parameters and meteorological measurements are transmitted with 1 Hz frequency in real time to portable computers on ground stations during each flight. Full specifications of the MASC-3 with its standard payload are described in detail in Rautenberg et al. (2019). Furthermore, computation of TKE using the MASC-3, is explained in Platis et al. (2016); Zum Berge et al. (2021); Schön et al. (2022).

For aerosol particle measurements, the UAS has an aerodynamically shaped pod installed on one wing (referred to as OPC-Pod), which is based on the commercially available optical particle counter (OPC) of type N3 (Alphasense, United Kingdom). The N3 is a lightweight instrument ($\approx$ 105 g) that covers an aerosol size range from 0.35 to 40 µm in diameter, distributed among 24 discrete channels based on scattering from a 658 nm laser beam, with scattering angles of $32-88^{\circ}$ and operating at a sampling frequency of 1 Hz. For the OPC-N3, particle spherical shape with a complex refractive index of $n = 1.5 \cdot i + 0j$ and density of 1.65 g $cm^{-3}$, are internally assumed. The sensor has been modified to accommodate measurements at the cruising speed of the aircraft, specifically by removing its parent fan and designing the OPC-Pod so that it maintains passive aspiration, caused by pressure differences at its inlet and an exhaust point at its top (Mashni et al. 2023). A validation study including detailed description of the OPC-Pod's operation and components, showed the sensor's reliability for operation on the MASC-3 after comparison with a reference station on the ground, airflow experiments in a wind tunnel and experimental flights during and after the Saharan dust layer in Cyprus (Schön et al. 2024). Data from the MASC-3 were further compared with additional flights of the UCASS system (Smith et al. 2019; Kezoudi et al. 2021b), on a UAS of type Skywalker operated by the Cyprus Institute. The two airborne platforms measured similar PNC absolute values ($35-40$ $cm^{-3}$ at a size range up to 31 µm) and at the same altitude ranges.

Space charge is measured using small charge sensors in a similarly shaped pod (referred to as the Charge-Pod), attached on the other wing of the aircraft. These sensors consist of a spherical metal electrode connected to an electrometer, which is sensitive to displacement currents produced by changes in the electric field (Nicoll and Harrison 2009). The electric current between the sensor and the surrounding air is calculated from the voltage output of the sensor. Space charge is then calculated by a conversion

formula that uses the calculated current, the sensor effective area, and the ascent rate of the aircraft. A comprehensive description of this procedure and the components of the charge sensor itself can be found in Nicoll and Harrison (2009). The operation of the Charge-Pod on the MASC-3, with validation flights including data correction for the aircraft movement, and vertical profiles in the atmospheric boundary layer (ABL), is presented in Schön et al. (2022).

### 2.2. Location and flight pattern

During a Saharan dust event passing over the Eastern Mediterranean, MASC-3 flights were performed near Orounda, Cyprus on the 6 April 2022. The base of operations was the private airfield at the Unmanned Systems Research Laboratory (USRL – coordinates: 35.095 N, 33.081 E) of the Cyprus Institute. The site has a wide runway, which is ideal for take-off and landing procedures with a fixed-wing aircraft like the MASC-3, and the surrounding area consists of low-level grassland with no obstacles, further ensuring the safety of all flight procedures (Kezoudi et al. 2021a). The area was affected by Saharan dust from late afternoon of 5 April, and persisted on 6 April. Aerosol levels notably decreased two days later, as the dust shifted eastwards.

Vertical profiling with the MASC-3 consisted of a 2 km zigzag pattern during both ascent and descent of the aircraft, with an ascent/descent rate of 1.5 m $s^{-1}$. To avoid the effect of aircraft turns (which adversely influences the charge measurements), data from only the first half of each flight section are retained for analysis, as in Schön et al. (2022), essentially omitting measurements during the turning procedures of the aircraft. A total of eight flights were carried out during the Cyprus campaign, of which two are presented here as representative of the dust event, each up to an altitude of 2800 m above sea level (a.s.l). Flight 1 took place on 6 April, at 08:29–09:32 UTC, and flight 2 at 11:54–12:53 UTC (add three hours for local EEST).

### 2.3. Additional dust observations

Apart from the in-situ measurements collected with the MASC-3, a number of other tools are used for the characterization and evolution of the dust event two days before and during the time of the flight operations. Back trajectories were retrieved from the Hybrid Single Particle Lagrangian Integrated Trajectory (HYSPLIT) model, by the National Oceanic Atmospheric Administration (NOAA) (Stein et al. 2015), to identify the origin of the airmasses observed above Cyprus during the times of measurements. Additionally, optical data were retrieved from the Spinning Enhanced Visible and Infrared Imager (SEVIRI), a radiometer on the Meteosat Second Generation (MSG) satellite Meteostat-8 (Indian Ocean Data Coverage – IODC) (Aminou 2002), which is operated by the European Organization for the Exploitation of Meteorological Satellites (EUMETSAT).

Further identification of the elevated dust was achieved by using the SEVIRI Dust RGB (red-green-blue) thermal infrared satellite imagery product (Lensky and Rosenfeld 2008; Martínez, Ruiz, and Cuevas 2009). With the SEVIRI Dust RGB, dust events are identifiable by their bright pink color, e.g., as in Brindley et al. (2012). Due to the high time resolution of SEVIRI imagery (15 min) this enables dust plumes to be manually traced backwards in time to identify their sources. The starting point and progression of the dust plume was inspected, covering a time period from the early morning of 4 April, until the late evening of 5 April, when it first arrived in Cyprus. For 6 April, dust presence was evaluated based on aerosol optical depth (AOD) data from two ground-based sun photometers, one located in Nicosia (approximately 30 km away from the USRL airfield) and the other in Agia Marina Xyliatou (5.5 km south of the USRL airfield), that operate within the framework of the AErosol RObotic NETwork (AERONET) (Holben et al. 1998), which has also been used for Saharan dust analysis before (Smirnov et al. 1998).

Vertical extent during the dust transport from the Sahara was investigated by using 532 nm wavelength total attenuated backscatter vertical profiles and from the Cloud-Aerosol Lidar with Orthogonal Polarization (CALIOP) LiDAR instrument related to the Cloud-Aerosol Lidar and Infrared Pathfinder Satellite Observations (CALIPSO) (Winker et al. 2010). The CALIOP also provided aerosol classification version 3.41 of the aerosol subtyping algorithm product by the National Aeronautics and Space Administration (NASA) (Kim et al. 2018). A CE376 (CIMEL, France) LiDAR instrument (Papetta et al. 2023), measuring at two wavelengths (404 and 832 nm) at the premises of the Cyprus Institute and collocated with one of the sun photometers (coordinates: 35.141 N, 33.381 E, 181 m a.s.l), provided depolarization ratio, extinction and backscatter coefficient profiles up to 3200 m a.s.l, derived through a backward Klett-Fernald inversion algorithm (Klett 1981; Fernald 1984). These profiles of the dust from the CE376 were then correlated to the

flight measurements with the MASC-3 at similar altitudes.

## 3. Results

### 3.1. Dust outbreak evolution

Figure 1 shows a 48-h back trajectory of the air mass that was present at the location of the measurements in Cyprus, at noon on 6 April 2022. As Saharan dust often resides in the free troposphere and above the ABL, three different starting points were selected: 2500, 3500, and 4000 m. The air masses traveled across the Mediterranean at approximately these altitudes, before slightly sinking on the morning of the 6 April 2022. Originating from central and northwest Algeria, as well as central central Morocco, this air mass was sampled thoroughly by the MASC-3. By profiling up to an altitude of almost 3000 m a.s.l, it effectively probed the air masses presented by the light green and blue lines in Figure 1.

A similar picture is acquired when looking at images from the SEVIRI Dust RGB (Figure 2). The

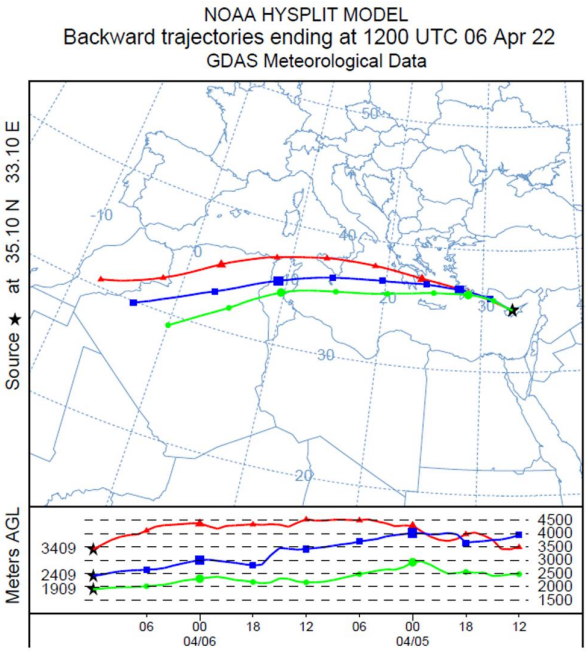


**Figure 1.** Single 48-h back trajectory of the sampled air mass during the day of measurements, from the HYSPLIT GDAS model (ending date time at 12:00 UTC on 6 April 2022). Three initial altitudes in m a.s.l (2500 – green, 3500 – red, and 4000 – blue line) and destination at the USRL in Orounda, Cyprus. Each colored line represents the path of the air mass with a starting altitude shown on the right and final altitude on the left, with the latter attached to a star that corresponds to the measurement location on the map. The back trajectories were similar for either flight, thus only one is shown here.

dust source area includes north west Algeria and Libya, and first indications of dust uplift appear already during noon of 4 April 2022, marked by black circles. In the evening of the same day (4 April, 17:00 UTC), uplift continued and the transport was initiated toward the north east direction and through the Mediterranean. Transport of dust continued throughout the night, when dust moved further north toward upper level clouds. As the plumes merged and spread spatially, they moved further east alongside cloud formations, which are also visible in the darker colored areas of Figure 2. During the morning of 5 April 2022 at 08:00 UTC, dust was widespread and co-located with the cloud. At 18:00 UTC, the homogeneously distributed thick dust layer first arrives in Cyprus and the surroundings. The satellite data for 6 April show dust that was widespread over the whole of the eastern Mediterranean, indicating a homogeneous distribution.

As seen in Figure 3 during the day of measurements (6 April), the total attenuated backscatter at 532 nm from CALIPSO shows higher values up to an altitude of approximately 3000 m a.s.l, which is around 2 $km^{-1}$ $sr^{-1}$ (yellow areas in Figure 3a) while also reaching a maximum of $3.5-4$ $km^{-1}$ $sr^{-1}$ (orange/red areas in Figure 3a) above and around Cyprus. According to Figure 3a, increased aerosol concentrations were widespread over the eastern Mediterranean. These aerosols consisted almost purely of dust, as noted from Figure 3b, which has yellow (i.e., identified dust cloud) areas predominantly present in the measurement area, indicated with the vertical white line in Figure 3. Elevated aerosol optical depth (AOD) levels were also recorded by the AERONET photometer in Nicosia, reaching 0.45 to 0.55 (from 08:00 to 15:00 UTC) for wavelengths between 340 and 870 nm, as well as the photometer in Agia Marina Xyliatou, which recorded values of $0.38-0.42$ for the same wavelengths in the early morning (values retrieved from AERONET, but not shown). This rise of AOD, which was significantly higher compared to what would be expected on a dust-free day, correlates with the evident existence of dust in the area for 6 April.

### 3.2. Vertical profiling

Figure 4 shows vertical profiles retrieved by the CE376 LiDAR instrument observations in Nicosia, on 6 April 2022, at 10:00 UTC, during the time when MASC-3 was performing its first flight. As the overlap region of this LiDAR is 1200 m, the vertical extent of the profiles covers a range from that altitude up to

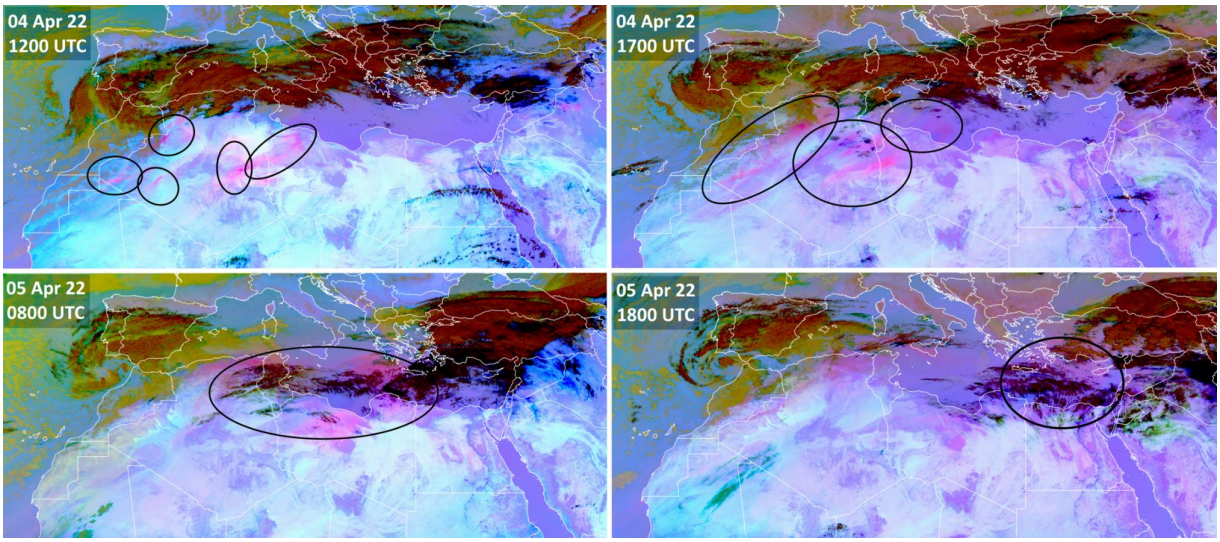


**Figure 2.** Images from the SEVIRI Dust RGB product on the Meteostat-8 satellite, covering two days prior to the measurement flights with the MASC-3 in Cyprus, on 6 April 2022. The images are color coded, specifically: magenta indicates dust clouds, black indicates cirrus clouds, dark red indicates ice clouds (more details on the image description can be found at EUMETSAT's website: https://www.eumetsat.int/). The black circled areas in each image depict the first appearance and uplift of dust (upper left) on 4 April, its transport with clouds to the east through the Mediterranean (upper right and bottom left), and its arrival in Cyprus on the evening of 5 April (bottom right).

3000 m a.s.l. These profiles display the volume depolarization ratio at 532 nm (VDR) (Figure 4a) and the calculated backscatter (Figure 4b) and extinction profiles (Figure 4c). Two local maxima can be identified in the extinction and backscatter coefficients' vertical structure, a minor one at 1750 m a.s.l. (extinction coefficient at 260 $Mm^{-1}$, backscatter coefficient at 7.5 $Mm^{-1}$ $sr^{-1}$), and a more pronounced one between 2300 and 2500 m a.s.l. (extinction coefficient at 430 $Mm^{-1}$, backscatter coefficient at 12 $Mm^{-1}$ $sr^{-1}$). VDR remained around 20% up to 2700 m a.s.l, a level of depolarization that is indicative of mineral dust particles and has been examined in previous studies, e.g., by Tesche et al. (2011). All three indicators decreased above that altitude, being close to zero at 3000 m a.s.l. This illustrates the presence of the Saharan dust layer with two peaks between 1750 and 2500 m a.s.l, from the CE376 measurements.

Results from the vertical profiling performed by the MASC-3 on 6 April, are shown in Figures 5 and 6. During the two flights, the UAS collected data for potential temperature and water vapor mixing ratio, horizontal wind and TKE, aerosol particle number concentrations (PNC) between 0.4 and 40 μm from the OPC-Pod and voltage output from the Charge-Pod.

In Figure 5a and e, a shallow ABL can be observed for both flights in the potential temperature (up to 700 m in flight 1, and 900 m in flight 2) and mixing ratio profiles. Considering the elevation of 327 m at the measurement location (Kezoudi et al. 2021a), the ABL height was at a lower altitude than normal for the middle of a spring convective day (usually above 1000 m). These two profiles suggest a stable troposphere with a shallow ABL, as shown in Figure 5a and e. Mixing ratio varied between 2 and 8 g $kg^{-1}$ (or, a maximum of 40% relative humidity throughout the whole vertical extent). Overall, the ABL was quite dry (5–8 g $kg^{-1}$) but the overlying layer was even drier (2–3 g $kg^{-1}$) for flight 1 and up to 4 g $kg^{-1}$ for flight 2. The wind speed at ground level varied between 6 and 8 m $s^{-1}$ during the morning and 9–10 m $s^{-1}$ during the afternoon flight, reaching 12.5–14 m $s^{-1}$ at higher altitudes. Higher amounts of TKE, calculated as explained in the Appendix of Schön et al. (2022), inside the ABL reached $0.4 - 0.85$ $m^2$ $s^{-2}$, while above it, the turbulence was, as expected, quite lower (below 0.2 $m^2$ $s^{-2}$). Additionally, small jumps of TKE could be identified at the boundaries of the different particle population layers (for instance in flight 1, at 2000 m a.s.l and at the upper dust layer edge between 2500 and 2600 m a.s.l) where TKE doubled, reaching 0.18 $m^2$ $s^{-2}$.

The Saharan dust layer can be identified from the MASC-3 data by the increased particle concentrations above 1500 m a.s.l in the PNC profiles (Figure 5c and g). A similar structure was observed by the CE376 LiDAR in Nicosia, which also captured two distinct

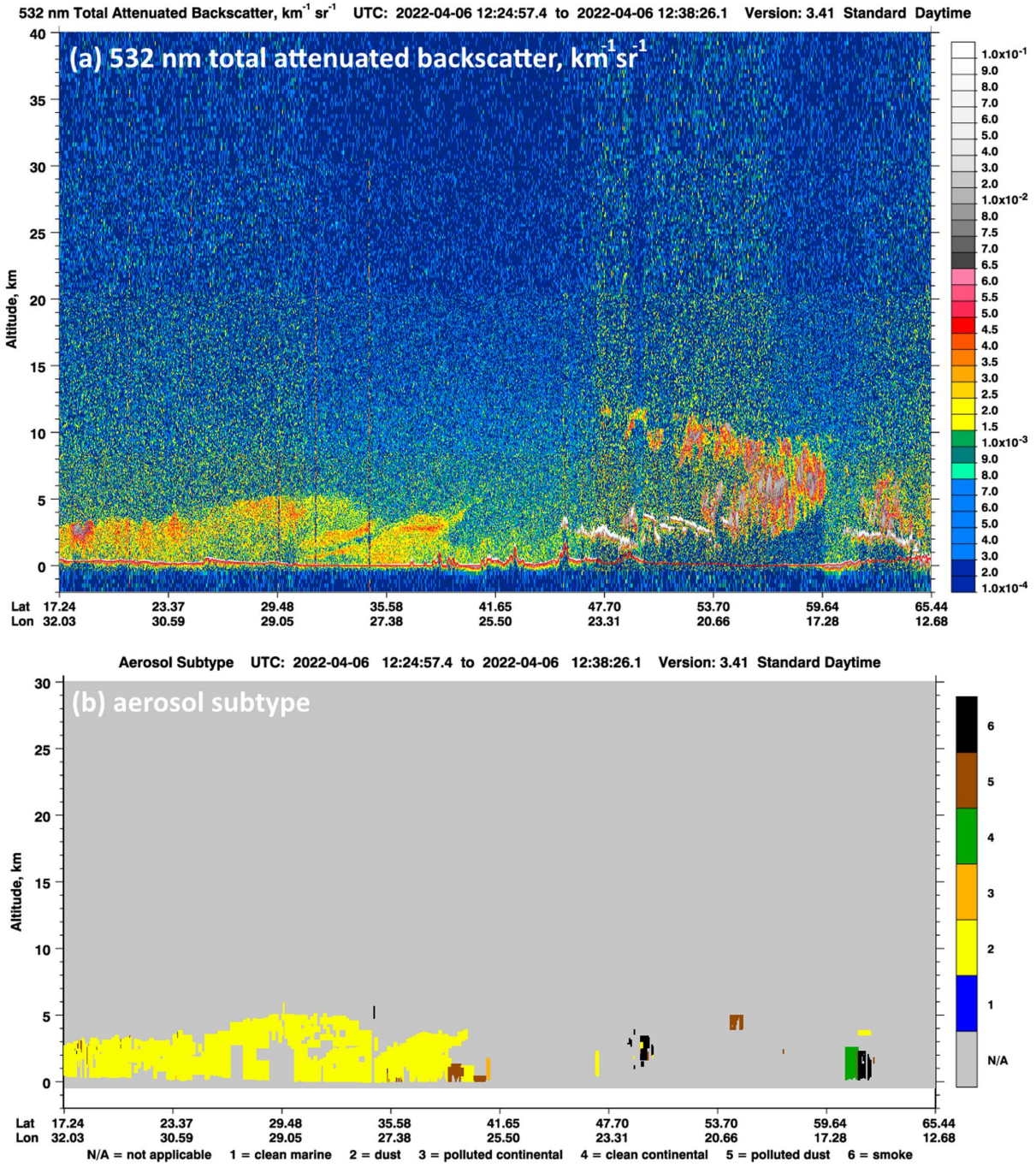


**Figure 3.** (a) Total attenuated backscatter at 532 nm and (b) aerosol subtype characterization, from the CALIPSO satellite, taken on 6 April at 12:24 UTC. Each plot has coordinates on the horizontal axis that cover a geographical strip that extends from North East Africa to Norway, Scandinavia (in this coordinate range, the measurement location is at: 35.095 N, 33.081 E). The satellite's overpass was still 5–7° west of Cyprus. In (a), the backscatter is color coded with the index on the side, and in (b), aerosol subtypes are also color coded and each type is denoted with a number and stated under the horizontal axis. Specifically, NA: not applicable, 1: clean marine, 2: dust, 3: polluted continental, 4: clean continental, 5: polluted dust, 6: smoke.

peaks in backscatter and extinction coefficient in the same altitude range (Figures 4 and 5c compared). During both flights of the MASC-3, the air layer containing Saharan dust extends roughly from an altitude of 1500 m a.s.l, which is also supported by vertical changes in mixing ratio and potential temperature (Figures 5a and e), TKE (Figures 5b and f) and from the CE376' profile of VDR (Figure 4). PNC levels

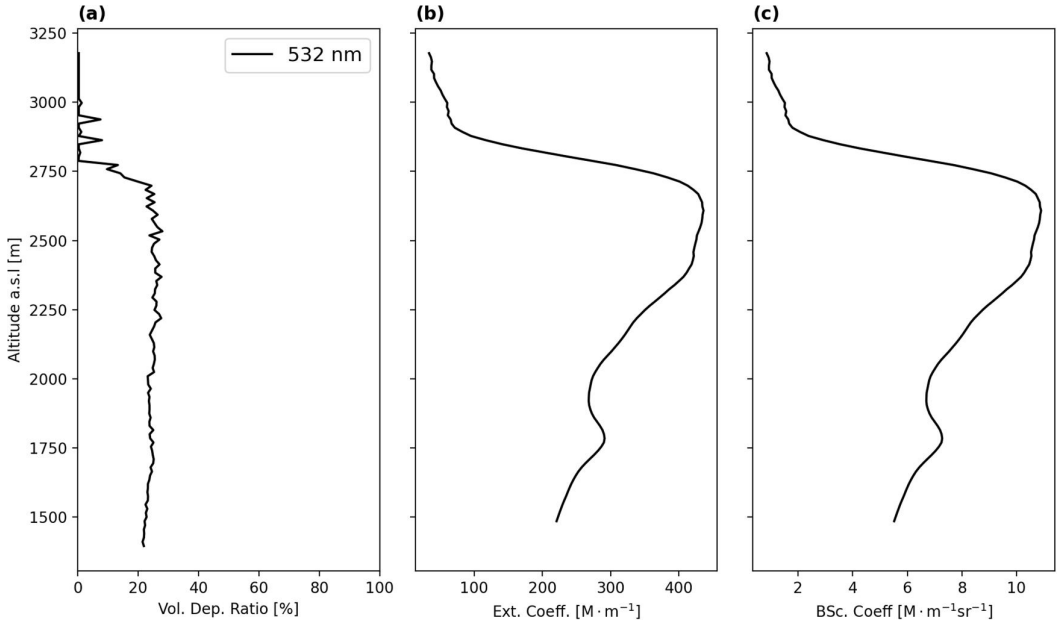


**Figure 4.** Volume depolarization ratio, extinction and backscatter coefficients at 532 nm wavelength, measured from the CE376 LiDAR operating in Nicosia. The profiles were captured on 6 April at 1000 UTC, at the time of the first flight of the MASC-3.

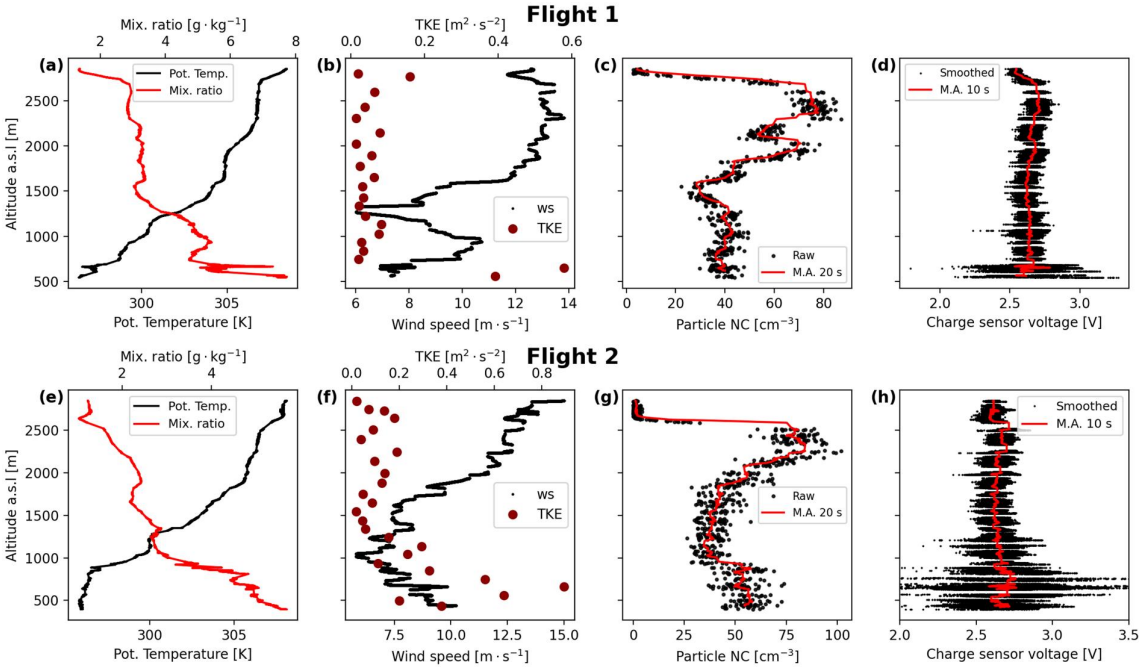


**Figure 5.** Vertical profiles from the two MASC-3 flights on 6 April (flight 1 at noon, flight 2 in the afternoon), showing meteorological parameters, aerosol particle number concentrations and charge sensor readings in voltages. Each row indicates a different flight. Specifically: (a) potential temperature and mixing ratio, (b) wind speed and TKE, (c) PNC (raw data and 20 s moving averaged) from 0.4 to 40 μm, and (d) charge sensor voltage as a black line, and a 10 s moving average as a red line. On the bottom row, the plots show the same parameters for the second flight, from (e) to (h). Only the ascent through the extent of the Saharan dust layer is shown in the figure.

showed maxima of $80-100$ cm$^{-3}$ within the Saharan dust layer and lower values of 40–50 cm$^{-3}$ within the ABL. There is a sharp drop in PNC above the dust layer, indicating a well defined top to the dust layer at 2500 m a.s.l, which is consistent between the two flights and the LiDAR profiles. Previous

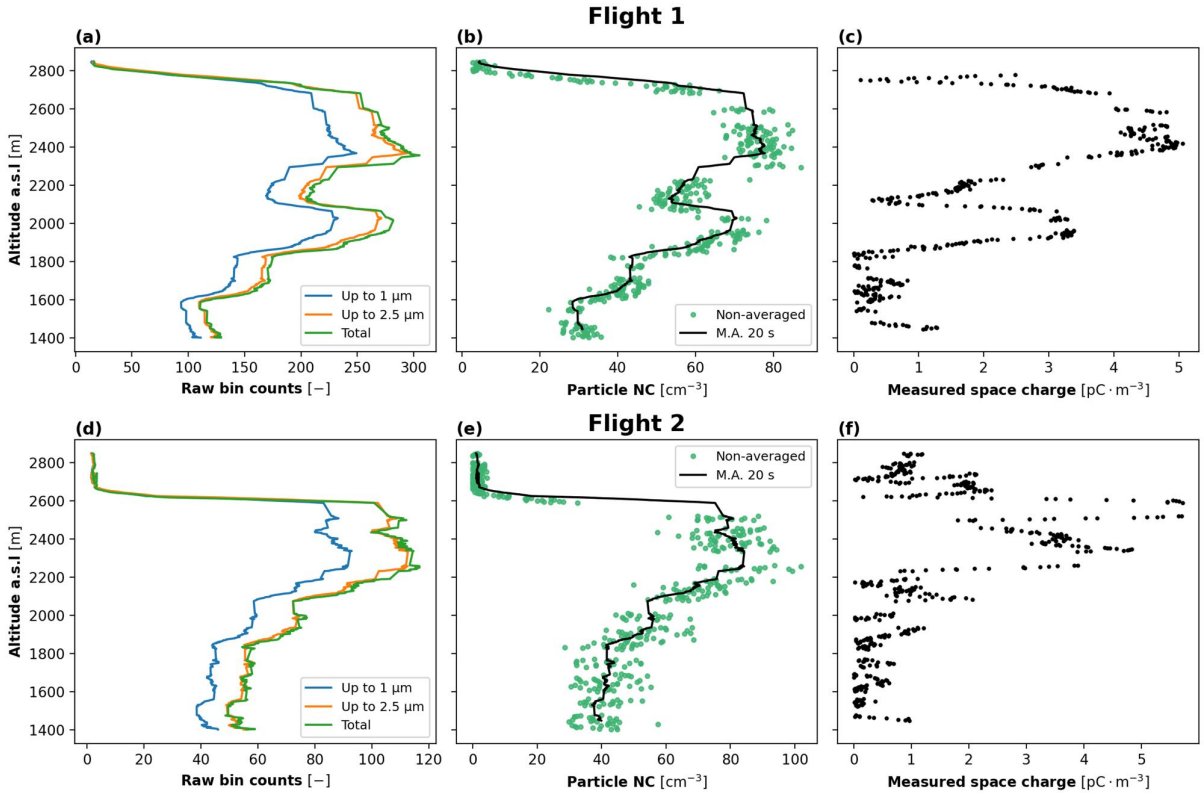


**Figure 6.** Aerosol particles and calculated space charge for the two flights. (a) Raw bin counts from the OPC-Pod (adding up aerosol numbers up to 1, 2.5 µm as well as the total size range of the sensor, i.e., 0.4–40 µm), (b) non-averaged PNC data in green, with a 20 s moving average as a black line, and (c) measured space charge from the Charge-Pod. On the bottom row, the plots show the same parameters for the second flight, from (d) to (f). Only the ascent is shown in the plots.

measurements of a different Saharan dust event with a balloon-borne OPC over Cyprus captured a layer from 3000 to 5000 m a.s.l, with peaks in PNC concentration at 50 cm$^{-3}$ in a size range from 0.6 to 13.9 µm (Kezoudi et al. 2021b). With the MASC-3, the dust plume was located at lower altitudes and higher PNC levels were measured, but also over a wider size spectrum.

The raw voltage from the charge sensor is shown in black in Figure 5d and h, demonstrating a large amount of charge in the ABL (i.e., below the temperature inversion), due to the interplay between higher turbulence levels and aerosol particles, that causes space charge dispersion across its extent. This is also consistent with previous measurements from the same sensor (Nicoll et al. 2018; Schön et al. 2022). Above the shallow ABL, the charge sensor voltage output is roughly constant (2.63±0.01 V) with height until it enters the dust layer, where a small increase (2.70±0.01 V) in voltage is evident.

More detailed analysis of the MASC-3 aerosol and charge data is presented in Figure 6. Figures 6a and d show a breakdown of PNC vertical profiles for flights 1 and 2 for particles according to their measured diameters (<1 µm <2.5 µm and all diameters up to 40 µm). The measured dust mainly consisted of particles in the submicron and micron range (with the majority being <2.5 µm in diameter), while concentrations decreased for larger sizes. The vertical distributions also indicate some of the larger particles inside the dust layer rather than below it, as seen from difference between the peaks in the 2.5 µm and total bin counts of Figure 6a and d. It is noteworthy to mention that the refractive index of Saharan dust is different than the one configured by the manufacturer of the OPC-N3, and this would affect the size bin boundaries (but not the absolute PNC values shown in Figure 6) of the sensor, as detailed in similar studies including optical measurement instruments, e.g., by Ryder et al. (2013); Renard et al. (2016). To account for this, and assuming a refractive index for Saharan dust being $n_{\text{dust}} = 1.53 \cdot i + 0.0015j$ (Johnson and Osborne 2011), the theoretical scattering cross section was calculated for two refractive indices (one assumed by the OPC-N3 and one of Saharan dust) considering the wavelength of the laser beam inside the instrument and integrated over its scattering angles, based on the formula explained in Jaenicke and Hanusch

(1993); Hagan and Kroll (2020). Then, correction factors for each bin boundary of the OPC-N3 were calculated based on the procedure explained in the Appendix of Nurowska et al. (2022), and these factors varied between 0.93 and 1.13 for sizes up to 10 μm and increased for larger sizes to about 1.5 – 1.6 at the OPC's upper size boundary limits. In essence, these kind of correction factors indicate that the refractive index difference between the internally assumed specifications of the OPC-N3 and Saharan dust would mostly affect particles in the larger/giant mode, where the OPC-N3 most likely understates the size, but the diameters before and after the correction are comparable in the smaller scales.

To convert the raw voltage measured by the charge sensor (and shown in Figures 5d and g) to space charge, the procedure described in Schön et al. (2022) was followed. This involves applying a correction for the roll velocity of the MASC-3 aircraft to the raw voltages, converting this to a current, and calculating the space charge using the the sensor effective area and the ascent rate of the aircraft (Nicoll and Harrison 2016; Schön et al. 2022). As per Schön et al. (2022), only the absolute values of space charge are discussed here. The calculated space charge values from the Charge-Pod are shown in Figures 6c and f. Generally, in conditions of a cloud or a dust layer, charge is expected to accumulate at the points of sharp change in conductivity, essentialy at the horizontal boundaries of the given layer, something that has been observed experimentally (Harrison et al. 2020), and also elaborated in Section 3.4 of this study. Our measurements demonstrate a clear, but small, increase in the space charge (up to 5 pC $m^{-3}$) within the dust layer in both flights, with the maximum in the space charge being located at the height of the largest particle concentration. Closer examination reveals a very close correlation between the space charge and PNC. As would be expected from existing literature on crewed aircraft flights through dust or ice cloud layers, some charging of the aircraft body is expected within the dust layer (Lekas et al. 2014), which would be expected to be proportional to the PNC (Perala 2009). Although we cannot be certain that the origin of this high correlation is due to aircraft charging, and not charge on the dust particles themselves, we investigate the effect of potential aircraft charging on the space charge measurement in the next section.

### 3.3. Accounting for aircraft charge

Within the Saharan dust layer (from 1500 to 2500 m a.sl), Figure 6 shows a strong correlation between PNC and measured charge. This indicates evidence of charging of the aircraft from interaction with the dust particles within the dust layer. The magnitude of the space charge within the dust layer (<5 pC $m^{-3}$) also illustrates this is a small effect, and many orders of magnitude smaller than what would be expected for crewed aircraft (Lekas 2019).

This is partly due to the design of the MASC-3 Charge-Pod, where the charge sensors are mounted in front of the pods, with the electrodes approximately 20 cm ahead of the leading edge of the wing (Figure 2 in Schön et al. 2022). The front of the Charge-Pod is also wrapped with conductive copper foil to reduce buildup of charge on the aircraft surface. Laboratory (Perala 2009) and modeling studies (Lekas et al. 2014) of the expected charge accumulation on crewed aircraft through dust layers suggests a dependence of the charge on the area of the aircraft impacted by the dust, which is minimized for MASC-3 due to the small surface area of the UAS, and the placement and design of the Charge-Pods.

Laboratory tests (Perala 2009) also demonstrate a dependence of charging on aircraft speed (typically 600 – 700 km $hr^{-1}$ cruising speed for crewed aircraft). For the MASC-3 flights the true air speed was an order of magnitude less than for crewed aircraft, and approximately constant (20 – 20.4 m $s^{-1}$, i.e., 72 – 74 km $hr^{-1}$) during the vertical profiles in flight 1 and 2. Therefore, the influence of changes in aircraft speed on charge accumulation are considered negligible in the flights described here. The main factor in controlling charge on the surface of the MASC-3 is expected to be the dust particle density, which has been found to scale linearly with aircraft charge (Perala 2009).

Figure 7 investigates the relationship between the dust particle number concentration (PNC) and the measured space charge within the dust layer, demonstrating a linear relationship between the two parameters (correlation coefficient $r^2 = 0.91$ in flight 1, and 0.75 for flight 2). This linearity is stronger in flight 1 than flight 2, possibly due to increased turbulence from the more convective conditions during the afternoon than during morning (as also shown from the small, but still relatively higher TKE values in the dust layer of Figure 5e, compared to Figure 5b). Since the focus of the measurements is to investigate the ambient dust particle charge, not the charge induced by the aircraft, a correction factor is developed based on the linearity between dust particle concentration and measured charge, for the dust layer only (and shown in Figure 7).

Considering PNC as the independent variable, the fitted line that results from a linear regression through

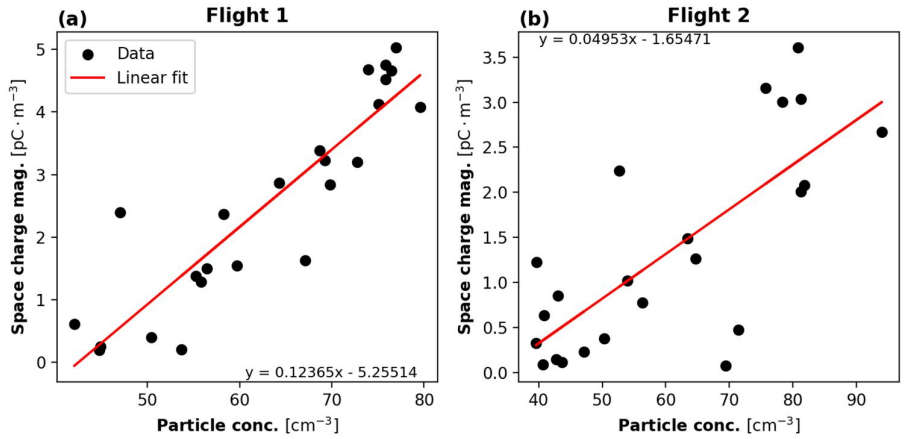


**Figure 7.** Scatterplot between measured particle concentrations and corresponding measured charge magnitude, covering the dust layer vertically during the MASC-3 flights. A linear fitted equation is also depicted as a red line, with the slope and intercept coefficients in the form of a line equation.

the least squares method is described by the well known equation:

$$\rho_{\text{pred}} = \text{slope} \cdot \text{PNC} + \text{intercept} \tag{1}$$

For our measurements, $\rho_{\text{pred}}$ is the measured charge and PNC is the measured dust concentration. For each flight, the slope and intercept are calculated from the linear regression and stated in Figure 7. Once the linear model is fitted to the data through Equation (1), it is used to correct the measured charge values based on the difference between the measured charge from the UAS, and predicted values from the linear regression. This difference is obtained by subtracting the predicted charge values from the measured charge (i.e., the residual), which is what we consider as the remaining dust charge variability after the aircraft charging has been removed:

$$\rho_{\text{corr}} = \rho_{\text{meas}} - \rho_{\text{pred}} \tag{2}$$

Figures 8a and c show the measured charge (gray), plotted alongside the corrected charge (black). Application of the correction factor removes the similarity between the charge and PNC (shown in green), but the corrected charge values are now smaller in magnitude (reaching a maximum of 1 pC $m^{-3}$ in flight 1 and 3 pC $m^{-3}$ in flight 2). In both flights, the largest charge is observed at the horizontal edges of the dust layer, the source of which is investigated in the following section.

### 3.4. Modeling dust layer charge

The two main mechanisms thought to be responsible for dust particle charging are triboelectrification and attachment of ions to particles (Mallios et al. 2021). To accurately predict the charge expected in a dust layer, a detailed model including both of these processes is required, as has been done in Mallios, Daskalopoulou, and Amiridis (2022). However, the development of such a model is outside the scope of the present work. Instead, here the expected charge in the dust layer is estimated only by employing ion-attachment considerations in one dimension (i.e., vertically), and then used as a basis for comparison with the corrected space charge. Ion generation occurs in the lower atmosphere due to ionization from Galactic Cosmic Rays (GCRs) and surface radioactivity (Bazilevskaya et al. 2008), with ions driven vertically due to the global electric circuit (GEC). This produces a vertical electric current flow $J_c$, which provides a constant supply of ions into the dust layer. Attachment of the small ions to the much larger dust particles causes the particles to charge, but also reduces the electrical conductivity of the air $\sigma$ (where "clean" particle free air has a high conductivity, and particle laden air has a low conductivity"). Conductivity is calculated according to:

$$\sigma = e \cdot (n_+ \mu_+ + n_- \mu_-) \tag{3}$$

where $e$ is the elementary charge ($1\ e = 1.6 \cdot 10^{-19}\ C$), $n_\pm$ and $\mu_\pm$ are the positive and negative ion number concentrations and ion mobilities, respectively. In the case where dust particles are present, ion concentrations are calculated from the ion-balance equation, modified to include the aerosol effect on ion reduction (Hoppel 1986; Harrison and Carslaw 2003):

$$\frac{dn}{dt} = q - \alpha n^2 - \beta n Z \tag{4}$$

where $q$ is the ion production rate, $\alpha$ is the ion-ion recombination coefficient, $\beta$ is the ion-particle

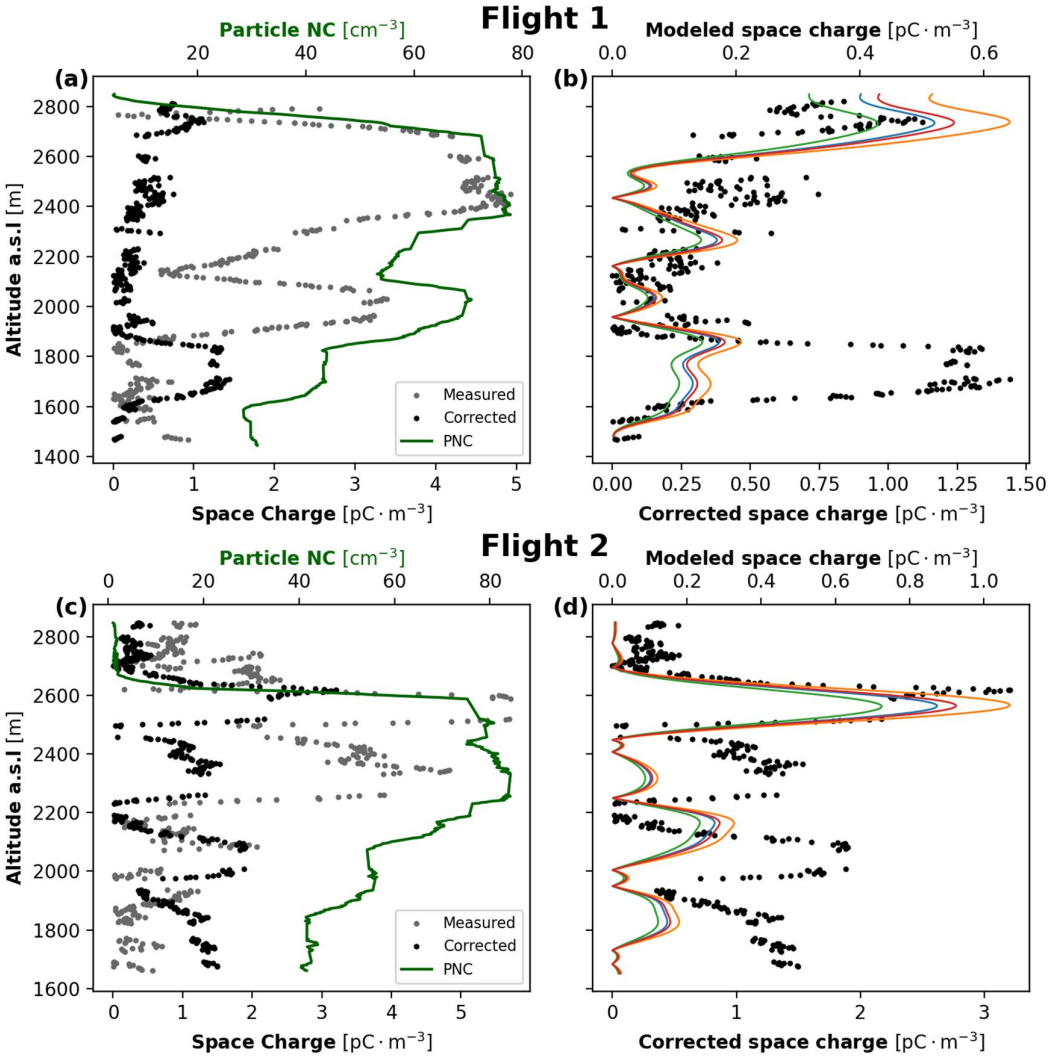


**Figure 8.** PNC, measured and modeled space charge, with the addition of corrected charge data, for the two flights. (a) 20 s Moving averaged PNC (green line), measured (gray points) and corrected charge (black points) on double horizontal axes, (b) modeled charge (solid lines) for different cases of background aerosol values (specifically: blue line for PNC = 1500 cm$^{-3}$ of 0.05 μm radius, orange line for PNC = 1500 cm$^{-3}$ of 0.2 μm radius, green line for PNC = 500 cm$^{-3}$ of 0.05 μm radius and red line for PNC = 500 cm$^{-3}$ of 0.2 μm radius), and corrected charge (black points) on double horizontal axes. On the bottom row, the plots show the same parameters for flight 2, from (c) to (d). Only the ascent is shown in the plots.

attachment coefficient, and $Z$ is the dust concentration. For Equation (4), the following values were assumed: $\alpha = 1.6 \cdot 10^{-12}$ m$^3$ s$^{-1}$, $\mu = 1.7 \cdot 10^{-4}$ m$^2$ V$^{-1}$ s$^{-1}$, $q = 4$ cm$^{-3}$ s$^{-1}$. It should be noted that in these basic calculations, these quantities are assumed to be constant with height, as the vertical variation is minimal over the depth of the dust layer (1.4 km). The ion production rate value of $q = 4$ cm$^{-3}$ s$^{-1}$ is estimated from the model of Usoskin and Kovaltsov (2006) at the altitude of the middle of the dust layer (2.2 km). The ion-particle attachment coefficients $\beta$ were calculated for neutral particles with the measured mean particle diameters from the UAS flights. A more accurate approach would calculate $\beta$ for bipolar charged particles, as well as consider how $\beta$ changes as particles gain and lose charge, but this is outside the scope of the present work. To calculate the space charge $\rho$, we employ Gauss' law in 1-D:

$$\rho = \varepsilon_0 J_c \frac{\mathrm{d}}{\mathrm{d}z}\left(\frac{1}{\sigma}\right) \tag{5}$$

where $z$ is the height ordinate and $\varepsilon_0$ is the permittivity of free space. In this form, Equation (5) has been

shown to be a valid approximation for estimating charge in stratified layer clouds (Nicoll and Harrison 2011), and for charged layers in thunderstorms (Stolzenburg and Marshall 1994). The approach has been further implemented in more recent studies as well for the same purpose (Nicoll and Harrison 2016; Harrison, Nicoll, and Aplin 2017). Thus, since $\rho$ depends on the vertical gradient in conductivity $d\sigma/dz$ we expect that space charge will exist at the upper and lower horizontal boundaries of the dust layer, where there is a substantial gradient in the dust particle concentration, and therefore conductivity, e.g., as in Zhou and Tinsley (2007); Nicoll and Harrison (2016). To estimate the space charge in flights 1 and 2, the conductivity is first calculated from Equations (3) and (4), using the measured PNC and sizes from the OPC-Pod. Space charge is then calculated from the derived vertical gradient in conductivity with Equation (5) (using interpolation spines to emphasize the dominant regions of charge). The resulting vertical profiles from the two flights are shown in Figure 8. A range of background values for the clean air aerosol concentration and radius (i.e., away from the plume, and smaller than the detection limit of the OPC) has been used to give an idea of the potential variability due to this factor (but this only affects the magnitude of the charge, not the location).

Figure 8 shows an expected layer of charge at the upper edge of the dust layer in both flights (due to the substantial vertical gradient in PNC and therefore $\sigma$), with several smaller charge layers in the lower regions of the dust layer. The vertical gradient in PNC is much less pronounced at the dust layer base than at the top, leading to a much less defined charge layer at the base. The black points in Figure 8 show the corrected space charge from the MASC-3 (i.e., with the effect of aircraft charge removed). Comparison between this and the modeled charge demonstrates close agreement between the location of the predicted and corrected space charge at the upper dust layer edge for both flights (albeit with a difference in the magnitude of the charge, with the corrected charge twice as large in flight 1, and three times as large in flight 2). For flight 1, the location of the lower charge layers is similar between the modeled and corrected profiles, but the magnitude of the lowest charge layer is larger than predicted, and also larger than the uppermost charge layer. For flight 2 there is more of a discrepancy between the location of the modeled and corrected space charge for the lower charge layers. This could be due to the lower correlation between particle number concentration and measured charge (as shown in Figure 7b), which may lead to an incomplete correction factor being applied to account for the aircraft charge.

## 4. Discussion

### 4.1. Vertical charge profiles

The airborne measurements from MASC-3 reported here demonstrated a weakly charged (0.2–3 pC $m^{-3}$) layer of aerosols at an altitude of 1500 − 2500 m a.s.l. The back trajectories discussed in Section 3.1 demonstrate that the aerosols were identified as dust particles originating from Algeria, with an initial transit time of 48 h. Although small, the observed magnitude of charge within the layer is consistent with other observations of charged dust particles in elevated layers above the surface. For example, using a similar sensor to the one reported in this paper but flown on balloons, Harrison et al. (2018) observed space charge up to +10 pC $m^{-3}$ in a Saharan dust layer between 2 and 3 km altitude over the UK. Nicoll, Harrison, and Ulanowski (2010) reported space charge from 5 to 25 pC $m^{-3}$ during balloon flights through high altitude Saharan dust layers over the Cape Verde Isles, and Silva et al. reported charges in the base of elevated Saharan dust layers (derived from near surface E-field measurements) up to 10 and 34 pC $m^{-3}$ at two locations during the same event in Portugal (Silva et al. 2016).

The magnitude of charge in elevated dust layers which have been transported far from their source region is generally orders of magnitude smaller than that observed in dust events close to the lofting region, e.g., in Yair et al. (2016), which is likely due to differences in the charge generation mechanisms. The similarity (both in location and order of magnitude) between the modeled and observed charge reported here supports the concept that one of the mechanisms by which particles in elevated dust layers can become charged is through ion-particle attachment, in a similar manner to stratiform water clouds (Zhou and Tinsley 2007). This supports the theoretical findings of Mallios, Daskalopoulou, and Amiridis (2022), whose calculations found that ion-particle attachment charging dominated over triboelectric charging in a modeled elevated dust layer. The observations of Nicoll, Harrison, and Ulanowski (2010) also showed a well defined charge layer at the upper horizontal boundary of the dust layer, as was found for the MASC-3 measurements reported here and discussed in Section 3.4. It should be noted that Gauss' law in the form of Equation (5) may still not fully apply in asymmetrical layers, or layers of small

horizontal extent, where the E-field may not be solely in the vertical direction (Baumgaertner et al. 2014), and could lead to estimation uncertainties. However, the motivations explained in Section 3.4, combined with the results from our measurements and previous literature, illustrate how the approach is still reasonable to employ. The location of the lower charge layers away from the upper dust layer edge correlates with some of the locations where there are vertical gradients in PNC (and therefore conductivity), but it is also possible that charge generated on the edges of the dust layer can be mixed turbulently into the bulk of the layer. There is some support for this in that the both MASC-3 flights show slightly larger TKE at the top of the dust layer, which may act to transport charge down from the upper edge toward the middle of the layer, but this is not conclusive. Since only a basic approximation of ion-particle attachment charging is included here, this is likely also to be a source of the discrepancy between the modeled and measured charge within the dust layer and a more detailed modeling approach, such as that in Mallios, Daskalopoulou, and Amiridis (2022), may produce a better agreement between the two.

The long time (48 h) between the dust lofting stage and charge measurement period suggests that any initial charge on the particles, such as that generated through triboelectrification, would have decayed (e.g., based on the ion-balance equation and measured aerosol concentration and size, the relaxation time is on the order of several minutes). It is possible that further particle-particle collisional charging may have occurred during the dust transit phase, but at the time of the MASC-3 flight it is unlikely that substantial charge was generated due to the relatively small PNC and low likelihood of collisions. We therefore conclude that the majority of the charge observed in the dust layer was due to charge generation from ion-particle attachment, as per Mallios, Daskalopoulou, and Amiridis (2022). There is unlikely to be any effect of such small levels of charge on the motion of the dust particles, or particle alignment (Ulanowski et al. 2007) in this particular layer, but it is likely that layers with larger particle number concentrations, and sharper particle/clear air edges will become more highly charged through the ion-particle attachment layer charging mechanism supported by the observations reported here. Our observations are also in agreement with the modeling study by Mallios, Daskalopoulou, and Amiridis (2022), who surmised that these small charges suggest that the electrical forces on the particles would be an order of magnitude smaller than the gravitational force and therefore, large particles at least, would be unlikely to be held aloft by electrical influences in this particular dust layer.

### 4.2. Aircraft charge correction limitations

As discussed in detail in Section 3.3, the high correlation between the PNC and measured charge led to the conclusion that at least some of the voltage change measured by the charge sensor was due to accumulation of charge on the body of the aircraft. Previous studies, e.g., by Perala (2009) have suggested that this is due to triboelectrification of the aircraft body from interaction with the dust particles, and is independent of particle charge. Our assessment of the limited literature around dust electrification of aircraft, e.g., Perala (2009); Lekas (2019), is that quantifying dust particle charge from aircraft measurements has not fully been possible in the past with crewed aircraft, due to the large charge of the aircraft itself dominating the E-field measurements.

By using a UAS like the MASC-3, which has a smaller surface area and flies at much slower speeds, the density of dust particles intercepted by the aircraft is much lower than for a crewed aircraft. In addition, the careful placement of the sensor pods (mounted in front of the wings) on the MASC-3, coated in conductive foil, minimizes the effect of charge on the aircraft body on the charge measurement. Therefore, we suspect that the measurements reported here are the first successful measurements of dust charge during an aircraft flight. Limitations in the aircraft charge correction factor derived in Section 3.3 do, however, exist, such as the assumption that the aircraft charge is linearly dependent on PNC, and any error in the correction factor will couple through to the final value for the corrected space charge. However, the similarity, both in the location and order of magnitude, between the modeled and corrected space charge (shown in Figure 8) suggests that these errors are minor and the aircraft correction factor is sensible.

## 5. Conclusions

This study reports rare, simultaneous in-situ observations of vertical aerosol and charge profiles made through an elevated layer of Saharan dust passing over Cyprus, using a UAS of type MASC-3 on 6 April 2022. Back trajectory simulations and satellite imagery showed the dust layer's origins over Algeria approximately 48 h before the UAS flights. Vertical profiles (during the morning and afternoon) showed the dust layer at altitudes between 1500 and 2500 m, with

particle number concentration peaks between 80 and 100 $cm^{-3}$ (97% of particles less than 2.5 μm in size). Elevated values of charge were observed within the dust layer, and found to be highly linearly correlated with the particle number concentration, suggesting a small influence of aircraft surface charge on the charge measurements. A correction factor (based on linear regression between the measured charge and particle number concentration) was developed and applied to the charge data, resulting in corrected charge values of 1.5–3 pC $m^{-3}$ inside the dust layer. The largest magnitude of charge (from both flights) was found to be associated with the horizontal edges of the dust layer, in the region where a sharp boundary between particle laden and clear air was identified. A comparison was made between the charge predicted from particle-ion attachment through the dust layer and the observed corrected charge, and close agreement found for the location and magnitude of the charge from both flights. This suggests that by the time of the UAS measurements (48 h from the source region), any residual charge on the dust particles which was generated from triboelectrification during the lofting phase had decayed, with the observed charge likely being generated from attachment with ions in the dust layer. These measurements demonstrate for the first time that with careful design and placement of sensors, fixed wing UAS can be used for dust particle charge measurements, and this has not been possible previously on crewed aircrafts, which are subject to much higher levels of aircraft surface charging. Although the estimated corrected charge here is small, and unlikely to affect the behavior of large aerosols in this particular dust layer, these rare measurements provide valuable insight into the magnitude of charge and charging mechanisms expected in elevated layers of dust far from their source regions.

## Acknowledgements

The authors would like to thank the colleagues of the Environmental Physics work group at the university of Tübingen (Matteo Bramati, Kjell zum Berge, Ines Schäfer, Hasan Mashni), for providing logistical and technical support for the measurement flights in Cyprus. We'd also like to thank Henrik Rieth, who was the pilot of the UAS during the experimental campaign. Sincere thanks to Christos Keleshis and his colleagues, who supported us during our stay in Cyprus, and to Philippe Goloub, for curating the AOD data in AERONET. Lastly, thanks to R.G. Harrison for the discussions on the charge sensor data.

## Disclosure statement

No potential conflict of interest was reported by the author(s).

## Funding

This work is partly funded by the European Union Horizon 2020 Research and Innovation Framework Programme under [grant agreement no. 861291], as part of the Train2Wind Marie Sklodowska-Curie Innovation Training Network (https://www.train2wind.eu/). Funding for the operation of the LiDAR and sun photometers in Cyprus was obtained from the EMME-CARE project (https://emme-care.cyi.ac.cy/). Partial funding for the experimental flights was also obtained from the Trans-National Access (TNA) project IMSAP, by the European Commision and Horizon 2020 [H2020-INFRADEV-2019-2, under grant agreement no. 871115]. K.A.N. acknowledges an Independent Research Fellowship funded by the Natural Environment Research Council (NERC) [NE/L011514/1 and NE/L011514/2].

## ORCID

Vasileios Savvakis http://orcid.org/0000-0001-9568-1766
Franco Marenco http://orcid.org/0000-0002-1833-1102

## Data availability statement

Output of the HYSPLIT model was taken from NOAA's website, which is available online: https://www.ready.noaa.gov. CALIPSO data were obtained from the NASA Langley Research Center Atmospheric Science Data Center: https://asdc.larc.nasa.gov/. SEVIRI data were available from Center for Environmental Data Analysis: https://data.ceda.ac.uk/badc/msg/data, and provided by EUMETSAT. AOD data were retrieved from the website of the AERONET network: https://aeronet.gsfc.nasa.gov/. Data from the UAS flights can be provided by the corresponding author, upon reasonable request.

## References

Adebiyi, A. A., and J. F. Kok. 2020. Climate models miss most of the coarse dust in the atmosphere. *Sci. Adv.* 6 (15):eaaz9507. doi:10.1126/sciadv.aaz9507.

Aminou, D. 2002. MSG'S Seviri instrument. *ESA Bull.* 111 15–17.

Baumgaertner, A., G. Lucas, J. Thayer, and S. Mallios. 2014. On the role of clouds in the fair weather part of the global electric circuit. *Atmos. Chem. Phys.* 14 (16):8599–610. doi:10.5194/acp-14-8599-2014.

Bazilevskaya, G., I. Usoskin, E. Flückiger, R. Harrison, L. Desorgher, R. Bütikofer, M. Krainev, V. Makhmutov, Y. I. Stozhkov, A. Svirzhevskaya, et al. 2008. Cosmic ray induced ion production in the atmosphere. *Space Sci. Rev.* 137 (1–4):149–73. doi:10.1007/s11214-008-9339-y.

Brindley, H., P. Knippertz, C. Ryder, and I. Ashpole. 2012. A critical evaluation of the ability of the spinning

enhanced visible and infrared imager (Seviri) thermal infrared red-green-blue rendering to identify dust events: Theoretical analysis. *J. Geophys. Res.* 117 (D7). doi:10.1029/2011JD017326.

Carlson, T. N., and S. G. Benjamin. 1980. Radiative heating rates for Saharan dust. *J. Atmos. Sci.* 37 (1):193–213. doi:10.1175/1520-0469(1980)037<0193:RHRFSD>2.0.CO;2.

Daskalopoulou, V., S. A. Mallios, Z. Ulanowski, G. Hloupis, A. Gialitaki, I. Tsikoudi, K. Tassis, and V. Amiridis. 2021. The electrical activity of Saharan dust as perceived from surface electric field observations. *Atmos. Chem. Phys.* 21 (2):927–49. doi:10.5194/acp-21-927-2021.

Esposito, F., R. Molinaro, C. Popa, C. Molfese, F. Cozzolino, L. Marty, K. Taj-Eddine, G. Di Achille, G. Franzese, S. Silvestro, et al. 2016. The role of the atmospheric electric field in the dust-lifting process. *Geophys. Res. Lett.* 43 (10):5501–8. doi:10.1002/2016GL068463.

Fernald, F. G. 1984. Analysis of atmospheric Lidar observations: Some comments. *Appl. Opt.* 23 (5):652–3. doi:10.1364/ao.23.000652.

Franzese, G., F. Esposito, R. Lorenz, S. Silvestro, C. I. Popa, R. Molinaro, F. Cozzolino, C. Molfese, L. Marty, and N. Deniskina. 2018. Electric properties of dust devils. *Earth Planet. Sci. Lett.* 493:71–81. doi:10.1016/j.epsl.2018.04.023.

Ginoux, P., M. Chin, I. Tegen, J. M. Prospero, B. Holben, O. Dubovik, and S.-J. Lin. 2001. Sources and distributions of dust aerosols simulated with the GOCART model. *J. Geophys. Res.* 106 (D17):20255–73. doi:10.1029/2000JD00 0053.

Goudie, A. S., and N. J. Middleton. 2001. Saharan dust storms: Nature and consequences. *Earth. Sci. Rev.* 56 (1–4):179–204. doi:10.1016/S0012-8252(01)00067-8.

Granados-Muñoz, M. J., J. A. Bravo-Aranda, D. Baumgardner, J. L. Guerrero-Rascado, D. Pérez-Ramírez, F. Navas-Guzmán, I. Veselovskii, H. Lyamani, A. Valenzuela, F. J. Olmo, et al. 2016. A comparative study of aerosol microphysical properties retrieved from ground-based remote sensing and aircraft in situ measurements during a Saharan dust event. *Atmos. Meas. Tech.* 9 (3):1113–33. doi:10.5194/amt-9-1113-2016.

Gringel, W., and R. Muhleisen. 1978. Sahara dust concentration in the troposphere over the North Atlantic derived from measurements of air conductivity. *Beitr. Phys. Atmosph.* 2 (51): 121–8.

Hagan, D. H., and J. H. Kroll. 2020. Assessing the accuracy of low-cost optical particle sensors using a physics-based approach. *Atmos. Meas. Tech.* 13 (11):6343–55. doi:10.5194/amt-13-6343-2020.

Harrison, R., and K. Carslaw. 2003. Ion-aerosol-cloud processes in the lower atmosphere. *Rev. Geophys.* 41 (3). doi:10.1029/2002RG000114.

Harrison, R. G., K. A. Nicoll, and K. L. Aplin. 2017. Evaluating stratiform cloud base charge remotely. *Geophys. Res. Lett.* 44 (12):6407–12. doi:10.1002/2017GL073128.

Harrison, R. G., K. A. Nicoll, E. Mareev, N. Slyunyaev, and M. J. Rycroft. 2020. Extensive layer clouds in the global electric circuit: Their effects on vertical charge distribution and storage. *Proc. Math. Phys. Eng. Sci.* 476 (2238): 20190758. doi:10.1098/rspa.2019.0758.

Harrison, R. G., K. A. Nicoll, G. J. Marlton, C. L. Ryder, and A. J. Bennett. 2018. Saharan dust plume charging observed over the UK. *Environ. Res. Lett.* 13 (5):054018. doi:10.1088/1748-9326/aabcd9.

Haywood, J. M., P. N. Francis, M. D. Glew, and J. P. Taylor. 2001. Optical properties and direct radiative effect of Saharan dust: A case study of two Saharan dust outbreaks using aircraft data. *J. Geophys. Res.* 106 (D16): 18417–30. doi:10.1029/2000JD900319.

Holben, B. N., T. F. Eck, I. a Slutsker, D. Tanré, J. Buis, A. Setzer, E. Vermote, J. A. Reagan, Y. Kaufman, T. Nakajima, et al. 1998. Aeronet-a federated instrument network and data archive for aerosol characterization. *Remote Sens. Environ.* 66 (1):1–16. doi:10.1016/S0034-4257(98)00031-5.

Hoppel, W. A. 1986. Atmospheric electricity in the planetary boundary layer. In *Earth's Electrical Environment,* ed. National Research Council, 149–165. Washington, DC: National Academies Press.

Israelevich, P., E. Ganor, P. Alpert, P. Kishcha, and A. Stupp. 2012. Predominant transport paths of saharan dust over the Mediterranean Sea to Europe. *J. Geophys. Res.* 117 (D2). doi:10.1029/2011JD016482.

Jaenicke, R., and T. Hanusch. 1993. Simulation of the optical particle counter forward scattering spectrometer probe 100 (FSSP-100). *Aerosol Sci. Technol.* 18 (4):309–22. doi:10.1080/02786829308959607.

Johnson, B., and S. Osborne. 2011. Physical and optical properties of mineral dust aerosol measured by aircraft during the GERBILS campaign. *Quart. J. Royal Meteoro. Soc.* 137 (658):1117–30. doi:10.1002/qj.777.

Kamra, A. 1972. Measurements of the electrical properties of dust storms. *J. Geophys. Res.* 77 (30):5856–69. doi:10.1029/JC077i030p05856.

Katz, S., Y. Yair, C. Price, R. Yaniv, I. Silber, B. Lynn, and B. Ziv. 2018. Electrical properties of the 8–12th September, 2015 massive dust outbreak over the Levant. *Atmos. Res.* 201:218–25. doi:10.1016/j.atmosres.2017.11.004.

Kezoudi, M., C. Keleshis, P. Antoniou, G. Biskos, M. Bronz, C. Constantinides, M. Desservettaz, R.-S. Gao, J. Girdwood, J. Harnetiaux, et al. 2021a. The unmanned systems research laboratory (USRL): A new facility for UAV-based atmospheric observations. *Atmosphere* 12 (8): 1042. doi:10.3390/atmos12081042.

Kezoudi, M., M. Tesche, H. Smith, A. Tsekeri, H. Baars, M. Dollner, V. Estellés, J. Bühl, B. Weinzierl, Z. Ulanowski, et al. 2021b. Measurement report: Balloon-borne in situ profiling of Saharan dust over Cyprus with the UCASS optical particle counter. *Atmos. Chem. Phys.* 21 (9):6781–97. doi:10.5194/acp-21-6781-2021.

Kim, M.-H., A. H. Omar, J. L. Tackett, M. A. Vaughan, D. M. Winker, C. R. Trepte, Y. Hu, Z. Liu, L. R. Poole, M. C. Pitts, et al. 2018. The CALIPSO version 4 automated aerosol classification and Lidar ratio selection algorithm. *Atmos. Meas. Tech.* 11 (11):6107–35. doi:10.5194/amt-11-6107-2018.

Klett, J. D. 1981. Stable analytical inversion solution for processing LIDAR returns. *Appl. Opt.* 20 (2):211–20. doi:10.1364/AO.20.000211.

Lekas, T. I. 2019. Electrostatic charging of an aircraft due to airborne dust particles impacts. *CEAS Aeronaut. J.* 10 (3): 903–8. doi:10.1007/s13272-018-00355-0.

Lekas, T. I., J. Kushta, S. Solomos, and G. Kallos. 2014. Some considerations related to flight in dusty conditions. *AOP.* 3 (1):45–56. doi:10.3233/AOP-140043.

Lensky, I. M., and D. Rosenfeld. 2008. Clouds-aerosols-precipitation satellite analysis tool (CAPSAT). *Atmos. Chem. Phys.* 8 (22):6739–53. doi:10.5194/acp-8-6739-2008.

Mallios, S., V. Daskalopoulou, V. Spanakis-Misirlis, G. Hloupis, and V. Amiridis. 2023. Novel measurements of desert dust electrical properties: A multi-instrument approach during the ASKOS 2022 campaign. *Environ. Sci. Proceed.* 26 (1):22.

Mallios, S. A., V. Daskalopoulou, and V. Amiridis. 2022. Modeling of the electrical interaction between desert dust particles and the Earth's atmosphere. *J. Aerosol Sci.* 165: 106044. doi:10.1016/j.jaerosci.2022.106044.

Mallios, S. A., G. Papangelis, G. Hloupis, A. Papaioannou, V. Daskalopoulou, and V. Amiridis. 2021. Modeling of spherical dust particle charging due to ion attachment. *Front. Earth Sci.* 9:709890. doi:10.3389/feart.2021.709890.

Mamali, D., E. Marinou, J. Sciare, M. Pikridas, P. Kokkalis, M. Kottas, I. Binietoglou, A. Tsekeri, C. Keleshis, R. Engelmann, et al. 2018. Vertical profiles of aerosol mass concentration derived by unmanned airborne in situ and remote sensing instruments during dust events. *Atmos. Meas. Tech.* 11 (5):2897–910. doi:10.5194/amt-11-2897-2018.

Marenco, F., C. Ryder, V. Estellés, D. O'Sullivan, J. Brooke, L. Orgill, G. Lloyd, and M. Gallagher. 2018. Unexpected vertical structure of the Saharan Air Layer and giant dust particles during AER-D. *Atmos. Chem. Phys.* 18 (23): 17655–68. doi:10.5194/acp-18-17655-2018.

Maring, H., D. Savoie, M. Izaguirre, L. Custals, and J. Reid. 2003. Mineral dust aerosol size distribution change during atmospheric transport. *J. Geophys. Res.* 108 (D19). doi:10.1029/2002JD002536.

Martínez, M. A., J. Ruiz, and E. Cuevas. 2009. Use of seviri images and derived products in a wmo sand and dust storm warning system. *IOP Conf. Ser: Earth Environ. Sci.* 7:012004. doi:10.1088/1755-1307/7/1/012004.

Mashni, H., H. Knaus, A. Platis, and J. Bange. 2023. Development of an airfoil-based passive volumetric air sampling and flow control system for fixed-wing UAS. *Bull. Atmos. Sci. Technol.* 4 (1):6. doi:10.1007/s42865-023-00057-4.

Mauz, M., A. Rautenberg, A. Platis, M. Cormier, and J. Bange. 2019. First identification and quantification of detached-tip vortices behind a wind energy converter using fixed-wing unmanned aircraft system. *Wind Energ. Sci.* 4 (3):451–63. doi:10.5194/wes-4-451-2019.

Nicoll, K., and R. Harrison. 2009. A lightweight balloon-carried cloud charge sensor. *Rev. Sci. Instrum.* 80 (1): 014501. doi:10.1063/1.3065090.

Nicoll, K., and R. Harrison. 2011. Charge measurements in stratiform cloud from a balloon based sensor. *J. Phys: Conf. Ser.* 301:012003. doi:10.1088/1742-6596/301/1/012003.

Nicoll, K., R. Harrison, and Z. Ulanowski. 2010. Observations of Saharan dust layer electrification. *Environ. Res. Lett.* 6 (1):014001. doi:10.1088/1748-9326/6/1/014001.

Nicoll, K., and R. G. Harrison. 2016. Stratiform cloud electrification: Comparison of theory with multiple in-cloud measurements. *Quart. J. Royal Meteoro. Soc.* 142 (700): 2679–91. doi:10.1002/qj.2858.

Nicoll, K. A., R. G. Harrison, H. G. Silva, R. Salgado, M. Melgâo, and D. Bortoli. 2018. Electrical sensing of the dynamical structure of the planetary boundary layer. *Atmos. Res.* 202:81–95. doi:10.1016/j.atmosres.2017.11.009.

Nurowska, K., M. Mohammadi, S. Malinowski, and K. Markowicz. 2022. Applicability of the low-cost optical particle counter OPC-N3 for microphysical measurements of fog. *Atmos. Meas. Tech. Discuss.* 2022:1–25.

O'Sullivan, D., F. Marenco, C. L. Ryder, Y. Pradhan, Z. Kipling, B. Johnson, A. Benedetti, M. Brooks, M. McGill, J. Yorks, et al. 2020. Models transport Saharan dust too low in the atmosphere: A comparison of the MetUM and CAMS forecasts with observations. *Atmos. Chem. Phys.* 20 (21):12955–82. doi:10.5194/acp-20-12955-2020.

Papetta, A., F. Marenco, R.-E. Mamouri, A. Nisantzi, I. E. Popovici, P. Goloub, M. Kezoudi, S. Victori, and J. Sciare. 2023. Lidar depolarization characterization using a reference system. *EGUsphere* 2023:1–25.

Perala, R. 2009. A critical review of precipitation static research since the 1930's and comparison to aircraft charging by dust. Electro Magnetic Applications Inc 7655, Denver, CO.

Platis, A., B. Altstädter, B. Wehner, N. Wildmann, A. Lampert, M. Hermann, W. Birmili, and J. Bange. 2016. An observational case study on the influence of atmospheric boundary-layer dynamics on new particle formation. *Boundary-Layer Meteorol.* 158 (1):67–92. doi:10.1007/s10546-015-0084-y.

Rautenberg, A., M. Schön, K. Zum Berge, M. Mauz, P. Manz, A. Platis, B. van Kesteren, I. Suomi, S. T. Kral, and J. Bange. 2019. The multi-purpose airborne sensor carrier MASC-3 for wind and turbulence measurements in the atmospheric boundary layer. *Sensors* 19 (10):2292. doi:10.3390/s19102292.

Renard, J.-B., F. Dulac, G. Berthet, T. Lurton, D. Vignelles, F. Jégou, T. Tonnelier, M. Jeannot, B. Couté, R. Akiki, et al. 2016. LOAC: a small aerosol optical counter/sizer for ground-based and balloon measurements of the size distribution and nature of atmospheric particles–part 1: Principle of measurements and instrument evaluation. *Atmos. Meas. Tech.* 9 (4):1721–42. doi:10.5194/amt-9-1721-2016.

Renard, J.-B., F. Dulac, P. Durand, Q. Bourgeois, C. Denjean, D. Vignelles, B. Couté, M. Jeannot, N. Verdier, and M. Mallet. 2018. In situ measurements of desert dust particles above the western Mediterranean sea with the balloon-borne light optical aerosol counter/sizer (loac) during the Charmex campaign of summer 2013. *Atmos. Chem. Phys.* 18 (5):3677–99. doi:10.5194/acp-18-3677-2018.

Rudge, W. D. 1913. Atmospheric electrification during South African dust storms. *Nature* 91 (2263):31–2. doi:10.1038/091031a0.

Ryder, C. L., E. J. Highwood, P. D. Rosenberg, J. Trembath, J. K. Brooke, M. Bart, A. Dean, J. Crosier, J. Dorsey, H. Brindley, et al. 2013. Optical properties of Saharan dust aerosol and contribution from the coarse mode as measured during the Fennec 2011 aircraft campaign. *Atmos. Chem. Phys.* 13 (1):303–25. doi:10.5194/acp-13-303-2013.

Ryder, C. L., E. J. Highwood, A. Walser, P. Seibert, A. Philipp, and B. Weinzierl. 2019. Coarse and giant particles are ubiquitous in Saharan dust export regions and

are radiatively significant over the Sahara. *Atmos. Chem. Phys.* 19 (24):15353–76. doi:10.5194/acp-19-15353-2019.

Schön, M., K. A. Nicoll, Y. G. Büchau, S. Chindea, A. Platis, and J. Bange. 2022. Fair-weather atmospheric charge measurements with a small UAS. *Journal of Atmospheric and Oceanic Technology* 39 (11):1799–813. doi:10.1175/JTECH-D-22-0025.1.

Schön, M., V. Savvakis, M. Kezoudi, A. Platis, and J. Bange. 2024. OPC-Pod: A new sensor payload to measure aerosol particles for small uncrewed aircraft systems. *Journal of Atmospheric and Oceanic Technology* 41 (5):499–513. doi:10.1175/JTECH-D-23-0078.1.

Schrod, J., D. Weber, J. Drücke, C. Keleshis, M. Pikridas, M. Ebert, B. Cvetković, S. Nickovic, E. Marinou, H. Baars, et al. 2017. Ice nucleating particles over the Eastern Mediterranean measured by unmanned aircraft systems. *Atmos. Chem. Phys.* 17 (7):4817–35. doi:10.5194/acp-17-4817-2017.

Silva, H., F. Lopes, S. Pereira, K. Nicoll, S. Barbosa, R. Conceição, S. Neves, R. G. Harrison, and M. C. Pereira. 2016. Saharan dust electrification perceived by a triangle of atmospheric electricity stations in Southern Portugal. *J. Electrostat.* 84:106–20. doi:10.1016/j.elstat.2016.10.002.

Smirnov, A., B. Holben, I. Slutsker, E. Welton, and P. Formenti. 1998. Optical properties of Saharan dust during ACE 2. *J. Geophys. Res.* 103 (D21):28079–92. doi:10.1029/98JD01930.

Smith, H. R., Z. Ulanowski, P. H. Kaye, E. Hirst, W. Stanley, R. Kaye, A. Wieser, C. Stopford, M. Kezoudi, J. Girdwood, et al. 2019. The universal cloud and aerosol sounding system (UCASS): a low-cost miniature optical particle counter for use in dropsonde or balloon-borne sounding systems. *Atmos. Meas. Tech.* 12 (12):6579–99. doi:10.5194/amt-12-6579-2019.

Soupiona, O., A. Papayannis, P. Kokkalis, R. Foskinis, G. Sánchez Hernández, P. Ortiz-Amezcua, M. Mylonaki, C.-A. Papanikolaou, N. Papagiannopoulos, S. Samaras, et al. 2020. EARLINET observations of Saharan dust intrusions over the northern Mediterranean region (2014–2017): Properties and impact on radiative forcing. *Atmos. Chem. Phys.* 20 (23):15147–66. doi:10.5194/acp-20-15147-2020.

Stein, A., R. R. Draxler, G. D. Rolph, B. J. Stunder, M. D. Cohen, and F. Ngan. 2015. NOAA's HYSPLIT atmospheric transport and dispersion modeling system. *Bull. Am. Meteorol. Soc.* 96 (12):2059–77. doi:10.1175/BAMS-D-14-00110.1.

Stolzenburg, M., and T. C. Marshall. 1994. Testing models of thunderstorm charge distributions with Coulomb's law. *J. Geophys. Res. Atmos.* 99 (D12):25921–32.

Stuut, J.-B., I. Smalley, and K. O'Hara-Dhand. 2009. Aeolian dust in Europe: African sources and European deposits. *Quat. Int.* 198 (1–2):234–45. doi:10.1016/j.quaint.2008.10.007.

Tanré, D., J. Haywood, J. Pelon, J. Léon, B. Chatenet, P. Formenti, P. Francis, P. Goloub, E. Highwood, and G. Myhre. 2003. Measurement and modeling of the Saharan dust radiative impact: Overview of the Saharan dust experiment (SHADE). *J. Geophys. Res.* 108 (D18). doi:10.1029/2002JD003273.

Tesche, M., S. Gross, A. Ansmann, D. Müller, D. Althausen, V. Freudenthaler, and M. Esselborn. 2011. Profiling of saharan dust and biomass-burning smoke with multiwavelength polarization Raman lidar at Cape Verde. *Tellus B: Chem. Phys. Meteorol.* 63 (4):649–76. doi:10.1111/j.1600-0889.2011.00548.x.

Ulanowski, Z., J. Bailey, P. Lucas, J. Hough, and E. Hirst. 2007. Alignment of atmospheric mineral dust due to electric field. *Atmos. Chem. Phys.* 7 (24):6161–73. doi:10.5194/acp-7-6161-2007.

Ulanowski, Z., O. V. Kalashnikova, P. W. Lucas, and B. Berçot. 2008. Influence of alignment on the scattering properties atmospheric mineral dust. Proceedings of 11th Electromagnetic and Light Scattering Conference 2008, University of Hertfordshire.

Usoskin, I. G., and G. A. Kovaltsov. 2006. Cosmic ray induced ionization in the atmosphere: Full modeling and practical applications. *J. Geophys. Res.* 111 (D21). doi:10.1029/2006JD007150.

Van Der Does, M., P. Knippertz, P. Zschenderlein, R. Giles Harrison, and J.-B. W. Stuut. 2018. The mysterious long-range transport of giant mineral dust particles. *Sci. Adv.* 4 (12):eaau2768. doi:10.1126/sciadv.aau2768.

Varga, G., G. Újvári, and J. Kovács. 2014. Spatiotemporal patterns of Saharan dust outbreaks in the Mediterranean basin. *Aeolian Res.* 15:151–60. doi:10.1016/j.aeolia.2014.06.005.

Williams, E., N. Nathou, E. Hicks, C. Pontikis, B. Russell, M. Miller, and M. Bartholomew. 2009. The electrification of dust-lofting gust fronts ("haboobs") in the Sahel. *Atmos. Res.* 91 (2–4):292–8. doi:10.1016/j.atmosres.2008.05.017.

Winker, D., J. Pelon, J. Coakley, Jr, S. Ackerman, R. Charlson, P. Colarco, P. Flamant, Q. Fu, R. Hoff, C. Kittaka, et al. 2010. The CALIPSO mission: A global 3D view of aerosols and clouds. *Bulletin of the American Meteorological Society* 91 (9):1211–30. doi:10.1175/2010BAMS3009.1.

Yair, Y., S. Katz, R. Yaniv, B. Ziv, and C. Price. 2016. An electrified dust storm over the Negev Desert, Israel. *Atmos. Res.* 181:63–71. doi:10.1016/j.atmosres.2016.06.011.

Zhang, H., T.-L. Bo, and X. Zheng. 2017. Evaluation of the electrical properties of dust storms by multi-parameter observations and theoretical calculations. *Earth Planet. Sci. Lett.* 461:141–50. doi:10.1016/j.epsl.2017.01.001.

Zhang, H., and Y.-H. Zhou. 2020. Reconstructing the electrical structure of dust storms from locally observed electric field data. *Nat. Commun.* 11 (1):5072. doi:10.1038/s41467-020-18759-0.

Zhou, L., and B. A. Tinsley. 2007. Production of space charge at the boundaries of layer clouds. *J. Geophys. Res.* 112 (D11). doi:10.1029/2006JD007998.

Zhou, Y.-H., Q. Shu He, and X. Jing Zheng. 2005. Attenuation of electromagnetic wave propagation in sandstorms incorporating charged sand particles. *Eur. Phys. J. E Soft Matter.* 17 (2):181–7. doi:10.1140/epje/i2004-10138-5.

Zum Berge, K., M. Schoen, M. Mauz, A. Platis, B. van Kesteren, D. Leukauf, A. El Bahlouli, P. Letzgus, H. Knaus, and J. Bange. 2021. A two-day case study: Comparison of turbulence data from an unmanned aircraft system with a model chain for complex terrain. *Boundary-Layer Meteorol.* 180 (1):53–78. doi:10.1007/s10546-021-00608-2.